HAL
open science

Experimental study of desorption and reactivity of nitrogen bearing species on interstellar dust grains

Hoang Phuong Nguyen Thanh

To cite this version:

Hoang Phuong Nguyen Thanh. Experimental study of desorption and reactivity of nitrogen bearing species on interstellar dust grains. Solar and Stellar Astrophysics [astro-ph.SR]. Université de Cergy Pontoise, 2018. English. NNT : 2018CERG0977 . tel-02286147

HAL Id: tel-02286147

https://theses.hal.science/tel-02286147

Submitted on 13 Sep 2019

HAL is a multi-disciplinary open access archive for the deposit and dissemination of scientific research documents, whether they are published or not. The documents may come from teaching and research institutions in France or abroad, or from public or private research centers.

L'archive ouverte pluridisciplinaire **HAL**, est destinée au dépôt et à la diffusion de documents scientifiques de niveau recherche, publiés ou non, émanant des établissements d'enseignement et de recherche français ou étrangers, des laboratoires publics ou privés.

UNIVERSITÉ DE CERGY PONTOISE
Départment de Physique
LERMA-Cergy - Observatoire de Paris

Experimental study of desorption and reactivity of nitrogen bearing species on interstellar dust grains

A DISSERTATION PRESENTED
BY
NGUYEN Hoang Phuong Thanh

Supervisor: **Prof. François Dulieu**
Invited jury member: **Dr. Laurent Pagani**

Referee: **Prof. Naoki Watanabe**
Referee: **Dr. Fabrice Duvernay**

Examiner: **Prof. Nadia Balucani**
Examiner: **Dr. Valentine Wakelam**
Examiner: **Dr. Dahbia Talbi**

October 15th, 2018

Acknowledgements

My Ph.D. lifetime seems like an adventure not only in the field of study but also in a country that is half of the Earth's circle away from my homeland. LERMA laboratory is a very likely place and gives plenty of opportunities to meet bright people. During the three years, I have benefited from the support of my supervisor, colleagues, and friends at the LERMA laboratory of the University of Cergy Pontoise.

Firstly, I would like to thank my supervisor Prof. François Dulieu for teaching and sharing knowledge to me, as well as for encouraging and trusting me since the beginning of my Ph.D. journey. His encouragements helped me passing through the difficulties that I encounter during the Ph.D. period. He spent a lot of time to listen to my thinking so that I could share my idea and learned back many things from him.

Secondly, I acknowledge Prof. Laurent Pagani for guiding and supporting during my Ph.D. period. Although he was only my co-supervisor for the first year, I learned a lot of things from him.

I am obviously thankful my referees (Prof. Naoki Watanabe and Dr. Fabrice Duvernay) for their astute counsel and for interesting questions which extend and improve my works. Simultaneously, I would like to thank the jury members of my thesis (Prof. Nadia Balucani, Dr. Valentine Wakelam, and Dr. Dahbia Talbi) for excellent remarks, which are useful to the enhancement for my thesis.

Indispensably, I gratefully thank you to Emanuele Congiu, who advised and shared with me not only the experience of the experimental set-up but also favorite songs, singers, and natural pictures with a lot of enthusiasm. I am grateful to Saoud Baouche who guided me how to set-up the experiments and also helped me to solve the technical difficulties that happened. I want to thank Stephan Diana for helping me so much in computer setting and in running models. I want to thank Henda Chaabouni for her discussion and conservation about my works. Special thanks to Abdellahi Sow and AbdiSalam Mohammed for talking about the different cultures, family, and friends around me. I would also like to thank all the wonderful people from the laboratory of Theoretical Chemistry in Sorbonne University, ISM- University of Bordeaux, the Laboratory Universes and Particles of

Montpellier - Montpellier University, and Observatory of Paris for their supporting and in running the great models.

Of course, I am very grateful to my mother, who brought me to this beautiful world and who worked hard and traded off here life and health to make my dream comes true. She encourages me at every step and is always beside me during my journey. I also would like to send a special thank to my grandmother and my mother's brothers who supported me and covered up my mother when I could not be beside her.

Finally, I would also happy to thank all my friends for their lovely supports during three years.

English summary

The interstellar medium (ISM) is a key component of galaxies which is the matrix of the formation of stars and planets. It is composed of interstellar gas and dust grains. The presence of complex organic molecules (COMs) can be understood via reactions in the gas phase. However, the synthesis of some key species (i.e H_2, H_2O, CO_2, etc) needs the intervention of the solid-state reactions on dust grains surface. More than 200 molecules including COMs have been detected in ISM and circumstellar shells. Some of these COMs already contain carbon, oxygen, and nitrogen, which are the main chemical elements in the composition of the molecules on which terrestrial life is built. The aim of this thesis is to understand physical and chemical processes (i.e diffusion, desorption, and reactivity) occurring on interstellar dust grains. More specifically, my thesis focuses on the investigation of desorption and reactivity of nitrogen bearing species that lead to COMs by hydrogenation related processes.

All experiments were performed with the VENUS set-up located at the LERMA Cergy laboratory in the university of Cergy Pontoise, France. VENUS is composed of an Ultra High Vacuum (UHV) chamber, so called the main chamber, with a basis pressure around of 10^{-10} mbar. Atoms/molecules were injected onto a sample holder in the UHV chamber through a separated four beamline system. The sample holder is controlled in temperature from 7 K to 400 K. Products are probed by using mass spectrometer and reflection adsorption infrared spectroscopy. Different solid states environments have been used: gold surface or water ice substrates (compact amorphous solid water, porous amorphous solid water, and crystalline ice) to mimic different the astrophysical environments.

We proceeded experiments involving some atoms and molecules such as hydrogen, deuterium, oxygen, CO, N_2, NO, H_2O, H_2CO, CH_3CN, and CH_3NC. These species were deposited on the cold surface held at 10 K (up to 40 K). CO and N_2 were deposited on water ice substrates to study different adsorbed behaviours as well as the distribution binding energy and the segregation mechanism. We studied the efficiency of atoms (i.e oxygen and hydrogen) penetration into porous water ice. We used NO as a chemical tracer for the penetration of O and H atoms through water ice. From the analysis of the consumption of NO, we estimated the penetration of O or D atoms through porous water ice. We proceed new experiments on the hydrogenation of NO and found that there is an activation barrier at HNO +

H step. However, H atoms can cross the activation barrier via quantum tunneling on the cold surface maintained at 8 K. We indicated that hydroxylamine (NH_2OH) is the major product of the hydrogenation of NO at low temperatures, but N_2O is the major product at high temperatures. We also present possible chemical pathways of the pre-biotic formamide (NH_2CHO) through the co-hydrogenation of NO and H_2CO on the cold surface (typically at 10 K). Simultaneously, we analysed and discussed the efficient formation route of formamide on interstellar grains. We showed that the chemical network of the hydrogenation of CH_3CN and CH_3NC is complex and takes place via different mechanisms which tend to be competitive. We measured and indicated that the hydrogenation is the dominant mechanism. Furthermore, H_2O is always raising the reactive efficiency.

Solid state chemical processes have been simulated in the astrophysical context of the formation of COMs such as low pressures, low temperatures, low gas fluxes, and without the addition of external energy. According to the gas-solid coupling processes (i.e adsorption, thermal desorption, and chemical desorption), COMs are formed via competiting mechanisms and influenced surface substrates (i.e gold surface and water ice substrate), and by kinetic conditions.

Résumé Français

Le milieu interstellaire (ISM) est un élément essentiel des galaxies. Il est en effet la matrice de la formation des étoiles et des planètes. Il est composé de gaz et de poussières interstellaires.

Il est généralement admis que la présence de molécules organiques complexes (COM) est due aux réactions en phase gazeuse. Toutefois, la synthèse de certaines espèces clés (i.e. H_2, H_2O, CO_2, etc.) nécessite l'intervention des réactions en phase solide c'est à dire sur les grains de poussière. Plus de 200 molécules, dont des COM, ont été détectées dans l'ISM.

Et les enveloppes circumstellaires. Certaines de ces COM contiennent déjà du carbone, de l'oxygène, et de l'azote, qui sont les principaux éléments chimiques de la composition des molécules à partir desquelles la vie terrestre s'est construite. L'objectif de cette thèse est de comprendre les processus physiques et chimiques (diffusion, désorption et réactivité) qui se produisent sur les grains de poussière interstellaire. Plus spécifiquement, ma thèse se concentre sur l'étude de la désorption et de la réactivité des espèces azotées qui peuvent mener à des COM par des processus liés à l'hydrogénation.

Toutes les expériences ont été réalisées avec l'expérience VENUS située au laboratoire LERMA à l'université de Cergy Pontoise, France. VENUS est composée d'une chambre à ultra-vide (UHV), appelée chambre principale, dotée d'une pression de base d'environ 10^{-10} mbar. Des atomes/molécules sont dirigées vers un porte-échantillon dans la chambre UHV au moyen d'un système à quatre faisceaux séparés. La température du porte-échantillon peut être contrôlée entre 7 K à 400 K. Les produits sont sondés par spectrométrie de masse et spectroscopie infrarouge par réflexion en adsorption. Différents environnements ont été utilisés : surface d'or ou substrats de glace d'eau (glace amorphe compacte ou poreuse et glace cristalline) pour imiter les différents environnements astrophysiques.

Nous avons procédé à des expériences impliquant certains atomes et molécules comme l'hydrogène, le deutérium, l'oxygène, le CO, N_2, NO, H_2O, H_2O, H_2CO, CH_3CN et CH_3NC. Ces espèces ont été déposées sur une surface froide maintenue à 10 K (et jusqu'à 40 K). CO et N_2 ont été déposés sur des substrats de glace d'eau pour étudier les différents comportements des adsorbats ainsi que la distribution des énergies de désorption et le mécanisme de ségrégation.

Nous avons étudié l'efficacité de la pénétration des atomes (oxygène et hydrogène) dans la glace d'eau poreuse. Nous avons utilisé le NO comme traceur chimique. A partir de l'analyse de la consommation de NO, nous avons estimé la pénétration des atomes O ou D à travers la glace d'eau poreuse.

Nous avons procédé à de nouvelles expériences sur l'hydrogénation du NO et nous avons constaté qu'il existe une barrière d'activation à l'étape HNO + H. Cependant, les atomes H peuvent traverser cette barrière d'activation par effet tunnel sur une surface maintenue à 8 K. Nous avons montré que l'hydroxylamine (NH_2OH) est le principal produit de l'hydrogénation du NO à basse température, mais que le N_2O est le principal produit à haute température.

Nous présentons également les voies chimiques possibles de formation du formamide (NH_2CHO) , molécule clé de la chimie pré-biotique, par co-hydrogénation de NO et de H_2CO sur une surface froide (typiquement à 10 K). Nous avons analysé et montré l'efficacité de cette voie de formation du formamide sur les grains interstellaires.

Nous avons montré que le réseau chimique de l'hydrogénation du CH_3CN et du CH_3NC est complexe et se fait par différents mécanismes qui sont en compétition. Nous avons mesuré et montré que l'hydrogénation est le mécanisme dominant. De plus, la présence de H_2O augmente l'efficacité réactive.

De nombreux processus chimiques en phase solide ont été simulés dans le contexte astrophysique de la formation de COM. Ces conditions comprennent notamment de basses pressions, de basses températures, de faible flux de gaz, et pas d'ajout d'énergie externe. Grâce au couplage gaz-solide (c.-à-d. adsorption, désorption thermique et désorption chimique), les COM peuvent être formées par des mécanismes concurrents et leurs cinétiques sont influencées par les conditions de substrats (surface d'eau ou inerte) et de température.

Contents

Acknowledgements **i**

English summary **iii**

Résumé français **v**

Contents **vii**

Thesis Outline **1**

1 Introduction **3**
1.1 Star evolution 3
1.1.1 Interstellar gas 4
1.1.2 Interstellar dust 6
1.1.3 Surface chemistry 8
1.1.4 Interstellar molecules 9
1.1.5 Interstellar ices 10
1.2 Interaction of gas and grains 12
1.2.1 Gas phase 12
1.2.2 Solid phase sublimation 14

2 Experimental apparatus and Methods **17**
2.1 Experimental apparatus 17
2.1.1 The main chamber 18
2.1.2 The sample holder and cryostat system 19
2.1.3 The beamline system 19
2.1.4 Quadrupole Mass Spectrometer (QMS) 21
2.1.5 The infrared spectroscopy 23
2.2 Experimental methods 23
2.2.1 Mass spectroscopy 24
2.2.1.1 Cracking pattern 24
2.2.1.2 Thermal Programmed Desorption (TPD) 26
2.2.2 Water ice substrates on the sample holder 27
2.2.3 Calibration of the beamline system 29
2.2.3.1 Optimization of the injection flow 29

2.2.3.2 Determination of the geometrical area of the beam deposition zone on the sample holder 29
2.2.3.3 Determination of the beam overlap 30
2.2.3.4 Dissociation of H_2 and D_2 beam 33

3 Segregation effect and N_2 binding energy reduction in CO-N_2 system adsorbed on water ice substrates 34
3.1 Introduction 34
3.2 Experimental protocol 37
3.3 Experimental results 40
3.3.1 Pure species 40
3.3.2 Mixed species 46
3.4 Analysis and discussion 48
3.5 Conclusions 56

4 Experimental study of the chemical network of the hydrogenation of NO on interstellar dust grains 58
4.1 Introduction 59
4.2 Experimental setup 61
4.3 Experimental results 62
4.3.1 Completeness of the reactions of the {NO + H} system before the TPD 62
4.3.2 Temperature dependency 64
4.3.3 The {NO + D} reactive system at various temperatures . . 69
4.4 Catalytic role of water 72
4.5 The possibility of back reaction $NH_2OH+H \longrightarrow H_2NO+H_2$ 73
4.6 Experimental conclusions 75
4.7 Astrophysical implications 75

5 Study of the penetration of oxygen and deuterium atoms into porous water ice 77
5.1 Introduction 78
5.2 Experimental methods 80
5.2.1 Experimental set-up 80
5.2.2 Water ice characterization 82
5.3 Experimental results 83
5.3.1 Oxygenation of NO ices 83
5.3.2 Deuteration of NO ices 87
5.4 Model and Discussion 89
5.5 Astrophysical implications and conclusions 94

6 Efficient formation route of the pre-biotic molecule formamide on interstellar dust grains 97
6.1 Introduction 98
6.2 Experimental methods 99

6.3 Experimental results 100
6.4 Astrophysical implications 104

7 Experimental study of the hydrogenation of Acetonitrile and Methyl Isocyanide on Interstellar dust grains 107
7.1 Introduction 108
7.2 Experimental conditions 110
7.3 Experimental results 113
7.3.1 (Non) Reaction between Acetonitrile (CH_3CN) and H atoms at 10 K 113
7.3.2 Reactivity between Methyl Isocyanide CH_3NC and H atoms at 10 K 114
7.3.3 CH_3NC and its hydrogenation in presence of H_2O. 117
7.3.3.1 Desorption of CH_3NC mixed with H_2O 117
7.3.3.2 Reaction of CH_3NC and H atoms in the presence of H_2O 120
7.3.4 Reactivity of CH_3NC and D atoms on the golden surface at 10 K 121
7.3.5 Reactivity of CH_3NC and H atoms at various temperatures. 123
7.4 Analysis and Discussion 125
7.4.1 Activation barrier and quantum tunneling 125
7.4.2 The catalytic role of H_2O for chemical reactions 126
7.4.3 Orientation of CH_3NC at different surface temperatures . . . 126
7.4.4 Astrophysical implications 127
7.4.5 New estimation of the cracking patterns and of the binding energy of CH_3NCH_2 128
7.5 Summary and conclusion 128

8 Conclusions and perspectives 130
8.1 Remarks and Astrophysical implications 130
8.2 Perspectives 133

Appendix A Efficient formation route of the pre-biotic molecule formamide on interstellar dust grains 134
A.1 NO, H_2CO, and H atoms co-deposit on porous amorphous solid water ice 134

Appendix B Scientific material to be included in a forthcoming article/chapter 135
B.1 List of discussed experiments 135
B.2 Experimental results 136
B.2.1 NO, H_2CO, and H atoms co-deposit on the golden surface maintained at 10 K 136

B.2.2 NO, D_2CO, and D atoms co-deposit on the golden surface maintained at 10 K . . . 136
B.2.3 NO, H_2CO, and H atoms co-deposit on the golden surface maintained at 40 K . . . 138
B.2.4 Efficiency of layered experiments . . . 138
B.2.5 Co-deposition {NO + H_2CO + H} on porous water ice substrate maintained at 10 K or 40 K . . . 139
B.2.6 Table of radical reactions . . . 139
B.3 Conclusion . . . 142

Appendix C List of publications and conferences 143
C.1 List of publications . . . 143
C.2 List of conferences . . . 144
C.2.1 Contributed talks . . . 144
C.2.2 Contributed posters . . . 144
C.2.3 Other attended conferences . . . 145

List of Figures 145

List of Tables 153

Bibliography 155

Thesis Outline

This thesis presents an experimental study of solid state molecular physics. Our aim is to increase our understanding of the chemistry that occurs on interstellar dust grains. We focus on nitrogen bearing species. We study their thermal desorption as well as some chemical networks that lead to COMs by hydrogenation, although COMs may be subsequently injected into the gas phase via mechanisms such as the adsorption of UV photons, non-thermal desorption, or the disruption of products by collision (Bisschop et al., 2007, Miura et al., 2017).

Our investigations have proceeded with simple reactants which are considered some of the molecular precursors in the ISM, they provide the link between simple nitrogen-bearing species and formation routes of COMs.

More specifically, we have studied the segregation effect of CO and N_2 co-adsorbed on water ice mantles which has an impact on their binding energy and many impact their relative depletion in prestellar cores. To study the chemical link between small nitrogen bearing species and COMs we reinvestigate the hydrogenation of NO, which can be a precursor molecule in ISM, leads to the chemical pathway of the formation of molecular complexities such as NH_2OH, N_2O, NO_2, etc. We have found efficient chemical pathways for the formation of the pre-biotic molecules - NH_2CHO via the co-hydrogenation of NO and H_2CO on the grain. Their corresponding formation routes is presented.

The contribution of CH_3NC in particular, the R-NC isonitrile family in general on grain surfaces in the formation/transformation of COMs in the ISM is still an open question. Therefore, we have investigated the chemical network of the CH_3NC hydrogenation on grain surface to elucidate the possible formation of other COMs on grain surface.

Furthermore, a second goal is to study the influence of the water molecules in chemical reactions. Experiments are very useful to characterize the H_2O catalytic effects which occur in interstellar clouds.

In this thesis, I will report the results from experimental investigation I performed with the machine named VENUS ("Vers de NoUvelles Syntheses") at the LERMA laboratory in the University of Cergy Pontoise. The set-up simulates the conditions of the formation of COMs, such as low pressure, low temperatures, low gas fluxes, and no addition of external energy.

This thesis is organized as follows:

Chapter 1: This chapter is the brief description of the ISM. In particular, it introduces the different kind of interstellar gases, dusts, and ices. The gas chemistry and the grain surface play an important role for the formation of complex organic molecules.

Chapter 2: A detailed description of the different parts that constitute the set-up VENUS is given in this chapter.

Chapter 3: In this chapter, we present the study of the CO-N_2 system: segregation effect and N_2 binding energy reduction in CO - N_2 system adsorbed on water ice substrates.

Chapter 4: We investigate in detail of the hydrogenation of NO: Experimental study of the chemical network of the hydrogenation of NO on interstellar dust grains.

Chapter 5: We present experimental study of the penetration of oxygen and deuterium atoms into porous water ice.

Chapter 6: This chapter deals with the formation of formamide and demonstrates efficient formation routes of the pre-biotic formamide on interstellar grains

Chapter 7: This last chapter presents the experiments performed to study the hydrogenation of acetonitrile and methyl isocyanide.

Chapter 8: Conclusion of project and Perspectives

Chapter 1

Introduction

1.1 Star evolution

Stars form from the gravitational collapse of dense clouds in the interstellar medium of galaxies. The evolution of stars is played out in a complex cycle that links between stars and the interstellar medium. Therein, the giant molecular clouds are considered the precursors of stellar processes, protostars, and young stellar objects as intermediated products.

The interstellar medium (ISM) is the material which fills the space between stars. Interstellar regions have very low densities and contain mainly a mixture of gas (99 %) and dust (1%). Gas and dust are injected into the ISM from the remnants of stars that died in a former star cycle. There are different ISM regions, one of them is called diffuse cloud which will later evolute in dense clouds.

Dense clouds have gas densities of 10-10^3 cm^{-3} and temperatures of 50-100 K. In diffuse clouds, ions can be produced by photoionisation by extenal UV photons since the density of dust particles is insufficient to extinguish the interstellar radiation field to a great extent. When an interstellar cloud reaches the sufficient mass, it collapses by self gravitation to form a protostellar system.

Pre-stellar cores are believed to be on the verge of collapse and represent the initial conditions for star formations (Bergin and Tafalla, 2007). Pre-stellar cores are cores with densities above 1×10^5 cm^{-3}. The core is cold, with the temperature varies from 10-15 K at the edge to 7-8 K at the centre. In pre-stellar cores, the

heavy molecules such as CO, CS, and SO are highly depleted in the inner dense parts (Caselli, 1999).

Hot cores own a protostar. They are regions where the dust temperature reaches 100-300 K, even molecules which are strongly bound to grains like H_2O begin to evaporate into the gas phase accompanied with molecules trapped in H_2O ice mantles. There are many complex molecules formed and observed toward hot cores such as formamide (NH_2CHO), acetonitrile (CH_3CN), dimethyl ether (CH_3OCH_3), and ethanol (CH_3CH_2OH) (Solomon et al., 1971, Rubin et al., 1971, Snyder et al., 1974, Zuckerman et al., 1975).

Protoplanetary disks intermediately form after the collapse of a molecular cloud. Protoplanetary disks are composed of gas, dust, and are the place of planets formation. Dust in disks is accreted through collisions, while the gas in disk is mostly diatomic, and its accounts for 99 % of total the mass. The temperature of a protoplanetary disk gradually increases from the outer disk ($\sim$ 10 K) to the inner disk ($\sim 10^3$ K) where is closest to the star, so that the chemistry of the outer disk is similar to that of normal interstellar cloud. The protoplanetary disk will eventually become solar type planetary system or coagulate into comets, meteors, and planets which chemical compositions can vary with their formation history.

Our **solar system** is the result of the gravitational collapse of a small part of giant molecular clouds. The solar system consists of Sun and its planets, their moons formed 4.6 million years ago. Our Solar system belongs to the second-third generation of stars.

Figure 1.1 shows the star formation cycle which is credited by Bill Saxton, NRAO/AUI/NSF.

1.1.1 Interstellar gas

Gas elements of the ISM are 90 % of hydrogen, 9 % of helium, and 1 % of heavier elements such as carbon (C), oxygen (O), nitrogen (N), silicate (Si), and iron (Fe) (Lequeux, 2005). Ionized gas occupy the majority of the volume of the ISM but these components are not more than around 25% of the total gas mass. The majority of the mass is located in regions dominated by atomic gas (H, He) or molecular gas (H_2).

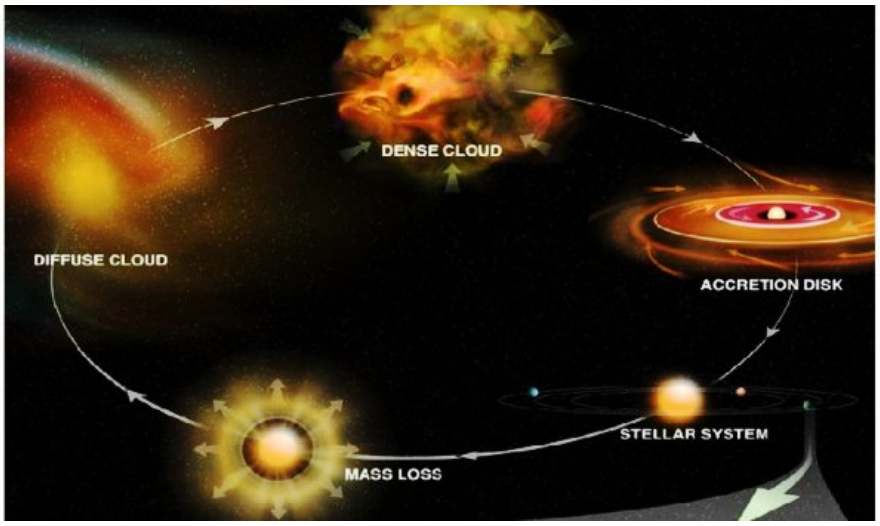

FIGURE 1.1: Star formation cycle. Credits: Bill Saxton, NRAO/AUI/NSF

TABLE 1.1: Density and temperature distribution in the ISM (Draine, 2011, Goldsmith et al., 1969)

Phase	**Density** cm^{-3}	**Temperature** K	**Volume** %
Dense molecular cores	10^3 - 10^6	10 - 20	0.01
Diffuse molecular gas	30 - 300	30 -100	0.1
Cold neutral medium	~30	40 - 100	1
Warm neutral medium	0.6	~ 5000	40
HII regions	10^2 - 10^4	10^4	0.01
Warm ionized medium (WIM)	0.3	~ 10^4	10
Coronal gas (HIM)	0.004	$10^{5.5}$ - 10^7	50

Because gas is not distributed uniformly over the ISM, there are some different environments having different densities and temperatures in the ISM. They are shown in table 1.1 (Draine, 2011, Goldsmith et al., 1969).

Dense molecular cores: These regions have a temperature lower than 20 K. The most dense clouds are gravitationally bounds with a density n $\geq 10^3$ cm^{-3}. In these dark clouds, the dust grains are coated with mantles composed of H_2O and the other molecular ices.

Cold neutral medium (CNM): It is cold dense gas with the temperatures around 40 - 100 K. Densities are around n $\approx$ 30 cm^{-3} filling $\sim$ 1 % of the volume of the local interstellar medium

Diffuse molecular gas: is like cold neutral medium in similar temperature range (40 - 100 K) with a slightly higher density up to 300 cm^{-3}. This is a region where

atomic species recombine forming molecules, mostly H_2.

Warm neutral medium (WNM): Predominantly atomic gas is heated to temperatures T $\approx$ 5000 K. The gas is found at the densities n $\approx$ 0.6 cm^{-3}. It fills about 40 % of the fraction of the volume.

Warm ionized medium (WIM): This region contains diffuse ionized gas. It is manily observed in nebulae by looking at recombination lines like Hα. It has a very low density (0.3 cm^{-3}) and a temperature of the order of 10^4 K.

HII regions: Regions where the hydrogen is photoionized by ultraviolet photons from hot stars. They have highest temperatures T $\approx 10^4$ K and the density ranges from 10^2 to 10^4 particles per cm^3.

Coronal gas: is observed via far UV absorption lines of highly ionized atoms and in the form of soft X-ray background. It is a product of hot gases ejected in stellar explosions and winds. It has the highest temperature around $10^{5.5}$ - 10^7 K and low density n $\approx$ 0.004 cm^{-3}.

1.1.2 Interstellar dust

Although interstellar dust represent only approximately 1% of the mass in the ISM, it consists of many different elements, including amorphous silicate, graphite, PAHs, amorphous carbon, nano-diamonds, icy grain mantles, and organic refractory grain mantles. It plays an important role in the astrophysics of the ISM, from thermodynamic and chemistry of gas to the dynamic of star formation. The main chemical reactions in the ISM are radical-radical reactions or radical-neutral reactions, and the chemistry on the surface of the interstellar dust. The absorbed atoms/molecules can diffuse, meet, and react on their surface and so the acting dust grains are considered to be the catalysts of the ISM.

Grains can influence the gas phase composition of molecular clouds indirectly because they may lock up some elements. They are also catalysts for chemical reactions, especially that of H_2, whose abundance cannot be explained without the presence of grains.

The presence of interstellar dust is inferred from extinction features of the spectra of background stars at wavelength in the UV and visible ranges. Composition of

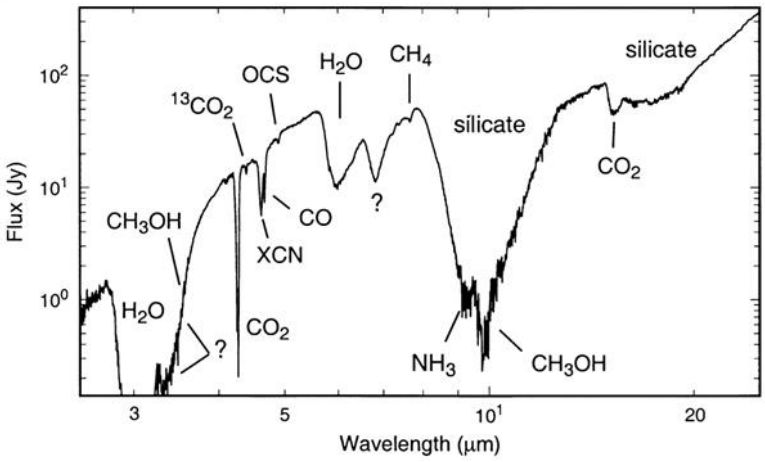

FIGURE 1.2: Infrared spectrum of W33A taken with the Infrared Space Observatory, taken from Gibb et al. (2000).

interstellar dust is defined through IR and UV features. From the analysis of the infrared absorption feature, we learn that interstellar dust is composed of silicate and carbonaceous materials with particle size distributed between 0.01 and 0.5 μm (Draine, 2003, Mathis et al., 1977, Zubko et al., 2004, Draine and Li, 2007). On the solid seeds, the chemical species from the gas phase form frozen molecular mantle in the cold dense clouds. A typically spectrum is shown in figure 1.2. Silicates absorption features can be clearly seen around 10 μm. Moreover, solid (board band) as well as gaseous (many rotational thin lines) molecular features of species such as H_2O, CO_2, and CO can also been observed.

On the other hand, dust grains can be analysed through the observed elemental depletion. The atoms (molecules) are missing from the gas phase must be locked up in dust grains (Snow and Witt, 1996). Thus, the elemental depletion provides a clue to the composition of interstellar dust.

Dust grains have an important role in the interstellar chemical inventory particularly because of the formation of molecular hydrogen (H_2) in the Universe (Van de Hulst, 1946). The formation of molecular hydrogen is usually explained as followed: atomic hydrogen sticks onto the dust grain, and subsequently encounters, reacts with another H atom and forms the molecular hydrogen (Hollenbach et al., 1971). Finally, H_2 is injected into the gas phase of the ISM when the surface temperature reaches its evaporation limit or steadily upon its formation (Congiu et al., 2009).

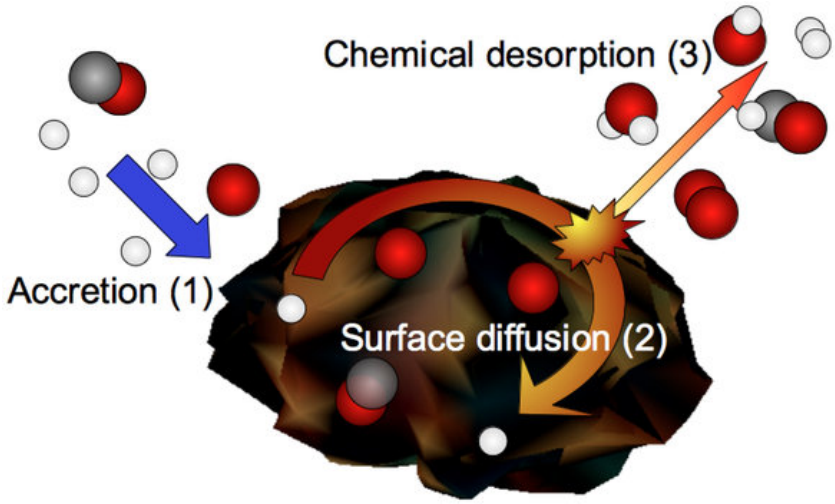

FIGURE 1.3: Schematic illustration of some processes that take place on dust grains. Image adapted from Dulieu et al. (2013)

On the other hand, where carbon is more abundant than oxygen. Oxygen is entirely locked up in carbon monoxide and the excess carbon produces a rich carbon-based molecules or carbonaceous dust and carbon monoxide on dust grain. Where oxygen is more abundant than carbon, the excess of oxygen makes metallic oxide that nucleate to form solid oxide and silicates (Williams and Herbst, 2002).

After their formation on dust grains, the molecular species can be injected into the gas phase by evaporation due to the absorption of UV photons, the thermal desorption, or the disruption of products by collision (Bisschop et al., 2007, Miura et al., 2017). Figure 1.3 displays some processes ranges such as the accretion, the diffusion, and the chemical desorption that take place on dust grains, and that may inject species into the gas phase (Dulieu et al., 2013).

1.1.3 Surface chemistry

There are three main chemical processes on grain surfaces. The first one is known as the Eley-Rideal (E-R) mechanism. One reactant (atom/molecule) is adsorbed on the grain surface and then impact and react directly with a atom/molecule coming from the gas phase. E-R mechanism is a non-thermal surface mechanism because it leads to a reaction between a thermally adsorbed surface species and a reactant which has not yet been thermally accommodated to the surface. The second mechanism occurs through the surface diffusion and is known as the Langmuir-Hinshelwood (L-H) mechanism. The new molecule is formed via the

reaction of two reactive partners are already adsorbed on the surface. The L-H mechanism is a thermal surface mechanism because the two reactants are thermalized to the surface. The last mechanism is the so called hot atoms mechanism. A gas phase species is landing on the surface with an excess of kinetic energy which implies an excess of mobility of a finite period on the surface. Thus one of the species has a temporary increased mobility, find and react with partners before reaching the thermal equilibrium. With the E-R and hot-atom mechanisms, reactions occur before reaching the thermal equilibrium. Thus, these mechanisms are different in regards to evaluate the activation barriers of reactions. Under typically conditions of dust-grain surface reactions, the L-H mechanism is the dominant reactive process. All three mechanisms can be followed by desorption of the reaction products, back into the gas phase.

1.1.4 Interstellar molecules

Molecular material in general and the complex molecules in particular can be either in the gas phase and in the solid phase (locked in the icy mantles on dust grains). They are mainly associated with molecular clouds and their dense clumps or in star forming regions. The probe of the ISM components and processes that occur in it, are derived from the molecular spectra and the chemical chain of reactions that yield to different molecular species. Molecular spectra provide some information about the physical conditions on gas and dust. In particular, the rotational and vibrational spectra give us information about the density and temperature of the gas as well as the collapse and rotation (Herbst and van Dishoeck, 2009b).

In recent years, more than 200 complex molecules have been detected in interstellar medium and circumstellar shells[1] including molecules from 2 atoms to 13 atoms. The diversity of molecular components in the ISM is evidenced by the large number of known molecules.

Interstellar molecules allow us to clarify the evolution of star formation that is occurring in the cold, dense pre-stellar globules and cores (density $n = 2 \times 10^4$ cm^{-3} and temperature $T \approx 10$ K) and the abundant molecules in both gas phase and ice mantles (Herbst and van Dishoeck, 2009b).

[1]https://www.astro.uni-koeln.de/cdms/molecules

1.1.5 Interstellar ices

Interstellar ices are formed in the cold and dense clouds where densities reach high enough (10^3 to 10^5 cm^{-3}). At average molecular cloud densities of 10^4 cm^{-3}, atoms and molecules accrete on the surface of a sub-micro sized dust grain once per day in average (Tielens and Allamandola, 1987). Low temperatures allow particles to accrete, to move on the surface and to form new molecules. Sheltered from the strong UV field, molecules are able to accumulate on the grain to form a mantle of interstellar ice.

Compositions of interstellar ice are determined by physical conditions in the ambient gas. Hydrogen (H), oxygen (O), and nitrogen (N) may be in atomic and molecular form, whereas carbon (C) arrives on the dust grain in the form of carbon monoxide (CO). At low temperature (typically of 10 K), atoms/molecules are able to scan on the grain surface, meet and react with other atoms/molecules. Hydrogen and oxygen atoms may perform quantum tunneling (Manicò et al., 2001, Minissale et al., 2013, Congiu et al., 2014b, Minissale et al., 2014), the atomic oxygen, nitrogen, and carbon can do thermal hopping (Tielens and Allamandola, 1987). Simultaneously, the ice layer is a result of atoms addition reactions. Thus, the primal interstellar ices are mainly formed of water H_2O with significant amount of H_2CO, CO, CO_2, N_2, and NH_3 (Tielens and Hagen, 1982).

There have been many surveys of interstellar ice to determine the ice compositions (Knez et al., 2005, Boogert et al., 2008, Pontoppidan et al., 2008, Öberg et al., 2011). Interstellar ices are dominated by water (H_2O); however, it is mixed with the significant amounts of CO, CO_2, CH_3OH, and as well as smaller abundances of NH_3, H_2CO, CH_4, HCOOH, NH_4^+, OCS and several ionic species (Van Dishoeck, 2004). Table 1.2 shows the molecular abundances are relative to the water ice (Van Broekhuizen, 2005).

Actually, these molecules freeze out onto the grain surface from the gas phase; however, mantle composition does not reflect gas phase composition or abundances. For instance, CO_2 has not been observed in the gas phase yet, while it is widely detected as an ice condensed onto dust grains (Boonman et al., 2000). Therefore, new molecules are formed when reactive gaseous species condense on the grain surface or when ices are energetically processed by UV radiation or cosmic rays.

TABLE 1.2: Molecules detected in interstellar ices towards protostars. Molecular abundances are related to the water ice (Van Broekhuizen, 2005)

Molecule	Abundance %	Molecule	Abundance %
H_2O	100	CO	3 - 50
CH_3OH	2 -25	CO_2	7-25
NH_3	< 10	NH_4^+	3-17
H_2CO	3 - 7	CH_4	0.9- 1.9
OCS	0.1	HCOOH	≤ 1.7

Although layer ices of interstellar ices are diverse, H_2O still dominates the composition of interstellar ices (Boogert et al., 2008, Pontoppidan et al., 2004). In the gas phase, H_2O has abundance with respect to H_2 of 10^{-8} in the cold dense regions, to 10^{-4} in warm gas and shocked regions (van Dishoeck and Helmich, 1996, Melnick and Bergin, 2005). D'Hendecourt et al. (1985) and Hasegawa et al. (1992) studied that gas phase chemistry cannot reproduce the H_2O abundance observed in ISM. However, there were laboratories that investigated and demonstrated the H_2O formation; the H_2O molecules was produced from the reaction of H-atoms and O-atoms initially trapped in a N_2O matrix (Hiraoka et al., 1998); the reactions between H atoms and O_2 produced efficiently the H_2O_2 and H_2O molecules (Miyauchi et al., 2008, Ioppolo et al., 2008). Moreover, experiments were preformed through set-up FORMOLISM (FORmation of MOLecules in the ISM, located at LERMA in the University of Cergy Pontoise) allowed to investigate the formation of water molecules by exposing the water ice substrate to D-atoms and O atoms and O_2 molecules, accordingly simulated the water formation in dense interstellar clouds (Dulieu et al., 2010). Based on the experiments, they have shown that D_2 does not react with O atoms or O_2 molecules residing on the amorphous solid water (ASW) ice surface. The research of Oba et al. (2012) showed that quantum tunneling was responsible for the reaction $OH + H_2 \rightarrow H_2O + H$ and thus could happen in the ISM. Therefore, the water formation process requires atomic hydrogen or (-OH) group and molecular hydrogen. Moreover, the experimental investigation has been confirmed that hydrogenation of the molecular oxygen produces amorphous solid water (ASW) with compact (porous) structures (Oba et al., 2009, Accolla et al., 2013).

In interstellar ices, the morphology of H_2O is controlled by its hydrogen-bonding

character. Depending on temperature and different structures can be distinguished. The ice growth conditions such as temperature, growth rate, and directionality H_2O deposition on grain surfaces affect the porosity of ASW (Berland et al., 1995, Westley et al., 1998, Stevenson et al., 1999a, Kimmel et al., 2001, Dohnálek et al., 2003). On the other hand, the porosity of ASW can be reduced by energetic processing in the ISM. Porous ASW is compacted and collapsed in structure under the bombardment of comic ray and UV photons (Palumbo, 2006, Palumbo et al., 2010, Raut et al., 2008) as well as by thermal processing (Bossa et al., 2012) or by chemical activity such as the H+H reaction (Accolla et al., 2011)

Simultaneously, ice porosity of ASW also influences the efficiency of H_2 formation (Roser et al., 2002), provides the effective surface areas for absorption of molecules and catalysis of chemical reactions.

1.2 Interaction of gas and grains

1.2.1 Gas phase

Although there is a significant fraction of neutral-neutral reactions, most of the reactions are of the ion-molecule variety and the produced species are detected via high resolution spectroscopy in the lab.

The molecular hydrogen is formed on dust grains, and then ejected to the gas phase, it can be ionised by reactions with cosmic ray to form H_2^+, and then reacts with its ion produced H_2^+ forming H_3^+(Herbst, 2001). The H_3^+ is relatively abundant because does not react with H_2 in the gas phase (Geballe, 2000) and detected via infrared absorption.

In the gas phase, carbon and oxygen atoms are also abundant atoms and they can react with the ion H_3^+ in interstellar clouds (Herbst, 2001). For instance, reactions with oxygen lead to the oxonium ion: $O \xrightarrow{H_3^+} OH^+ \xrightarrow{H_2} H_2O^+ \xrightarrow{H_2} H_3O^+$ or the reactions with atomic carbon: $C \xrightarrow{H_3^+} CH^+ \xrightarrow{H_2} CH_2^+ \xrightarrow{H_2} CH_3^+$. The transfer reaction between CH_3^+ and H_2 does not occur because it is endothermic. However, CH_3^+ can react with H_2 via a radiative association reaction to form CH_5^+: $CH_3^+ + H_2 \rightarrow CH_5^+ + h\nu$, which is the reactant to form methane (CH_4) via a competitive reaction with abundant CO: $CH_5^+ + CO \rightarrow CH_4 + HCO^+$. Furthermore, once

simple of hydrocarbon such as methyl (CH_3) and methane (CH_4) are formed, the complex hydrocarbons can be produced via several classes of reactions (Smith, 1992).

Therefore, there are many types of chemical pathways in the gas phase (Herbst, 2001, Herbst and Leung, 1989).

Firstly, carbon insertion reactions are one of the important pathways in the gas phase: $C^+ + CH_4 \rightarrow C_2H_3^+ + H$ or $C_2H_2^+ + H_2$.

The second is condensation reactions such as: $C_2H_2^+ + C_2H_2 \rightarrow C_4H_3^+ + H$, $C_4H_2^+ + H_2$.

It then is the radiative association reactions such as $C^+ + C_n \rightarrow C_{n+1}^+ + h\nu$. As another example, the reaction of C_3H^+ ion is thought to associate with H_2 to form a precursor to the cyclic species C_3H_2: $C_3H^+ + H_2 \rightarrow$ c-$C_3H_3^+ + h\nu$. Or ion-atom reactions followed by dissociative recombination such as: $N + C_3H_3^+ \rightarrow HC_3NH^+ + H$.

Gas phase chemistry of a variety of regions is affected by star formation. For instance, in hot cores where the temperature and densities are high, the molecular composition of gas is much more saturated than in the ambient material - molecules such as H_2O, NH_3, H_2S, and CH_3OH become much more abundant and larger molecules such as methyl formate, dimethyl ether, and ethanol are seen only in such regions. Before star formation, both gas phase and grain surface chemistry occur at low temperature and ice mantles build up on the grain surface. The ice mantles contain CH_3OH, mostly produced by the hydrogenation of CO by addition H atoms landing on grains (Watanabe and Kouchi, 2002, Fuchs et al., 2009). During star formation, the surface temperature reaches 100-300 K for the evaporation of the ice mantles.

CO is the second abundant molecule after H_2 in the gas phase, while the amount of N_2 is uncertain because it lack a permanent dipole moment. The abundance of N_2 is usually inferred from the presence of its daughter species N_2H^+ mainly formed via the reaction $N_2 + H_3^+ \rightarrow N_2H^+ + H_2$. The freeze out of these molecules, CO and N_2, on dust grains and ice mantles are different in pre-stellar cores. So, CO and N_2 should have different depletion behaviour in pre-stellar cores (Pagani et al., 2012) although they have similar masses, sticking properties and desorption efficiency (Bisschop et al., 2006).

Moreover, the depletion of CO relates to the freeze out of CO toward the center and is also reflected in the abundance of many other molecules either through correlation and anti-correlation (Jørgensen et al., 2004). For instance, CO is the main destroyer of N_2H^+ in the gas phase, yet N_2H^+ is the daughter of N_2 and its observational tracer, so CO freeze out is also a prerequisite to have an N_2 gas phase or depletion estimate.

There are molecular species which are considered to be pre-biotic species in space such as glycoladehyde (CH_2OHCHO) (Hollis et al., 2004), acetamide (CH_2CONH_2) (Hollis et al., 2006), amino acetonitrile (NH_2CH_2CN) (Belloche et al., 2008), formamide (NH_2CHO), etc which exist in the gas phase. In particular, the presence of formamide (NH_2CHO) has been observed in the gas phase in several astronomical environments such as pre-stellar cores and protostellar objects (Kahane et al., 2013), or massive hot molecular cores (Bisschop et al., 2007). There are hypothesises that suggest that the formamide formation in the gas phase via the reaction of two molecular precursors, H_2CO and NH_2 (Barone et al., 2015, Vasyunin and Herbst, 2013b, Vasyunin et al., 2017, Codella et al., 2017). Hence the gas phase chemistry has an important role for the synthesis of pre-biotic species which are involved in processes of the life origin.

There are many molecules observed in the ISM. Some of them, like CO can be used as a tracer of the dense media and can be synthetized in the gas phase. However, many other molecules such as H_2 or hydrogenated complex organic molecules need the intervention of the solid state, which is provided by the surface of interstellar dust grains.

1.2.2 Solid phase sublimation

Many molecular species are formed and detected in the gas phase. However, it cannot explain the observed abundance of some complex organic molecules, therefore the grains surface should have an important role. As the chemistry in the gas phase proceeds, atoms and molecules can collide with the grain surface to accrete, diffuse, meet, and react to form more molecular complexity than it is possible in the gas phase alone. Even if gas phase species can condense onto the grain surface, the grain species can desorb back into the gas phase through the thermal desorption when the grain surface increases from 10 K to 100-300 K. At temperatures are higher than 20 K, H_2 does not reside long enough on the grain

surface, CO, CO_2, N_2, and CH_4 also start to sublimate, and the other heavier elements remaining on the grain surfaces may begin to diffuse. Hence reaction networks and desorption process depends on physical parameters such as cloud densities, gas temperatures, compositions of grain surfaces or illumination, but for these processes the most important parameter is the grain temperature. In return, molecules injected from the solid phase into the gas phase will continue to chemically evolve making complex the interaction between gas and grain surface chemistry.

Hydrogen is the most abundant species in the ISM and under typical conditions of dense clouds (n $\approx 10^4$ cm^{-3} and T = 10 K), hydrogen atoms land on dust grain and due to its relative high mobility it makes hydrogenation reactions the dominant grain chemistry process. Therefore, hydrogenation reactions are a key to understand and interpret the formation of complex organic molecules which cannot be formed in the gas phase. Extensive laboratory works have been achieved some of the species are formed on cold grains through reactions between H, O, CO, and NO such as the hydrogenation/deuteration of O, O_2, and O_3 for the formation of water (Dulieu et al., 2010, Ioppolo et al., 2011, Jing et al., 2011), the formation of CO_2 via the non-energetic routes: O_2 + CO + H and O_3 + CO + H (Noble et al., 2011), the formation of methanol (CH_3OH) through the hydrogenation of CO: CO $\xrightarrow{+H}$ HCO $\xrightarrow{+H}$ H_2CO $\xrightarrow{+H}$ CH_3O $\xrightarrow{+H}$ CH_3OH (Ioppolo et al., 2011, Minissale et al., 2016, Hiraoka et al., 2005, Watanabe et al., 2004, Hidaka et al., 2007, Fuchs et al., 2009), the hydrogenation of nitrogen to form ammonia (NH_3) (Hiraoka et al., 1995, Fedoseev et al., 2015), the formation of hydroxylamine (NH_2OH) by the hydrogenation of NO: NO $\xrightarrow{+H}$ HNO $\xrightarrow{+H}$ NH_2O $\xrightarrow{+H}$ NH_2OH (Congiu et al., 2012a, Fedoseev et al., 2012).

After hydrogenation reactions, one has to consider other important solid phase route, CO is the second most abundant molecule in the ISM (10^{-4}-10^{-5} times the hydrogen abundances) (Pontoppidan et al., 2005). When CO freeze out occurs, and then CO-rich ice mantles are formed on top of the water ice. The CO reactions formed some species on grain surface such as the formation of CO_2 via {CO + O} reaction (Minissale et al., 2013) or {CO + OH} (Ioppolo et al., 2011, Oba et al., 2011, Minissale et al., 2013). Most reactions are the interaction between radicals and radicals or radicals and molecules, hence they do not require or have any activation energies and can proceed at low temperatures (typically of 10 K).

Regarding the formation of COMs other than methanol on grains surface and in the gas phase, Isocyanic acid (HNCO), is the simplest molecule containing the four abundant atoms: hydrogen, nitrogen, carbon, and oxygen. Previous hypothesises assumed that HNCO was only formed in the gas phase (Iglesias, 1977), but there were studies which introduced that HNCO forms on grain surface via the thermal reaction NH + CO or hydrogenation of OCN (Garrod et al., 2008). Furthermore, the hydrogenation of HNCO was predicted to be the pathway of the formamide formation. However, Noble et al. (2015) simultaneously demonstrated that formamide is not formed from the hydrogenation of HNCO and the presence of HNCO in the gas phase can be partly due to the desorption from grains.

Therefore, grain surface chemistry is not only responsible for the formation of hydrogen (H_2) but also for the hydrogenated molecules of the pre-collapse phase in particular, and almost the whole set of observed complex organic molecules (COMs). In 2006, the basic ideas of model of Garrod and Herbst (2006), radicals are trapped in the iced mantles obtained mobility and react forming COMs when the grain surface reaches the temperature ~ 30 K. Moreover, at later stages of stars formation, other sources of energy are available for the solid phase chemistry. Jones et al. (2011) showed the formation of formamide in CO-NH_3 solid state complexes via energetic electron bombardment in interstellar ice on grains at 10 K. Formamide has also been produced by hydrogenation and UV photolysis of NO in CO-rich interstellar ice analogues (Fedoseev et al., 2016).

For understanding the formation of COMs many aspects have to be considered and studied: gas phase chemistry, non-energetic solid state chemistry, energetic solid state chemistry, and finally the interplay of solid and gas phases have to be understood. The present thesis only focus on non-energetic solid state chemistry and especially hydrogenation reactions, and on some aspect of the desorption of accreted or formed species.

Chapter 2

Experimental apparatus and Methods

This chapter presents the experimental apparatus and methods used to carry out the experiments. All experiments described in this thesis have taken place at LERMA-Cergy (Laboratoire d'Etude du Rayonnement et de la Matiere en Astrophysique et Atmospheres) in the University of Cergy Pontoise thanks to a machine named VENUS ("Vers de NoUvelles Syntheses"), with means in English "Toward New Synthesis". It is used to investigate the physical-chemical processes of atoms and molecules on cold surfaces under dust grain environments.

2.1 Experimental apparatus

Figure 2.1 describes the schematic structure of VENUS. The set-up consists of different parts:

1. An Ultra High Vacuum (UHV) chamber called the main chamber;

2. An intermediate stage consists of two chambers called the first and second chambers;

3. A sample holder connected to the cryostat. It has the location in the main chamber;

4. A Quadrupole Mass Spectrometer (QMS) which is in the main chamber;

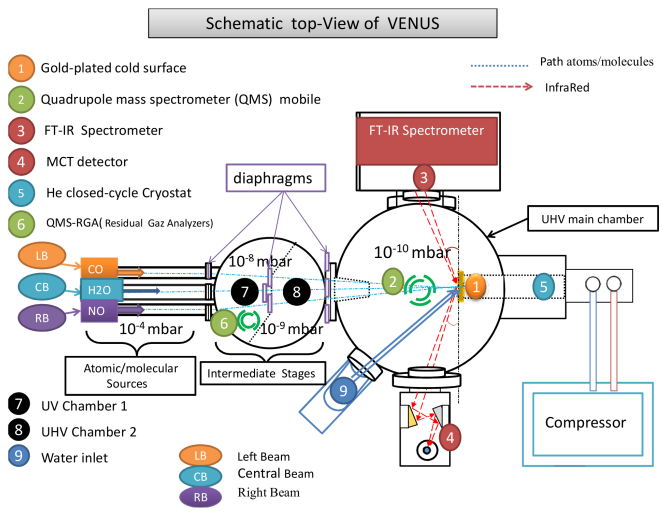

FIGURE 2.1: Schematic top view of VENUS at LERMA Cergy. Image adapted from *Sow et al in preparation*

5. An Infrared Spectroscopy (FT-RAIRS) which assembles in the main chamber;

6. A separated four beamlines system used to inject molecules into the main chamber through the first and second chambers;

7. A water tube system connected directly to the main chamber;

Each part will be described in detail in the next sections.

2.1.1 The main chamber

The UHV chamber consists of a stainless steel chamber. It is connected to a turbo molecular pump and a titanium sublimation pump. The residual pressure inside the chamber reaches the value of 1×10^{-10} mbar.

The UHV is maintained to keep the surface clean and prevent residual water molecules that are in the main chamber to be adsorbed on the surface. In fact, with the base pressure of 1×10^{-10} mbar, it takes $\sim$ 5000 minutes to grow 1 monolayer (ML) of water ice (Accolla, 2010). During the beam injection, especially the pressure of the hydrogen beam may rise up to few 10^{-10} mbar, is low enough to keep low the pollution on the sample surface. Indeed, water and others residual gases can form film of ice on the sample surface, so it may affect of the physical-chemical processes. In order to check this aspect, the residual gas analysis is made at any steps.

Moreover, there are two intermediate stages, which are called the first and the second chambers. The connection between the intermediate stages and the sources of the main chamber are made through diaphragms. It permits to create differential pumping. They have the residual pressures of 10^{-8} mbar for the first chamber and 10^{-9} mbar for the second chamber, respectively.

2.1.2 The sample holder and cryostat system

The sample holder is located in the center of the main chamber. It is made of a circular copper mirror coated with gold. It diameter is equal to 9 mm. The sample holder is larger than the beams which have an aperture of about 3 mm diameter. It is mounted onto the cold head of the closed cycle He cryostat (see figure 2.2). The sample temperature can be controlled in the range of 7 - 400 K by using a regulated resistive heater clamped behind the sample holder. It connects to a *Lakeshore* controller, that controls the temperatures by varying the current injected in the resistive heater in an automated way.

Figure 2.2 displays the place of the sample holder in the main chamber and the schematic of the cryostat with longitudinal section of the sample holder. A cryoshield is made of copper coated with nickel to protect and isolate the sample holder.

The sample holder can be translated (x, y, z) in order to get from room radiation the best alignment with both IR spectroscopy and molecular beams.

2.1.3 The beamline system

The separated four beamlines system allows us to deposit different molecular species at the same time on the same surface. They are called the right, central, top, and bottom beams (see figure 2.3). We used alignment lasers to find the best position for each beam. A gas expansion zone and a nozzle are located in a chamber pumped by a turbo molecular pump. For each beam, the gases are regulated by an automated flow regulator by Bronkhorst High-tech. The incoming flux is around 0.1 sccm[1] which correspond to 0.1 cm^3 per minute of gas at atmospheric pressure. A small fraction of the molecules passes into the first chamber

[1] 1sccm = 592 cm^3 Pa s^{-1} SI units

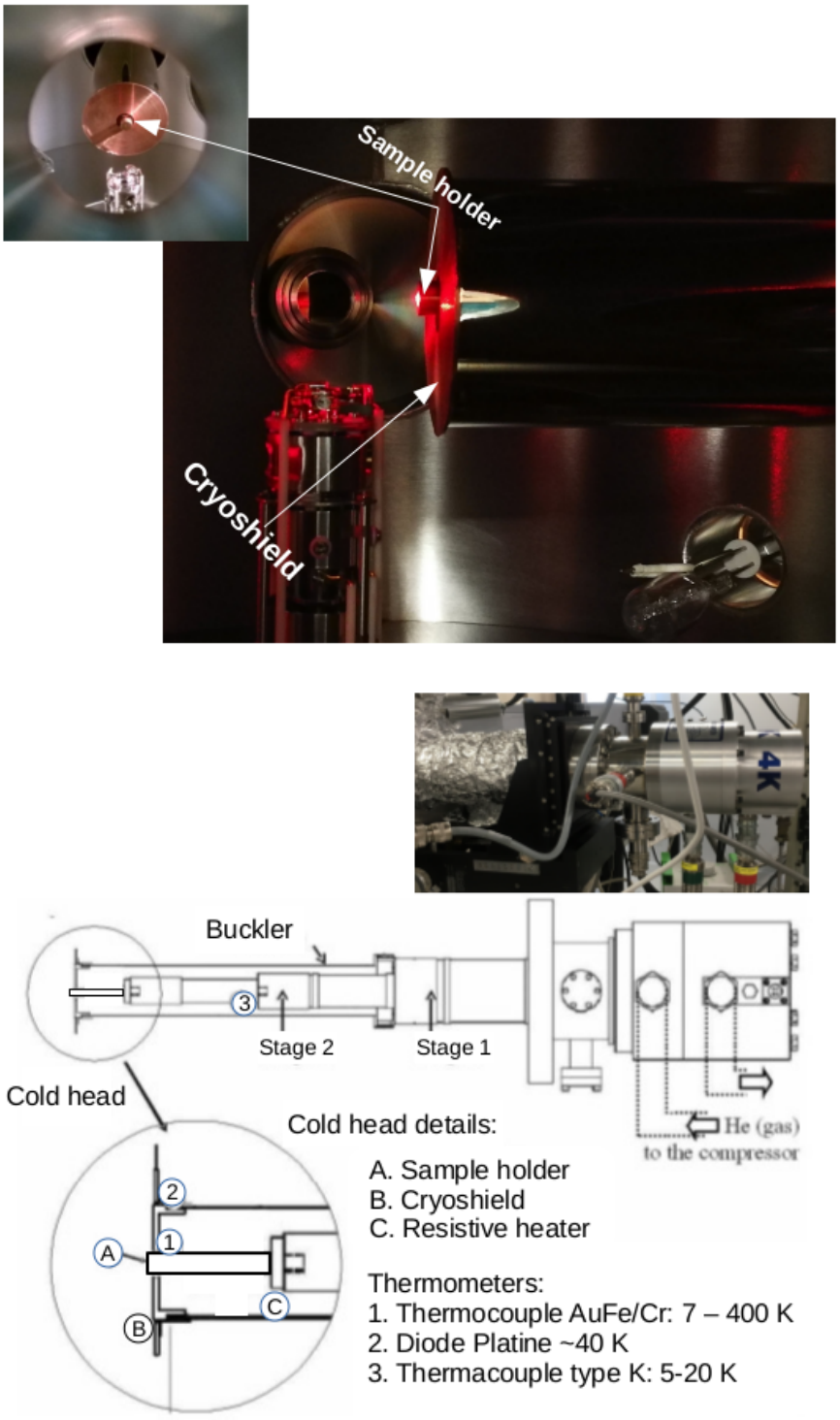

FIGURE 2.2: The location of the sample holder in the main chamber (top panel), four laser beams are shined through the atomic/molecular beamlines to ensure a good centering and a correct overlapping. The schematic of cryostat with longitudinal section of the sample holder (bottom panel).

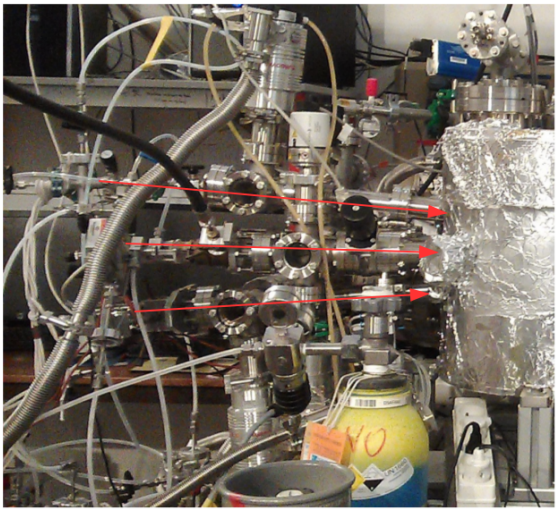

FIGURE 2.3: Photo of the beamlines system for VENUS before moving to the new laboratory in March 2018. The beamline system component consists of the right, central, top and bottom beams. Central beam is behind the right beam on the photo.

and then the second chamber through the tiny diaphragms, pumped down by the turbo molecular pumps. Finally, when the gas arrives in the main chamber, it does not change the pressure in the main chamber too much where the residual pressure is of about 10^{-10} mbar. But the flux in the beam at the sample surface is around 2×10^{12} mol/cm^2/s (8 minutes for a monolayer (ML)).

2.1.4 Quadrupole Mass Spectrometer (QMS)

The QMS is able to detect and measure the composition and the abundance of the residual gas in the main chamber or analysing the atomic/molecular jet coming from the beamlines. It can also check the molecules desorbing from the sample holder during a Thermally Programmed Desorption (TPD) experiment.

The QMS is mounted on the bottom of the main chamber. The QMS can be translated vertically or rotated. In a low position, the QMS can analyze the composition of present residual species in the main chamber. At the higher position, it is in front of the beamline and the sample holder. It can therefore characterise species coming from the beamlines or measure the desorption rate from the sample holder. We put the QMS in the low position during gas deposition or IR recording.

Figure 2.4 shows the QMS is in the low position (left panel) and the high position (right panel) where the QMS is positioned in front of the sample holder.

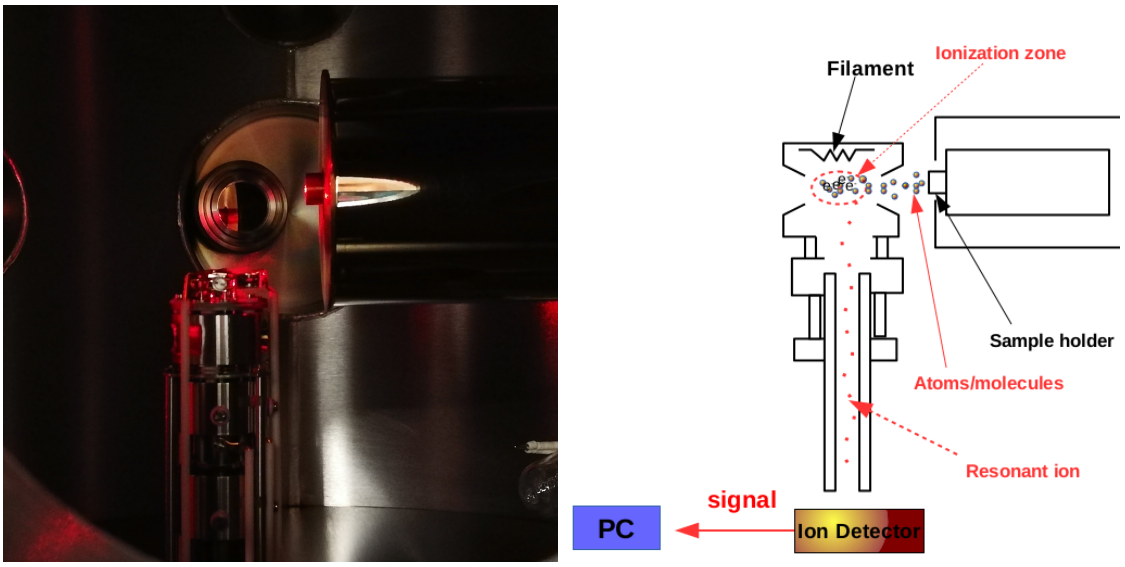

FIGURE 2.4: Photo of QMS is at the low position (left panel) and the schematic of QMS at the high position (right panel).

A QMS consists of an ionizer (bombardment by electron from a hot filament), an ion accelerator, and a mass filter consisting of four parallel metal rods. Residual molecules or desorbing molecules from the sample surface enter the quadrupole probe, they are ionized via electron bombardment by passing near to a heated tungsten filament and they are subsequently accelerated toward the four metallic rods. These four parallel rods represent the ion mass filter to select the species according to their mass charge ratio (m/z); In fact, a voltage combination of a direct and a radio frequency component is applied between adjacent and opposite rods. Varying the direct and the radio frequency component, the QMS is capable of scanning all ions up to a chosen mass to charge ratio technically fixed.

The ion detector is a *Channeltron* (an electron multiplier). The current output generated in the *Channeltron*, is converted into a digital signal. The digitalized signal is then controlled by a software provided by HIDEN. It allows not only to monitor and record the acquired information, but also to adjust the electronic setting of the QMS and the dwelling times between two measurements. Moreover, it is possible to record simultaneously the sample temperature measured by the *Lakeshore* controller during TPD experiments. In our experiments, we use a 30 eV kinetic energy for the electrons which is limitative somehow the cracking of the molecules.

2.1.5 The infrared spectroscopy

VENUS is equipped with a VERTEX 70v Fourier transform Infrared Spectrometer (FTIR) which used to monitor adsorbed/formed species *in situ*. Figure 2.5 shows the photos of external and internal FTIR. It consists of the mid-infrared (MIR) source. It is the global thermal source made of a silicon carbide rod heated up to 1000°C-1500°C, and emitting a polychromatic infrared radiations from 2.2 to 14.3 μm wavelength. The light passes through an aperture (typically of 1.5 mm). For studies mid-infrared is ranged from 4500 - 750 cm^{-1} for vibrational identification for species. The interferometer is composed of a beamsplitter (KBr) that is used for splitting the light into two parts, a fixed mirror, and a moving mirror (see figure 2.5). The moving mirror is the basic linear scanner with different optical path length. The beamsplitter recombines the beams coming from two of the mirrors. The resulting beam passes through an exit port and focuses on the sample holder of the UHV chamber. External to the UHV chamber, the reflected infrared beam from the sample holder is directed on the gold-plated mirrors which are mounted in a differentially pumped housing adjacent the UHV chamber and combined with an external pump. The reflected infrared beam is subsequently collected and focused onto the liquid nitrogen cooled mercury cadmium telluride (MCT) detector (see figure 2.5 in the right panel). MCT detector collects the raw data, and are subsequently sent to the computer. Afterwards, OPUS software assembles all these data and turn the interferometer (the raw data, light absorption for each mirror position) into the typical IR spectrum through a Fourier transform. Each spectrum is obtained with a resolution of 4 cm^{-1} prior or subsequently to either deposition or TPD.

2.2 Experimental methods

This section presents the experimental methods. We describe the technique used to probe the products, to calibrate the beams, and to grow the ice substrate.

FIGURE 2.5: Photos of the external and internal Vertex 70v (top and left panel) and MCT detector (right panel)

2.2.1 Mass spectroscopy

2.2.1.1 Cracking pattern

We have described the QMS operation for the detection of atoms/molecules coming from the sample surface. We have shown that molecules were detected after their ionization. Because of the electron impact, dissociation of species could occur in addition to ionization. The fragments distribution of species which result from the dissociation and the ionization of molecules is called cracking pattern. The probabilities of ionization or dissociation of species depend on molecular geometry, energy of ionizing electron, and angle impact between molecules and ionizing electron of the QMS. Hence we obtain different peaks/signals of the same molecules through the QMS.

TABLE 2.1: Fragment distribution of some species are detected through QMS. The desorption temperature range corresponds to these molecular species. The highest intensity is the main mass signal of species. Mass and relative intensity are indicated in blue and in red respectively.

Molecule	Temp K	peak 1	peak 2 mass	peak 3 intensity %	peak 4	peak 5
Nitric Oxide (NO)	50-70	30-100	31-5	-	-	-
Formaldehyde (H_2CO)	90-110	30-100	29-85	28-15	-	-
Acetonitrile(CH_3CN)	110-135	41-100	40-40	39-20	-	-
Methyl Isocyanide (CH_3NC)	105-125	41-100	40-60	39-20	-	-
Hydroxylamine (NH_2OH)	160-200	33-100	32-20	30-17	31-5	-
Methanol(CH_3OH)	125-150	31-100	32-67	15-50	29-45	30-16

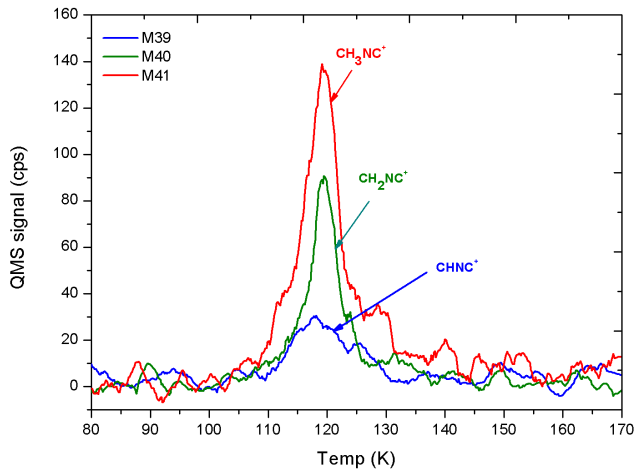

FIGURE 2.6: The fragment distribution of the CH_3NC molecule with the different relative intensity. Mass 41 represents CH_3NC^+ (red curve), mass 39 and 40 correspond to $CHNC^+$ (blue curve) and CH_2NC^+ (green curve).

Table 2.1 shows the fragment distribution of some species: NO, H_2CO, CH_3CN, CH_3NC, NH_2OH, and CH_3OH. This knowledge is useful for determining the composition of mixed ices. Results are obtained in our experimental conditions from pure adsorbate. We note that for methanol (CH_3OH), the radical ion CH_3OH^+ is less detected than CH_2OH^+ (m/z 31) which is more in the table (Minissale, 2014). Sometimes the ambiguities (e.g mass 32) could provide both from CH_3OH or O_2 or NH_2OH can be clarified by the range of the desorption temperature. Mass 32 without a similar temperature profile of mass 31 cannot be CH_3OH.

Figure 2.6 shows the different TPD traces of pure CH_3NC. There are three different fragments with various intensities. Mass 41 is CH_3NC^+, whereas masses 40 and 39 correspond to CH_2NC^+ and $CHNC^+$.

2.2.1.2 Thermal Programmed Desorption (TPD)

Thermal Programmed Desorption is an important method to study thermal desorption of atoms and molecules from the sample holder. TPD experiments operate when a sample surface at low temperature is heated with a linear ramp to observe the desorption of molecules from the sample surface. When the surface reaches a specific temperature (desorption temperature), the energy transferred adsorbed species causes the desorption of species into the gas phase. During the operated TPD experiments, the temperature T is increased linearly with the time from the initial temperature T_0. Temperature and time is related by:

$$\mathrm{T} = \mathrm{T}_0 + \beta \mathrm{t} \tag{2.1}$$

With $\beta = \frac{dT}{dt}$ is the heating rate in the unit of K/s.

In our experiments, we have used the heating ramp, $\beta = 0.2$ K/s.

During the heating phase, the QMS is placed in front of the sample surface to record the mass spectra of desorbing species. The thermal desorption of an absorbed specie from the cold surface follows an Arrhenius law describes by the Polanyi-Wigner equation:

$$\mathrm{r}(\mathrm{N}, \mathrm{E_b}, \mathrm{T}) = -\frac{\mathrm{dN}}{\mathrm{dt}} = \mathrm{AN^n e^{-E_b/k_B T}} \tag{2.2}$$

Where:

r: the desorption rate (molecules.cm^{-2}.s^{-1})

E_b: the adsorption energy (K)

A: the exponential factor (s^{-1})

N: the number of absorbed atoms or molecules

n: the order of the desorption process

k_B: the Boltzmann constant; $k_B = 1.38 \times 10^{-23}$ J.K^{-1}

T: the desorption temperature (K)

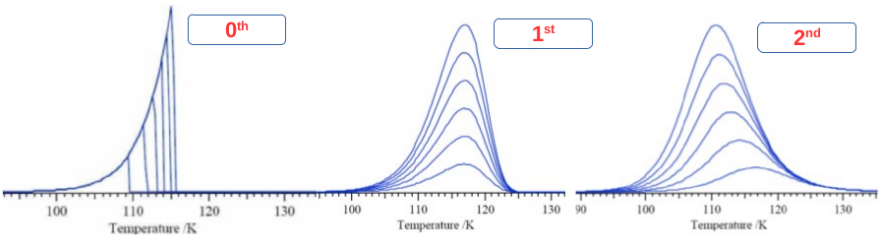

FIGURE 2.7: Three different TPD profiles corresponds to the zero, first, and second order n of the desorption kinetics.

The order n corresponds to the number of reactants necessary to activate the desorption. It consists of zero, first, and second order kinetics. Figure 2.7 displays three the different TPD profiles corresponding to the zero, first, and second order n of the desorption kinetics. The typically zero order (n = 0) reflects desorption independent of the coverage. The first order (n = 1) corresponds to the thermal desorption of molecules absorbed on the surface, the peak positions of desorption spectra does not change with the coverage; the peak shapes are asymmetric. For the second order (n = 2), the peak positions shifted toward the low temperatures when the coverage increased, in which it implies the reaction rate is proportional to the products of the concentration of the reactants.

The TPD experiment is therefore a tool to study chemical reaction mechanisms which happen on the sample surface.

2.2.2 Water ice substrates on the sample holder

Water ice exits in a large number of phases (Line and Whitworth, 1996, Kuhs, W. F. et al., 1987, Van Dishoeck et al., 2013). The influence of water ice substrates is an important question when studying chemical reactions take place on grains (Watanabe et al., 2004). The morphology of deposited water ice substrates is determined by the temperature of grains (Petrenko and Whitworth, 2002). There are some different types of water ice structures such as amorphous water ice (compact and porous) and crystalline ice.

Different morphologies of water ice substrates are formed in the VENUS set-up. Water ice substrates are formed by depositing water vapour on very cold substrates under the UHV conditions. During the deposition, the micro-channel array doser is placed higher above the sample holder. This method allows water vapour to

fill the entire volume of the main chamber before its condensation on the sample holder surface. The liquid water vial is connected to a turbo molecular pump. Water pressure obtained thanks to the liquid water equilibrium and is measured in the gas inlet before being injected in the UHV chamber. Water vapour is sprayed onto the sample surface through a capillary vaporiser having the throttling valve to adjust the pressure of water vapour before depositing on the sample surface. The pressure of the UHV chamber reaches about 10^{-8} mbar, while the residual pressure into the chamber is of 10^{-10} mbar. The gas composition is checked by the QMS.

Knowing pressure (P), temperature in the main chamber (T) and the mass impinging molecules (m), the flux φ of molecules hitting the cold surface can be evaluated as follows:

$$\varphi = \frac{1}{4}\overline{v}n = \frac{1}{4}\frac{P}{KT}\sqrt{\frac{8KT}{\pi m}} \tag{2.3}$$

Where $\overline{v}$ is the mean velocity and n is the number density, while 1/4 is a corrective factor due to the projection of a sphere on a disk.

For all types of water ice substrates, the base pressure in the UHV chamber is maintained at 10^{-10} mbar. Depending on the kind of water ice substrates which we adapt the surface temperature. For c-ASW, the temperature is maintained at 110 K, while we spray water vapour onto the surface. We usually introduce the water vapour to grow 15 to 20 monolayers (MLs). In the case of p-ASW, after completing c-ASW on the sample holder, the temperature of the sample holder is cooled down to 10 K or 40 K. Subsequently, water is continuously deposited on c-ASW to form p-ASW at 10 K or 40 K. Usually more 5 monolayers are grown before the injection is stopped. For the crystalline ice substrate, the sample holder is still kept at 110 K during the deposition, and then annealed to 145 K. The water ice phase transition is monitored by both mass spectroscopy (desorption rate is reduced) and IR spectroscopy (water ice band is highly shifted and narrowed). After completing the water ice substrate, the temperature of the sample holder is cooled down to 10 K in order to start experiments.

It is also possible to grow faster ice by spraying directly on the substrate. Such as a 15 MLs thick ice is grown in 4 minutes instead of about 1 hour. We control the amount thanks to the IR absorbance benchmarked with background deposition.

2.2.3 Calibration of the beamline system

2.2.3.1 Optimization of the injection flow

We can use four separated beams to inject molecules and atoms in the main chamber. However, we only used three beams corresponding to the right, top, and central beams for all experiments.

In fact, we usually perform chemical reactions of complex organic molecules by depositing two to three molecular species on the sample holder at the same time. The calibration of beams is necessary to determine the fluxes and the good geometrical overlaps of species on the sample holder.

For the investigation of source fluxes, the method is to deposit CO_2 on the surface with different fluxes. Changing the gas flow injection leads to the change of the beam flux at the sample surface. We stress that the beam flux is the flow of atoms or molecules in the beamline in ML/s or mol/cm^2/s, while the gas flow injection in the source is called the source flux and is exposed in sccm. The amount of the CO_2 molecules coming from the beams are recorded by monitoring the QMS located at the high position. Figure 2.8 displays the amount of CO_2 measured in the main chamber (beam flux) with the different source fluxes for three beams. The amount of CO_2 tends to saturate when the source flux reaches the value of 0.6 sccm. The amount of CO_2 of the top beam is less than the others. Accordingly, the source flux works better when the flow value is lower than 0.6 sccm. The saturation is due to the collisions in the expansion zone. At too high pressure the mean free path of molecules becomes too small and and molecules are ejected from the beam path.

2.2.3.2 Determination of the geometrical area of the beam deposition zone on the sample holder

The aim is to determine the geometrical area of the beams. So, CO_2 is deposited on the sample holder maintained at 10 K for each beam. The flow of CO_2 used is 0.3 sccm. The doses of CO_2 are increased with prolongation of the deposition time. After completing the deposition, the surface temperature is heated up from 10 K to 150 K. The adsorption and desorption of CO_2 are obtained by IR spectrometer and TPD-QMS.

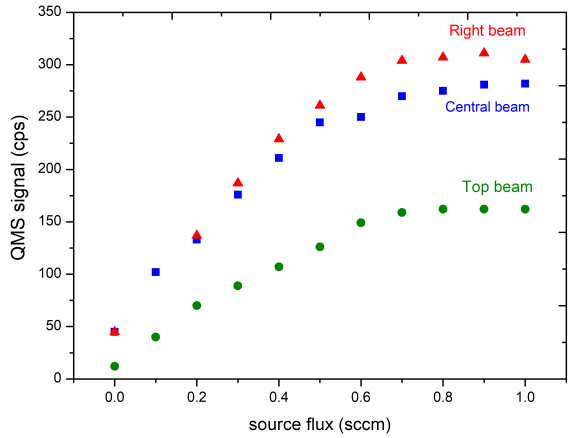

FIGURE 2.8: CO_2 beam flux as a function of source flux.

Figure 2.9 shows the integrated areas of absorbance and desorption band of CO_2 as the function of exposure time. The absorbance and desorption areas of CO_2 corresponding to the right beam are larger than the central and top beams, whereas signals of the central and top beams are almost the same. It demonstrates that the exposure surface of the right beam is larger and it could cover the exposed surface both of the central and top beams. For all experiments, we have selected the right beam to inject the H_2 or D_2 molecules becoming H or D atoms after switching on the discharge. The central and top beams are used to deposit the other species.

2.2.3.3 Determination of the beam overlap

To determine the overlap between the top and central beams, we have investigated the consumption of NH_3 and H_2CO through their reactions (Bossa et al., 2008, Duvernay et al., 2014). NH_3 and H_2CO are deposited on the sample holder through the top and central beams, respectively. Figure 2.10 shows the evolution of the integrated areas of NH_3 and H_2CO when they are co-deposited on the sample holder. ΔN (NH_3) and ΔN (H_2CO) indicate the quantitative consumption of the NH_3 and H_2CO molecules. We have calculated the different consumptions between NH_3 and H_2CO. Remaining H_2CO and NH_3 are composed of molecules which are unreacted or molecules are outside the overlap region. Remaining H_2CO and NH_3 on the sample holder are approximately 25 % and 30 %, respectively. The consumed region of NH_3 is larger than H_2CO with a factor of 0.05.

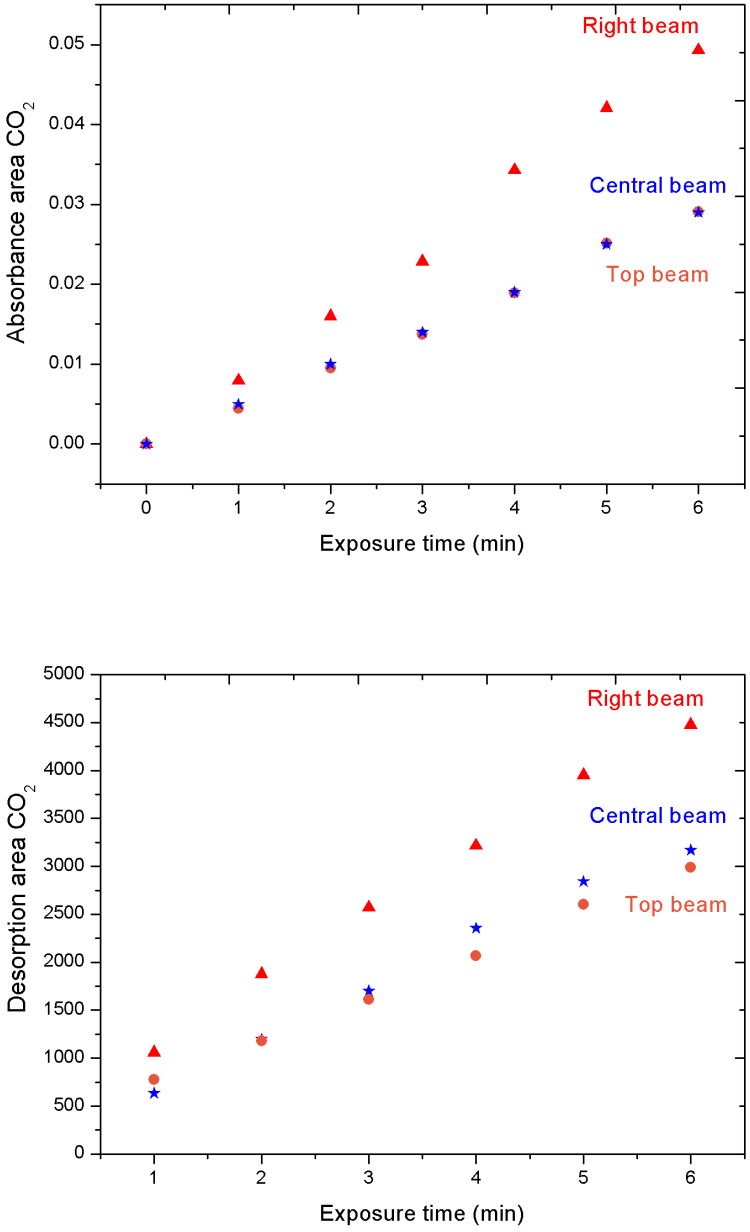

FIGURE 2.9: Integrated area of CO_2 by using IR spectrometer (top panel) and TPD-QMS (bottom panel) for three beams. The red triangles, blue stars, and orange circles exhibit the integrated area of CO_2 for the right, central, and top beams, respectively.

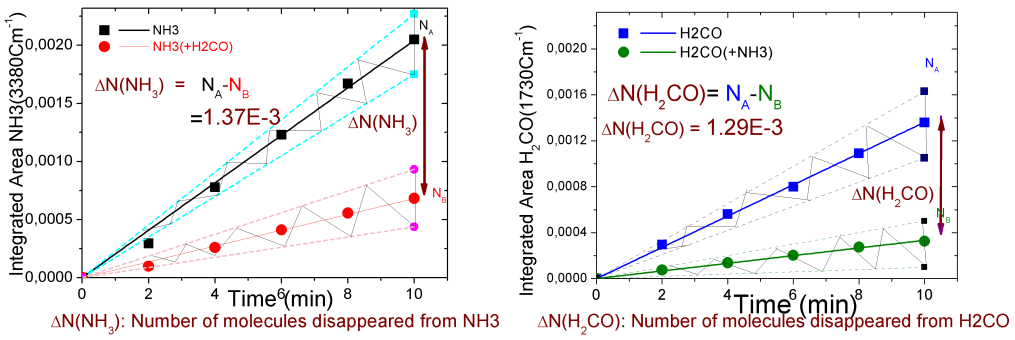

FIGURE 2.10: Evolution of the integrated area of NH_3 and H_2CO as the function of exposed time.

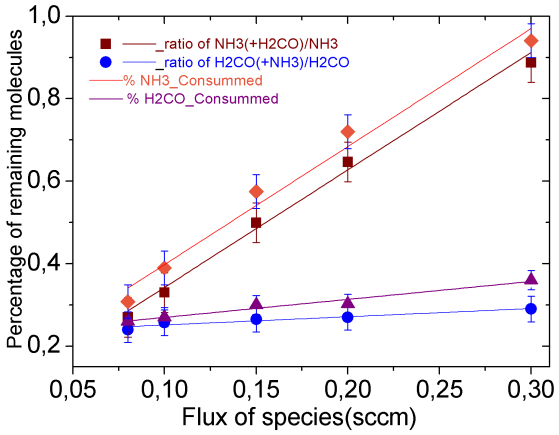

FIGURE 2.11: Ratio between remaining NH_3 and original NH_3 (brown squares); remaining H_2CO and original H_2CO (blue circles) as the function of the NH_3 flux. The remnant and consumption of NH_3 (brown and red squares) increased with the NH_3 flux, whereas the remnant (blue circles) and consumption (violet triangles) of H_2CO are mostly unchanged during the process.

The analysis of remaining H_2CO and NH_3 are elucidated in figure 2.11. It is done thanks to a new experiment where we increase the flux of NH_3 while H_2CO's flux is kept constant. Remaining NH_3 (brown squares) increases with the injected flux of NH_3, whereas remaining H_2CO (blue circles) is constant with the variation of the flux. The constant value of H_2CO occupies approximated 25 % which is the amount of molecules non-covering by NH_3. The increase of NH_3 is due to the disequilibrium in the stoichiometry.

Finally, the right beam overlaps whole the exposure surface of the central and top beams. Indeed, we can obtain a full hydrogenation of a sub-monolayer of NO. The top beam has the smallest exposure surface and only covers approximately 75% the surface of the central beam.

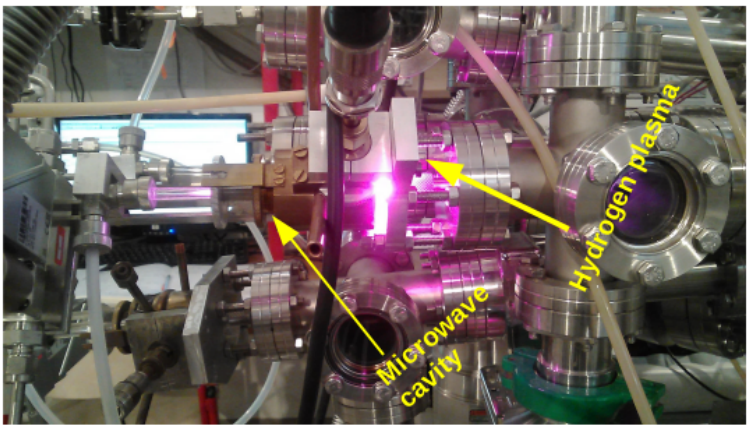

FIGURE 2.12: H_2 plasma in the right beam of VENUS.

2.2.3.4 Dissociation of H_2 and D_2 beam

Because the right beam is overlapping the others, it is chosen for the atomic gas such as H or D or O. On the right beam is mounted a microwave cavity for dissociating molecular gases. Figure 2.12 shows the picture of dissociation of H_2 gas through the right beam of VENUS.

In order to evaluate the atomic H (or D) flux, we first produce a H_2 (D_2) beam and we compare it with a discharge of typical 70/40w of power. The amount of atomic H(D) is monitored by using QMS intercepting the atomic beam. The typical efficiency of the dissociation τ is calculated via the formula (2.4) below:

$$\tau = \frac{S_{off} - S_{on}}{S_{off}} \tag{2.4}$$

Where S is the amount of atomic H (or D or O) detected when the discharge switched OFF and ON. We estimates the τ efficiency of the dissociation is approximately 75% $\pm$ 5% for H_2 and 65 % $\pm$ 5% for D_2. It means that every 100 molecules of H_2, we have 150 atomic hydrogen and 25 molecules.

Chapter 3

Segregation effect and N_2 binding energy reduction in CO-N_2 system adsorbed on water ice substrates

CO and N_2 are two abundant species in molecular clouds. CO molecules are heavily depleted from the gas phase towards the centre of pre-stellar cores, whereas N_2 maintains a high gas phase abundance. For example, in the molecular cloud L183, CO is depleted by a factor of ≈ 400 in its centre with respect to the outer regions of the cloud, whereas N_2 is only depleted by a factor of ≈ 20 (Pagani et al., 2012). The reason for this difference is not yet clear, since CO and N_2 have identical masses, similar sticking properties, and a relatively close energy of adsorption (Fayolle et al., 2016). We present a study of the CO-N_2 system in sub-monolayer regimes, with the aim to measure, analyse and elucidate how the adsorption energy of the two species varies with coverage, with much attention to the case where CO is more abundant than N_2.

3.1 Introduction

CO and N_2 are two of the most abundant species in molecular clouds and they affect the abundances of many other molecules. CO is the second most abundant

molecule after H_2 in the gas phase and is highly abundant in the solid phase. CO ice absorption features are seen superposed on the spectra of background sources or embedded protostars (e.g. Chiar et al. 1995, Pontoppidan et al. 2003). The solid CO abundance varies strongly from source to source, but can be as high as 10^{-4} with respect to H_2 in the coldest cores (Pontoppidan et al., 2005).

The amount of N_2 in the gas and in the solid state is uncertain, since N_2 cannot be detected directly as it lacks a permanent dipole moment. The abundance of gas phase N_2 is usually inferred from the presence of its daughter species N_2H^+ mainly formed via the reaction $N_2+H_3^+ \longrightarrow N_2H^+ + H_2$. Similarly, HCO^+ is formed from CO following a similar reaction scheme $CO+H_3^+ \longrightarrow HCO^+ + H_2$. But CO is also one of the main destroyers of N_2H^+ in the gas phase via the reaction $CO + N_2H^+ \longrightarrow N_2 + HCO^+$. When CO freezes out on to dust grains, N_2H^+ abundance is enhanced, as confirmed by the anti-correlation of the abundances of N_2H^+ with CO and HCO^+ in the pre- and proto-stellar regions (Bergin et al., 2001, Tafalla et al., 2002, Di Francesco et al., 2004, Pagani et al., 2005, Jørgensen et al., 2004). This anti-correlation was sometimes quantitatively explained by assuming that a ratio of 0.65 exists between the binding energies of N_2 and CO, allowing N_2 to stay in the gas phase while CO can freeze out on to H_2O-covered grains (Bergin and Langer, 1997). However, for pure species in thin layers or mixed species thick layers, such a high difference in binding energy between N_2 and CO has never been reported (Öberg et al., 2005, Bisschop et al., 2006, Fayolle et al., 2016).

Freeze-outs of CO and N_2 are difficult to quantify in dark clouds. N_2 is not directly detectable as explained above, and emission of the depleted CO in the central parts of the clouds is so weak that it is completely masked by the strong, unattenuated emission of the envelope. Since H_3^+ reacts with both species, the products of the reactions (DCO^+, N_2H^+, and N_2D^+) can be used to trace their abundance as shown in Pagani et al. (2012). By using this method, Pagani et al. (2012) reported a steeper depletion profile of CO with respect to N_2 towards the centre of the L183 pre-stellar core. The origin of this selective depletion remains unknown.

There are many possible explanations, although none of them is fully convincing. It can be due to the imperfection of the gas phase chemical network, which was recently improved (Le Gal et al., 2014). If the microphysics at the surface of grains plays a role, we can basically think of two possibilities. The first possible explanation is of chemical origin, namely can be a differentiation in the chemical

properties once CO and N_2 are both present on the surface of grains. It is known that CO can be hydrogenated into methanol (Hiraoka et al., 1994, Watanabe and Kouchi, 2002, Minissale et al., 2016), whereas N_2 does not react with H atoms (Ioppolo et al., 2015, Fedoseev et al., 2015). Moreover, N-atom diffusion is faster than that of O atoms (Minissale, M. et al., 2016), and N_2 is also very stable when compared to O_2 or CO. However, there are not quantitative studies about the {N+H} or {N_2+H} reactive networks to be able to make a clear prediction about the impact of the surface chemistry. The second possible explanation is of physical origin, since there exist reasons to think that some physical processes can play an important role, and especially a surface segregation effect of certain species. Previously, we found that H_2 isotopologues as well as molecular hydrogen of different spin states desorb at different temperatures (Dulieu et al., 2005, Amiaud et al., 2008, 2015), which can lead to appreciable changes in the abundance of H_2 isotopologues adsorbed on dust grains (Kristensen et al., 2011). Later, we have demonstrated that this segregation mechanism can also apply to molecules whose binding energy distributions are close, like O_2 and CO (Noble et al., 2015). We have shown that a small average difference of 85 K between the centres of two binding energy distributions can fully explain the observed kick–out mechanism of O_2 by CO during the desorption phase. We used the Fermi-Dirac statistics in order to calculate the adsorption site population distribution, and we managed to reproduce all the features of the CO and O_2 desorption traces.

In the present chapter, we propose a study of the desorption of N_2 and CO mixtures from different water ice substrates in the sub-monolayer regime. As for multi-layer regimes see Bisschop et al. (2006). Since the desorption mechanism takes place in the very outer layer, our study focuses on thin layers to mimic the action of the underlying icy template as in Fayolle et al. (2016). Here, we study CO:N_2 mixtures relevant to polar ices (water-dominated) covering dust grains, with CO being always the most abundant species (Taquet et al., 2012, Pagani et al., 2012). We use ^{13}CO molecules and $^{15}N_2$ molecules in order to be able to distinguish the two species by mass spectrometry. The water ice substrates used in this study are compact and porous amorphous solid water, and poly-crystalline water ice. Experimental studies have shown that interstellar porous ice analogues can be compacted quite efficiently by UV irradiation, cosmic ion bombardment, and H-atom recombination at their surface (Palumbo et al., 2010, Palumbo, 2006, Raut et al., 2008, Accolla et al., 2011), which suggests that water ice in space is almost certainly amorphous and non-porous (compact). We have however carried out a series of

experiments also on poly-crystalline ice as it provides a more ordered surface, and because studying water ice templates other than a compact amorphous substrate alone can be of interest for specific interstellar environments where ices may have undergone energetic processing, for example protostellar objects (Dartois et al., 2002).

3.2 Experimental protocol

All experiments were performed using the UHV set-up named VENUS (VErs de NoUvelles Synthèses) based in the LERMA laboratory at the University of Cergy Pontoise. VENUS is a new apparatus that will be described in detail in a forthcoming paper so the set-up and the experimental techniques are only summarized here. The experiments take place under ultra-high vacuum (UHV) conditions (base pressure 8×10^{-11} mbar) in a stainless steel chamber. The sample holder is made of a circular copper mirror coated with gold, and mounted onto the cold head of a closed-cycle He cryostat. The sample temperature can be controlled in the 7–350 K range by using a regulated resistive heater clamped on the back of the sample holder.

The first step of each experimental run is the deposition of a water ice layer. To grow the water ice substrate we use the so-called background deposition as follows: water vapour is injected into the main chamber until a pressure of 1.2×10^{-8} mbar is reached, and is kept constant during the deposition process until the desired ice thickness is attained. The purity of the water vapour, meaning the absence of air contamination or H_2 release from the walls of the chamber, is monitored via a quadrupole mass spectrometer (QMS). The water ice thickness deposited on the gold surface is monitored via a Fourier Transform InfraRed Spectrometer (FTIRS), used in a grazing-angle reflection absorption configuration. The calibration of the water ice thickness via FTIRS and QMS was carried out in a separate set of experiments, when the amount of water ice deposited was benchmarked against pressure gauge. The calibration of the water ice thickness via FTIR and QMS was carried out in a separate set of experiments when the amount of water ice deposited was measured as a function of time using the H_2O partial pressure in the chamber, since a given pressure corresponds to – within the accuracy of the pressure gauge – a precise flux of molecules impinging on the walls of the chamber. Subsequently, the comparison between the number of deposited water

layers and the infrared/mass spectra allows definition of the one-monolayer standard expressed in IR-band area units or TPD peak area units, with an accuracy of ±0.2 monolayers. Typically, a substrate of 15 layers of compact amorphous solid water ice (c-ASW) is grown by keeping the surface temperature at 110 K during water deposition. Once the deposition phase is finished, we wait until the partial pressure of water vapour in the main chamber has reached its pre-dosing value ($<10^{-10}$ mbar), and only then the sample temperature is cooled further or increased. To obtain a poly-crystalline ice (PCI) substrate, the sample holder is held at 110 K during the deposition, then flash heated to 145 K, and simultaneously the water ice film phase transition, from amorphous to crystalline, is monitored via both QMS and FTIRS. When the phase transition is complete, we cool the surface to 10 K before commencing the experiments. During the crystallisation phase, we estimated a loss of about 3 out of 15 initial layers of water ice, although we determined – by analysis of the desorption profiles of CO and N_2 – that the icy substrate remains thick enough that the adsorbed molecules interact with the crystalline template only. Finally, the porous amorphous solid water (p-ASW) ice substrate is formed by growing 5 monolayers of ice at a surface temperature of 40 K on top of the c-ASW substrate, then it is annealed to 55 K to stabilize the film morphology before the subsequent heating-cooling experiments between 10 and 55 K. Although the degree of porosity of the p-ASW substrate is less pronounced than that of an ice film grown at 10 K and not annealed, the p-ASW ice substrate we use maintains the same overall properties as far as the physisorption binding energies are concerned (Fillion et al., 2009).

Once the desired water ice substrate is formed, the surface temperature is cooled to 10 K. CO and N_2, isotopically labelled (^{13}CO and $^{15}N_2$), can be dosed onto the surface via one triple-differentially-pumped molecular beam. The composition of the beam is monitored through a second QMS located in the second stage of the beam-line. The surface is held at 10 K during every CO/N_2 depositions. In case of depositions with CO-N_2 mixtures, the gas is previously prepared in a dedicated reservoir to be connected to the beam source. The injected flow of gas is set to 0.3 standard cubic centimetre per minute (sccm[1]), which gives a pressure of around 2×10^{-4} mbar in the first stage of the beamline. After going through 3 stages of differential pumping and two diaphragms, the molecular beam is well collimated (2-mm diameter) and reaches the main chamber causing here an increase in pressure less than 1×10^{-11} mbar.

[1] 1 sccm = $592\,\mathrm{m}^3$ Pa s^{-1} in SI units

The temperature-programmed desorption (TPD) technique is a powerful method for determining the binding energies of the molecules adsorbed on surfaces. It consists in increasing the surface temperature linearly with time and simultaneously recording the desorbing molecules using mass spectrometry. VENUS is equipped with a QMS placed 5 mm in front of the sample. The heating ramp is constant, $\beta = 0.2$ K/s, for all experiments, and starts from a temperature of 10 K, which is the CO/N_2 deposition temperature. TPD analysis is used to derive multi-layer desorption energies of species deposited as thick films, and it also allows us to derive the distribution of adsorption energies on a given surface in the case of sub-monolayer regimes. The adsorption energy is in fact dependent on the amount of molecules deposited, that is the coverage. Therefore, we have to keep in mind that there are three important experimental parameters to take into account: the type of species, the type of surface, and the coverage (Kimmel et al., 2001, Fillion et al., 2009, Noble et al., 2012).

The coverage is given in monolayer (ML) units, with the typical approximation that 1 ML $= 1 \times 10^{15}$ molecules cm^{-2}, which corresponds to the number of adsorption sites per cm^2 on compact amorphous solid water. It is a unit of surface density: when the coverage equals 1 ML, it means that all the adsorption sites of the ice surface are occupied in the case of a fully wetting molecule, such as CO or N_2. Should another molecule come to the surface it will adsorb onto an already adsorbed molecule so as to begin a second-monolayer layer. With respect to first-layer particles, molecules that belong to the second layer exhibit weaker interactions with the substrate, and their desorption properties are, in general, dominated by molecule-molecule interactions. The first-monolayer layer is complete and the surface coverage is equal to 1 ML only for substrates that have a planar geometry, namely c-ASW and PCI substrates. In the case of porous substrates, the number of binding sites per cm^2 increases with water ice film thickness. In fact, porous water ice possesses a 3D structure and the number of adsorption sites is proportional to the geometrical area of the porous ice 3D network.

3.3 Experimental results

3.3.1 Pure species

Figure 3.1 shows three typical sets of TPD curves : $^{15}N_2$ desorbing from c-ASW (top panel), ^{13}CO desorbing from c-ASW (middle panel), and ^{13}CO desorbing from p-ASW (bottom panel). Figure 3.2 shows TPD spectra of ^{13}CO (top panel) and $^{15}N_2$ (bottom panel) desorbing from PCI. Each curve corresponds to a given dose, that is the initial coverage at 10 K. For each species deposited on a specific water ice substrate, a family of TPDs exhibits the so-called 'filling behaviour', described by Kimmel et al. (2001). Each type of substrate shows a distribution of adsorption sites with various energy depths, which is why desorption from a full first-monolayer layer occurs over a wide window of temperature, from around 25 K to 55 K. When only a small fraction of a monolayer (e.g. <0.25 ML) is initially present, the desorption only occurs at temperatures in the high end of the TPD peaks, which corresponds to desorption of molecules from sites with the highest binding energies. As the dose is increased, because the best (high-depth) sites are already occupied, molecules are forced to occupy lower energy sites, so desorption occurs earlier and the TPD peak shifts towards lower temperatures. In fact, available sites are progressively filled beginning from high-depth sites towards low-energy ones. The TPD profiles have a leading edge appearing at lower temperature with increasing coverage as is apparent from Figures 3.1 and 3.2, while TPD spectra of a given molecule-substrate system all share a common tail. When the deposited amount reaches 1 ML, a second-monolayer is begun by molecules that form physisorption bounds with molecules of the first-monolayer layer. The presence of molecule-molecule bindings produces a new low-temperature feature (a bump or a real peak) in the TPD profiles corresponding to coverages >1 ML. If the exposure is increased further, the low-temperature peak maximum shifts towards higher temperatures, although the leading edge of all the high-coverage exposures remains unchanged. This is the signature of the second-monolayer or multi-layer desorption, which follows a so–called zeroth order desorption. It should be noted that the multi-layer peaks of N_2 and CO, desorbing from c-ASW or PCI, appear for the same dose, which indicates that the number of adsorption sites is the same for the two molecule-substrate systems. On the contrary, the multi-layer peak of CO appears after an exposure of 1.5 ML when the substrate is p-ASW ice, which

means that the porous substrate exhibits 1.5 more adsorption sites with respect to c-ASW and PCI, due to its 3D structure.

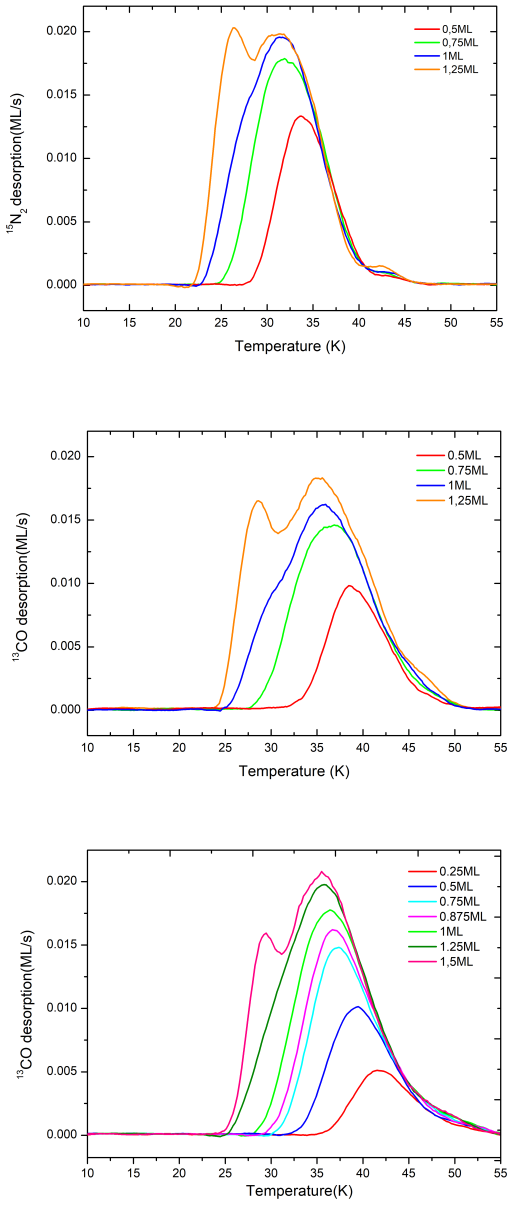

FIGURE 3.1: TPD curves of different doses of $^{15}N_2$ desorbing from c-ASW (top panel), of ^{13}CO from c-ASW (middle panel) and from p-ASW (bottom panel).

From the analysis of the TPD profiles it is possible to estimate the distribution of binding energies. The desorption rate can be described in terms of an Arrhenius law:

$$r(N, E_b, T) = -\frac{dN}{dt} = A\, N^n e^{-(E_b/k_B T)}, \tag{3.1}$$

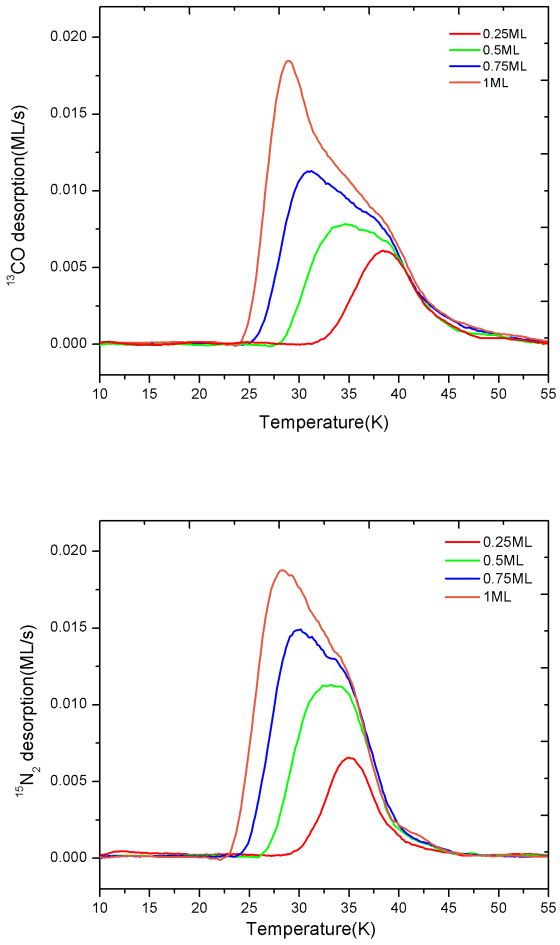

FIGURE 3.2: TPD spectra of different doses of ^{13}CO (top panel) and $^{15}N_2$ (bottom panel) from poly-crystalline water ice (PCI).

where r is the desorbing flux in ML s^{-1}, E$_b$ is the binding energy in J, A is the pre-exponential factor in s^{-1}, N is the total number of molecules adsorbed on the surface expressed in ML, n is the order of the desorption kinetics, k$_B$ = 1.38×10^{-23} J K^{-1} is the Boltzmann constant, and T is the temperature of the surface in K. The order n corresponds to the number of reactants necessary to activate the desorption. It corresponds to a stoichiometric coefficient in the desorption equation. The zeroth order represents a desorption kinetics that is independent of the amount of available adsorbate. This is the case of thick films consisting of multi-layers, whose number of molecules at their surface remains constant during desorption, as one molecule that comes off the surface is replaced by another one lying just underneath. The first-order desorption corresponds to the desorption of an adsorbate whose coverage is lower or equal to one monolayer, which is the case of the present study. First-order kinetics implies that the desorption rate

is proportional to the number of molecules present on the surface, provided that each molecule has no strong interaction with its neighbours, which means that no reaction is at play. Therefore, for CO and N_2 physisorbed on water ice we assume that $n = 1$. The pre-exponential factor can be specifically determined, but it turns out to be coupled with the binding energy E_b. However, for the purposes of this work, and to obtain results that can be easily compared to previous publications, we adopt the generally accepted value A= 10^{13} s^{-1}, corresponding to the typical vibrational frequency of CO and N_2 physisorbed on the surface.

By inverting equation 3.1, the desorption energy E_b can be calculated as a function of coverage N. We use the inverted Polanyi-Wigner equation following Dohnálek et al. (2001), also called the *classical inversion method*, which is now commonly used in laboratory astrophysics (Noble et al., 2012, Collings et al., 2015, He et al., 2016). The first step consists in calculating the number of molecules that have desorbed at a given temperature T. To perform this step, the TPD spectrum is integrated between T_0 (deposition temperature) and T, then divided by the area of the TPD peak $A_{1ML} = \int_{10K}^{55K} \frac{dN}{dt} dT$ corresponding to 1 ML exposure:

$$N'(T) = \frac{\int_{T_0}^{T} \frac{dN}{dt} dT}{A_{1ML}}. \tag{3.2}$$

$N'(T)$ is thus the fraction of molecules (expressed in ML units) that has already desorbed at temperature T. The coverage as a function of T can be expressed as the amount of deposited molecules, the initial coverage N_0, minus the fraction of molecules desorbed at temperature T:

$$N(T) = N_0 - N'(T). \tag{3.3}$$

Knowing N(T), it is now possible to invert equation 3.1:

$$E_b = k_B T \times \ln \left[\frac{A\, N(T)}{r(T)} \right]. \tag{3.4}$$

E_b is the desorption barrier and will be expressed in kelvins (J/k_B) henceforth.

Fig. 3.3 shows the distributions of binding energies for ^{13}CO and $^{15}N_2$ on c-ASW. At zero coverage the binding energy of CO is close to 1600 K and that of N_2 is

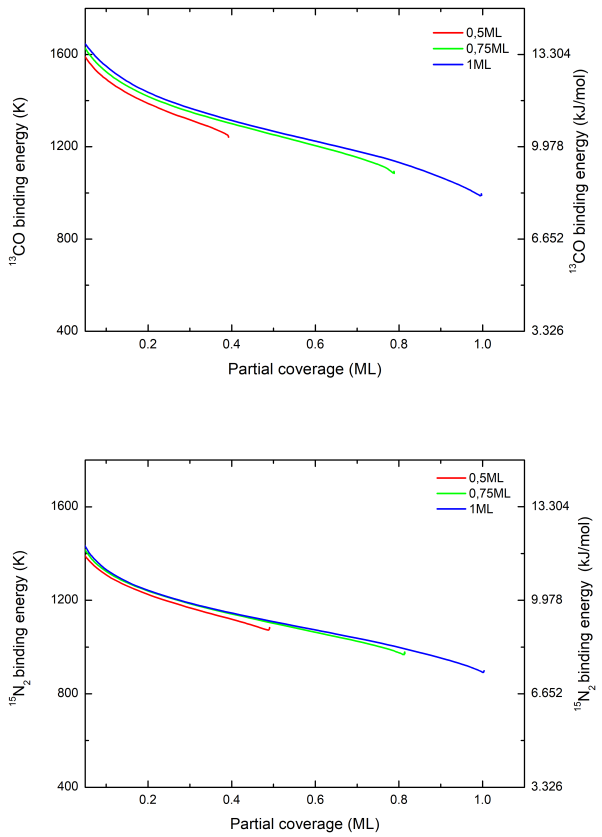

FIGURE 3.3: Binding energy of pure ^{13}CO (top panel) and pure $^{15}N_2$ (bottom panel) on compact amorphous solid water ice, as a function of coverage, obtained using the classical inversion method, assuming $n = 1$ and A $= 10^{13}$ s^{-1}.

around 1400 K. Each curve corresponds to a given TPD shown in Figure 3.1. The longer the curve the greater the deposited dose, until a maximum value reaching 1 ML (monolayer regime). As expected, the binding energy decreases with coverage, and the curves have a typical half bell shape. Just before monolayer completion, the binding energy of CO molecules is around 1000 K, while it is around 900 K for N_2. On the other end of the curves (corresponding to zero coverage), the highest values are 1600 K and 1400 K for CO and N_2, respectively. Our results are in agreement with all the previous values given in the literature (see Fayolle et al. 2016 and references therein).

Fig. 3.4 shows the distributions of binding energies of pure ^{13}CO and pure $^{15}N_2$ on PCI, while in Fig. 3.5 we reported the distribution of binding energies of pure ^{13}CO on p-ASW.

All the binding energy data for pure species are reported in Table 3.1. The most

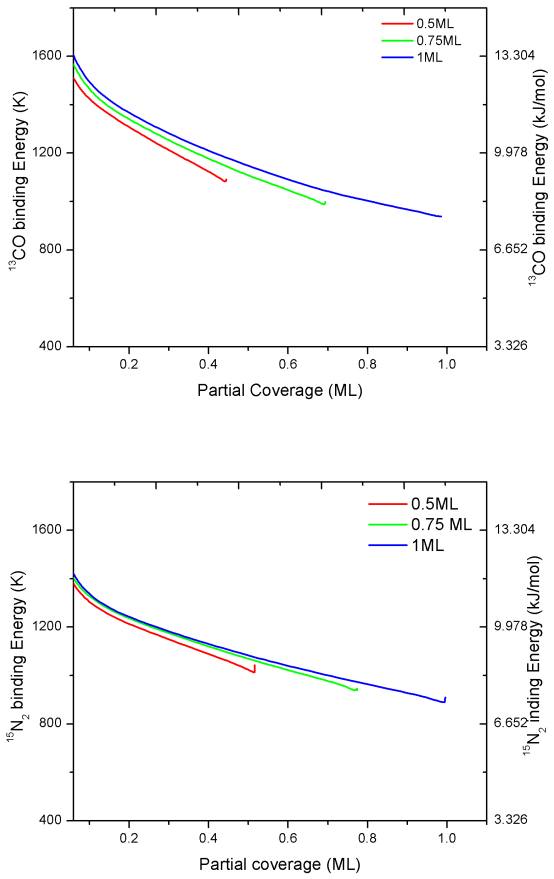

FIGURE 3.4: Binding energy of pure ^{13}CO (top) and pure ^{15}N$_2$ (bottom) on poly-crystalline water ice, as a function of coverage ($n = 1$, A $= 10^{13}$ s^{-1}).

useful information is the case of 1 ML dose because its two extrema correspond to i) the bare surface case (highest values of the desorption energy), ii) the full coverage case (lowest values). We note that the maximum of the binding energy has a slight tendency to increase with the dose, which may indicate that at higher coverages a larger fraction of deepest sites is occupied so the desorption process is slowed down. In fact, the more molecules on the surface, the more molecules are pushed to diffuse and occupy all the available sites. Also, at full coverage on c-ASW ice, the binding energy of the least bound molecules is close to the multi-layer barrier value.

On the other hand, an exposure of 1 ML on porous ASW ice does not correspond to complete occupation of the available sites, because porous ASW has a larger effective area as we explained above. An exposure of about 1.5 ML is necessary before build-up of the second layer on porous water ice (see Fig. 3.1, bottom panel). We can also notice that the maximum binding energy found on p-ASW is close

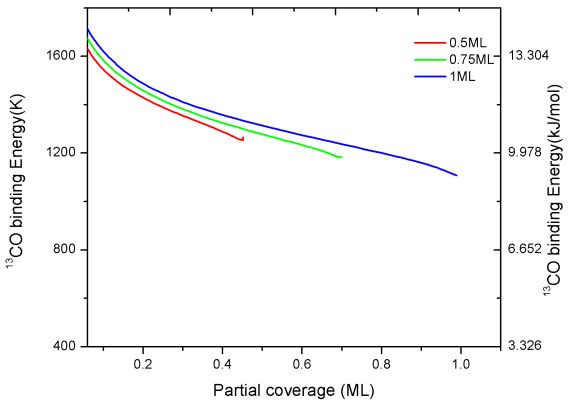

FIGURE 3.5: Binding energy of pure ^{13}CO on porous amorphous water ice, as a function of coverage ($n = 1$, A $= 10^{13}$ s^{-1}).

to the maximum value obtained for c-ASW (1600 K, corresponding to molecules desorbing up to 55 K). This result seems to be not consistent with experiments carried out using H_2 (Fillion et al., 2009), or with the elegant demonstration by Kimmel et al. (2001) who used N_2. In fact, TPD tails from p-ASW tend to extend to higher temperatures with respect to more ordered substrates, which indicates the presence of deeper adsorption sites associated to larger topological disorder. In this work this does not seem to be the case. The reason for this is that the deposition temperature of water molecules (40 K) and the subsequent thermal annealing until 55 K smoothen the deepest adsorption sites, located on less stable configurations of water clusters showing a reduced number water molecules coordinations. Moreover, the ice thickness that was used in this study is so low that there cannot be a geometrical pore effect (Dohnálek et al., 2003). Yet, if the two binding energy upper values are similar for p- and c-ASW, the shape and a greater number of binding sites on porous water ice results in a global shift towards the high-energy (-temperature) half of the TPD peak.

3.3.2 Mixed species

We have performed different TPD experiments of mixed species varying the total doses as well as the relative ratios. Figure 3.6 shows the change in TPD shape obtained by increasing the CO dose (from 0.45 to 1.27 ML) and keeping relatively constant and small the N_2 dose (from 0.065 to 0.11 ML). The gas mixture is prepared in a reservoir before injection into the beam source. We cannot control

TABLE 3.1: Pure species: energy ranges of CO and N_2 binding energy distributions measured as a function of coverage on different water ice substrates.

Substrate	Dose (ML)	E_b $^{15}N_2$ (K)	E_b ^{13}CO (K)
c-ASW	0.5	1077 -1385	1255 - 1585
c- ASW	0.75	970 - 1400	1090 - 1594
c-ASW	1	890 - 1430	990 - 1630
PCI	0.5	1014 - 1298	1075 - 1541
PCI	0.75	939 - 1325	986 - 1600
PCI	1	887 - 1335	932 - 1639
p-ASW	0.5	-	1254 - 1477
p-ASW	0.75	-	1182 - 1511
p-ASW	1	-	1104 - 1545

precisely the partial pressure of each species, which implies that we have fluctuations of the N_2 dose. For this reason, we do not have a very good control *a priori* of the individual amounts deposited, although we can finely control the total deposited amount of the mixed species. Finally, we can precisely measure the mixture composition *a posteriori*, by integrating the TPD curves. Figure 3.6 shows that the CO desorption profiles seem to be unaffected by the presence of the other co-adsorbate. The CO TPD set exhibits all the features of the filling behaviour. With the increase in dose, the leading edges are shifted toward low temperatures whereas the tails follow a common path. The multi-layer peak appears when the coverage exceeds one monolayer. On the contrary, the N_2 desorption profiles are hugely modified by the presence of CO. In particular, *the mean temperature of desorption of N_2 decreases with CO coverage*. The N_2 TPD tails do not overlap and, more importantly, N_2 desorption is almost completed within the same temperature range where the leading edge of CO curves develops. This is possibly a sign that N_2 tends to desorb before CO if the two species are present on water ice simultaneously.

For at least three combinations of sub-monolayer coverage and surface, a series of depositions were made, varying the ^{13}CO-$^{15}N_2$ system coverage from 0.5 to 1 ML. The ranges of binding energies found for N_2 and CO are presented in Table 3.2.

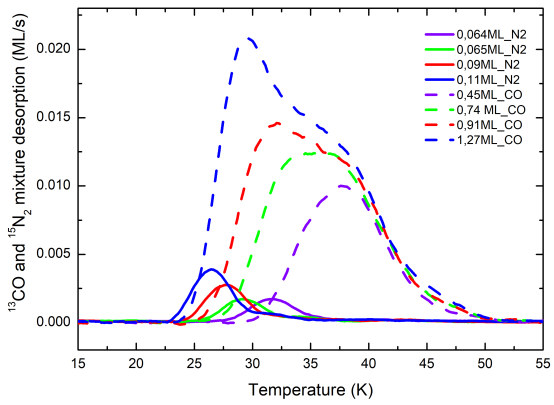

FIGURE 3.6: TPD profiles of various mixtures of CO and N_2 deposited on poly-crystalline water ice (PCI) substrate. CO and N_2 are plotted with dashed and solid lines, respectively. Each colour corresponds to one experiment. CO is always the most abundant species with and its coverage varying between 0.45 ML to 1.2 ML, whereas N_2 coverage remains around 0.1 ML.

TABLE 3.2: CO:N_2 mixtures: energy ranges for N_2 and CO obtained as a function coverage and [CO]/[N_2] ratio on c-ASW and PCI.

Substrate	Dose (ML)	[CO]/[N_2] ratio	$E_{b,M}$ $^{15}N_2$ (K)	$E_{b,M}$ ^{13}CO (K)
c-ASW	0.5	2.1	1100-1220	1240 - 1580
	0.75	2.3	1030 - 1220	1220 -1620
	1	1.9	920-1200	1200 - 1600
PCI	0.5	7	950 - 1100	1160 - 1600
	0.75	11.4	920 - 1100	1050 - 1610
	1	10.1	900 - 1000	1000 - 1620

3.4 Analysis and discussion

We have previously shown that mixed species or isotopologues physisorbed in sub-monolayer regimes compete for occupying the adsorption sites. Because each site can harbor only one molecule, the repartition of each species among sites of various depth can be calculated using the Fermi-Dirac statistics (Dulieu et al., 2005, Amiaud et al., 2006, 2015, Kristensen et al., 2011). Here, for both CO and N_2, the binding sites are described by a binding energy distribution, approximated as a Gaussian function. We assume that the molecules are spread over the binding sites following the Fermi–Dirac statistical equilibrium. For one species, we have

$$p(E,T,\mu) = g(E) \times \left[1 + exp\left(-\frac{E-\mu}{k_b T}\right)\right]^{-1}, \tag{3.5}$$

where $p(E,T,\mu)$ is the population distribution given in the Fermi-Dirac formalism, the function $g(E)$ represents the number of sites between the binding energy E and $E + dE$, and μ is the Fermi energy or chemical potential, which in turn is linked to the total number of molecules, N, given by

$$N = \int_0^\infty p(E,T,\mu)dE. \tag{3.6}$$

The rate of desorption, obtained by integrating the desorption probability over the full binding energy distribution and weighted by the probability of occupying the given sites, is

$$\phi = \int_0^\infty \mathrm{p(E,T,\mu)} \times \mathrm{A\,e^{-(E/k_b T)}dE}. \tag{3.7}$$

The Fermi-Dirac statistical method describes the distribution of one adsorbate over the binding site distribution for experiments of pure molecules. Nevertheless, it is not hard to implement in the case of a mixtures of species. Equation 3.5 can be rewritten for CO, assuming that the number of sites available, $g(E)$, is reduced by the presence of the other adsorbate $p_{N_2}(E)$:

$$\begin{aligned} &p_{CO}(E,T,\mu_{CO},p_{N_2}) \\ &= (g_{CO}(E) - p_{N_2}(E)) \times \left[1 + exp\left(-\frac{E_{CO}-\mu_{CO}}{k_b T}\right)\right]^{-1}. \end{aligned} \tag{3.8}$$

There is a similar equation for N_2 and there are two relationships required to calculate the two chemical potentials μ_{CO} and μ_{N_2}. The coupled desorption of both adsorbates is calculated for each species, using equation 3.7, at each step of the simulation.

The probability that an adsorption site is vacant decreases with binding energy, namely, the deepest sites are more likely to be populated. Moreover, if two species have different adsorption energies, molecules with higher absorption barriers have a higher probability of occupying a binding site. Taking into account this simple

statistics, we have shown that it is fair to assume that there can be binding energy distributions having identical shapes for two (or more) different species, provided that the centres of each energy distribution are spaced by a constant value. Even for molecules such as O_2 and CO, which exhibit larger differences of desorption profiles with respect to CO and N_2 used in this study, we were able to successfully fit the experimental TPD curves (Noble et al., 2015).

Here we have tested our Fermi-Dirac model for the simpler case of N_2 and CO mixtures. It is a simpler case because pure N_2 desorption peaks seem to be only slightly shifted toward lower temperatures when compared with pure CO profiles. Figure 3.3 shows that CO and N_2 distributions of binding energies are separated only by a value of ≈ 200 K, at least for a coverage in the range $0-0.5$ ML. In the case of CO and O_2 it was not so obvious, because the multi-layer peak of O_2 appears at higher temperatures than the multi-layer peak of CO, which indicates that the multi-layer energy of O_2 is higher than that of CO. Therefore, the assumptions made above were certainly not warranted for a coverage close to 1 ML. In the present study concerning N_2 and CO mixtures deposites on c-ASW and PCI, we can see that the experimental profiles shown in the top panel of Fig. 3.7 (c-ASW substrate, [CO]/[N_2] ratio between 1.9 and 2.3) are well fitted. The CO profiles are well reproduced. Looking at the TPD tails, it should be noted that the difference between simulations and experiments is of the same order of uncertainty that exists from one experimental curve to another, as can be easily seen in Fig. 3.1. In Fig. 3.7 (bottom panel), we show the fitted TPD profiles of CO and N_2 mixtures from PCI ([CO]/[N_2] ratio between 7 and 11.4). The good quality of the fits in Fig. 3.7 is the verification of our hypothesis that the competition for adsorption sites is the main physical source of the differentiated desorption of CO and N_2. Hence, by adding a constant energy shift of 100 K between the energy distributions of CO and N_2, it is possible for us to simulate the desorption behaviour of the CO-N_2 system in a sub-monolayer regime, independently of the their relative abundance and of the type of water ice substrate. As far as N_2 traces are concerned, we could have increased the quality of the fit if we had fitted the N_2 energy distribution separately, but we believe that it is not necessary. Our main goal is to develop a model based on simple assumptions, that will be easily applicable to grains in astrophysical conditions, where the exact composition of the surfaces is not well known and so neither are the exact binding energy distributions.

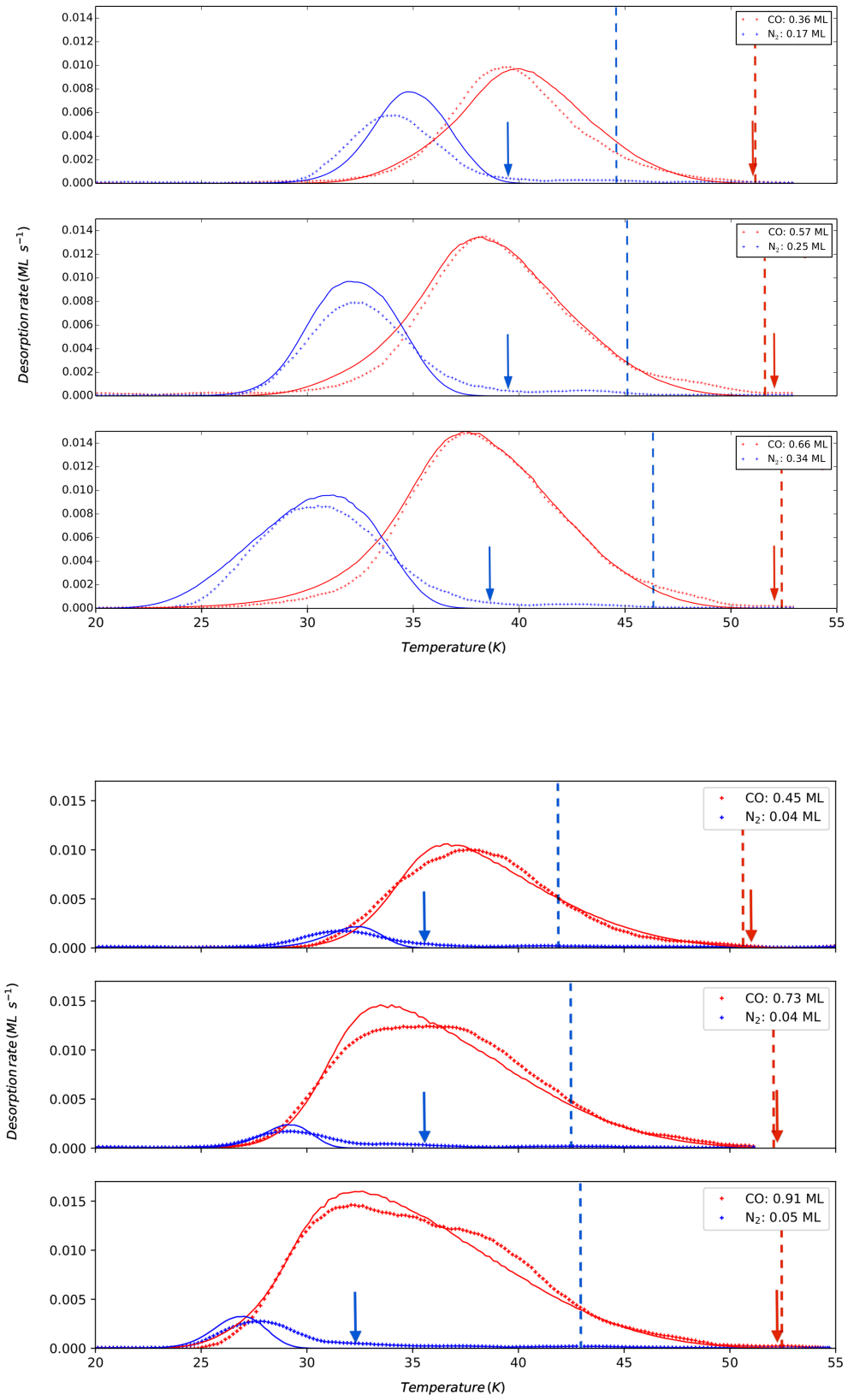

FIGURE 3.7: Experimental (dotted) and simulated (solid) desorption traces of CO:N_2 mixtures from c-ASW (top panel) and from PCI (bottom panel). Blue and red arrows indicate the position of the highest temperature at which the most tightly bound molecules desorb, calculated from the energy values reported in Table 3.2. Vertical dashed lines represent the highest temperature desorption in pure ices experiments, calculated from the energy values reported in Table 3.1.

From our experiments and analysis, it is evident that the small difference in binding energies of N_2 and CO has a dramatic effect on the desorption temperature of N_2 whenever the two species are both present on the surface. This is apparent from Fig. 3.7 by looking at the locations of the arrows and of the vertical dashed lines. The position of the arrows (corresponding to highest temperature desorption in CO:N_2 experiments) and the position of the vertical dashed lines (highest temperature desorption in pure ices desorption) were calculated using equation (12) of Luna et al. (2017), which allows us to express the high-energy desorption values displayed in Table 3.1 and 3.2 as temperatures in kelvins. It is evident that blue arrows (N_2 in CO-N_2 system) exhibit a considerable shift towards lower temperatures with respect to the blue dashed lines (pure N_2 experiments). Conversely, red arrows (CO in CO-N_2 system) show no or very little shift with respect to the pure ice case, which confirms that CO molecules always tend to populate the most energetically favourable adsorption sites in CO:N_2-mixture ratios ≥ 2.

The shift in temperature between red arrows and red dashed lines can be used to estimate the errors on each energy value and is around ± 30 K in all cases. The Fermi-Dirac analysis of the desorption of mixed species is a powerful tool to simulate TPD spectra, as well as other fine effects measurable in the laboratory, such as the difference in binding energy of the ortho- and para-state of D_2 molecules (Amiaud et al., 2008). However, it is not used in astrophysical models because it is highly demanding in terms of computing time. Therefore, it would be good to know if we can describe the competition mechanism between different molecules in a simpler way and, in particular, by adopting the commonly used approach based on the classical Arrhenius-type model.

Figure 3.8 displays the distribution of binding energies on c-ASW (top panel) and on PCI (bottom panel) obtained from the classical inversion method. On compact amorphous water ice, the case of pure CO (dotted blue curve) and pure N_2 (dashed red curve) monolayer exposures are the same as those shown in Fig. 3.3. We can clearly see that these curves are nearly parallel, except for the very high coverage region (>0.8 ML) where they tend to converge. The other three solid lines presented in Figure 3.8 concern a TPD experiment where a 1 ML-dose CO:N_2 mixture (0.65 ML of CO + 0.35 ML of N_2) was deposited on compact water ice. As expected, the CO trace (solid blue line) is unchanged with respect to the pure case (dashed blue curve), it goes from 0 ML coverage to 0.65 ML (point C, corresponding to the onset of desorption). On the contrary, the N_2 binding energy

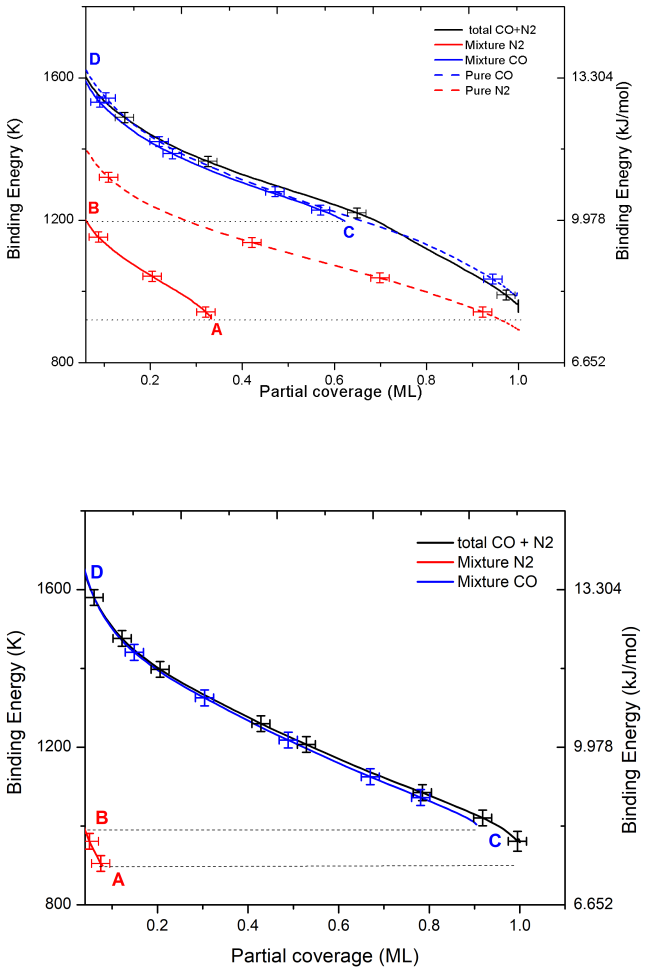

FIGURE 3.8: Binding energy distributions of pure CO and N_2 (dashed lines) and of a 0.65 ML-CO–0.35 ML-N_2 mixture (solid lines) on c-ASW (top panel) and of a 0.91 ML-CO–0.09 ML-N_2 mixture on PCI (bottom panel), obtained using the classical inversion method. The black solid line is the sum of CO (solid blue line) and N_2 (red solid line) energy distributions calculated during the CO:N_2 mixture experiment.

profile (solid red curve) is strongly shifted towards lower energies by about 200 K. Actually, the desorption of the deposited mixture begins with the desorption of N_2 (point A), which continues and terminates at point B. Only then, CO desorption starts (point C), and finishes when zero coverage is reached (point D), as expected. The most striking feature of the energy profiles described above is that points B and C have exactly the same value of binding energy ($\approx$ 1200 K). It is like the desorption process is continuously evolving from point A to point D, except that CO desorption takes over only when there is no more N_2 on the surface. To demonstrate this extreme simplification, in Figure 3.8 we also plotted the sum

of CO and N_2 energy traces, considering them as a single desorbing population. The sum of the two is shown in black, and we can see that it is very similar to the energy distribution of the pure CO case. The same competition effect is even more prominent on the PCI substrate, which confirms that CO occupies the highest energy binding sites, pushing N_2 to less favourable surface adsorption sites. This case is represented in Figure 3.8 (bottom panel), where we show the energy distribution of a CO:N_2=10:1 mixture (0.91 ML of CO + 0.09 ML of N_2). The onset of the desorption corresponds to the desorption of N_2 (point A) and the desorption process is complete at point D (end of the desorption of CO), corresponding to zero coverage.

It should also be noted that when the surface coverage is nearly full and a second layer is beginning to be built, the binding energy distribution of the CO-N_2 system tends the N_2-multi-layer binding energy, though it never reaches this lower limit value, indicating that the CO-N_2 interaction is slightly stronger than the N_2-N_2 interaction.

From this analysis, a very simple and straightforward conclusion that we can draw is that the effective binding energy of N_2, in presence of CO molecules, depends on the total coverage (CO+N_2), and not on the partial coverage of N_2 alone. On the contrary, the binding energy of CO is due only to the coverage of CO molecules, and is unaffected by the presence of N_2.

As opposed to what experiments have shown before (Fuchs et al., 2006, Fayolle et al., 2016), there could actually be a relatively high difference between the effective binding energy of CO and N_2 on cold interstellar dust grains. One simple model that could explain this hypothesis is that the effective binding energy of N_2 is reduced from 1400 K (pure N_2, at very low coverage) to 900 K (CO+N_2 mixture, at monolayer coverage almost complete), corresponding to a reduction by a factor of $\approx 1 - 900/1400 \simeq 0.35$. This is consistent with the scenario proposed from the analysis of binding energies vs coverage of Figure 3.8. However, this is also a rather simplistic approach, because as the CO:N_2 mixture is deposited and the surface gets filled the CO binding energy decreases too.

A more consistent view is to consider that N_2 is always desorbing prior to CO whenever N_2 and CO are both present on the surface of icy grains. Of course, the two different behaviours will be apparent only if the temperature is high enough that desorption or accretion is under way. Therefore, in the case of very cold dust

(T_{dust} <13 K), thermal desorption will be too weak and both N_2 and CO will keep accreting on dust grains. In pre-stellar cores, the inner part of the cloud meets this condition (Bergin and Tafalla, 2007). However, even in these dark and cold media, dust grains can experience temperature fluctuations (e.g. Bron et al. 2014) induced by cosmic rays (or secondary UV photons). This concept has been largely used in models since the work of Hasegawa and Herbst (1993). In fact, Hasegawa and Herbst (1993) consider that the binding energy is a key parameter that determines the abundance of a certain species in the gas phase, via the Arrhenius-like desorption rate. Therefore, if we imagine a distribution of temperature jumps, also in case of small spikes (>35 K), N_2 is likely to desorb, but not all CO, as confirmed by our experiments. We can even consider that, as to nano–sized grains, temperature variations can also be induced by release of chemical energy, see for example calculations by Navarro-Ruiz et al. (2014). Nonetheless, the presence of nano–sized grains in pre-stellar core is unlikely because of the coagulation that leads to the coreshine (Pagani et al., 2010), grain sized distribution under coagulation processes (Ormel et al., 2009), and because the observational signature of very small grains at 60 μm (Laureijs et al., 1991, Stepnik et al., 2003) vanishes on the edge of the cloud.

It is also striking to note that the values of desorption energy used in previous models, as in Caselli (2002), are 1210 K and 787 K, for CO and N_2 respectively, are quite consistent with the range of energy values that can be extrapolated from the present work. The former energy barrier coincides with CO binding energy on compact water ice at a relatively low coverage of 0.2 ML, or may also coincide with CO binding energy on porous ice at moderate coverage. The N_2 energy barrier can be considered a typical value of binding energy of pure molecular nitrogen multi-layers.

The complex modelling of pre-stellar cores, that should include dynamics of clouds as well as an accurate rate of accretion on grains and chemical reactions, is beyond the scope of this paper. In fact, none of the pre-stellar core models currently in use apply Fermi–Dirac statistics or a binding site distribution when simulating the solid–gas exchange. Although we cannot determine a single effective value for the binding energy of N_2 and CO on grains, we can however provide a distribution of all ranges of binding energy of the CO-N_2 systems investigated, that can be used to simulate the surface segregation/competition of the adsorbates in specific, astrophysically relevant situations. The values are reported in Table 3.2.

Our results imply that CO and N_2 mixtures deposited on water-dominated icy mantle present different ranges of thermal desorption temperatures in different interstellar and circumstellar environments. In particular, in pre-stellar cores different CO and N_2 binding energies may explain the later freeze-out, or early sublimation, of N_2. On the other hand, in circumstellar disks, where radial temperature profiles greatly affect freeze-out of different volatiles, the segregation effect could explain why the observed N_2H^+ emission is such a robust tracer of the CO condensation front (Qi et al., 2013, 2015).

Previously, we already proposed an analytical expression to fit TPD profiles of pure CO in Noble et al. (2012), and other authors extended this subject to cover different conditions and regimes (He et al., 2016, Collings et al., 2004). The present case, where two species are present on the surface at the same time, makes very difficult to derive the absorption energy as a function of several variables. To know the effective binding energy, as long as both N_2 and CO are on the surface, one has to know the relative coverage, which depends on the cloud conditions and history, then has to assume that CO will not desorb and that the lowest energy binding sites are occupied by N_2. Assuming that CO and N_2 sub-monolayer mixtures are adsorbed on a water ice template, only when N_2 is completely gone, CO can start to leave the surface.

3.5 Conclusions

In this work, we studied sub-monolayer mixtures of N_2 and CO deposited on two types of water ice substrates. N_2 and CO co-adsorbed on an amorphous surface show very different desorption behaviour when mixed than when adsorbed separately. We derived the distribution of binding energies and put in evidence that a segregation mechanism is at play. N_2 and CO have close binding energies, with N_2 adsorption barrier being slightly lower. If taken as pure species, the shape of their binding energy distribution as a function of coverage is similar. When mixed, CO molecules push-out N_2 molecules of the highest energy adsorption sites, thus nitrogen is forced to almost completely leave the surface before CO begins to desorb. We conducted TPD experiments of CO:N_2 mixtures from compact amorphous ice and poly-crystalline ice, and obtained similar results in the two cases. Experiments clearly show that the presence of CO reduces the effective binding energy of N_2 in CO:N_2-mixture ratios of $\sim$2:1 and $\sim$10:1, whereas we

determined that the opposite effect does not occur within the same N_2:CO-mixture ratios. In dark clouds, or in other environments where CO and N_2 can meet on the surface of water-dominated icy mantles, a selective desorption may be the most probable scenario. It is yet to be confirmed that this is one of the main reasons explaining the lower depletion of N_2 towards the centre of pre-stellar cores with respect to CO, although it is certainly a possibility that modellers have to take into consideration.

Chapter 4

Experimental study of the chemical network of the hydrogenation of NO on interstellar dust grains

Nitrogen Monoxide (NO) is observed in the gas phase of molecular clouds. It may accrete on dust grains and there, its hydrogenation should lead to hydroxylamine (NH_2OH), the same way that CO is transformed in methanol (CH_3OH) on the surface dust grains. NO hydrogenation has been said barrier-less, whereas CO hydrogenation proceed through quantum tunneling, and is thus slower. However, CH_3OH is widely observed and is considered as a proxy of complex organic molecules while hydroxylamine remains undetected We aim at studying, analyzing, and understanding the chemical network of NO hydrogenation on cold surfaces. Experiments are carried out using a new Ultra-Hight Vacuum (UHV) set-up named VENUS. NO molecules and H atoms are co-deposited on a golden mirror at different temperatures. Infrared spectroscopy as well as Thermally Programmed Desorption (TPD) are used to follow the NO reactivity, with both H and D, and in presence or absence of water substrate. Quantum calculations on water ice cluster models are computed separately. During the hydrogenation of NO, 10 reactions proceed concurrently. They are identified and constrained by changing physical conditions in experiments or in calculations. Among them we demonstrate that the HNO+H reaction has a barrier which is crossed via quantum tunneling at 10 K. Moreover, abstraction reactions are occurring although they

are limited by H and O bonding with their environment. Chemical desorption should occurs especially in absence of water which enhances the total production of hydroxylamine. The chemical network of the hydrogenation of NO has been re-investigated. Each of the 10 reactions are sorted by efficiency. We exclude the possibility of a chemical loop between NO and HNO, especially in presence of water. Therefore hydroxilamine remains the main product of the hydrogenation of NO on grains and the question of its non-detection in ices or in the gas phase, especially in shocked regions where ice mantles should be sputtered, is still open.

4.1 Introduction

With the unprecedented capability of mapping at small scale and at high sensitivity astrophysical regions, the origin and the evolution of the molecular complexity is permanently questioned. As an example Ando et al. (2017) have shown that chemical composition of two molecular clouds, separated by only 10 pc in the nearby galaxy NGC 253, exhibit a very different chemistry. In particular, in one clump both NO and CH_3OH are detected, whereas another one presents a poor chemical composition. Progressively a long and subtle inventory possible chemical links emerges from the observations. For example we pinpoint the possible correlation of HNCO and NH_2CHO (López-Sepulcre et al., 2015) or the possible link of O bearing compounds (Pagani et al., 2017). Less demonstrative but probably as meaningful, the non detection of CH_2OH (Cernicharo et al., 2012) or the detection of very low concentrations of the CH_3O molecule is an important but unsolved problem Ceccarelli et al. (2017). Because the chemical link in the gas phase with CH_3OH is firmly established (Shannon et al., 2014), how to explain their non detection in shocks where CH_3OH is very abundant?

The presence of methanol in the gas phase and many other hydrogenated molecules is thought to be due to the sublimation of ice mantles. The identified species of the ice such as water, carbon dioxide, formaldehyde, and methanol are formed on the cold grains, by surface reactions combining H, O and CO, (Dulieu et al. (2010), Jing et al. (2011), Watanabe and Kouchi (2002), Hiraoka et al. (2002), Oba et al. (2010), Ioppolo et al. (2011), Noble et al. (2011), Minissale et al. (2013), Minissale, M. et al. (2016), Fuchs et al. (2009), Minissale et al. (2016)). Under dense cloud conditions, just like CO molecules, NO molecules can also accrete and react with

many species on the surface and with H the first of them, leading to an increase of the chemical complexity of both O- and N- bearing species.

Even if the NO abundance is not as high as CO, it is however relatively abundant. In circumstellar oxigen-rich envelopes NO relative abundance is as high as 10^{-6} of Velilla Prieto et al. (2015), whereas even in pre-stellar cores that undergoes gas depletion it is still at the 1-3 $\times$ 10^{-8} level (Akyilmaz et al., 2007). NO is an important gas phase molecule detected towards many dark and warm clouds with the abundance from 1 $\times$ 10^{-8} to 1 $\times$ 10^{-7} relative to H_2 abundance (Liszt and Turner, 1978), and is at the corner-stone of the N and O chemistry. Therefore the case of the non detection of hydroxilamine (NH_2OH) is an enigma, since its production by hydrogenation of NO on grains should occur without barrier (Congiu et al., 2012a). Taking into account the low reactivity of CO with H, the absence of NH_2OH in space and the omnipresence of CH_3OH is questioning our understanding of their synthesis, or their destruction pathways.

From experimental works (Congiu et al., 2012a,b, Fedoseev et al., 2012), a reactive network for the NO+H reactive system has been proposed. 5 reactions were able to satisfactorily explain the measurements:

$$\mathrm{H} + \mathrm{H} \xrightarrow{\mathrm{k1}} \mathrm{H_2} \tag{4.1}$$

$$\mathrm{NO} + \mathrm{H} \xrightarrow{\mathrm{k2}} \mathrm{HNO} \tag{4.2}$$

$$\mathrm{HNO} + \mathrm{H} \xrightarrow{\mathrm{k3}} \mathrm{H_2NO} \tag{4.3}$$

$$\mathrm{H_2NO} + \mathrm{H} \xrightarrow{\mathrm{k4}} \mathrm{NH_2OH} \tag{4.4}$$

$$\mathrm{HNO} + \mathrm{NO} \xrightarrow{\mathrm{k5}} \mathrm{N_2O} + \mathrm{OH} \tag{4.5}$$

followed by

$$\mathrm{OH} + \mathrm{H} \xrightarrow{\mathrm{k6}} \mathrm{H_2O} \tag{4.6}$$

Or alternatively to k5 and

$$\mathrm{HNO} + \mathrm{HNO} \xrightarrow{\mathrm{k5bis}} \mathrm{N_2O} + \mathrm{H_2O} \tag{4.7}$$

However, in models is sometimes inserted the back reaction.

$$\mathrm{HNO} + \mathrm{H} \xrightarrow{\mathrm{k2B}} \mathrm{NO} + \mathrm{H_2} \tag{4.8}$$

This is an abstraction reaction, well known in methyled systems (Hiraoka et al., 2002, Oba et al., 2014, Minissale et al., 2016, Kobayashi et al., 2017), or even in sulfur bearing species Oba et al. (2018). This kind of looping reactions k_2 and k_{2B} is a problem for astrochemical models including solid phase reactions (e.g. Vasyunin and Herbst (2013a), Ruaud et al. (2016), Cuppen et al. (2017a), because their inclusion in the surface reaction network dissipates a large number of H atoms, deviating hydrogenation processes toward simple H_2 production. Therefore, the final degree of hydrogenation of the ice mantle is very sensitive to this balance of addition and abstraction mechanisms (private come from Vasyunin et al. (2017)).

Thus it is important to put into the scope of our study the possibility of abstraction reactions. We add :

$$H_2NO + H \xrightarrow{k3B} HNO + H_2 \tag{4.9}$$

and

$$NH_2OH + H \xrightarrow{k4B} H_2NO + H_2 \tag{4.10}$$

There are 10 competing reactions on the surface, 8 actually belonging to the hydrogenation of NO. The reaction 4.6 is the completion of water, and the reaction 4.1, the self-reaction of H, is the most important from the kinetic point of view. Because it's a fast reaction only limited by H diffusion, other reactions cannot compete if they are too slow, and thus the system won't evolve chemically.

4.2 Experimental setup

Experiments have been performed using the VENUS (VErs de NoUvelles Synthèses) setup at the LERMA laboratory in the University of Cergy Pontoise.

VENUS has 4 different beam lines, but only two are used in this study. The top beam was used to inject the NO molecules onto the surface. The source pressure is 2.05×10^{-4} mbar, which corresponds to a flux at the surface level of 2×10^{12} molecules/cm^2/s. The atomic hydrogen was sent to the surface through the right beam. Its flux is around 8×10^{12} atoms/cm^2/s. H/D atoms were generated by dissociating of H_2/D_2 molecules within a microwave discharge of 75W/40W. The dissociation efficiency of H_2/D_2 was 75 ± 5 %. We use FT-RAIRS to probe the new features during the co-deposition duration. After the deposition, the products are detected with the TPD technique, which consist in measuring with the QMS the

different products desorbing during the linear increase of the surface temperature (0.2 K $\times$ s^{-1}).

In order to calibrate the mono-layer of NO (ML, 1ML = 10^{15} molecules cm^{-2}), we performed series of NO TPD (like in Noble et al. (2011), Nguyen et al. (2018)) with different doses deposited at 10 K, then heated to 80 K. Thus, we determined that 1 ML of NO is obtained after 8 to 10 minutes of deposition. All the experiments presented here consist in co-deposition experiments, which means that NO and H(D) were sent simultaneously on the substrate (varied in composition, gold or water) at different temperatures, kept constant during the deposition. At the end of the codeposition, the hydrogenation is continued for 10 minutes.

We note {NO+H}, the reactive system, to make the difference with the NO+H ($\longrightarrow$ HNO) reaction. Actually as mentioned earlier the {NO+H} system include at least a ten of reactions, and at higher temperatures, some desorption pathways can also be activated.

To understand the possible role of the substrate, we have performed similar co-deposition experiments, but on a water substrate. The substrate was previously grown at a surface temperature of 10 K by background deposition of 5ML of H_2O. So the substrate is porous and exhibits a larger surface area due to its 3D structure.

4.3 Experimental results

4.3.1 Completeness of the reactions of the {NO + H} system before the TPD

Because the TPD diagnostic requires the heating of the sample, it is important to know if all the initial reactants are consumed during the co-deposition phase. The use the infrared spectroscopy gives precious indications because it can be performed during the reacting phase so before any thermal transformation of the sample. It is sometimes called *in situ* measurements. Figure 4.1 shows in red the IR spectrum recorded after NO deposition (without co-deposition of H). We can see the characteristic, N=O asymmetric stretch ν_5 and the N = O symmetric stretch ν_1, observed at 1770 and 1860 cm^{-1}, respectively, of NO dimers (Fateley et al., 1959, Congiu et al., 2012a). In blue is displayed the IR spectrum obtained

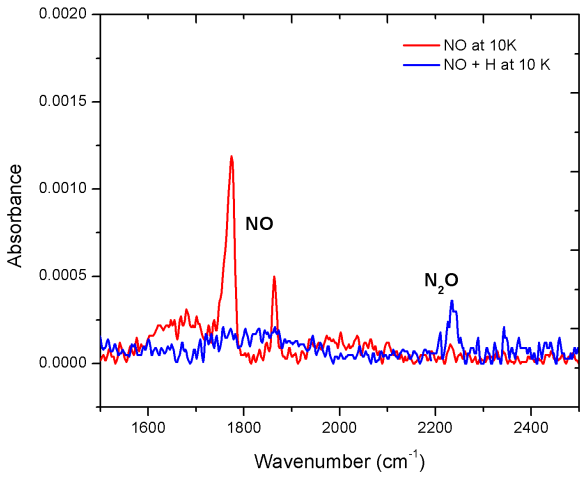

FIGURE 4.1: IR spectra obtained after the deposition of 4 ML of NO at 10K on gold (red line), and after NO (4ML) and H (16 ML) codeposition (blue line).

after the co-deposition of NO and H on the gold surface held at 10 K. NO dimers (nor monomers) features are no longer detectable but in place we observe a peak at 2233 cm^{-1} which is attributed to N_2O. We note here that the IR features of NH_2OH is composed of broad bands from (900 - 1800) cm^{-1} and (2700 - 3500) cm^{-1}, that are hardly detectable and furthermore usable for quantitative analysis in our experimental conditions, because of their relative low contrasts compared to thinner peaks such as those of NO or N_2O. No evolution of the IR signal is observable during the heating phase of the TPD, except of course the disappearance of the N_2O peak due to its desorption of N_2O.

These results are similar to those previously published (Congiu et al., 2012a, Fedoseev et al., 2012). Taking into account the sensitivity of the method, we note that more than 90% of the NO should have reacted during the co-deposition phase so at low temperature.

We shown the TPD curves in figure 4.2. For pure {NO} experiments (in red) we observe a desorption peak at around 50 K. In blue are displayed desorption after the {NO+H} reactive system completion. We can clearly see both N_2O desorption (140-160 K) and NH_2OH desorption (160-200 K). Their ratios are clearly indicating that NH_2OH is the major product, whereas N_2O is the minor product.

Around 50 K, there is still a weak desorption of NO, slightly shifted and broadened compared with the case of pure {NO} experiments, indicating some remaining NO. However the NO consumption is ∼90 %, in agreement with the IR observations.

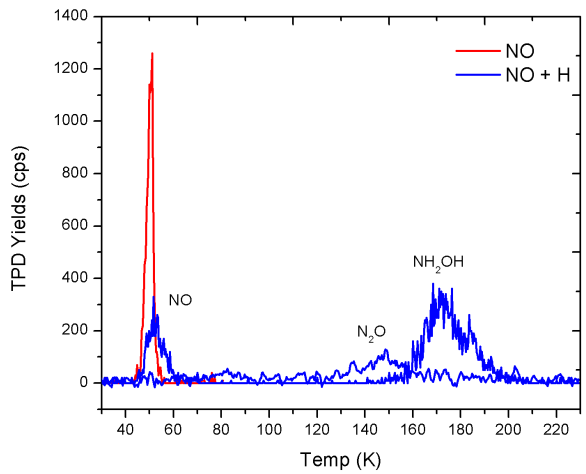

FIGURE 4.2: TPD profiles of pure {NO} (red curve) and {NO +H} (blue lines). m/z 30, 33 and 44 are displayed corresponding respectively to NO, NH_2OH, and N_2O.

The shift and broadening of the peak is due to the change of the molecular surrounding of the desorbing NO. Actually, in case of {NO+H} experiments the NO molecules have to escape from an ice film now composed in majority of NH_2OH and N_2O. These two compounds are desorbing at higher temperatures (∼180 K and ∼150 K respectively) and therefore are slightly delaying the NO desorption.

The remaining NO could originate from incomplete NO consumption, although we cannot exclude some default in our physical beams overlap on the sample, making a geometrical zone of NO less exposed to H atoms. Longer H expositions time on thinner NO films rule out this possibility. In these conditions we can achieve a full NO disappearance. We better consider that the remaining part of NO can be due to an insufficient total number of H atoms compared to NO molecules, but it is also possible that a back reaction HNO+H$\longrightarrow$ NO+H_2 (reaction 4.8) prevents from a complete consumption of NO by repopulating NO from is product HNO. This possibility will be discussed later.

4.3.2 Temperature dependency

In previous experiments, reactivity of NO with H has been tested at different temperatures (Congiu et al., 2012a), up to 42 K using porous amorphous ice as a substrate. The aim was to establish that the H+NO reaction is barrier-less. However, only NO consumption was tested, and no products were analyzed. Such

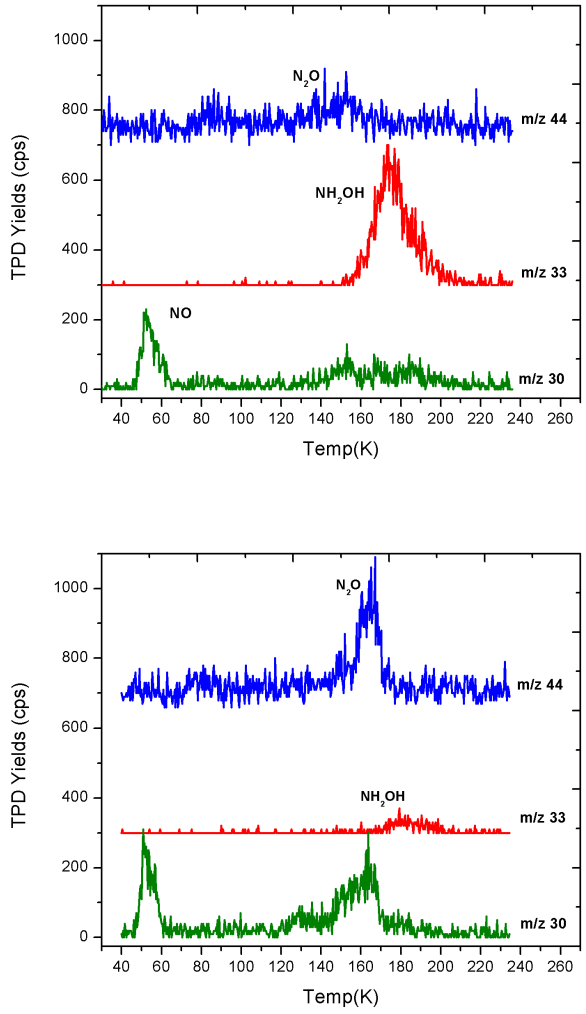

FIGURE 4.3: Influence of the surface temperature: TPD traces of m/z=30 (NO, green lines), m/z= 33 (NH_2OH, red lines) and m/z= 44 (N_2O, blue lines) for co-deposition experiments of {NO+H} on gold substrate held at 8 K (upper panel), and 40 K (lower panel). Curves are offset for clarity purpose.

product analysis has only been realized for experiments made on surfaces held at 10 K.

Figure 4.3 shows the main products of NO hydrogenation which are hydroxylamine (NH_2OH m/z=33) and nitrous oxide (N_2O m/z=44) for two surface temperatures of 8 K and 40 K. For both experiments, there is a remaining part of NO. It corresponds to the desorption peak at around 50 K (green curve). The other features of m/z = 30 at higher temperature are due to the cracking patterns of both NH_2OH (peak at 160-200 K) and N_2O (around 140-170 K). More important is the extreme difference in intensity of the NH_2OH and N_2O TPD peaks. At

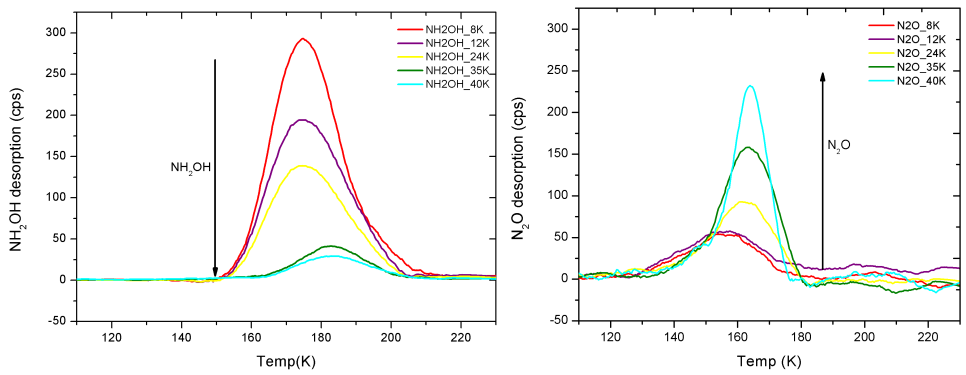

FIGURE 4.4: NH_2OH TPD (left panel) and N_2O TPD (right panel) at different surface temperatures. Each temperature (8, 10, 12, 20, 24, 30, 35, 40, 42K) correspond to one specific co-deposition experiment {NO+H}. Curves are smoothed by adjacent averaging for a better visibility. NH_2OH amounts is decreasing with T_s whereas N_2O is increasing. The vertical black arrows represent the evolution of the peak with the temperature of the substrate.

8 K, NH_2OH is the major product whereas at 40 K N_2O becomes the major product whereas NH_2OH is almost no longer formed. We calculated the ratio of the integrated TPD areas between NH_2OH and N_2O, it is 6.7 at 8 K, and 0.01 at 40 K.

Figure 4.4 shows the TPD series of NH_2OH (left panel) and N_2O (right panel) at different surface temperatures. By looking at NH_2OH and N_2O peaks, we see a clear decrease for NH_2OH, whereas N_2O yield is increasing with the surface temperature. We have calculated the integrated area of NH_2OH and N_2O desorption peak for each temperature. It is displayed in Figure 4.5. We can see an exchange of the chemical output of the {NO+H} reactive system. There is a clear pseudo exponential decrease of the NH_2OH, whereas the N_2O yield may exhibit a double inset, one at the lowest temperature and the other one at around 30 K.

The main learning of this new set of experiment is that the ratio between the different reactions are varying with the surface temperature. The yields of all kinetic experiments, as those presented here, are always the result of a competition between the different reactions. Each rate of reaction evolves differently with the temperature. In the set of equation we can distinguish and sort some of them. Reaction 4.1 ($H+H \longrightarrow H_2$), is central to this reactive system, since it regulates the H surface density, so the efficiency of the hydrogenation. In absence of any other reactants, the H surface density reduces with the surface temperature. Between 8 and 14 K it is due to the increase of the H mobility that limits the reaction. At higher temperature, desorption of H start to be significant and opens a new

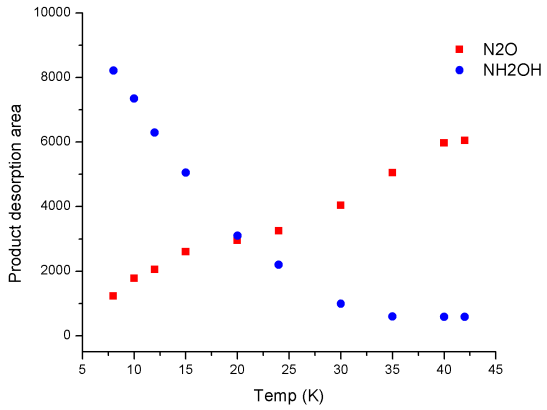

FIGURE 4.5: Integrated areas of NH_2OH (blue circles) and N_2O (red squares) desorptions as a function of the surface temperature, obtained after the same co-deposition of NO and H

competitive exit channel. However, even if the residence time of H is really short, the reaction 4.2 (NO+H (H+H) $\longrightarrow$ HNO) is faster since the all reactive system is fed by this reaction and that NO is still highly consumed at 42 K.

To calculate a rate such as k_1 or k_2, it is usually assumed that it can be decomposed in different parts, one which is intrinsic to the reaction, and corresponds to the probability per attempt to cross the barrier, and one which depends on the conditions which are determining the number of attempts per second, so the diffusion and the surface density (or concentration). As an example we write k_1 and k_2.

$$k_1 = k_{diff(H)} p_{R1} [H][H]$$

$$k_2 = k_{diff(NO,H)} p_{R2} [NO][H]$$

where [H] is the surface density of H.

In first approximation we can consider that the diffusion is dominated by H diffusion so the diffusive terms $k_{diff(NO,H)}$ $k_{diff(H)}$ are equal. Moreover, the probability to overcome the barrier of reaction p_{R1} and p_{R2} are equal and close to unity because the two reactions are associating two radicals. In other words we suppose that the reaction is barrier-less. Therefore, we can see that once the [NO] surface is larger than the [H] surface, the rate k_2 will dominate over k_1. Therefore a decrease of [H] does not necessary reduce the efficiency of the reaction 4.2, because it

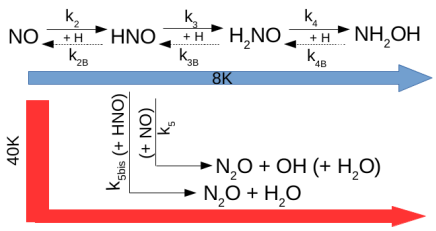

FIGURE 4.6: The sketch of the NO+H reactive system

affects firstly the reaction 4.1 because of the square function of [H]. The reaction 4.4 (H_2NO+H⟶NH_2OH) is also barrier-less and thus should proceed promptly as soon as some H_2NO is appearing on the surface, and is kinetically behaving like the reaction 4.2.

Reactions 4.5 or 4.7, which lead to N_2O and H_2O, are not hydrogenation reactions. Therefore, the limiting factor compared to hydrogenation reactions for these reactions is certainly the diffusive part of the reaction because the diffusion of H is though to dominate over all other diffusions of species. At low temperatures, only the increase of the surface density of HNO, so the relative inefficiency of its destruction, is able to explain why at 10 K we can observe the formation of N_2O.

Now we have to consider other reactions, especially reaction 4.3 (HNO+ H⟶ H_2NO), which enable hydroxylamine to be produced. We have seen before that the environmental part (diffusion and surface concentration) of the rate k_3 is very favourable. It is hydrogen addition so the diffusion is about the same level as other hydrogenations, and follow the same temperature trend, and the surface concentration of HNO should be high enough to open up the reaction 4.5. Therefore, the limiting factor should be the probability p_{R3} which should be lower than other hydrogenation reactions, implying a barrier to the reaction.

We observe a relative decrease of hydroxylamine with the temperature. Therefore, the effective relative p_{R3} is reducing. The simplest hypothesis is therefore that reaction 4.3 is proceeding via tunneling. This can be experimentally and/or computationally tested.

Figure 4.6 shows a sketch of the {NO+H} reactive system, including the main change with temperature of the chemical pathways, which is probably induced by the different dependency to the temperature of the reaction 4.3 compared to other hydrogenation reactions.

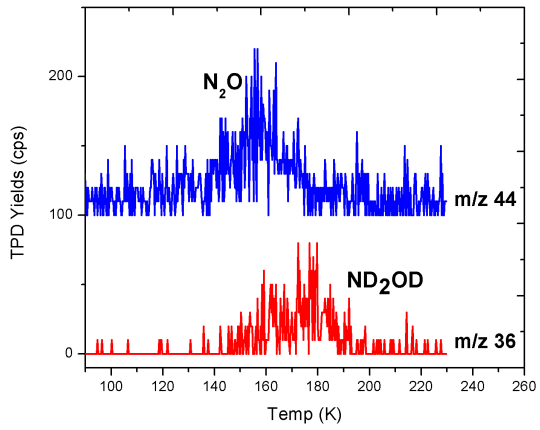

FIGURE 4.7: TPD profiles of masses $m/z = 36$ a.m.u. (in red) and $m/z = 44$ (in blue) corresponding respectively to ND_2OD and N_2O recorded after a co-deposition experiment of {NO+D} at 10 K.

Experiment	N_2O/NO*	NX_2OX/NO*	NO/NO*
{NO*}	> 2%	>1%	100%
{NO + D}	16%	8%	25%
{NO + H}	14%	53%	13%
{NO + H} on H_2O	12%	82%	2%

TABLE 4.1: Ratios of the TPD areas of N_2O, NH_2OH (or ND_2OD) obtained after co-deposition experiments and the TPD area of NO in the pure NO experiment. {NO + D} and {NO + H} are performed on a gold substrate hold at 10 K whereas {NO + H} on H_2O is made on a H_2O substrate.

4.3.3 The {NO + D} reactive system at various temperatures

It is possible to test the hypothesis of the reaction proceeding through quantum tunneling by substituting H atoms by D atoms. Indeed, the mass variation is supposed to lower considerably the reaction rate in case of quantum tunneling.

Figure 4.7 shows the TPD profiles of the {NO+D} co-deposition experiment for a surface held at 10 K. ND_2OD is desorbing between 170 K and 190 K and N_2O between 140 K and 180 K. The presence of the two main products indicates that the reactive network is similar but if we consider the height of the peak of hydroxylamine, we can see by comparison with this of Figure 7.3 that it is relatively smaller, whereas N_2O is about the same size.

The table 4.1 presents the relative production of N_2O and NH_2OH (or ND_2OD), at the end of co-deposition experiments performed at 10 K. We divide the TPD areas of the products by the TPD area of the NO molecules obtained during the NO experiment. We have added a star in the table to remind that the normalization is not made taking the remaining NO in experiments, but with the amount of NO obtained without reactions. Thus the ratio NO/NO* is 100 % in the first experiment. We first point out that the efficiency of detection of QMS is not exactly equal from one molecule to the other. It can vary within a few tens of % for these molecules. It is due to the different ionisation cross sections (which could be calculated), but also to the different spatial and kinetic distributions of the different desorbing species (which is unknown). We added TPD areas of all the cracking patterns of a given molecule. It is feasible, even with ambiguous masses such as mass 30, which appears for 3 parent molecules (NO, N_2O, NH_2OH) because they do not desorb in the same window of temperature. As a conclusion, the ratios presented in the table do not exactly represent the ratios of the species, but they give a good indication. In the same column, the relative error is similar, so if we underestimate or overestimate a species, we do the same for all the experiments. Therefore if the absolute values can be discussed, the relative values can be trusted.

In the table we first notice that the total is 80% for the {NO+H} experiment. It is less than 100% which could be due to the inaccuracy of the method. But this is certainly not an explanation for the {NO+D} experiment which total is 49%. So there are missing products in the deuterium experiment.

Our hypothesis is that some of the products are lost because of the chemical desorption (or reactive desorption). The chemical desorption is the direct return in the gas phase of a newly formed molecule on a surface due to the excess of energy released in case of exothermic reaction (Dulieu et al., 2013). Following our previous finding (Minissale et al., 2014, Minissale et al., 2016), it has a greater chance to happen when the excess of chemical energy is large and when the products have small number of atoms such as in these reactions for example:

$$\mathrm{NO} + \mathrm{H} \longrightarrow \mathrm{HNO}_{\mathrm{gas}} \tag{4.11}$$

$$\mathrm{HNO} + \mathrm{H} \longrightarrow \mathrm{NO}_{\mathrm{gas}} + \mathrm{H}_2 \tag{4.12}$$

$$\mathrm{HNO} + \mathrm{H} \longrightarrow \mathrm{NO} + \mathrm{H}_{2\mathrm{gas}} \tag{4.13}$$

However the chemical desorption efficiency is not supposed to change dramatically by changing of isotope and remains a low probability (<10-20% per reaction) most of the time. So we conclude that to increase the lost of products, the number of reactions should increase, and that probably the reactions 4.12 and 4.8 which are abstraction reactions are enhanced in the case of the {NO+D} experiments. This would be due to enhancement of the concentration of DNO species on the surface, because of the barrier to reaction of the next step of deuteration. The reaction 4.3 should have a barrier and be harder to cross for D atoms. Thus in a sense the back reaction is forced.

From the table 4.1 we can see that the production of N_2O is may be higher, but it is at the limit of our experimental uncertainties. The increase of DNO on the surface, that is induced by the reduction of the second step of deuteration favors the N_2O production. However the absence of mobility of the reactants at low temperature, keep the yield relatively low, because N_2O does not come directly from an hydrogenation reaction. So the only remaining possibility for DNO to react is the back reaction 4.8, which favors the chemical desorption so the losses.

Figure 4.8 compares the yields of NH_2OH and ND_2OD after {NO+H} and {NO+D} experiments at different temperatures. We can see that the trend is the same. Hydroxylamine is less produced when the temperature is increased. But the hydrogenation is always more efficient than the deuteration, especially at low temperatures. On the other hand, the formation yield of N_2O is slightly favored in the deuteration experiments, but the most striking point is the lost of a large fraction of the initial reactants, probably expelled from the surface due to the chemical desorption. This last process total efficiency is enhanced in case of looping reactions. We can conclude that DNO+D $\longrightarrow$ D_2NO is really slower than HNO+H $\longrightarrow$ H_2NO. This is an indication that quantum tunneling should be at play for this specific reaction. Of course, it could also be an effect of 0 point energy shift, D atoms lying usually deeper in adsorption wells, and therefore may have higher barrier to cross. However, in this peculiar case one has to explain why the abstraction reaction DNO+D $\longrightarrow$ NO+D_2 is relatively more efficient than the reaction HNO+H $\longrightarrow$ NO+H_2. Our best explanation remains that reaction 4.3 has a high barrier to reaction and that it should be crossed thanks quantum tunneling.

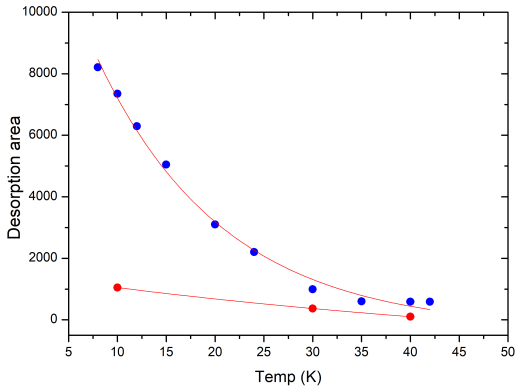

FIGURE 4.8: Blue circles: NH_2OH integrated areas after the co-deposition of NO molecules and H atoms. Red circles: ND_2OD integrated areas after the co-deposition of NO molecules and D atoms. ND_2OD is less than NH_2OH at the same surface temperatures.

4.4 Catalytic role of water

In dark molecular clouds, the major component of molecular mantles which cover dust grains is the solid water (Boogert et al., 2015). Water substrate should have an effect on the kinetic of surface reactions because it changes at least the environmental factors of the hydrogenation. Indeed the H diffusion is dependent on the type of substrate (Wakelam et al., 2017) and is known to affect the hydrogenation of CO (Watanabe et al., 2004). The comparison of the efficiency of formation of hydroxylamine is presented in the figure 4.9. The blue curve, obtained with the {NO+H} experiment on a porous ice substrate, has the same shape but a higher amplitude than the one obtained after the hydrogenation of NO on a gold substrate (in red). Therefore we can conclude that the presence of water is helping the formation of hydroxylamine. The last line of table 4.1 displays the amount of the different products. The consumption of NO is higher, the formation of NH_2OH is also enhanced while the production of N_2O is stable or slightly reduced. The higher consumption of NO is a precious indication. Actually we know that the reaction 4.2 is barrier-less and therefore that the NO should be all the time consumed. The unreacted NO at the end of the experiment is therefore probably due to the presence of the (reverse) abstraction reaction 4.8. So we can conclude that the presence of water is limiting the reaction 4.8, probably by imposing geometrical constraints on the orientation of HNO. Quantum calculations will show that HNO is bound to water via the H atoms, making the access of a second H atoms harder, and so limiting the abstraction reaction. If the reaction 4.8 is less efficient,

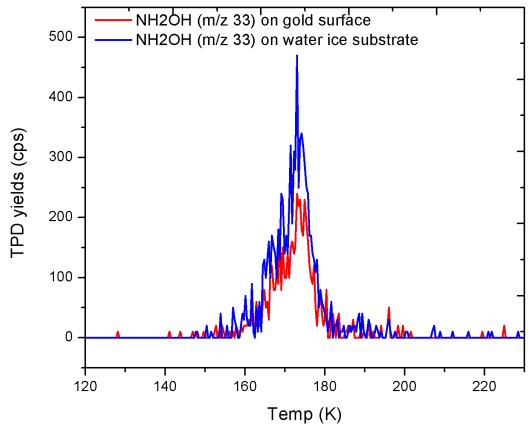

FIGURE 4.9: TPD profiles of NH_2OH desorbing after {NO+H} codeposition experiment on gold surface (red) and water ice substrate (blue), at the same sample temperature of 10 K.

there are less chemical loops between HNO and NO and therefore the chemical desorption total efficiency is lesser. Moreover the water is usually preventing the chemical desorption (Dulieu et al., 2013, Minissale et al., 2016). We note that the total of NO-bearing products in table 4.1 is the highest of all experiments. There is no increase of N_2O since its chemical pathway is not much changed. There is not more HNO formed, and the water does not help or even reduce the probability of having NO close to HNO, because of its larger surface area.

4.5 The possibility of back reaction NH_2OH+H $\longrightarrow$ H_2NO+H_2

To test this possibility, we first synthesize a ND_2OD film in *situ* and later expose it to H atoms. The ND_2OD is obtained by co-depositing {NO+D} at 10 K and thus we heat the sample to 160 K. At this temperature ND_2OD does not desorb, but other species do (i.e D_2, NO, and N_2O). Then, the surface temperature is cooled down to 10 K and H atoms (half of the dose) are sent.

The top panel of figure 4.10 shows that the ND_2OD amount is reduced by the addition of H atoms. The bottom panel shows a large peak of mass 35. This mass can be attributed to NDHOD, or its isomer ND_2OH. This substitution reaction is unlikely to proceed directly, actually D bonds are usually slightly stronger than H

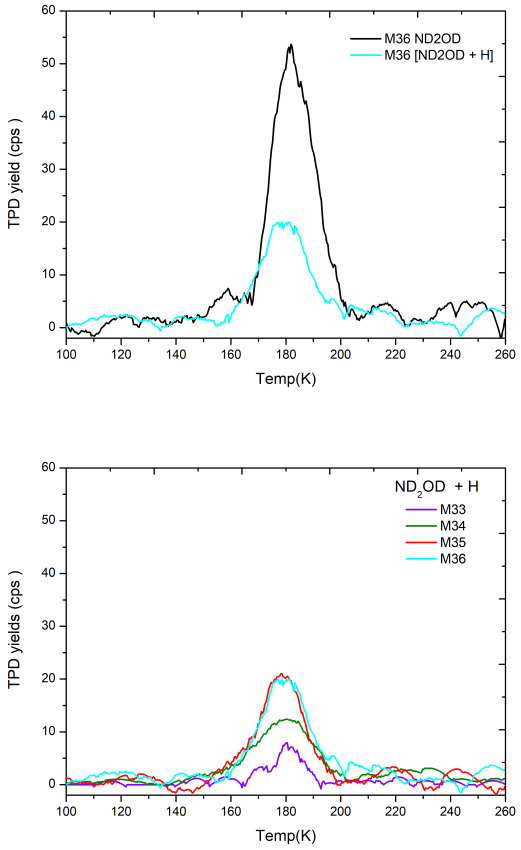

FIGURE 4.10: *Top panel:* TPD profile of initial ND_2OD (black curve) and remaining ND_2OD (cyan curve) after reacting with H atoms at 10 K. *Bottom panel:* TPD profiles of products detected after the exposition of H atoms to a ND_2OD a film. m/z 35 (red curve), m/z 34 (green curve), m/z 33 (violet curve), and m/z 36 (cyan curve)

bonds due to the shift of zero point energy. So the most probable is that a loop of abstraction and addition occurs, making the substitution efficient.

Abstraction step :

$$ND_2OD + H \longrightarrow NDOD/ND_2O + HD \tag{4.14}$$

$$NDOD/ND_2O + H \longrightarrow NDHOD/ND_2OH \tag{4.15}$$

The presence of mass 34 can only be the cracking pattern of ND_2OD. But in this case, it should be around a tenth of the mass 36. Therefore a large fraction of the mass 34 is probably the doubly hydrogenated hydroxylamine. This would be

the indication that the abstraction - addition mechanism is probably occurring on the ND_2 group more than on the OD group (leading to simple hydrogenation). However, this is speculative because we know that proton exchange is occurring during the TPD (R. Scott Smith et al., 1997, Mokrane et al., 2009, Dulieu et al., 2017), making direct interpretations hazardous.

4.6 Experimental conclusions

Our re-investigation of the NO+H reactive system has demonstrated the following points

(i) It exists an activation barrier to the H+HNO reaction (ii) this barrier is likely crossed at low temperature through quantum tunneling (iii) the direct evidence of the back reaction NH_2OH+H has been shown, and remind us the importance of taking account for them. It makes the NHOH or NH_2O radicals possible efficient intermediates in the synthesis of COMs. Latter we will show that it can be the intermediate for formamide formation. Indirect evidence of the H+HNO back reaction has been provided. (iv) Water has a catalytic role. It increases the efficiency of the hydrogenation probably by reducing the efficiency of the back reaction HNO+H $\longrightarrow$ H_2. Alternatively, its propension to retain products after reaction, or in other words its property to reduce the chemical desorption can also partly explain why more products are obtain on a water ice substrate.

Quantum chemistry should shed light on our findings. More precisely the presence or absence of barrier can be checked, both in the case of addition and back reaction. Moreover, the most probable isomers (NH_2O or NHOH) can probably be determined.

4.7 Astrophysical implications

Our present study does not change the conclusion of the previous experimental studies. At low temperatures, hydroxilamine is the major product of the direct hydrogenation. However, if the grains temperature increases, hydrogenation becomes less efficient. But, back reactions have to be taken into account. In this reactive scheme, and under the assumption that H atoms are the most frequent

reactants on interstellar dust grains, their landing can produce in *situ* radical, even from stable molecules such as NH_2OH. These radicals, issued from hydrogenation of saturated molecules could be the carrier of a new generation of COMs.

Chapter 5

Study of the penetration of oxygen and deuterium atoms into porous water ice [1]

Many interstellar molecules are thought to form on dust grains. In particular, hydrogenation is one of the major mechanism. To date it is not clear if the H atoms can penetrate in the bulk of the ice mantle, or it has only a chemical activity on the external surface of grains. We wish to study the efficiency of atoms deposited on the outer surface of the amorphous solid water to penetrate into the ice bulk. NO molecules react with O and H atoms. They are easily detected by infrared (IR) spectroscopy. These two properties make this molecule an ideal chemical tracer for the penetration of O and H atoms through water ice. In our experiments, we first deposit a NO undercoat and we cover it (at 40 K) with a variable amount of water ice. Then, we expose to D (10 K) or O (40 K) atoms, and we follow via IR signatures the NO consumption and the products which appear, and we finally analyse the desorption of all species through Temperature Programmed Desorption technique. We experimentally characterize the accessible surface of the ice and provide a model to interpret quantitatively our measurements.

[1] M.Minissale, T.Nguyen, and F.Dulieu, submitted to Astronomy & Astrophysics, (2018)

5.1 Introduction

The formation of certain molecules (such as H_2, H_2O or CO_2) in different astrophysical environments is possible thanks to the catalytic effect of dust grains (e.g. Anders et al. (1974), Pirronello et al. (1999), Cazaux et al. (2010), and references therein). In dense clouds, where the UV photons flux is rapidly attenuated, atoms and molecules accumulate on dust grains and react to form increasingly complex molecules (Caselli and Ceccarelli, 2012). The diffusion of the lightest species, in particular hydrogen and oxygen atoms, is often considered as the trigger of chemical reactions which are at the base of the growth of these molecular mantles, which then differ in composition from the gaseous phase. It was shown very early (Tielens and Hagen, 1982) that grain chemistry was mainly limited by diffusion (Cuppen et al., 2017b). Experimentally it has been demonstrated that H, O, and N atoms can effectively diffuse on the surface of iced grains at low temperature ($\sim$10 K) (Matar et al., 2008, Watanabe et al., 2010, Hama et al., 2012, Minissale et al., 2013, Congiu et al., 2014a, Minissale et al., 2016, Wakelam et al., 2017).

This type of catalysis dominated by surface diffusion is very effective. The synthesis of methanol from the CO-hydrogenation is an emblematic example, since despite the reaction barriers (Hiraoka et al., 2002, Hidaka et al., 2007, Rimola et al., 2014), this molecule is abundantly produced and detected (e.g. Kristensen et al. (2010), Ceccarelli et al. (2017)). It is not yet well understood if, once the molecular mantle is built thanks to surface reactions, it can evolve due to reactions in the interior of the mantle. It is known for example that UV penetrates many molecular layers (e.g. 1 μm at 163 nm, Orzechowska et al. (2007)) creating radicals in the inner layers of the mantle leading to chemical recomposition. It is therefore necessary to understand what is the diffusion in the bulk. Several studies have focused on the experimental determination of bulk diffusion rates of molecules such as NH_3, CO, and CO_2 (Mispelaer et al., 2013, Lauck et al., 2015, He et al., 2017, Cooke et al., 2018, Ghesquière et al., 2018) on relevant astrophysical ice, but little is known about the bulk diffusion of atoms. However, it is very important to determine if and how the diffusion of atoms takes place in ice, since some increase of the mobility may be expected for atoms, especially H. An efficient diffusion in bulk can indeed allow a rich chemistry in the ice of dense clouds thus favor the dynamic and temporal evolution of the ice in its whole thickness. A lack of bulk mobility, in the absence of subsequent processing, will cause the ice composition

to be governed by the surface diffusion and the composition of the accreted gas, until the ice is heated or processed.

Water ice is the main compound of astrophysical ices (Boogert et al., 2015), but it is a multiform matrix. In astrophysical environments, water ice can be crystalline or amorphous (Amorphous Solid Water: ASW), but in dense clouds it is thought to be amorphous, because some energy processes must take place before it crystallizes (Papoular, 2005, Palumbo, 2006). Furthermore amorphous ice can be porous or compact: if it is deposited at low temperature (< 70 K), it is porous (Stevenson et al., 1999b), but it can be recompacted by ionic or UV irradiation (Palumbo et al., 2010) or by simple chemical activity such as hydrogen recombination (Accolla et al., 2011). Finally, if the ice forms directly on the dust grains, it is amorphous and compact (Oba et al., 2009, Accolla et al., 2013). Of course, the diffusion rates of species in the bulk of ice depend on the ice morphology (amorphous or crystalline) and its degree of porosity.

The reactivity of atoms with another compound inserted in the ice (used as a chemical tracer) can be used to experimentally measure atomic diffusion on/in the water ice. If the reaction is barrier-free, the disappearance of the reactive species allows to infer the access of the atoms to the reactants, so their mobility. This is the method we used in Matar et al. (2008) using O_2 consumption as a marker for surface diffusion of D. If we now deposit water ice on top of a reactive partner, by examining the consumption and formation of species according to the thickness of the water ice deposited on top of it, we must be able to deduce the penetration of atoms into the ice. In the present case we use NO, which has no reaction barrier with H (Congiu et al., 2012a) and O (Minissale et al., 2014b) and which is detectable in the infra-red, contrarily to O_2. However this approach presents certain constraints from an experimental point of view. Compact water ice (amorphous or crystalline) can only grow at sample temperatures above 100 K. Such temperatures are sufficiently high to induce immediate desorption of the "marker", the reactive compound NO. We are therefore limited by the desorption temperature of the chemical marker (i.e. $\sim$40 K for NO). This temperature does not allow the formation of compact ice. The amorphous and porous water ice is what can be studied by this method.

It is quite a general consensus that water ice in dark clouds is mainly amorphous, but the nature of its porosity degree still remains poorly known (Öberg et al., 2009, 2011, Accolla et al., 2013). For this reason we decided to perform a first

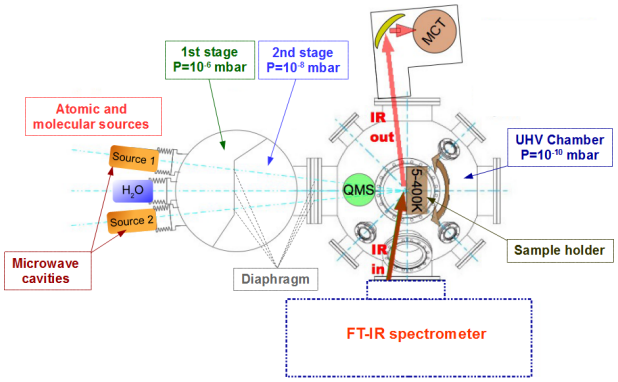

FIGURE 5.1: Schematic top-view of the VENUS set-up and the FT-RAIRS facility.

experimental study of volumetric diffusion rates of H and O atoms on porous ASW .

Strictly speaking, diffusion on porous ice is both a surface diffusion and a bulk diffusion. There is surface diffusion on the external surface of the pores of the ice, and therefore this surface diffusion allows the ice to be swept within its volume by the diffusive atoms. It is sometimes called percolation. Bulk diffusion may occur, but refers to the crossing of a compact/closed ice layer. In particular, if closed pores are present, the atoms must penetrate through the wall of the pores, before possibly continuing the surface diffusion on the inner surface of the closed pore.

5.2 Experimental methods

5.2.1 Experimental set-up

Adsorbates and products were probed *in situ* through a Fourier Transform Reflection Absorption Infrared Spectrometer (FT-RAIRS), and a quadrupole mass spectrometer (QMS) used for measuring the beams fluxes and beams compositions and for performing the temperature-programmed desorption (TPD) experiments.

All the experiments were performed following these steps:

a deposition of 1 monolayer (ML = 10^{15}molecules/cm^2) of NO on gold sample held at 40 K;

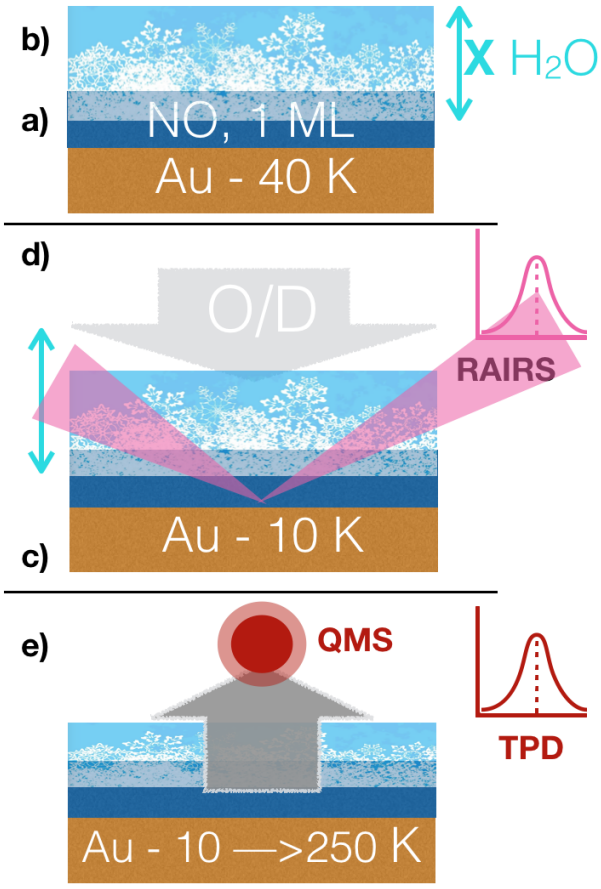

FIGURE 5.2: Scheme of the experimental protocol: a) deposition of 1 ML of NO at 40 K; b) deposition of X ML of H_2O at 40 K; c) cool down at 10 K in the case of D-exposure experiments; d) deposition of D atoms at 10 K or of O atoms at 40 K, recording continuously IR spectra; e) TPD profiles of the species of interest.

b deposition of X ML of H_2O on top of NO ice at 40 K with X=0, 2, 3, 6, and 10 ML;

c cool down to 10 K in the case of D atoms study. The surface is kept at 40 K for O study.

d exposure of NO-H_2O ice to a D- or O-atom beam. RAIRS spectra recorded during exposure.

e TPD performed after D or O exposure.

This protocol is schematized in figure 5.2.

Deuterium is used in place of hydrogen to increase the signal to noise ratio. In the case of D atoms exposure, we held at 10 K after the same procedure of ice

formation at 40 K. The ice is not supposed to change upon cooling, but can change of morphology if heated. During the O atoms exposure, NO-H_2O ice is held at 40 K to enhance O_2 desorption and prevent an efficient formation of O_3 (Minissale et al., 2014a).

Atomic species, D and O atoms, were generated by dissociating D_2 and O_2 molecules in a quartz tube placed within a Surfatron cavity, which can deliver a maximum microwave power of 200 W at 2.45 GHz. Atoms and undissociated molecules were cooled and instantaneously thermalized upon surface impact with the walls of the quartz tube. Deuterium and oxygen beams were free of electronic excited atoms (Congiu et al., 2009, Minissale, M. et al., 2016). The dissociation efficiency of D_2 and O_2 was $\tau = 50\pm5$ %, where τ represents the percentage of dissociated molecules. τ defines the atom/molecule ratio in the beam. For example if τ is 0.5, every 10 molecules we have 10 atoms and 5 undissociated molecules.

We have calibrated the molecular beam as described in Amiaud et al. (2007) and Noble et al. (2012). The first monolayer of NO was reached after an exposure time of about 15 minutes which give a flux of ϕ_{NO}=(1.0±0.3)×10^{12} molecules $cm^{-2}s^{-1}$. D_2 and O_2 molecular fluxes were ϕ_{D_2,O_2}=(1.05±0.3)×10^{12} molecules $cm^{-2}s^{-1}$ while D and O atoms fluxes were $\phi_{D,O}$=(2.1±0.3)×10^{12} atoms $cm^{-2}s^{-1}$.

Adsorbates and products were probed continuously through FT-RAIRS during atoms exposure. TPD was performed after D or O atoms exposure and the sample is heated up to 250 K or 190 K, respectively. Those temperatures allow the desorption of NO-H_2O ice and of newly formed molecules (ND_2OD and N_2O in the case of D, and NO_2 in the case of O).

5.2.2 Water ice characterization

Water ice deposited at 40 K is porous (Stevenson et al., 1999b). The presence of cavity and pores on the surface increases the Number of Adsorption Sites (NAS) and thus the effective surface. We have studied how the effective surface seen by the atoms evolves as a function of water ice layer. We used a standard Kings and Wells method (King and Wells, 1972) by depositing D_2 as a function of water ice layer thickness. We monitor the partial pressure of D_2 in the chamber while a D_2 beam is sent to the surface held at 10K. Typical measured curves can be seen in Figure 5.3 of Amiaud et al. (2007). For each ice substrate there is a specific

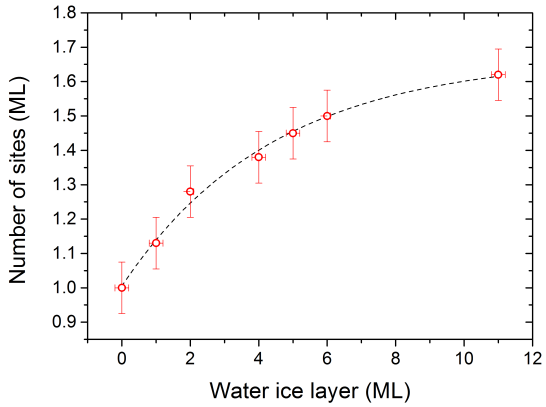

FIGURE 5.3: Number of adsorption sites expressed in ML as a function of water ice thickness, derived from a King and Wells methods.

saturation time which scales to the NAS. The results are shown in Figure 5.3. Without addition of amorphous porous water, the surface is considered as planar. The initial surface is a compact ASW of 15 ML thickness grown at 110 K. It is by definition equal to 1 ML. With the addition of extra layers of porous water, the saturation time increases, which corresponds to an increase of the NAS. The effective surface reaches 1.6 for 11 ML of extra water ice deposited at 40 K. In order to take into account the evolution of NAS in the model presented in section 5.4, we fitted the experimental results with the following exponential law

$$NAS = 1.67 - 0.67 \cdot e^{-\frac{H_2O}{4.43}} \tag{5.1}$$

We stress that this is an empirical law and it is far from being a general law to describe the evolution of NAS as a function of water ice thickness. It is only valid in our specific experimental conditions.

5.3 Experimental results

5.3.1 Oxygenation of NO ices

The diffusion of oxygen in ASW is studied using nitric oxide as a reactive marker. Oxygenation of NO can occur through NO reactions with the three oxygen allotropes O_x (O, O_2, and O_3). Solid state reactions generally have two limiting

factors, the reagent diffusion barrier and the reaction barrier. As the NO+O reaction is barrier-free, it represents a system suitable for the study of O diffusion. We note that the presence of atomic oxygen on a surface easily leads to the formation of diatomic oxygen and ozone therefore, reactions NO+O_2 and NO+O_3 could occur in solid phase and would make the interpretation of experimental results more difficult. To avoid this problem, the presence of diatomic oxygen and ozone can be limited by performing experiments at a sample temperature of 40 K. At this temperature, O_2 is efficaciously released in the gas phase and, therefore, O_3 cannot be effectively formed in the solid phase (Minissale et al., 2014a).

Figure 5.4 shows typical IR spectra obtained by exposing 1 ML of NO held at 40 K to O atoms. The red spectrum has been taken before O-atom exposure. This curve does not present any IR signature since it has been taken as reference spectrum. The other spectra have been taken after 0.2, 0.4, 0.8, and 2.0 ML of O-atom exposure, respectively. We can assign four main signatures: the NO dimer at 1770 and 1860 cm^{-1} and the NO_2 at 1605 and 1315 cm^{-1}. From the decreasing of NO peak as function of O-atom exposure, we have evaluated the kinetics of NO consumption. Similarly, by integrating the increasing of NO_2 signatures, we have evaluated the formation rate of NO_2.

The kinetics of NO consumption and NO_2 formation are shown in figure 5.5 as a function of O-atom exposure for different thickness of H_2O ice (0, 2, 3, 6, and 10 ML). Each curves shows a decrease of the reagent (NO, top panel) correlated with an increase of one of the product (NO_2,bottom panel). As expected for a barrier-less reaction the kinetics reach a steady state plateau after an exposure about equal to one ML, which corresponds to a perfect stochastic reaction.

As evident from experimental data in figure 5.5, the level of the steady state of NO consumption (or NO_2 formation) depends on the thickness of water ice. When no water ice is deposited on top of NO, 1 ML of oxygen atoms is able to react with all the NO previously growth ($\sim$1 ML). Two ML of porous water ice are able to prevent a complete consumption of NO ice since less than 0.7 ML are consumed. For 10 ML of water ice, only 0.1 ML of NO reacts with O atoms. We note that once the steady state plateau is reached, there is no measurable slower increase, within our experimental uncertainties.

As explained in the experimental procedure, the NO ice deposit is followed by a H_2O deposit on the NO ice. However, due to the porous structure of the water

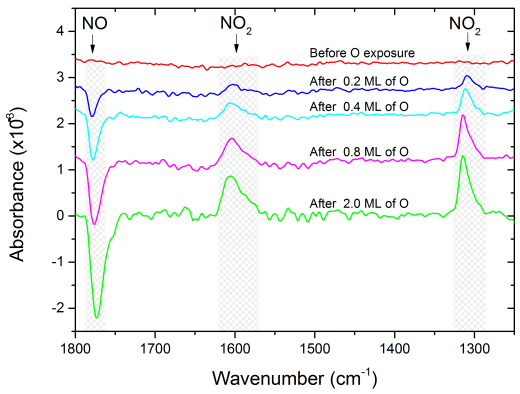

FIGURE 5.4: IR spectra obtained by exposing to 1 ML of NO held at 40 K to different amount of O atoms: 0, 0.2, 0.4, 0.8, and 2.0 ML. The red curve does not present any IR signature since it has been considered as the reference spectrum. Curves are offset for clarity.

ice and diffusion, NO molecules may be present in an "uncovered" adsorption site after water ice deposition.

Two populations of NO can therefore be considered:

- covered NO, accessible only by pure bulk diffusion of O atoms (hereinafter NO_b)
- uncovered NO, present on the surface or in the pores of water and accessible by surface diffusion of O atoms (hereinafter NO_s).

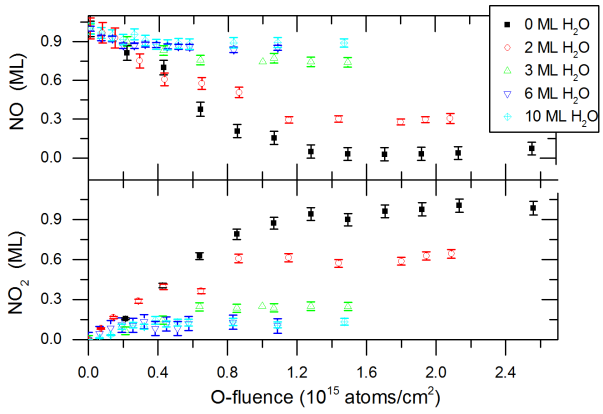

FIGURE 5.5: Kinetics of NO consumption and NO_2 formation obtained by integrating IR peaks of NO and NO_2 as a function of O-atom fluence for five different thickness of water ices (0, 2, 3, 6, and 10 ML) held at 40 K.

In the NO_s population, there are two different sub-categories, that could be called "outer surface", and "inner accessible surface". The first one corresponds to NO located on the outer surface, and thus can interact directly with the gas. Even though water ice is deposited on top of the NO layer, we cannot neglect the possibility for NO to diffuse during the ice building at 40 K. The second category of NO_s correspond to NO located in a pore, and it requires surface diffusion of O (or D) to react.

The details of TPD profiles can help to discuss these possible locations: outer surface, inner surface, or bulk. In figure 5.6 panel *a* is present the TPD traces of mass 30 (in red) and mass 46 (in green) after the oxydation of NO without water overlayer. As we have shown in Minissale et al. (2013), TPD desorption curves of NO_2 ices are characterized by two peaks at masses 30 and 46 (with a constant ratio m46/m30∼13%) at around 125 K. We stress that only the presence of both mass 30 and 46 represents the desorption of NO_2. In panels *b* and *c* we can see 3 peaks at mass 30, named A, B, and C for sake of clarity. The peak A at 125 K is related to the the desorption of surface NO_2 since both masses 30 and 46 are present. The peak B at 148 K has no mass 46 components and it is therefore due to the desorption of NO. It is indeed the NO unreacted that is released during the rearrangement of the ASW, prior to the crystallization. This peak correspond to NO_b in water bulk (or inaccessible pores). The peak C shows masses 30 and 46 and it corresponds to the release of NO_2 trapped in the pores of the water. Its origin can be either NO_b or NO_s trapped during the reconstruction of the ice during the TPD. On panel *d*, we have over plot the shape of the water desorption. It shows a two peaks desorption. The first peak corresponds to desorption of ASW. ASW desorption is reduced when the crystallization occurs. The second peak corresponds to desorption of crystalline water (Scott Smith et al., 1997). We can see here that the NO desorption (peak B) is occurring during the ASW desorption, whereas the NO_2 desorption exactly match with the water crystallization. This is known as the so called Volcano effect (May et al., 2013), when the water crystal is expending, it expels all the impurities, which are NO_2 in our present case.

From *a* to *d* panels in figure 5.6, one can note a decrease of the peak at A; it is no longer visible in the panel *d* meaning that all NO_2 is formed from NO trapped inside the ice.

We now return to the different scenarios of NO reactivity depending on their initial location. NO_2 desorbing from peak A comes from the surface or from an open pore.

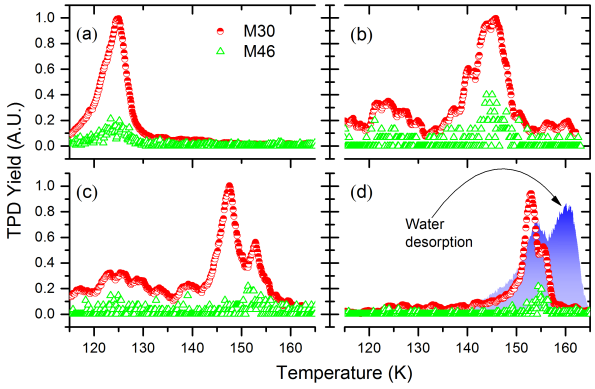

FIGURE 5.6: TPD curves at mass 30 and 46 after O-exposure of NO/H_2O ice for different thickness of water ices held at 40 K: 0 ML in (*a*), 3 ML in (*b*), 6 ML in (*c*), and 10 ML in (*d*).

The C peak indicates an origin within the volume, in bulk or in open pores. We can clearly see the change in the balance from peak A to C, corresponding to more and more NO that reacted in the pores or in the bulk. The increase of the B peak corresponds to the unreacted NO, which matches perfectly plateau values observed in the IR spectra. TPD traces show that the thicker the ice, the higher the proportion of reaction inside the pores. This was not certain before the study: one could have imagined that the NO film remains at the surface because completely repelled by water growth (water molecules impinging with the kinetic energy of room temperature) or segregated forming islands. Moreover, it seems that NO diffusion during the growth of water ice over layer is not efficient. This could be due to the ability of NO to form dimers (Minissale et al., 2014b) that may have a low diffusion rate.

5.3.2 Deuteration of NO ices

In this section we describe experimental results of deuteration of NO. As studied by Congiu et al. (2012a), the deuteration of NO bring to the formation of deuterated hydroxilamine (ND_2OD) via the three subsequent D-atom additions to nitrogen monoxide. Side reactions may lead to some N_2O formation. The first step (NO consumption) is barrier-less. Here we have exposed NO ices held at 10 K to different amount of D atoms (up to 2.1 ML). We have studied three different chemical kinetics by varying the amount of water ice deposited on top of NO, i.e. 0, 3, and 6 ML of porous water ice. As in the case of NO+O ice, we can easily follow the kinetics of NO consumption by looking to the decrease of IR band at

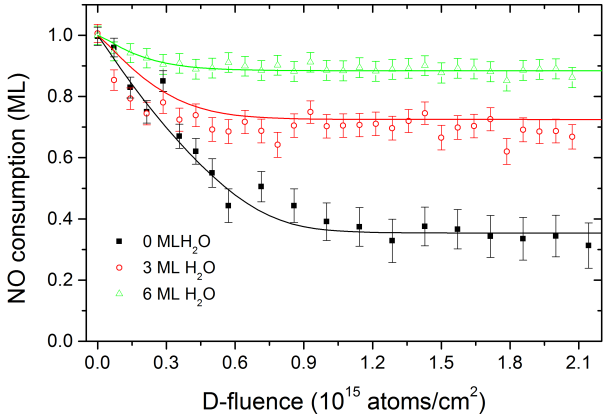

FIGURE 5.7: Comparison between model (solid lines) and experimental data (dots). Experimental data have been obtained by integrating IR peak of NO following to different fluences of D atoms for three different thickness of water ices (0, 3, and 6 ML) deposited on top of NO held at 40 K. Simulated curves have been obtained by using the α_0 law for a deuterium bulk diffusion of 280 K.

1770 cm^{-1}. Differently from the NO+O case, we cannot follow the kinetics of reaction products (ND_2OD) since theirs IR signatures are hidden by the noise. Nevertheless by performing TPD experiments, we have checked the presence of deuterated hydroxilamine after each experiment. NO kinetics are shown in figure 5.7; astonishingly NO is not consumed after a D-fluence of 2.1 ML in the case of bare NO. This could be explained by a cover effect of NO by the newly formed hydroxilamine: at very beginning of experiments NO can react efficiently with D through Eley-Rideal mechanism; once hydroxilamine starts to be formed on surface can partially cover NO and D atoms have to diffuse to react with it. This means that surface density of D atoms increases and facilitates D_2 formation through D+D reaction. Somehow hydroxilamine could play the same role of water ice preventing a full NO consumption [2]. The role of water ice is clearly visible for the experimental data plotted in figure 5.7. When 3 ML of H_2O are deposited, 0.3 ML of NO are consumed, while only 0.1 ML of NO reacts when 6 ML of H_2O are deposited on top of it.

If we now compare the unreacted NO for the O and D experiments, we find that it is 0.67±0.09 (for D) and 0.74 ±0.04 (for O) for the case of 3 ML of water overlayer, and respectively 0.88±0.07 and 0.89±0.02 for 6 ML of water. It is equal, within

[2]We see in previous chapter that the back reaction 4.8 ($HNO + H \longrightarrow NO + H_2$) can also be responsible for incomplete consumption of NO.

our experimental error bars. We can conclude at this stage that the accessibility to NO for O atoms and D atoms seems to be identical.

5.4 Model and Discussion

The model used to fit our experimental data is very similar to that described in Minissale et al. (2013), Minissale, M. et al. (2016). In the case of NO oxygenation we follow the density of six chemical species: O-surface atoms (O_s), coming exclusively from the beam and diffusing only on the surface; O-bulk atoms (O_b), reacting and diffusing only in the ice bulk; NO-surface molecules (NO_s), deposited on the surface and reacting only with O_s; NO-bulk molecules (NO_b), deposited on the surface and reacting only with O_b; NO_2 formed via NO_s+O_s or NO_b+O_b; and finally O_2, coming both from the beam and formed by solid-state reactions. Each differential equation is composed of different terms:

- positive terms contribute to the increase of species amount, i.e., a molecule (or atom) arrives from the gas phase or it is formed on the surface;
- negative terms indicate a decrease of species amount, i.e., a molecule (or atom) is consumed on the surface or it desorbs and returns to the gas phase.

The terms involving the Eley-Rideal (ER) (gas-surface reactions) and Langmuir-Hinshelwood (LH) mechanisms (reaction induced by surface diffusion) are independent. For such reason we can determine the amount of a species formed (or consumed) via the ER or the LH mechanism. Below we show the set of differential

equations built to simulate NO consumption and NO_2 formation:

$$\begin{aligned}
O_s'(ML) =& \phi_O(1-2O_s-O_2) - \phi_{O_2}\,O_s - 4k_{OsDif}\,O_s\,O_s \\
& - k_{OsDif}\,O_s\,O_2 - \phi_O\,NO_s - k_{OsDif}\,O_s\,NO_s \\
& + k_{ObDif}\,(O_b - O_s) - O_s\,Des_{O_s}, && (5.2)\\
O_b'(ML) =& -k_{ObDif}\,(O_b - O_s) - k_{ObDif}\,O_b\,NO_b, && (5.3)\\
O_2'(ML) =& \phi_{O_2}\,(1-O_s) - \phi_O\,O_2 + \phi_O\,O_s + \\
& + 2k_{OsDif}\,O_s\,O_s - k_{OsDif}\,O_s\,O_2 - O_2\,Des_{O_2}, && (5.4)\\
NO_s'(ML) =& -\phi_O\,NO_s - k_{OsDif}\,O_s\,NO_s - NO_s\,Des_{NO_s}, && (5.5)\\
NO_b'(ML) =& -k_{ObDif}\,O_b\,NO_b, && (5.6)\\
NO_2'(ML) =& \phi_O\,NO_s + k_{OsDif}\,O_s\,NO_s + k_{ObDif}\,O_b\,NO_b, && (5.7)
\end{aligned}$$

O_s, O_b, O_2, NO_s, and NO_b, NO_2 are the densities (expressed in fractions of ML) of the different species, ϕ_O is the flux of O atoms and ϕ_{O_2} is the non dissociated fraction of O_2 defined in Section 2. We define :

$$\begin{aligned}
Des_{O_s} =& \nu\, e^{\frac{-E_{O_s des}}{T}}, \text{with } O_s des = 1400K && (5.8)\\
Des_{O_2} =& \nu\, e^{\frac{-E_{O_2 des}}{T}}, \text{with } O_2 des = 1100K && (5.9)\\
Des_{NO} =& \nu\, e^{\frac{-E_{NO des}}{T}}, \text{with } NO des = 1300K && (5.10)\\
k_{OsDif} =& \nu\, e^{\frac{-E_{O_s dif}}{T}}, \text{with } O_s dif = 750K && (5.11)\\
k_{ObDif} =& \nu\, e^{\frac{-E_{O_b dif}}{T}}, \text{with } O_b dif \text{ a free parameter} && (5.12)
\end{aligned}$$

where T is the sample temperature and ν=$10^{12}s^{-1}$ is the trial frequency for attempting a new event; $Des_{O_s,O_2,NO}$ are the desorption probabilities of O_s, O_2 and NO, respectively; k_{Osdif} and k_{Obdif} are the thermal diffusion probability of O atoms on surface (s) and in the bulk (b). We stress that the only free parameters are $E_{O_b dif}$ and the initial amounts of NO_s and NO_b.

As described before water ice is deposited on the top of NO molecules. Depending on the amount of water ice deposited, NO molecules can be accessible by bulk (NO_b) or surface (NO_s) paths. We use a single parameter, called α, to take into account the initial amount of NO_b (α) and NO_s (1-α) molecules.

The main difficulty of the analysis lies in the fact that we do not know what is the amount of NO initially presents in the bulk (NO_b). The consumption of

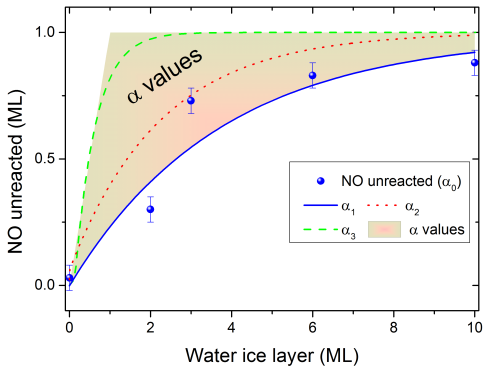

FIGURE 5.8: Colored zone: possible values of NO located inside the bulk of ice (NO_b=α) as a function of the water ice layer thickness (WIL). Blue points : measured amounts of unreacted NO. Blue, red and green lines are representing 3 possible parametrized repartitions of initially covered NO molecules

NO can occur via surface reactions of NO_s or via diffusion through the ice. We have a unique observable NO, but two competing and potentially compensating pathways. Actually we can obtain the same level of consumption if we increase both α and bulk diffusion. In other words, more NO can be initially covered if the bulk diffusion is more efficient. Therefore, we need to explore the whole domain of bulk diffusion and initial α coefficient to simulate the full kinetic of NO consumption.

Let's first focus on the possible values of α (NO_b). The amounts of NO_b and NO_s are related by the obvious closure relation NO=NO_b + NO_s. Because NO= 1 (one ML of NO is initially deposited) in all our experiments, NO_s =(1-α). At the present stage, we ignore what is the dependency of α with the thickness of ASW. By definition α=0 when there is no water deposition. We can suppose that α is monotonically increasing with the Water Ice Layers (WIL) and that α cannot be larger than the WIL. Here we suppose that at least one water molecule is required to occupy one adsorption site. α tends toward 1 when the ASW thickness tend to infinity.

Moreover, we know that the NO+O reaction is a barrier-less reaction and so all the NO accessible via surface paths should react. This means that the amount of NO_s (i.e. 1-α) cannot be greater than the amount of NO reacted. This hypothesis is reinforced by the fact that in all our experiments, we reach a plateau, indicating that all the possible reactants have been consumed. In figure 5.8 we plot in blue dots the amount of NO unreacted as a function of WILs deposited on top of the

NO layer. The possible values of α are represented by the colored zone. The values of α, whatever is the WIL are comprise between 0 for WIL=0, and 1 for WIL $=\infty$. Moreover, taking into account the previous remark that NO_s (i.e. 1-α) cannot be greater than the amount of NO reacted, therefore α is necessarily greater than the unreacted NO. In other words, the contribution of bulk diffusion cannot be negative. So the α domain is restricted to the portion of the figure 5.8 above the experimental values (α_0). To materialize the inferior limit of the possible α, we have taken an exponential saturation law: $\alpha(WIL) = 1 - e^{-\frac{WIL}{P_1}}$ where P_1 is the fitting parameters. The curve $\alpha_1(WIL)$ is represented in blue in figure 5.8 and it corresponds to the situation of low number of NO initially present in the bulk, α_2 (red dotted curve) to an intermediate number of initial NO_b and α_3 (green dashed curve) represents the case where NO molecules are perfectly covered with water ice, and therefore the reactivity can only proceed through bulk diffusion. The three laws are given by:

$$\alpha_1(WIL) = 1 - e^{-\frac{WIL}{3.447}}, \tag{5.13}$$

$$\alpha_2(WIL) = 1 - e^{-\frac{WIL}{2.247}}, \tag{5.14}$$

$$\alpha_3(WIL) = 1 - e^{-\frac{WIL}{0.515}}. \tag{5.15}$$

We stress that these are empiric laws which have been defined to explore the space parameter of the possible α values as we can see in figure 5.8.

Figure 5.9 presents typical comparison of our model and the experiments. We use the kinetic of the NO consumption (and NO_2 formation), for different O fluences. We can very satisfactorily reproduce our experimental data using the α_0 values, which are indeed the values of α equal to the unreacted NO obtained from the plateaus observed in IR spectra. In this case, the best fit is obtained for any value of bulk diffusion greater than 950 K as can be seen on the right panel of the figure 5.9. This value is to be compared with the value of surface diffusion taken as 750 K. It corresponds to a ratio of $\sim$150 of the two diffusion rates.

Other scenarios of initial covering of NO are tested using different α_x laws. We can see on the χ^2 graph that it exists a minimum for which it is possible to compensate an initial coverage with a lower diffusion barrier. These minima have higher absolute values with the increase of the initial NO coverage (from 1 to 3), and logically show values with a lower and lower diffusion barriers, in line with what expected. The values of χ^2 are higher but, taking into account that the α_0

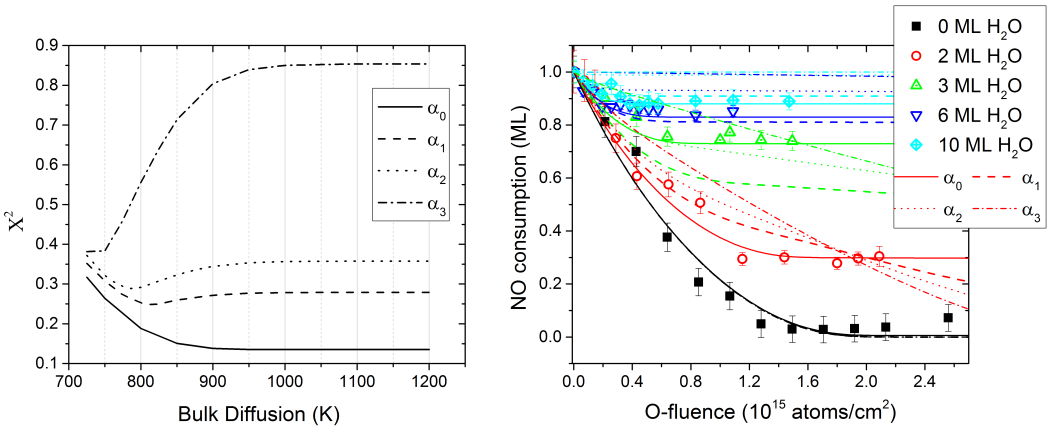

FIGURE 5.9: Left panel: χ^2 values comparing model and data for different α laws as a function of bulk diffusion energy. α_0 corresponds to exact experimental values of unreacted species. Right panel: Comparison between model (lines) and experimental data (dots). Experimental data have been obtained by integrating IR peaks of NO and NO_2 as a function of O-atom fluence for five different thickness of water ices (0, 2, 3, 6, and 10 ML) held at 40 K. Simulated curves have been obtained by using three laws for the α parameter (α_1, α_2, and α_3) and measured experimental values (α_0) for the best case corresponding to the minimum χ^2 of left panel. For α_0 any choice of diffusion parameter greater than 950 K gives similar results.

has the best possible absolute values of χ^2 because it is made from the right plateau values, it is not a strong reason to reject these possibilities of initial coverage. We can for example argue that our α_x laws are not exactly representative of the initial coverages, and that another repartition would probably get a lower, so better, minimal value of χ^2. However, on the right side of the figure 5.9 we can see that the best fits, are corresponding to unrealistic situations. In particular, the values predicted at high fluencies are always decreasing and therefore there is no plateau, as observed in experimental data. Therefore, the best solution is the case of α_0 which corresponds the scenario of the minimum of NO initially covered with the water ice, and thus to a slow bulk diffusion, which need to be at least two order of magnitude slower than the surface diffusion.

We have also built a similar model to simulate the NO+D kinetics. We have considered 8 species NO_s, NO_b, D_s, D_b, D_2, NOD, NDOD, ND_2OD. The desorption energy of D and D_2 was fixed to 600 K and the diffusion energy for D_s to 210 K (Wakelam et al., 2017). Even in this case we considered three laws for α and different values of bulk diffusion. We obtained results similar to the case of NO oxygenation. The best fit, shown in figure 5.7 has been found for the α_0 law, (NO_s=$NO_{reacted}$) and the minimum value of bulk diffusion is E_{Dbdif}=280 K. In

this case, the ratio between surface diffusion rates and bulk diffusion rates is larger than 1000.

In both cases, NO oxygenation and deuteration, the chemistry seems to be driven by surface reactions (including in the pores). Lowering the value of E_{bdif} to values closer to E_{sdif} induces a faster kinetics, that would slowly consumed the NO_b which is not observed experimentally. A good agreement between experimental and simulation results can be found using

$$\frac{E_{bulk-diffusion}}{E_{surface-diffusion}} \geq 1.3$$

5.5 Astrophysical implications and conclusions

In this paper we present an experimental estimate of bulk diffusion energies of oxygen and deuterium atoms on and through porous amorphous water ice. We use NO as a chemical tracer. Under O or D exposure, NO is rapidly consumed, down to a plateau indicating that NO cannot longer be reached by atoms in our experimental conditions. To mimic the initial fast consumption and the following plateau, only a bulk diffusion (through water ice) two orders of magnitude slower than surface diffusion for O and three orders of magnitude for D can fit our data. We found a lower limit for bulk diffusion of 950 K and 280 K for O and D, respectively, and a $E_{diffbulk}/E_{diffsurf} \geq 1.3$ in both cases.

In the Interstellar Medium (ISM), the existence of ice mantle is ubiquitous as soon as visual extinction reaches a value of 3. It corresponds to regions where density raises to $\sim 10^{3-4}$ mol cm^{-3}. In these conditions, one layer of the mantle takes about 1000 year to build-up for a total of 10^5 years to reach a 100-layers thick mantle. After this point, most of the gas species should already have accreted on grains, with few notable exceptions such as H, He, H_2, and some of close related species like H_3^+ and N_2H^+. This is why interstellar ices enter a second stage of their chemical evolution, which duration depends on the mass of the to be born star, before ongoing processes linked to the more energetic next phases of star formation. During the growth of the mantle, one H atom lands on grains every $\sim 2 \cdot 10^4$ s (see figure 8 of Congiu et al. (2014a)). It can completely scan the surface of a grain (radius $\simeq 0.1$ μm) in about 10^3 s. In the case of D atoms, the lower limit of the bulk diffusion (280 K) corresponds to a life time on the surface of

$\sim$1 s at 10 K ($\tau = k^{-1}_{DbDif}$). It means that H atoms can scan the surface before penetrating the bulk of the ice, but they could penetrate the ice before the arrival of another H atoms. This implies that the H diffusion through the bulk of the ice cannot be fully ruled out with our lower limit of H bulk diffusion. Only a factor of more than 10^6 between the surface and bulk diffusion rates would prevent bulk penetration, the latter being too slow to compete with the H accretion of the gas phase, and its subsequent transformation into H_2. However, since the surface diffusion rate is still at least 1000 times faster than the bulk diffusion, any surface reactant with a concentration greater than a thousandth would statistically react with the H atoms. In other words, H could penetrate deeper in the ice mantle only if very few reactants are present on the outer surface of grains. Thus, we conclude that the surface hydrogenation, in our experiments as well as in the ISM, is dominant over bulk diffusion, which cannot be totally excluded only on the basis of a direct extrapolation of our experiments. In such considerations, we neglect isotopic effects that are probably important but hard to take into account since both surface and bulk diffusions should be affected.

For O atoms, crossing the first water bulk layer should take $\sim 10^{29}$ s, which means that it is not possible (within the frame of the classical formalism we use here).

However, we point out our values are lower limits for the bulk diffusion barriers as show by the flat shape of the χ^2 curve of figure 5.9. The present experiments do not show directly if H diffusion through the ice bulk can reduce the life time of radicals formed inside the volume of the ice mantle during UV irradiation or during other energetic processes. The presence of radicals during the initial building of the ice mantle is probably excluded thanks to the high mobility of H atoms at any temperature (Senevirathne et al., 2017). Our experiments show that the only very first layers of the mantle are reacting and models considering that surface reactions rule the ice building (e.g. Vasyunin et al. (2017)) seem thus coherent with our laboratory experiments. Hydrogenation or oxidation experiments (Hiraoka et al., 2002, Watanabe et al., 2004, Fuchs et al., 2009, Jing et al., 2011, Ward and Price, 2011) have used similar or greater atomic fluxes. This means in a first approximation that the surface to bulk diffusion efficiency is the same or greater. Actually, the higher the flux, the higher the self reactivity, the lower the possibility to penetrate inside the molecular substrate. With the present study, we can understand why by construction laboratory experiments favor surface instead of bulk reactivity. However, we provide here a lower limit confirming that surface

diffusion of H is order of magnitude faster than bulk diffusion through the ice, even though it certainly changes with the type of molecular layer used.

Finally some works suggest the existence of an efficient ice segregation mechanism of both interstellar (Öberg et al., 2011, Allodi et al., 2014) and cometary ices (Dello Russo et al., 2011, McKay et al., 2018). Nevertheless ice segregation is still an open question in astrochemistry (Boogert et al., 2015). The possible H atoms migration inside the bulk can strongly change the chemical composition in the whole ice thickness, but simple thermal differentiation could also be the reason of the observed segregation. This aspect could now be tested thanks to MonteCarlo simulations (Cazaux et al., 2010, Cuppen et al., 2017b) using our boundary limits of bulk diffusion barriers.

Chapter 6

Efficient formation route of the pre-biotic molecule formamide on interstellar dust grains

Interstellar Complex Organic Molecules are thought to be the building blocks of more complex pre-biotic compounds. In particular, formamide (or methanimide, NH_2CHO), is presented as a multifunctional pre-biotic precursor, the starting point of both pre-genetic and pre-metabolic species. NH_2CHO is widely observed in different astrophysical media, as well as in comets that may have had a crucial role in the delivery of exogenous material to Earth. In star forming regions, gas phase synthesis of formamide is possible, even if it is still debated. In this paper, we present laboratory experiments demonstrate that formamide formation in interstellar ice analogues at astronomically relevant temperatures via simultaneous hydrogenation of NO and H_2CO, two abundant molecules found in icy mantles covering dust grains in star-forming regions. Inclusion of the experimental results in an astrochemical gas-grain model confirms the importance of the investigated solid-state reaction channel leading a high yield of formamide in dark interstellar clouds, and adds a valuable perspective about the way this refractory molecule may have been part of the pre-biotic molecular building blocks delivered to the young Earth.

6.1 Introduction

Among interstellar complex organic molecules (iCOMs), formamide has always attracted attention, since it is the pre-biotic compound par excellence containing nitrogen, oxygen, carbon, and hydrogen. Recently, it has been presented as the link in the chemical chain able to reconcile the "genetic first" and "metabolism first" paradigms (Saladino et al., 2012). It has been observed early (Rubin et al., 1971) and extensively (Bockelée-Morvan et al., 2000, López-Sepulcre et al., 2015, Adande et al., 2013, Takahiro et al., 2012, Muller et al., 2013, Jiménez-Serra et al., 2016, Taquet et al., 2017), but unlike for other pre-biotic molecules, a debate exists whether its origin occurs via a gas-phase pathway (Redondo et al., 2014) or via a solid state synthesis (Jones et al., 2011, Quénard et al., 2018).

Of all iCOMs, formamide has a very high binding energy, is known to survive on dust grains beyond sublimation of water (Urso et al., 2017, Chaabouni et al., 2018) and is therefore a very important molecule being also a source of interstellar nitrogen locked into a refractory animated species. Formamide has been detected in comet comae with a relatively low abundance (some 10^{-4}), with respect to water (Biver et al., 2014, Le Roy et al., 2015), while it is the second most abundant cometary soil compound (1.8 % relative to water ice) as measured by the COSAC mass spectrometer on board the *Philae* lander that touched down on comet 67P/C-G (Goesmann et al., 2015).

There are three different possible scenarios to explain the presence of NH_2CHO at rather high concentrations in the solid state, and all of them might have occurred at the time of the pre-solar nebula when pristine material from the origin of the solar system condensed and part of it remained locked up in comets (Mumma and Charnley, 2011).

The first scenario shows the formation of formamide only in the gas phase, then its freeze-out onto dust grains. However, this hypothesis would lead to a small amount of formamide since its gas phase concentration is never high enough ($\sim 10^{-11}$ relative to H) (Barone et al., 2015). The second scenario implies the production of formamide via energetic processing of ice mantles (Urso et al., 2017, Gerakines et al., 2004, Jones et al., 2011). That pathway to NH_2CHO leads to a low but reasonable production rate, although it should be noted that several secondary products are synthesized at the same time (e.g., HNCO or C_2O_3), depending on the initial composition of the icy mantle and the type of particle/energy

employed (UV, ions, or electrons). One experimental study also involves simultaneous UV irradiation and addition of H atoms onto mixtures of NO:CO, NO:H_2CO or NO:CH_3OH ices, which leads to a relatively high efficiency of NH_2CHO production (Fedoseev et al., 2016). However, the initial ice composition used in those experiments may be quite different from the observed water-dominated interstellar icy dust grains.

The third and last scenario of formamide formation implies its direct synthesis as soon as the molecular mantle covering dust grain is being formed. This is usually called the non-energetic pathway, because at this stage the temperature remains as low as the typical molecular cloud value (10 K), and no external energy source (except for chemical energy) is involved. Such conditions are found before the birth of a star has commenced. Conversely, within proto-solar nebulae the energy processes are highly variable, both locally and over time, due to the very complex mixing and dynamics of the surrounding matter.

6.2 Experimental methods

Our new experimental device VENUS ("VErs de NoUvelles Synthèses"), a ultra-high vacuum (UHV) setup, allows us to simulate the cold molecular phase where interstellar ices are grown. A gold-coated OFHC copper substrate is placed in the centre of the UHV chamber (base pressure 10^{-10} mbar), and can be exposed to up to five atomic or molecular beams. The substrate is mounted in thermal contact with the cold finger of a closed-cycle He cryostat and its temperature is computer-controlled in the range 7-380 K. Deposited and newly formed species are monitored in *situ* by means of Fourier Transform Reflection Absorption InfraRed Spectroscopy (RAIRS) using vibrational fingerprint spectra in the 4000–700 cm^{-1} region and in the gas phase by means of Quadrupole Mass Spectrometry (QMS) upon temperature-programmed desorption (TPD) by steadily heating the Cu substrate (by 0.2 K/s) and monitoring evaporated species. The beams have fluxes in the order of 2×10^{12} molecules/cm^2/s, which means that one monolayer (1 ML, corresponding to 10^{15} molecules/cm^2) is deposited in about 10 minutes. This also means that a molecule already sitting on the surface will wait on average 10 minutes before another incoming particle from the beam hits it or sticks on top of it. Under these conditions, surface diffusion processes (Langmuir-Hinshelwood mechanism) are preferred over gas-surface interactions (Eley-Rideal type).

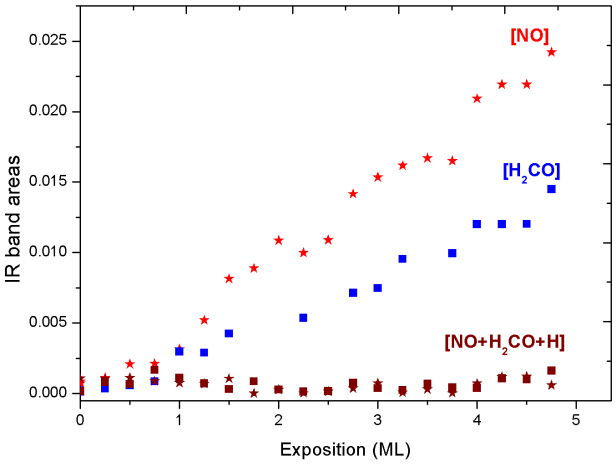

FIGURE 6.1: Integrated areas of NO band (stars) and H_2CO band (squares) as a function of deposited dose on the gold-coated substrate held at 10 K. Blue and red symbols are obtained in pure H_2CO and pure NO experiments, and brown symbols are obtained in the NO+H_2CO+H (co-deposition) experiment.

6.3 Experimental results

Figure 6.1 shows the integrated area of the NO bands at 1774 and 1865 cm^{-1} (red stars) and the H_2CO band at 1730 cm^{-1} (blue squares) when NO and H_2CO are separately deposited on the surface maintained at 10 K. Despite the dispersion of the signal due to the small number of molecules deposited (about 10^{14} in total, i.e. less than one nano-mole), there is a linear increase in absorbance with exposure, as expected. Brown squares and brown stars represent the integrated area of the H_2CO and NO bands, respectively, measured during a co-deposition of H_2CO, NO and H atoms. The brown symbols are below noise level which indicates that all H_2CO and NO molecules reacted during exposure. Therefore, the reactants are completely consumed at 10 K, suggesting that all reactions occur at such a low temperature.

In very thin layers of adsorbates and under the continuous addition of H atoms, very few radicals should remain at the end of the exposure phase. In fact, the flux of H atoms is about 5 times more intense than either H_2CO or NO flux, and under these conditions the complete hydrogenation of NO or H_2CO alone is consistent with previous works (Congiu et al., 2012c, Minissale et al., 2016). We know that hydrogenation of H_2CO produces both CO by abstraction of protons and CH_3OH by sequential addition of H atoms (Hidaka et al., 2007, Hiraoka et al.,

TABLE 6.1: List of discussed experiments

Experiment	Thickness (ML)	Substrate	T_{dep} (K)	Products/ratio
NO + H_2CO + H	0 to 5	gold	10	NH_2OH:NH_2CHO:CH_3OH - 0.46:0.21:0.33
NO + D_2CO + D	0 to 7.5	gold	10	ND_2OD:ND_2CDO:CD_3OD - 0.73:0.24:0.03
NO + H_2CO + H	0 to 5	p-ASW	10	NH_2OH:NH_2CHO:CH_3OH - 0.50:0.40:0.10

2005, Minissale et al., 2016), which allows us to assume that HCO and CH_3O radicals are transiently produced whenever both H_2CO and H are deposited on the cold surface. The other reactive channel is the hydrogenation of NO, which leads to hydroxylamine (NH_2OH) (Congiu et al., 2012) and if some dimers of NO are present on the surfaces, is also a source of N_2O and H_2O in small amounts (Congiu et al., 2012c). It would be necessary to add the possible role of H_2NO and OH to the list of radicals. However, in our experiments co-deposition of all reactants is used. NO is readily consumed and NO dimers are unlikely to be present at any time, therefore it is fair to assume that H_2NO remains the only active radical. All the relevant experiments discussed in this work are summarized in Table 6.1 .

Figure 6.2 shows the TPD profiles of the co-deposition experiment of {NO + D_2CO+D} at 10 K on the gold coated surface (top panel). Deuterated reactants were used in this case to cross check the mass of the newly formed species as to ensure that the final products are chemically identical though they have masses corresponding to the deuterated forms. In the bottom panel of Figure 6.2, we show the TPD profiles obtained after co-deposition of {NO + H_2CO + H} on 4 ML of previously porous water ice substrate of held at 10 K. In this second experiment, H_2O is used as a substrate. We first grow a 4 ML thick porous amorphous solid water ice substrate at 10 K before commencing the co-deposition of NO, H_2CO, and H atoms in order to test the reactivity of the system in the presence of H_2O, since water is the main agent of molecular cloud ice structuring. It should be noted that ASW ice is porous when deposited at 10 K, hence this experiment is carried out under conditions that more realistically mimic interstellar ices where molecular complexity develops on dust grains, and where ASW is the dominant solid species (Boogert et al., 2015).

The top panel of Figure 6.2 shows the mass profile for m/z = 48, corresponding to ND_2CDO, (deuterated formamide). Formamide is also accompanied by the

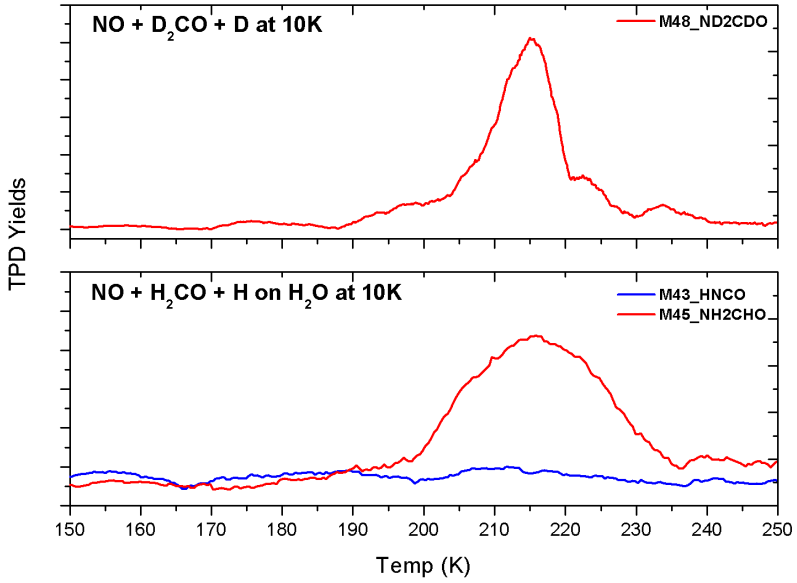

FIGURE 6.2: TPD profiles obtained after co-depostion of NO+D_2CO+D on gold held at 10 K (top panel), and TPD profiles after co-deposition of NO+H_2CO+H on porous ASW ice at 10 K(bottom panel).

desorption of CD_3OD (deuterated methanol) and ND_2OD (deuterated hydroxylamine), not shown. The lower panel shows the desorption profiles for m/z = 45 (NH_2CHO) and m/z = 43 (HNCO). Given i) the high desorption temperature (above 210 K) of the mass spectrum peak for m/z=45, ii) the unambiguous identification of the fragments induced in the QMS head upon ionization and iii) the correct value of the masses in the deuterated-species experiment, there is no doubt that formamide was synthesized in our experiments. Also, we determined that HNCO was not produced at all (Figure 6.2, bottom panel).

In the appendix A, we show the TPD profiles of methanol (m/z=32, desorption peak at around 150 K), NH_2OH (m/z=33, peak at 180 K) and NH_2CHO (m/z=45, peat at 215 K). From these mass spectra and from the fragments mass profiles (such as for m/z=29, 30, 31) integrated over the appropriate desorption temperature range, it is possible to measure the relative ratios of the three major products, namely methanol, hydroxylamine, and formamide.

In the pie diagrams displayed in Figure 6.3, we show the relative abundance of products obtained in two key experiments. The product ratios change considerably in the presence of water molecules. An analysis of these ratios in the light of the different chemical pathways shows that hydrogenation of NO is the most effective

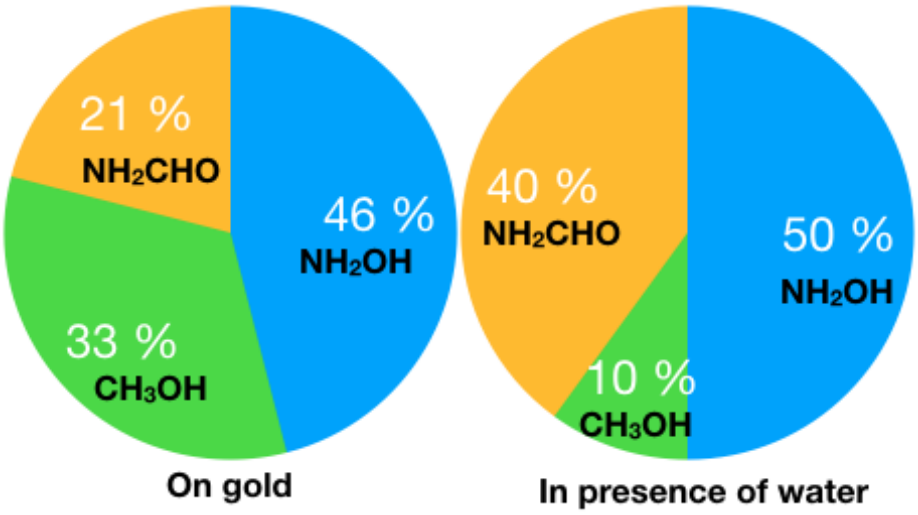

FIGURE 6.3: Relative abundance of products obtained from co-deposition of NO, H_2CO, H on bare gold and on porous water ice at 10 K.

reactive subsystem as proven by the high NH_2OH formation rate. This is because its first reactive step (NO+H $\rightarrow$ HNO) has a very low or no energy barrier (Congiu et al., 2012c), whereas hydrogenation of H_2CO possesses a small activation barrier that can only be overcome by quantum tunnelling effect at 10 K (Hidaka et al., 2013). In addition, a small fraction of H_2CO can also be transformed into CO, which eventually reduces the CH_3OH production. Part of the newly formed species (<10 %) may also be lost via chemical desorption (Dulieu et al., 2013, Minissale et al., 2016).

Without water molecules, only one-third of the H_2CO is diverted from its hydrogenation pathway leading to methanol, and contributes to the formation of formamide. In the presence of water, most H_2CO is converted into NH_2CHO, which eventually becomes four times more abundant than methanol. These simple experiments demonstrate that formamide is naturally formed following the co-hydrogenation NO and H_2CO, two relatively abundant iCOM precursors found in icy mantles covering cosmic dust grains. To prove the impact of the new chemical pathway presented in this work and leading to NH_2CHO in the solid phase, we used a standard astrochemical model that includes gas-grain chemical networks (Taquet et al., 2012, Taquet et al., 2014). Conditions are chosen as in typical molecular clouds with constant physical conditions: n_H=10^4 cm^{-3}, A_V=20 mag, ζ =10^{-17} s^{-1}, and an equilibrium temperature of gas and grains of 10 K. We have added the following reaction to the solid-phase chemical network:

$$H_2NO + H_2CO \rightarrow NH_2CHO + OH \tag{6.1}$$

and the complete list of reactions involving NO and its subsequent hydrogenated forms on grains, based on Ioppolo et al. (2014). Furthermore, we have added the possibility of abstraction of protons from NH_2OH:

$$NH_2OH + H \rightarrow H_2NO + H_2 \tag{6.2}$$

which may be a key reaction since it contributes to the increase in H_2NO, a precursor of formamide. This specific point has been tested experimentally and will be addressed in a forthcoming publication.

In experiments as well as in the dense interstellar medium, NO and H_2CO must neighbours to react together since they are not mobile at 10 K. Our experimental observations confirm that the barrier-less hydrogenation of NO leads to reaction 6.1 more efficiently than the hydrogenation of H_2CO, which activates reaction 6.1 and makes it the dominant chemical route consuming H_2CO molecules.

6.4 Astrophysical implications

In the model, we did not consider other possible reactions such as CH_3O + HNO, because it is not efficient under our experimental conditions. In any case, whatever the details of the actual chemical network may be, the proximity of H_2CO and NO molecules on the surface represents the limiting factor in astrochemical models and as such it has to be evaluated according to the molecular abundances on cosmic grains.

Figure 6.4 shows the abundance of NO, NH_2CHO, CH_3OH, and N_2O ices relative to water at different ages of the molecular cloud. The right panel represents the solution assuming a high barrier (1000K) to reaction 6.2, whereas reaction 6.2 is supposed to be barrier-less in the left panel of figure 6.4.

The time needed for growing a molecular layer on a grain is typically 10^4 years, and about one million years is the length of time employed by interstellar icy mantles to reach their final thickness of a few hundred layers. Therefore, the predicted

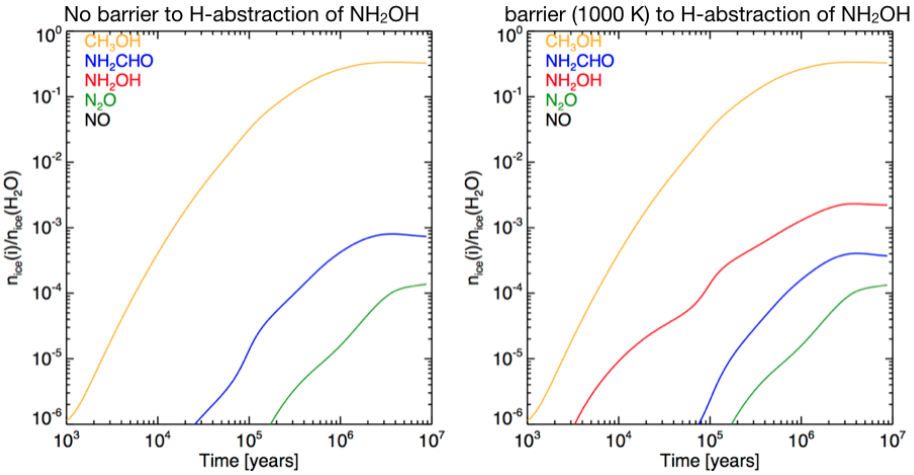

FIGURE 6.4: Fractional abundance of solid species on grains relative to water ice for an astrochemical model in which the effect of a H-abstraction of NH_2OH is shown. The left panel indicates abundances with H-abstraction and the right panel shows abundances when H abstraction is not taken into account.

abundances at one million years represent the molecular composition of the ice at the onset of the formation of a solar system. After this time, there are almost no more reactive gas-phase species that can accrete on grains. In Figure 6.4, we observe a production of NH_2CHO of about 10^{-4} relative to water. In the case of instant gas release from the mantle due to sputtering, as in the case of shocks, this would produce a gas phase abundance of some 10^{-8} relative to H_2, which is slightly higher than the observed values of $0.4 - 1.1 \times 10^{-8}$ (López-Sepulcre et al. (2015)). However, these values may be considered to be consistent, given that the sublimation of ices would be followed by gas phase chemistry that, in its turn, would modify the abundance ratios. In addition, the model accounts for an effective reduction of NH_2OH that, though it is a direct product of hydrogenation of NO on grains, remains an elusive species in space (Codella et al., 2017) and is for this reason an unsolved problem in today's astrochemistry. In the case of a relatively low or no energy barrier for H-abstraction of NH_2OH, hydroxylamine would be consumed and formamide would be formed at the surface of the dust grains, as shown in the left panel of Figure 6.4. As opposed to what we observe in the laboratory, we find that methanol production is not affected in the model. The different results concerning methanol can be explained by the great proximity between H_2CO and NO molecules in the experiments, during the deposition phase, which favours formamide production and eventually becomes the dominant process. In space, abundances are much weaker so most H_2CO undergoes a series of hydrogenation steps that lead to methanol.

Taking into account the very low volatility of formamide and the efficient mechanism to form this pre-biotic molecule in the solid state as presented in this work, allows us to reconcile observations of a high amount of formamide in material sampled by COSAC at the comet 67P surface and its low gas phase abundance. In addition, the relative low abundance of HNCO measured in cometary soil corroborates a solid state formation route to formamide decoupled from HNCO formation.

Our work shows that the simple hydrogenation of two abundant molecular precursor molecules in the interstellar medium leads to the formation of formamide, a key molecule in pre-biotic chemistry. Formamide is produced more efficiently than methanol under our experimental conditions. In dark molecular clouds, this chemical pathway would produce NH_2CHO on grains with an abundance of about 10^{-4} relative to water, which is insufficient to allow detection of this species by current IR space telescopes. We expect, however, that in the future the next generation instruments with increased capabilities, such as the James Webb space telescope, may detect a faint absorption signature of NH_2CHO ice.

Furthermore, the existence of an effective and direct mechanism of formation of formamide in the solid state, without the need of energetic processes, supports the argument that cometary materials have strong and direct chemical links with their interstellar matrix, the pre-solar nebula. Comets that collide with planets would contribute to the delivery of exogenous materials, and the same mechanism might have contributed to bring about life on Earth. Some authors rely on the high degree of deuteration found in our oceans and that found in comets to determine if comets have been an essential contribution to the Earth's water reservoir. If this is confirmed, of all the species that comprise cometary bulks and have been locked up at the time of the early solar system, formamide is the most likely to withstand thermal desorption. Therefore, formamide is to be considered a key molecule for the early development of life, and its origin is to be found at the heart of dark clouds, on the surface of dust grains synthesized at temperatures as low as 10 K, well before the formation of our own planet Earth.

Chapter 7

Experimental study of the hydrogenation of Acetonitrile and Methyl Isocyanide on Interstellar dust grains

Methyl Isocyanide (CH_3NC) and Acetonitrile (CH_3CN) are two complex organic molecules (COMs) which are detected in the interstellar medium and in comets. They are nodes of the very entangled chemical network leading to the molecular complexity in space. We aim at exploring the solid-state chemistry which may lead to COMs. We have developed a new experimental set-up named VENUS, in which we can deposit different reactants together on a cold surface (10-40 K). CH_3NC, (CH_3CN) and H (D) atoms were co-deposited at different temperatures in presence or absence of water. Hydrogenation, fragmentation, and possible isomerization mechanisms take place concurrently in the chemical network of [CH_3NC + H] while CH_3CN does not react with H atoms. In the mixture with H_2O, the hydrogenation mechanism is enhanced. Furthermore, quantum tunneling of H atom seems to be efficient at low temperature ($\sim$ 10 K). Inversely, at higher temperatures (20- 40 K), activation barriers prevent from an efficient hydrogenation.

7.1 Introduction

One of the main questions for the study of the Interstellar Medium (ISM) is to understand why and how complex organic molecules (COMs) develop in molecular clouds. The detection of COMs and the knowledge of chemical networks that leads to them is a valuable tool for the diagnosis of the very varied, dynamic, and often out-of-equilibrium physical conditions and history of the ISM.

Some of these COMs already contain carbon, oxygen and nitrogen, which are the main chemical elements in the composition of the molecules on which terrestrial life is built (Ceccarelli et al., 2017). Accordingly, the appearance of life on Earth is linked to the evolution of the molecular complexity in space, COMs being the constituent elements at the beginning of the chemical evolution of the Solar System. However, the chemical pathways of formation of COMs in interstellar clouds are still the subject of debate and generate many studies. (Herbst and van Dishoeck, 2009a, Caselli and Ceccarelli, 2012, Vasyunin and Herbst, 2013, Vasyunin et al., 2017, Balucani et al., 2015).

Observing isomers is a good way to constrain the problem. Indeed excluding diatomic molecules, 30% of all interstellar molecules have observed isomeric counterparts (Remijan et al., 2005). Therefore, the formation and evolution of interstellar clouds and the stars they generate can be explored through isomer comparison studies. Among these the class of isomers of nitrile (-CN) and isonitrile (-NC) groups is commonly used (Belloche et al., 2014, Kawaguchi et al., 1992, Schilke et al., 2001, Ziurys, 2006).

For instance, Acetonitrile (CH_3CN), VinylCyanide (CH_2CHCN), Cyanoacetylene (HC_3N) and Ethyl Cyanide (CH_3CH_2CN) are COMs frequently detected (Solomon et al., 1971, Johnson et al., 1977, Friedel et al., 2004, Turner, 1971, Nummelin et al., 1998). But for the isonitrile (-NC) group, few molecular species have been detected. For instance, Isocyanoacetylene (HC_2NC), which is an isomer of very abundant cyanoacetylene (HCCCN), has been detected in TMC-1 (Kawaguchi et al., 1992) and methyl Isocyanide (CH_3NC) has been tentatively detected toward Sgr B2 for the first time by Cernicharo et al. (1988). CH_3NC was previously possibly detected in the cold dark cloud TMC- 1 (Irvine and Schloerb, 1984), and has been confirmed in other cold clouds (e.g. L1544), in hot cores of Orion KL (Remijan et al., 2005, Cernicharo et al., 1988, López et al., 2014, Jiménez-Serra

et al., 2016) and in the Horsehead photo dissociation region (PDR) by Gratier et al. (2013).

For typical dense cloud conditions, theoretical calculations of Defrees et al. (1985) estimated the ratio of CH_3NC/CH_3CN to be in the range of 0.1-0.4. However, Cernicharo et al. (1988) deduced from their observations an abundance ratio of ∼0.03-0.05, showing that CH_3CN is an order of magnitude higher than previous estimated.

Such a difference in abundance of stable isomers has been tentatively explained by their different intrinsic stabilities (Lattelais et al., 2009) or/and by their different binding energies to solid particle, one of the isomers being more effectively trapped on dust grains, and so depleted from the gas phase (Lattelais et al., 2011). To check this possibility, Bertin et al. (2017a) have done a laboratory study showing that the adsorption energy of CH_3CN on carbonaceous surfaces is higher than the adsorption energy of CH_3NC, which rules out the hypothesis of a lack of CH_3NC in the gas phase because of a very high binding energy. So the origin of the low isomeric ratios should have entirely a chemical origin.

Hudson and Moore (2004) have bombarded a film of CH_3CN with UV photons and energetic protons and have demonstrated that CH_3CN can partially isomerize to CH_3NC indicating a direct chemical link between the two isomers in the solid phase. Recently Mencos and Krim (2016) have demonstrated that CH_3CN may react with ground state N atoms to form CH_3NC and CH_3CNH in the solid phase at temperatures ranging from 7 K to 11 K.

Yet, the most efficient chemical transformation of the molecular mantle during its formation on grains is the hydrogenation. H atoms are always orders of magnitude more abundant than N atoms. Hydrogenation drive the formation of many molecules in the solid state. According to the astrophysical conditions, the hydrogenation efficiency has been mostly studied at low temperatures (∼ 10 K) (Sandford et al., 2006), from the simplest (H_2, H_2O) to the more complex ones such as formaldehyde (H_2CO), methanol (CH_3OH), hydroxylamine (NH_2OH), formic acid (HCOOH) and ethanol (CH_3CH_2OH) or even formamide (NH_2CHO) (Congiu et al., 2012a, Minissale et al., 2016, Hiraoka et al., 2005, Watanabe et al., 2004, Ioppolo et al., 2011, Bisschop et al., 2007). The hydrogenation of HCN has been studied (Theule et al., 2011) but the one of CH_3CN and CH_3NC has not yet been undertaken.

However, selective destruction pathways of CH_3NC relative to CH_3CN would help astrochemical modellers to better reproduce observed values. This is the starting point of our study. We compare the hydrogenation of the two isomers on a surface maintained at low temperature (8-40 K). Our objective is to understand the details of the chemical network and the possible influence of water, which is the main constituent of molecular mantle on dust grains.

In this chapter, we present the study of the chemical network of hydrogenation of acetonitrile (CH_3CN) and methyl isocyanide (CH_3NC) on grains, as possible chemical pathways of evolution towards complex organic molecules (COMs) in ISM.

7.2 Experimental conditions

The experiments were carried out with the VENUS experimental system at the LERMA laboratory of the University of Cergy Pontoise. It consists of an ultra-high vacuum chamber (UHV) with a base pressure of 2×10^{-10} mbar. The solid sample is a gold-plated surface which is maintained at low temperature using a helium closed-cycle cryostat. The surface temperature is controlled from 7 K to 350 K thanks to a resistive heater. Absorbance spectra of adsorbates are recorded by Fourier Transform Reflection Absorption Infrared Spectroscopy (FT-RAIRS) from 750 cm^{-1} to 4500 cm^{-1}. Products (or remnant reactants) are desorbed from the surface by using thermally programmed desorption (TPD). In our experiments, the surface is heated up from 10 K to 260 K. The heating ramp is kept constant with the value of $\beta = 0.2$ K/s. Traces of products are detected through Quadrupole Mass Spectrometer (QMS) positioned in front of the surface.

The injection of atoms or molecules is carried out using a separate system of 4 atomic or molecular beams. For this study we used only two beams, the central beam is injecting CH_3NC or CH_3CN and the right beam is used for H atoms. The entrance H_2 flux of the right beam is controlled by an automated regulator from Bronkhorst High-Tech and is run at about 10 sccm[1]. A microwave discharge with a power of 70 W dissociates H_2. The dissociation efficiency of H_2 and D_2 is 75% and 65%, respectively.

[1] 1 sccm = $592\,m^3$ Pa s^{-1} in SI units

CH_3NC (or CH_3CN) are liquid at room temperature and their saturation vapour is high enough so that they turn to gas which entrance flux is regulated manually thanks to a needle valve. The expansion chamber of the central beam is kept constant at a pressure of 1.5×10^{-4} mbar. The length of the free flight of molecules in this chamber is about 2 cm before molecules are entering the second stage which remains in the 10^{-7} mbar range on load. The third stage is kept in the 10^{-9} mbar range while the main chamber remains in the low 10^{-10} mbar range to achieve good vacuum conditions for cold surface experiments. Ten grams of CH_3NC have been synthesised by J.C. Guillemin in Rennes, and travelled frozen. The experiments have been performed twice. CH_3NC has been prepared using freeze thaw cycles in order to eliminate the residual atmospheric gases. Purity of CH_3CN and CH_3NC has been measured to be > 98 % (our maximum sensitivity) at the sample level using the movable QMS.

Figure 7.1 displays the FT-RAIRS spectra of CH_3CN and CH_3NC. They are obtained at different surface coverages. The surface is kept at 10 K. The black curve corresponds to no exposure, blue to 1.6 monolayers (ML), purple to 2.4 ML, and red to 4 ML. The accuracy of the determination of the monolayer is about 20%. It is scaled from different species such as CO, which have good wetting properties to determine the first adsorption layer (see ref (Nguyen et al., 2018) for details). IR band strength benchmarking confirms the determination of the adsorbate dose. In figure 7.1 we can clearly observe the difference of the stretching vibrations of cyanide (-CN) group at 2250 cm^{-1} and isocyanide (-NC) group at 2176 cm^{-1}. Features around 3003 cm^{-1} for CH_3CN is more marked than the one of 3008 cm^{-1} for CH_3NC. IR spectra are in agreement with those of literature (Bertin et al., 2017a, Murphy et al., 2000).

TPD analysis complete IR in situ observations. TPD profiles obtained after the separate deposition of 4 ML of each isomers are shown in figure 7.2. Despite the fact that CH_3CN and CH_3NC have the same mass (m/z 41), it is possible to identify the isomer by observing their different cracking patterns consisting of mass 40 and 39. But the most interesting point is that CH_3NC desorbs earlier (its maximum is at 120 K for this specific coverage and heating ramp) than CH_3CN which maximum occurs at 127 K. So it is easy to distinguish both isomers, thanks to their IR features or desorption profiles.

For experiments performed in a water ice environment, the water inlet is connected directly to the main chamber and the H_2O pressure is controlled by a throttling

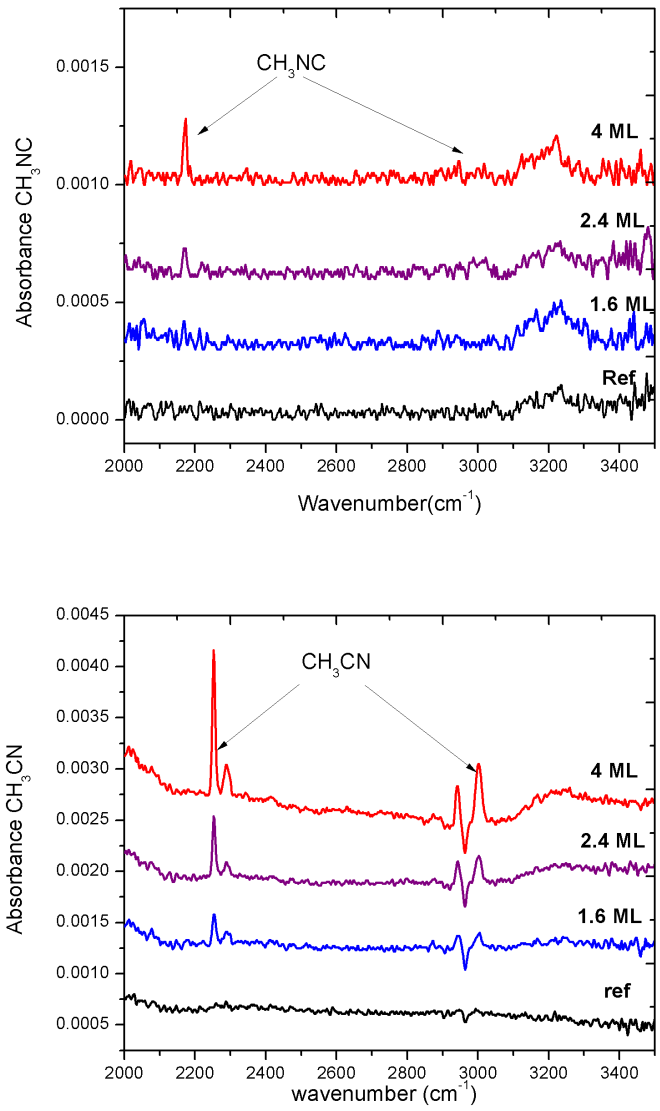

FIGURE 7.1: FT-RAIRS spectra of pure CH_3NC (top panel) and CH_3CN (bottom panel) deposited separately at 10 K for different surface coverages.

valve. The pressure of the main chamber is few $\times$ 10^{-8} mbar before injecting the reactants and is kept constant. Water deposition is controlled via IR and QMS during all the process. CH_3NC, H atoms, and H_2O are co-deposited on the surface during 30 minutes, thus CH_3NC is stopped while H and H_2O continue to be deposited 10 extra minutes. In total 6 monolayers of CH_3NC and 20 monolayers of H and H_2O are deposited. Because the surface is held at 10 K, the water ice network is very porous and does not prevent efficiently the access of H to CH_3NC (Minissale et al., 2018), but taking into account the relative fluxes (water flux is 2.5 higher than CH_3NC's), most of CH_3NC adsorbate should have at least one

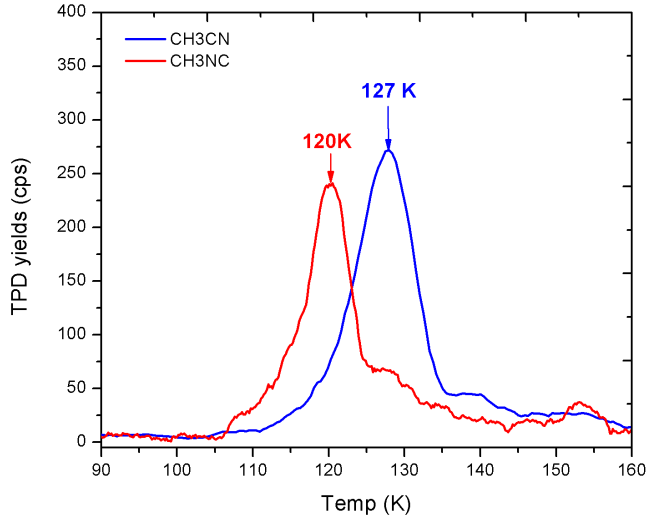

FIGURE 7.2: TPD traces of CH_3NC (red curve) and CH_3CN (blue curve) obtained after separate depositions of 6 ML of the species, on the gold surface held at 10 K.

H_2O neighbour.

7.3 Experimental results

7.3.1 (Non) Reaction between Acetonitrile (CH_3CN) and H atoms at 10 K

The first experiment consist in monitoring the growth of the 2250 cm^{-1} IR feature of CH_3CN with or without H addition. During the first 16 minutes CH_3CN is co-deposited with H atoms. Area of the IR band is represented in black dot in figure 7.3. It shows a linear increase. Thus the H beam is turned off and the growth of the IR band is plotted in red. After 40 minutes the H beam is switched ON again. Infrared band areas are plotted in blue. Dots can be fitted by a straight line. Independently from the presence of absence of H atoms, the increase of CH_3CN molecules is perfectly linear with time. We conclude that in our experimental conditions, CH_3CN does not efficiently react with H atoms on a golden surface held at 10 K.

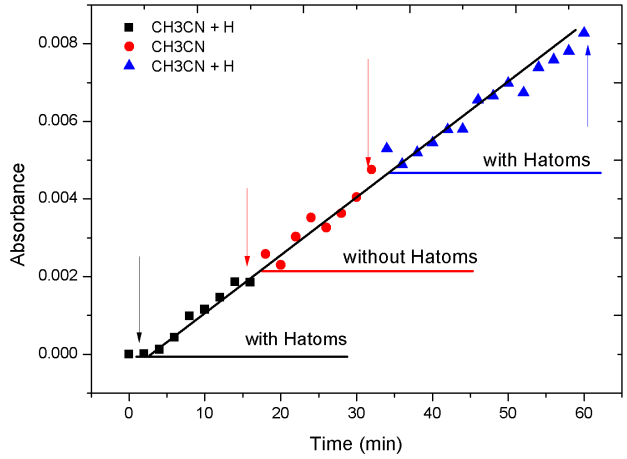

FIGURE 7.3: Evolution of the area of the 2250 cm^{-1} IR band of CH_3CN as function of deposition time on the substrate held at 10 K. H is co-deposited during the initial and final phases (black squares and blue triangles) and is absent (red circles) in the second phase.

7.3.2 Reactivity between Methyl Isocyanide CH_3NC and H atoms at 10 K

Similarly we can compare depositions of Methyl isocyanide (CH_3NC) on the golden surface maintained at 10 K in presence and in absence of H atoms co-deposition . Contrarily to the case of acetonitrile, slopes are very different. For the {CH_3NC+H} experiment, the IR bands are under the noise level. Including error bars, we obtain a reduction factor of more than 87% in the amount of consumed CH_3NC. Moreover, the TPD profiles of pure CH_3NC (blue curve) and remaining CH_3NC (red curve) are obtained after completing both depositions. They are shown in the bottom panel of figure 7.4. Similarly to areas of FT-RAIRS band, the amount of CH_3NC molecules desorbing are reduced from 875 counts.K to 80 counts.K corresponding to a reduction factor of 1 - $\frac{80}{875}$ = 90%. Both FT-RAIRS spectra and TPD profiles provide the same reduction factor for CH_3NC indicating its high consumption by H atoms. It demonstrates that the CH_3NC molecules are reacting efficiently with H atoms on a 10 K surface.

It is not possible to isolate in the IR spectra some growth of bands which would have been characteristic of products. But the IR spectra informs us that whatever is the origins of the products, they are not made from the initial reactants during

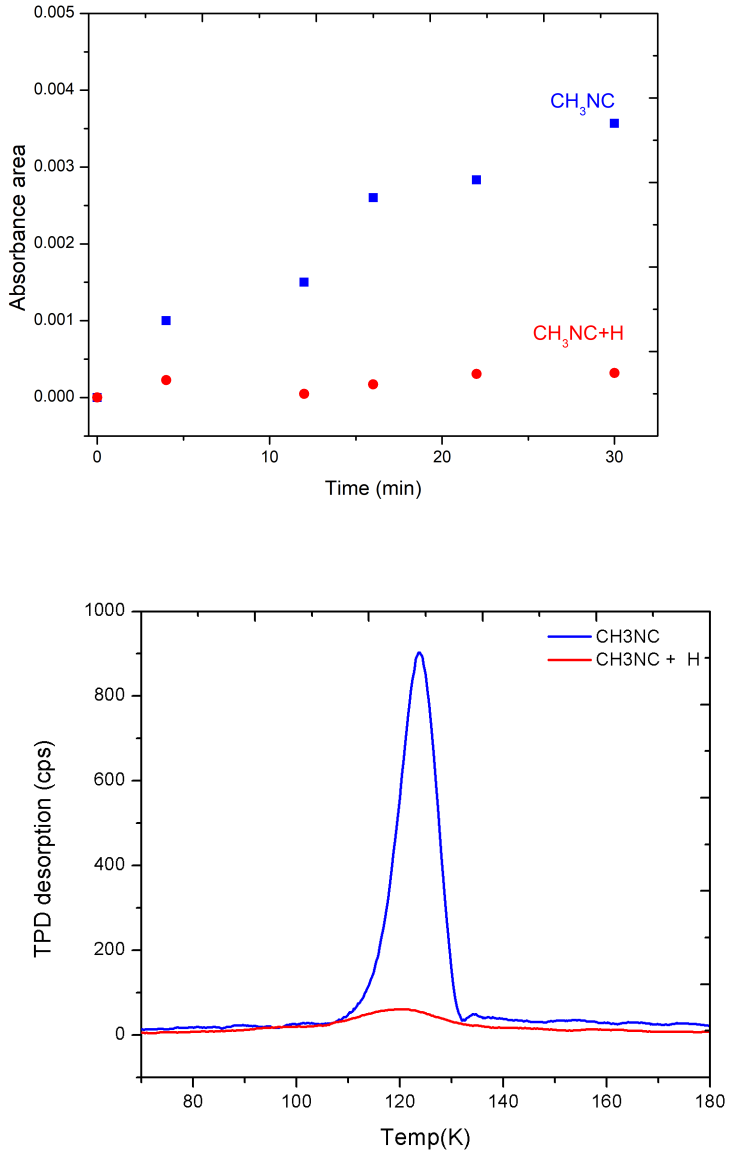

FIGURE 7.4: Top panel: Evolution of the area of the 2176 cm^{-1} IR band of CH_3NC as function of deposition time on the substrate held at 10 K. CH_3NC deposition in blue, and {CH_3NC + H} co-deposition in red. Bottom panel: TPD trace (m/z 41) of pure CH_3NC (blue curve) and the remaining part of CH_3NC (red curve) obtain after the same depositions.

the TPD because they are all consumed at 10 K. Actually, CH_3NC remains undetectable, and H is known to be steadily transformed in H_2 even on a cold surface (Amiaud et al., 2007, Hama et al., 2012, Wakelam et al., 2017) .

Figure 7.5 shows the TPD traces of products which are formed from the reactions between CH_3NC and H atoms. There are 3 successive desorption zones peaking at 105 K, 120 K, and 132 K, indicating at least three different molecules are formed. The first peak (from 87 to 117 K) is dominated by CH_3NCH^+ (mass 42 - dash red curve), which corresponds to one extra H to CH_3NC and the mass 43 (solid red curve) which corresponds to the addition of 2 H atoms. Due to the perfect similarity of the temperature profiles, both peaks comes from the same mother molecule which should be $CH_3NCH_2^+$. In mass spectroscopy, methyl groups -CH_3 are often ionised in -CH_2^+, because -CH_3^+ is a radical and so is less energetically favorable. As examples, the major products of the 70 eV electron impact of methylamine CH_3NH_2 ($m/z = 31$) and methanol CH_3OH ($m/z = 32$), are respectively $m/z = 30$ and $m/z = 31$ (Nist webbook).

The second peak around 120 K is a small signal of CH_3NC (mass 41 - solid blue curve). It is the same peak shown in figure 7.4, but the vertical scale is very different. The peak is slightly shifted toward higher temperatures. It could be the signature of some isomerization, because CH_3CN is desorbing at higher temperature than CH_3NC. However, molecular environment has also changed, because of the presence of others products and the binding energy can be affected and therefore the desorption profiles. So we cannot firmly conclude that there is isomerization, but we can't exclude it.

The last peak from 120 K to 150 K is dominated by mass 44 and 45 which correspond to the reported cracking patterns of dimethyl amine CH_3NHCH_3 so the addition of 4 H atoms to ($CH_3NHCH_3^+$- solid green curve) (see details in Table 7.4 in the discussion section). The bottom panel shows the mass 16 (main peak of methane CH_4 - solid red curve). Its desorption temperature (40-60 K) is typical and very different from other molecules, so there is no doubt about the methane production. If CH_3NC is fragmented during hydrogenation, some correlation with CH_4 and HCN or HNC should be found. The corresponding mass 27 is also shown in blue in the bottom panel of figure 7.5. The temperature of desorption around 130 K could indicate that it is a cracking pattern of dimethylamine, but it is reported in databases and in Table 7.4 that this fragment is only few % of the

major ion, so it is not measurable out of the noise in our experimental conditions. The temperature of desorption corresponds to sublimation of HCN (Theule et al., 2011). So there is no doubt that some fragmentation occurs during the hydrogenation of CH_3NC.

We can sum up the CH_3CN/CH_3NC + H first experimental results through the following statements:

(i) CH_3CN does not react with H atoms at low temperatures.

(ii) CH_3NC reacts with H atoms forming: CH_3NCH_2, CH_3NHCH_3, CH_4, HCN, and possibly CH_3CN.

(iii) We can explain the presence of these products through the following reaction paths:

$$CH_3NC \xrightarrow{+2H} CH_3NCH_2 \xrightarrow{+2H} CH_3NHCH_3 \tag{7.1}$$

$$CH_3NC + 2H \rightarrow CH_4 + HCN/HNC \tag{7.2}$$

$$CH_3NC \xrightarrow{?} CH_3CN \tag{7.3}$$

7.3.3 CH_3NC and its hydrogenation in presence of H_2O.

7.3.3.1 Desorption of CH_3NC mixed with H_2O

Before performing hydrogenation experiments, it is important to determine if water and CH_3NC react together. Indeed, some stable molecules (such as NH_3, CO_2, H_2CO, H_2O_2) are known to undergo activated thermal reactions that may be modified by the presence of water (Theulé et al., 2013, Duvernay et al., 2014, Dulieu et al., 2017).

We apply the protocol described in the experimental section. CH_3NC is injected using the central beam whereas H_2O is grown by background deposition while the surface is maintained at 10 K. The doses correspond to 6 MLs for CH_3NC and 20 MLs for H_2O. However, since the surface deposition of the beam is a diameter of about 3 mm and the total diameter of the gold sample is 9 mm, the water signal is much more intense. Most of the surface of the sample is only covered with water. Still, CH_3NC is perfectly and homogeneously overlapped by H_2O.

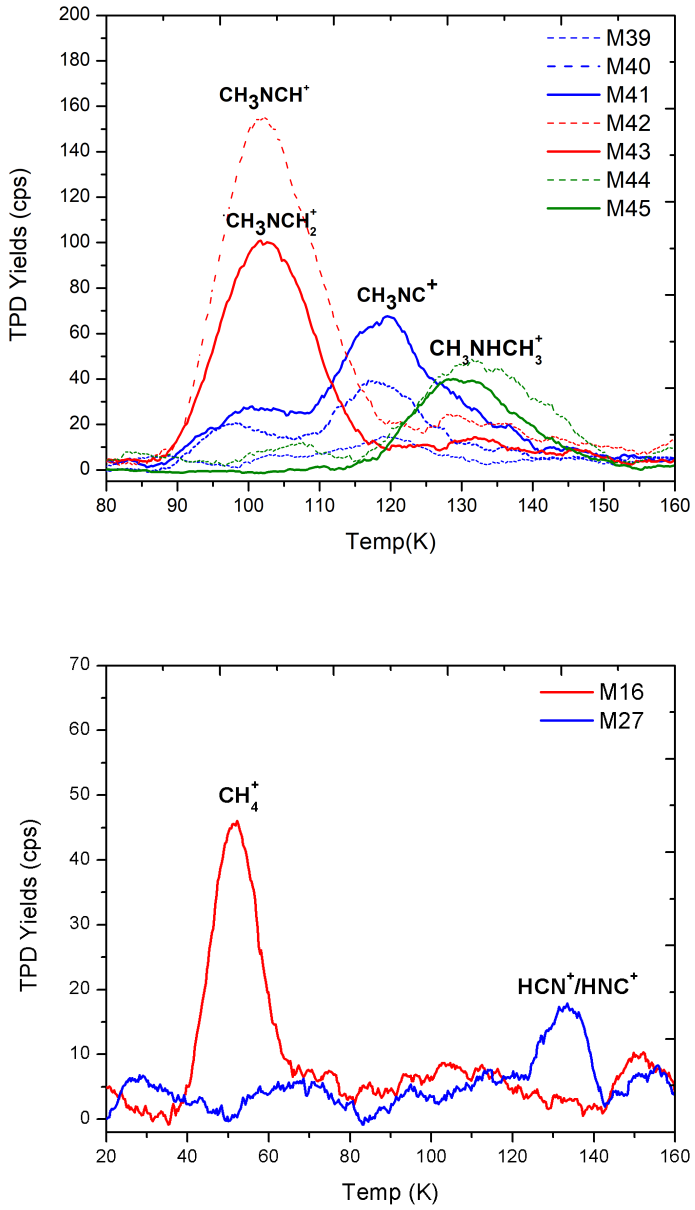

FIGURE 7.5: *Top panel:* TPD traces of $CH_3NCH_2^+$ (m/z 43 - solid red curve) and cracking pattern m/z 42 (CH_3NCH^+-dash red curve) desorb around 90-115 K; remaining CH_3NC^+ (m/z 41 - solid blue curve) and cracking pattern m/z 39 and 40 (dash blue curves) desorb around 110-125 K; finally, dimethylamine ($CH_3NHCH_3^+$) (m/z 45 - solid green curve) and cracking patterns m/z 44 (dash green curve), m/z 43 (solid red curve), and m/z 42 (dash red curve) desorb around 120-145 K. *Bottom panel:* TPD traces of CH_4^+ (m/z 16-red curve) and HCN^+/HNC^+ (m/z 27-blue curve) are formed from other chemical pathways between CH_3NC and H atoms.

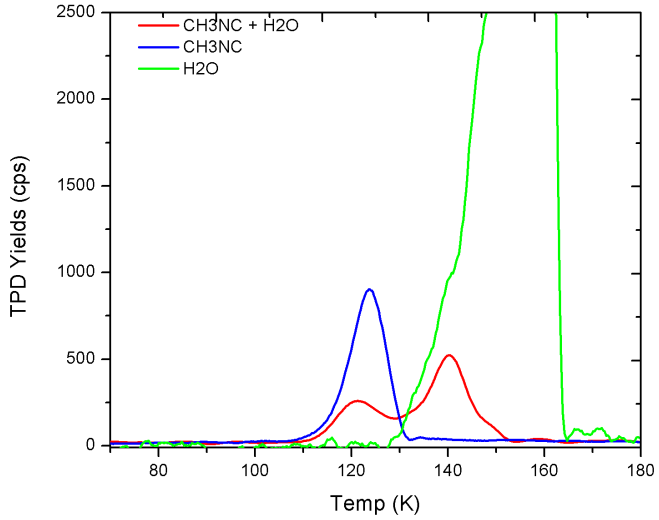

FIGURE 7.6: Desorption profiles of pure CH_3NC (blue curve) and {CH_3NC + H_2O} (red and green curves).

The TPD profiles of the {CH_3NC} and {CH_3NC + H_2O} systems are shown in figure 7.6. In the absence of H_2O, CH_3NC (blue curve) desorption is finished at lower temperature than the desorption of water (measurable in our experimental conditions above 130 K), meanwhile the CH_3NC desorption (red curve) is split in two parts when co-deposited with H_2O. A fraction desorbs before H_2O and the other part is co-desorbing with H_2O. More precisely CH_3NC mostly desorbs during the amorphous desorption phase (Speedy et al., 1996), which occurs before the change in the slope of desorption of water at around 140 K. A smallest and last fraction of CH_3NC is desorbing just after the crystallization. We note no obvious volcano effect, nor desorption after the water, as can be seen for others species and/or substrates (Collings et al., 2004, Chaabouni et al., 2018). It means that a part of CH_3NC is trapped inside H_2O and then it desorbs when released from H_2O. We have calculated the desorption areas of pure {CH_3NC} and {CH_3NC + H_2O} and the ratio gives a factor of 1. It means that CH_3NC does not react with H_2O although CH_3NC is trapped inside H_2O. No indication of reactivity can be addressed for this system.

To sum up the experimental results of the interaction between CH_3NC and H_2O, we give the statements:

(iv) CH_3NC does not react with H_2O.

(v) CH_3NC is trapped and released by H_2O.

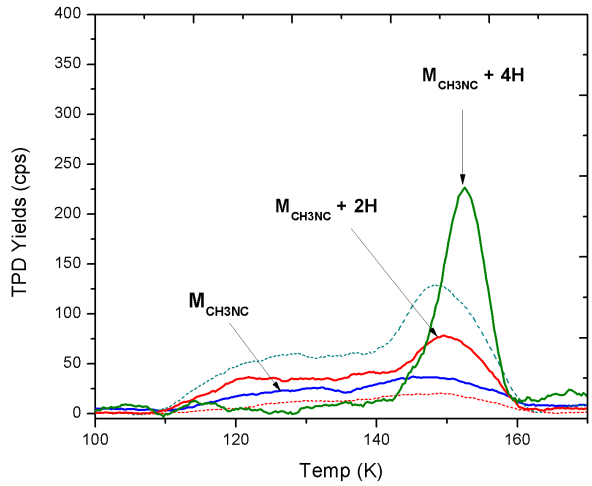

FIGURE 7.7: TPD profiles of the reactivity between CH_3NC and H atoms in the presence of H_2O. CH_3NHCH_3 (M_{CH_3NC} + 4H) (solid green curve) is enhanced after completing the deposition. A part of CH_3NC (M_{CH_3NC} - solid blue curve) and CH_3NCH_2 (M_{CH_3NC+2H} - solid red curve) desorb before H_2O and the other parts are trapped and desorbed with H_2O.

7.3.3.2 Reaction of CH_3NC and H atoms in the presence of H_2O

For this experiment both H (via the right beam) and H_2O (via background deposition) are deposited during 40 minutes, while CH_3NC is only injected 30 minutes. The doses are respectively 6 ML for CH_3NC and 20 ML for H and H_2O.

Figure 7.7 shows the TPD profiles obtained after the reactions between CH_3NC and H atoms in the presence of H_2O. Remnants and products present broad and less featured desorption profiles. This is due to the necessity to diffuse out of the water ice. The dynamic of the desorption of mixed ice is not the purpose of this article. The key observation is that the ratio in the products have changed. Especially CH_3NHCH_3 (solid green curve) is clearly enhanced, dominating all the other products or remnants. We propose in equation 7.1 that the hydrogenation occurs in two main steps, first CH_3NCH_2 and second CH_3NHCH_3. It is clear that in absence of water the hydrogenation is less complete, CH_3NCH_2 being the major product at the end, whereas in the presence of water the second step is easier and complete hydrogenation is more often reached. The fragmentation is still occurring.

The quantitative amounts of the different products or remnants are displayed in table 7.1. They are obtained by calculating the area under the TPD profiles

TABLE 7.1: Percentages (%) of the products and remnants after the deposition of pure CH_3NC, {CH_3NC + H_2O}, {CH_3NC + H} and {CH_3NC + H + H_2O} co-depositions on surface held at 10 K.

Experiment	M_{CH_3NC} (%)	M_{CH_3NC} + 2H (%)	M_{CH_3NC} + 4H (%)	Fragmentation (%)	Isomerization (%)	Total (%)
CH_3NC	100	0	0	0	0	100
CH_3NC + H_2O	100	0	0	0	0	100
CH_3NC + H	15	34	16	7	2	74
CH_3NC + H + H_2O	12	21	35	8	unknown	76

(including cracking patterns as shown in table 7.4). They are normalized to the amount of CH_3NC injected in the first experiment. First of all, we stress that the efficiency of QMS detection is not exactly identical from one molecule to another. It can vary by a few tens of percent for these molecules. It is due to the different ionization cross sections (which can be calculated), but also to the different spatial and kinetic distributions of the different species that desorb (unknown). Even though cracking patterns are included in the estimation, the ratios presented in the table do not exactly represent the species ratio, but they give a good indication. In the same column, the relative error is similar, so if we underestimate or overestimate one species, we do the same way for all the experiments. Therefore it is possible that the total which is less than 100% in case of reactivity experiments, does not represent a real lost of reactants, but more the inaccuracy of the method. However, it could also be due to losses investigated by the chemical desorption process (Dulieu et al., 2013). This aspect will be discussed later. Whatever are the source of uncertainties, the table makes clear that the hydrogenation in presence of water is more efficient. There are less remaining products (12% instead of 15%) and the first measurable step of hydrogenation (CH_3NCH_2) is largely transferred in the second one CH_3NHCH_3.

We can give the following statement for the experiment of CH_3NC and H atoms in the presence of H_2O:

(vi) H_2O has a catalytic role for the hydrogenation of CH_3NC.

7.3.4 Reactivity of CH_3NC and D atoms on the golden surface at 10 K

We have performed deuteration of CH_3NC with D atoms in the same conditions (i.e., surface temperature and molecular dosage).

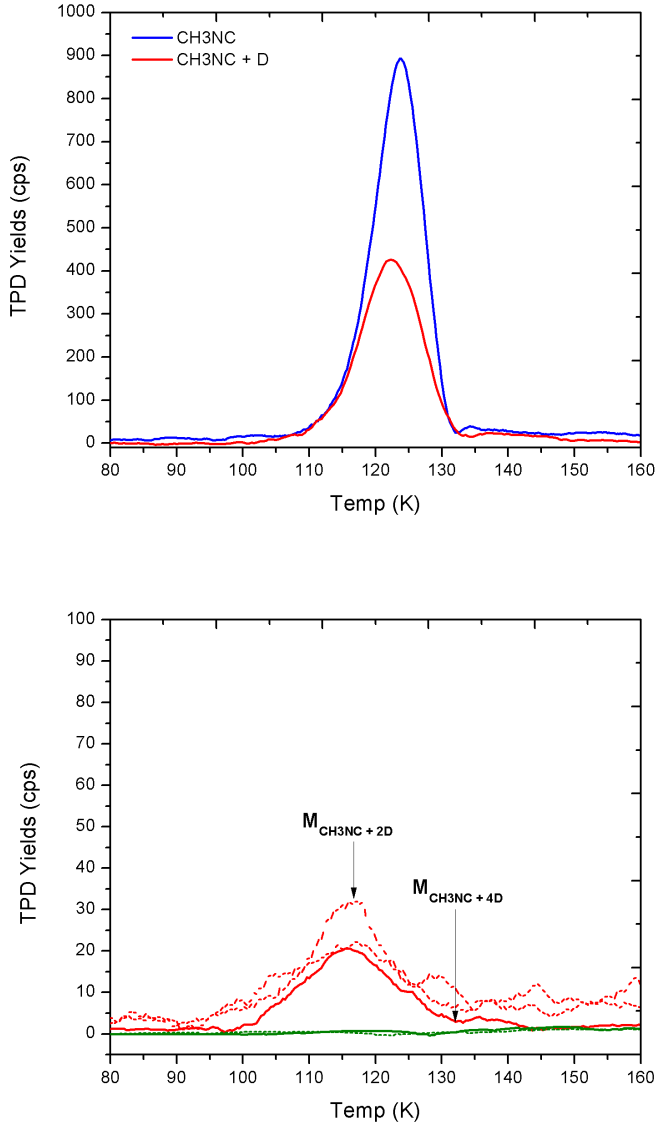

FIGURE 7.8: *Top panel*: Pure CH_3NC (blue curve) and remaining CH_3NC (red curve) after completing the reaction with D atoms at 10 K. *Bottom panel*: TPD traces of mass 45 (M_{CH_3NC} + 2D - solid red curve) and cracking pattern (m/z 43, and 44) (dashed red curves) corresponding to CH_3NCD_2. No traces of CH_3NDCD_3 (M_{CH_3NC} + 4D - solid green curve) are detected.

CH_3NC and D atoms co-deposited during 30 minutes and additional 10 minutes of D atoms exposure is applied. In contrast with H experiments, only $\sim 56\% \pm 6\%$ of CH_3NC is consumed by D atoms. Figure 7.8 shows the comparison between pure CH_3NC (blue curve) and remaining CH_3NC (red curve) after completing the reaction (top panel). Thus, CH_3NC is less reactive with D at low temperature, and the first step of the reaction is far to be complete.

TABLE 7.2: Percentage (%) of remnants (CH_3NC) and products after completing the co-deposition of CH_3NC and H/D atoms at 10 K.

Experiment	M_{CH_3NC} (%)	M_{CH_3NC} +2H(2D) (%)	M_{CH_3NC} + 4H(4D) (%)	Fragmentation (%)	Isomerization (%)	Total (%)
CH_3NC	100	0	0	0	0	0
CH_3NC + H	15.	34	16	7	2	76
CH_3NC + D	56	9	0	4	0	63

The bottom panel of figure 7.8 shows the products obtained after deuteration of CH_3NC. The first step of the deuteration can be seen through the parent mass 45 corresponding to CH_3NCD_2 and is desorbing around 115 K. Cracking patterns of m/z 43, 44, are also present, and of about the same intensity. On the contrary the trace for m/z 46, 47 corresponding to Dimethylamine (CH_3NDCD_3) and its fragmentations are undetectable. Moreover, the fragmentation pathway is observed and some CH_3D (m/z 17) and DCN (m/z 28) are detected. The quantitative analysis is displayed in table 7.2.

We can describe the chemical network of {CH_3NC + D} atoms with the reactions:

$$CH_3NC + 2D \rightarrow CH_3NCD_2 \tag{7.4}$$

$$CH_3NC + 2D \rightarrow CH_3D + DCN/DNC \tag{7.5}$$

From the present set of the {CH_3NC + D} experiment, we summarize our finding:

(vii) Deuteration of CH_3NC is uncomplete at low temperatures.

(viii) D atoms have an entrance activation barrier.

7.3.5 Reactivity of CH_3NC and H atoms at various temperatures.

We have seen earlier that CH_3NC can be almost fully consumed by H atoms at 10 K whereas it is not the case with D atoms, implying that it exists an entrance activation barrier, which crossing is slower for D atoms. Surface reactivity is actually a kinetic competition between many different reactive pathways, the most important in the case of hydrogenation being the self reaction H+H $\longrightarrow$ H_2. Thus by changing the surface temperature, we can change the kinetics and see how the products are affected.

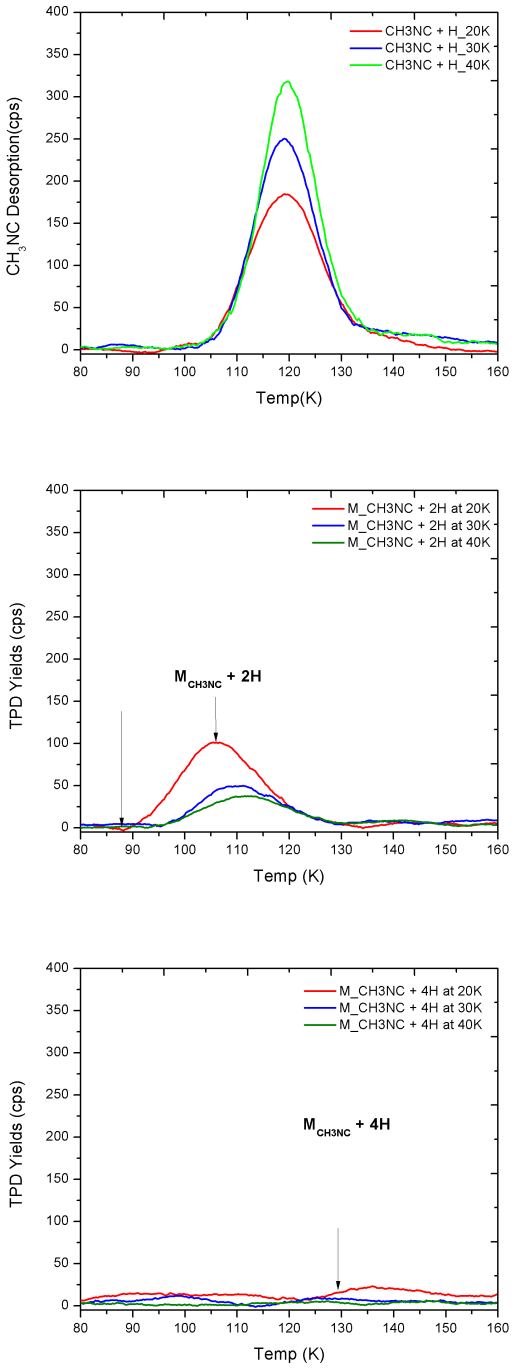

FIGURE 7.9: *Top panel:* Remaining CH_3NC (from red to green curves) after completing the reaction with H atoms on the surface with the temperature is ranging from 20 K to 40 K. *Middle panel:* TPD traces of CH_3NCH_2 (M_{CH_3NC} + 2H) (from red to green curves) are gradually reduced with the surface temperature. *Bottom panel:* The trace of Dimethylamine (CH_3NHCH_3 - M_{CH_3NC} + 4H) is not detectable at high temperatures.

TABLE 7.3: Percentages (%) of the products and remnants after completing the depositions at different surface temperatures

Temperature (K)	M_{CH_3NC} (%)	M_{CH_3NC} + 2H (%)	M_{CH_3NC} + 4H (%)	Fragmentation (%)	Isomerization (%)	Total (%)
10	15	34	16	7	2	74
20	37	20	7	6	3	73
30	42	9	0.3	4	3	58.3
40	52	8	0.0	1.4	0	61.4

The top panel of figure 7.9 shows the remaining CH_3NC at different surface temperatures after completing the same {CH_3NC+H} co-depositions. The remaining CH_3NC increases with the surface temperature. The products are shown in the middle and bottom panels. CH_3NCH_2 yield decreases when the surface temperature increased as well as for CH_3NHCH_3 which becomes undetectable above 20 K on TPD profiles. The table 7.3 displays the quantitative values.

We point out that the consumption of reactants is different at 30 K and 40 K (respectively 58% and 48%), whereas the product yield (CH_3NC + 2H) is about the same (9% and 8%).

We can give a statement for this experimental results:

(ix) At higher temperatures, the reaction between CH_3NC and H atoms is reduced because of the activation barriers.

7.4 Analysis and Discussion

7.4.1 Activation barrier and quantum tunneling

In our experimental conditions, barrier-less entrance reactions such as NO+H$\longrightarrow$ HNO can lead to a high degree (>90%) of consumption of reactants, even at surface temperatures above 20 K (Congiu et al., 2012c). So as mentioned earlier, incomplete reaction can be the signature of an entrance barrier.

The reduction of the consumption of CH_3NC with the temperature is due to the enhancement of the H diffusion and so of the main competitive reactive channel H+H$\longrightarrow$ H_2. Moreover at 20 K and higher the evaporation rate of H also limits all hydrogenation reactions especially those with an activation barrier. Another

possibility to explain an incomplete reaction, even with barrier-less reactions would be that it exists a chemical loop. For example, CH_3NC +H $\longrightarrow$ CH_3NCH could be followed by the abstraction reaction CH_3NCH + H $\longrightarrow$ CH_3NC + H_2. This abstraction reactions (and substitution in case of isotopic studies) are common, especially for the case of methyl groups (Oba et al., 2014). But this would not explain why D reactivity is so low in comparison to H. The best explanation is that the crossing of the barrier is done through quantum tunneling, so the mass difference between H and D, makes a large difference in the crossing probability.

7.4.2 The catalytic role of H_2O for chemical reactions

The enhancement of the hydrogenation of CH_3NC in presence of water can be due to different properties:

(i) Water, by enlarging the physical surface because of its 3 dimensional network dilutes the H surface concentration. In other words there are more adsorption sites, so less H atoms in average on each of them. So the H_2 formation, which is a function of the square of H surface density has a relative lower efficiency in regard to reactions having only one H as reactant.

(ii) Water can change the geometrical orientation of CH_3NC. In terms of quantum chemistry, it may affect the geometry of the reaction and so lower the reaction barrier.

(iii) Water can also slightly change the geometry of the molecule CH_3NC itself, and/or displace slightly charges changing reaction barrier's height.

(iv) Water can participate by helping proton transfer (Rimola et al., 2014)

Only quantum chemistry can give answer to this observations.

7.4.3 Orientation of CH_3NC at different surface temperatures

We may change the orientation of CH_3NC with the surface temperature (Murphy et al., 2000). We assume that the (-NC) bonds moves on the orientation with the surface temperature. Figure 7.10 displays the schematic top-view of the orientation

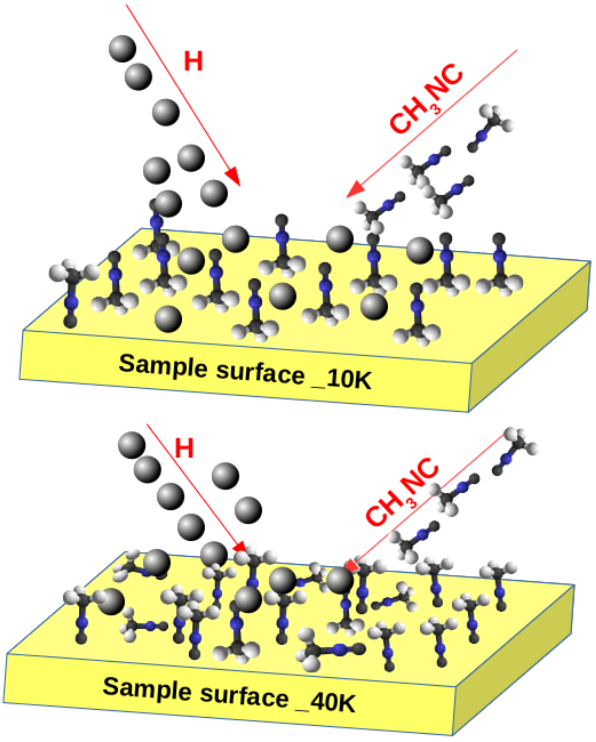

FIGURE 7.10: Schematic top-view of the orientation of the CH_3NC molecules which are deposited on the golden surface maintained at 10 K (top panel) and 40 K (bottom panel).

of CH_3NC which is deposited on the golden surface maintained at 10 K (top panel) and 40 K (bottom panel). Even if (-NC) bond group is orientated perpendicular to the surface through CH_3 symmetry or parallel to the surface (Bertin et al., 2017b) at low temperatures. Thus, the exposition and reaction between CH_3NC and H atoms easily take place and achieve the high efficiency. On the contrary, the (-NC) bond can be changed the orientation and the (-NC) group might be perpendicular directly to the surface at higher temperatures. Therefore, the exposition with H atoms may be prevented to CH_3NC by surface leading to the reaction limitation.

A remark about the chemical network of CH_3NC at high temperatures.Chemical reactions are limited, resulting in less interaction due to evaporation and bond orientation (-NC).

7.4.4 Astrophysical implications

The very different reactivity of CH_3NC and CH_3CN is a possible explanation for the observed ratio of CH_3NC and CH_3CN factor of 0.03-0.05 (Cernicharo et al.,

1988), which is less than expected by pure gas phase routes. Indeed, CH_3NC and CH_3CN have a different fate on the surface of grains. CH_3NC will likely evolved under hydrogenation, whereas CH_3CN is unaffected by the main chemical driving force for surface reactivity in molecular clouds. So, if part of the mantle is feeding the gas phase, as it occurs in shocks or hot cores, thus chemical differentiation on grains can induce differences in the gas phase.

Under astrophysical conditions, the flux of H atoms is orders of magnitude lower than in our experimental conditions. Therefore, the H concentration on the surface is also lower, and therefore the H+H $\longrightarrow$ H_2, is less competitive than in our experimental conditions. We have seen that even under our "high" flux conditions, hydrogenation of CH_3NC is efficient, so it should also be the case in dense molecular clouds. On the contrary, if the temperature of the grain raise above 20 K, thus the hydrogenation efficiency drops and dimethyl amine have probably no chance to be formed this way.

7.4.5 New estimation of the cracking patterns and of the binding energy of CH_3NCH_2

There are no reported values for CH_3NCH_2, nor binding energy of this molecule. We provide here the missing information. Taking a regular first order Arrhenius law for desorption with a pre-exponential factor (Chaabouni et al., 2018) fixed at A= 10^{12} s^{-1}, we find a good fit for the binding energy $E_b = 3200 \pm 100$ K/k_b, where k_b is the Boltzman constant.

7.5 Summary and conclusion

In this work, we investigated the chemical networks of the hydrogenation of CH_3CN and CH_3NC in the presence or absence of H_2O. CH_3CN does not react with H atoms at low temperatures, whereas CH_3NC reacts with H atoms forming CH_3NCH_2, CH_3NHCH_3, CH_4, HCN, and possibly CH_3CN. In the presence of H_2O, CH_3NC does not react with H_2O but it is trapped and released by H_2O. Furthermore, H_2O acts as a catalyst for the hydrogenation of CH_3NC. On the contrary to hydrogenation, deuteration of CH_3NC is uncompleted at low temperatures and the entrance activation barrier prevents the deuteration of CH_3NC.

TABLE 7.4: Intensities of CH_3NC, CH_3CN, and products after completing the reactions with H atoms. Comparison between NIST Chemistry webbook data and our experimental results

Mass	CH_3NC (%)		CH_3CN (%)		CH_3NCH_2 (%)		CH_3NHCH_3 (%)	
	NIST	Work	NIST	Work	NIST	Work	NIST	Work
M16	0	0	0	0	0	0	1	0
M27	5	0	1	0	-	0	2	2
M39	20	20	20	20	-	1	0	0
M40	50	60	40	40	-	10	3	0.5
M41	100	100	100	100	-	15	3	2
M42	0	0	0	0	-	100	19	20
M43	0	0	0	0	-	65	15	15
M44	0	0	0	0	0	0	100	100
M45	0	0	0	0	0	0	65	75

When the hydrogenation of CH_3NC takes place at high temperatures, the reaction between CH_3NC and H atoms is reduced because of the activation barriers. In molecular clouds, CH_3NC and CH_3CN have the different destiny. CH_3NC will be likely evolved under hydrogenation, whereas is unaffected by the main chemical driving force for surface reactivity in molecular clouds.

Chapter 8

Conclusions and perspectives

8.1 Remarks and Astrophysical implications

Formation of complex organic molecules (COMs) in the interstellar medium (ISM) is the result of the cumulative outcome from many chemical processes on grains as well as in the gas phase. The formation of COMs is still an open question and makes exciting the debate about pathways of their origin (Herbst and van Dishoeck, 2009b).

VENUS has been used to carry out all experiments in this thesis. VENUS is a convenient tool to investigate complex chemistry on grains. Experimental conditions are mimicking the astrophysical environments such as low temperatures (8 K up to 40 K) and the presence or absence of H_2O. There can be 2-3 molecular species deposited and interacted at the same time on the sample surface because of the separated four beamlines system, that allows us study complex chemical reactions on grains.

This thesis presents an experimental study of solid-state molecular physics. On grains, COMs mostly are formed via the hydrogenation on grains such as the formation of hydroxylamine (Congiu et al., 2012a, Fedoseev et al., 2012) or the formation of H_2CO and CH_3OH via the hydrogenation of CO (Fuchs et al., 2009, Hidaka et al., 2007, Watanabe et al., 2004, Minissale et al., 2016) or the formation of NH_3 via the hydrogenation of nitrogen (Hiraoka et al., 1995, Fedoseev et al., 2015). However, hydrogenation on grains is very complex because of some reasons. Sometimes, the back reaction takes place in chemical chains such as hydrogenation

of HNCO (HNCO $\xrightarrow{+H}$ H_2NCO $\xrightarrow{+H}$ HNCO + H_2) (Noble et al., 2015). Competitive mechanisms (i.e fragmentation and isomerization) occur in the chemical reactions of the hydrogenation of CH_3NC or too high barrier like for the reaction [CH_3CN + H]. Additional, cycling mechanism can promote some chemical pathways such as the formation of NH_2CHO via the combination between H_2CO and the hydrogenation of NO ({NO + H} $\rightarrow$ NHOH $\xrightarrow{+H_2CO}$ NH_2CHO + OH). Maybe it is one of the reasons why NH_2OH is not observed on interstellar grains. On the other hand, the competition of many routes or rates influence the efficiency of the hydrogenation. For instance, low temperatures and the presence of H_2O enhance the hydrogenation, whereas the chemical desorption reduces the efficiency of the hydrogenation such as H_2NO $\xrightarrow{+H}$ NH_2OH $\xrightarrow{+H}$ NHOH + OH. H_2O can be considered as a catalyst with different roles that are a physical or chemical catalyst. H_2O may be a physical catalyst by changing H mobility or changing position reactants and its role can be a chemical catalyst by exchanging proton or changing barriers. A remarkable point is that nitrogen, oxygen, and carbon can be linked on grains via H_2CO and NO which are considered to be two precursors in the interstellar medium.

In chapter 3, we have studied the segregation effect and CO-N_2 systems adsorbed on water ice substrates (compact amorphous solid water, porous amorphous solid water, and crystalline ice). N_2 and CO co-adsorbed on an amorphous surface show very different desorption behavior when mixed than when adsorbed separately. We derived the distribution of binding energy and put in the evidence that a segregation mechanism is at play. If N_2 and CO are taken as pure species, the shape of their binding energy distribution, as a function of coverage, is similar. When they are mixed, N_2 is pushed out of the highest energy adsorption sites, thus nitrogen is forced to almost completely leave the surface before CO begin to desorb. Therefore, N_2 and CO may deplete differently on grains.

In chapter 4, we have dealt with the hydrogenation of NO on interstellar dust grains. We have carried out the co-deposition of {NO + H} (or D) on the sample surface maintained at 10 K or 40 K. We have demonstrated that a barrier exits at the entrance of the reaction HNO + H. However, H atoms can efficiently cross the barrier via quantum tunneling at temperatures of 8 K - 15 K. There are 9 reactions that happen in the chemical network of the hydrogenation of NO. The main product of the hydrogenation of NO is hydroxylamine (NH_2OH) on the cold surface at low temperatures. NH_2OH is detected on grains in experiments but its

non-detection in astrophysical ices or in the gas phase, it is still an open question. At high temperatures, N_2O is the major products instead of NH_2OH because of the activation barrier and conjugated action and the evaporation of H atoms from the sample surface.

In chapter 5, we have studied the efficiency of atoms to penetrate into the ice bulk for the outer surface of amorphous solid water. We presented an experimental estimate of bulk diffusion energies of oxygen and deuterium atoms on and through porous amorphous water ice. NO is used as a chemical tracer and is deposited on the sample surface held at 10 K or 40 K. It is subsequently covered by a variable amount of water ice. Then we exposed to D (10 K) or O (40 K) atoms. Water ice limits the destruction of tracer of NO molecules. The thicker the ice, the more NO remains unreacted. We found a lower limit for bulk diffusion of 950 K and 280 K for O and D, respectively, and an $E_{diffbulk}$ /$E_{diffsurf}$ $\geqslant$ 1.3 in both cases. The surface diffusion followed by reaction with NO or by self reaction is faster than bulk diffusion. We propose lower limit values for penetration barriers. Therefore the building of astrophysical ice mantles should be mostly driven by surface reactivity.

For chapters 6 has been devoted to the experimental study of the formamide formation and the efficient formation of formamide routes of the pre-biotic formamide on interstellar dust grains. We have investigated the chemical pathways of formamide through the co-deposition of two molecular precursors (i.e NO and H_2CO) on the grain surface maintained at 10 K. Formamide is formed through the hydrogenation of NO on the presence of H_2CO via the reactions: NHOH + H_2CO and NH_2O + H_2CO or NH_2CHO + H. The yield of formamide is enhanced by the presence of H_2O because radicals NHOH and NH_2O are favoured in the process. Hence H_2O is a catalyst in the chemical pathway leading to formamide. While NH_2OH and CH_3OH are the major products of the chemical networks of the hydrogenation of NO and H_2CO, formamide is formed more efficiently than methanol (CH_3OH) when NO and H_2CO are co-deposited on ASW surface held at 10 K. The existence of an effective and direct mechanism of formamide formation in the solid phase, without the use of transformation/energy mechanisms, supports the argument that cometary materials have strong and direct chemical links with their possible interstellar matrix.

The last chapter has presented the chemical reactions of the hydrogenation of methyl isocyanide (CH_3NC) and its isomers (CH_3CN) on the cold surface held at various temperatures. We demonstrated that CH_3NC reacts with H atoms,

whereas CH_3CN does not. CH_3CN can therefore be stored on grains. The chemical network of CH_3NC consists in different mechanisms (i.e hydrogenation, fragmentation, and isomerization). These mechanisms are competitive and the yields and efficient pathways are changing. Furthermore, we have demonstrated that activation barriers exist. However, H atoms can overcome barriers by tunnel effect to form some COMs such as CH_3NCH_2 and CH_3NHCH_3. The hydrogenation of CH_3NC is enhanced in the presence of H_2O, whereas the other mechanisms are not. On the other hand, some chemical reactions are prevented when the surface temperature increases. At high temperatures, the relative efficiency of reactions is lower. So products especially CH_3NCH_2, CH_4, and HCN/HNC are reduced because of activation barriers, while CH_3NHCH_3 is no longer formed.

8.2 Perspectives

Mantle surface: Because substrate is changing the balance of the chemical routes, we would need to work with different mantle surfaces such as CO rich or CO_2/H_2O matrix.

Fluxes ratio: How the efficiency of chemical networks does transpose to real grains? In order to investigate the influence of physical and chemical conditions as well as the low limit of astrophysical rates, we should estimate the efficiency of reactions by changing the flux ratio of H atoms (more or less fluxes) or the fluxes of other species.

Proton exchange: In order to probe the role of water, we can investigate the proton exchange by doing experiments at high temperatures (60 K up to 140 K).

Appendix A

Efficient formation route of the pre-biotic molecule formamide on interstellar dust grains

A.1 NO, H_2CO, and H atoms co-deposit on porous amorphous solid water ice

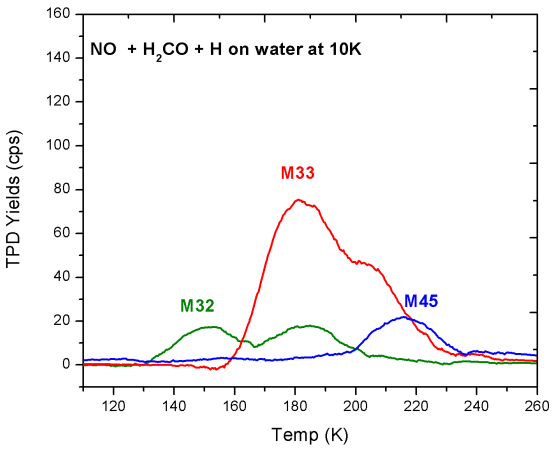

FIGURE A.1: TPD profiles of methanol (m/z=32), NH_2OH (m/z=33), and NH_2CHO (m/z=45) after co-deposition of {NO+H_2CO+H} on porous-ASW ice at 10 K.

Appendix B

Scientific material to be included in a forthcoming article/chapter

B.1 List of discussed experiments

Table B.1 displays all the experiments relative the study for the formation of formamide. Experiments are carried out on gold surface or in the presence of water ice substrate maintained at 10 K or 40 K.

Table B.1: List of discussed experiments

Experiment	Thickness (ML)	Substrate	T_{dep} (K)
{NO+H}	5	gold	10
{H_2CO + H}	5	gold	10
{NO+H_2CO+H}	5	gold	10
{NO + D_2CO + D}	7.5	gold	10
{NO+H_2CO+H}	5	gold	40
{NH_2OH} + {H_2CO}	5	gold	10
{NO} + {H_2CO + H}	5	gold	10
{H_2CO} + {NO+H}	5	gold	10
{NO+ H_2CO + H}	5	porous ASW	10
{NO+H_2CO+H}	5	porous ASW	40

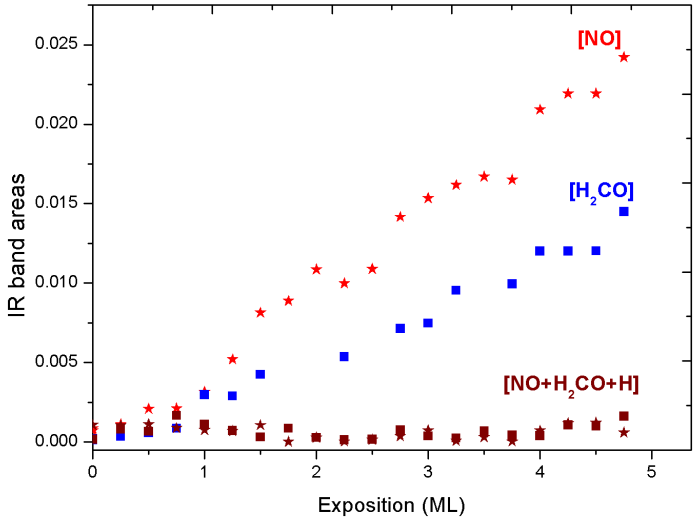

FIGURE B.1: Integrated areas of IR bands of pure NO (red stars), pure H_2CO (blue squares) compared to remaining NO and H_2CO (brown stars and squares) that are obtained during the exposure time of H atoms on the gold surface maintained at 10 K. The consumptions of NO and H_2CO (brown stars and squares) indicate that the co-hydrogenation of NO and H_2CO are complete reactions.

B.2 Experimental results

B.2.1 NO, H_2CO, and H atoms co-deposit on the golden surface maintained at 10 K

Figures B.1 displays the integrated areas of IR bands during exposure time of H atoms. Figure B.2 shows the TPD profile obtained after co-deposition {NO + H_2CO + H} on the golden surface maintained at 10 K. The layer thickness is grown up to 5 ML.

B.2.2 NO, D_2CO, and D atoms co-deposit on the golden surface maintained at 10 K

Figure B.3 displays the TPD trace after co-deposition {NO + D_2CO + D} on the golden surface held at 10 K. In this case, these reactants are grown up to 7.5 ML.

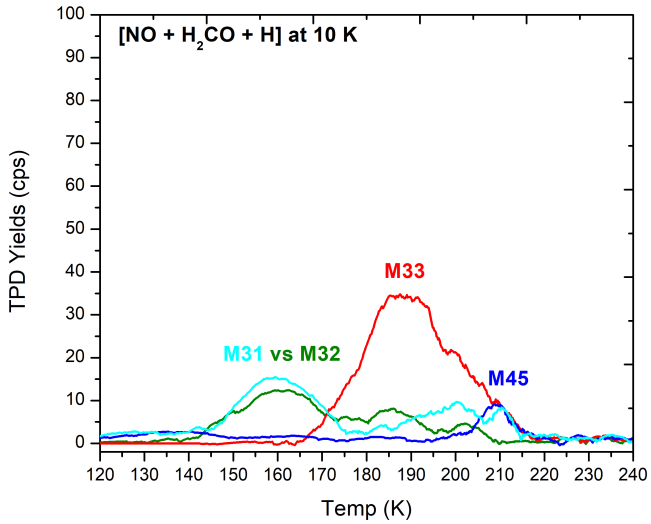

FIGURE B.2: TPD profiles obtained after co-deposition {NO + H_2CO + H} on the golden surface maintained at 10 K. TPD masses *m/z* 31 and 32 (first peaks - cyan and green curves) represent methanol (CH_3OH) desorbing from around 140-170 K. Mass 33 (red curve) is the trace of hydroxylamine desorbing from around 160-210 K. The second peaks of masses 31 and 32 are the cracking pattern of hydroxylamine (M33). The trace of NH_2CHO (*m/z* 45 - blue curve) desorbs around 190-230 K.

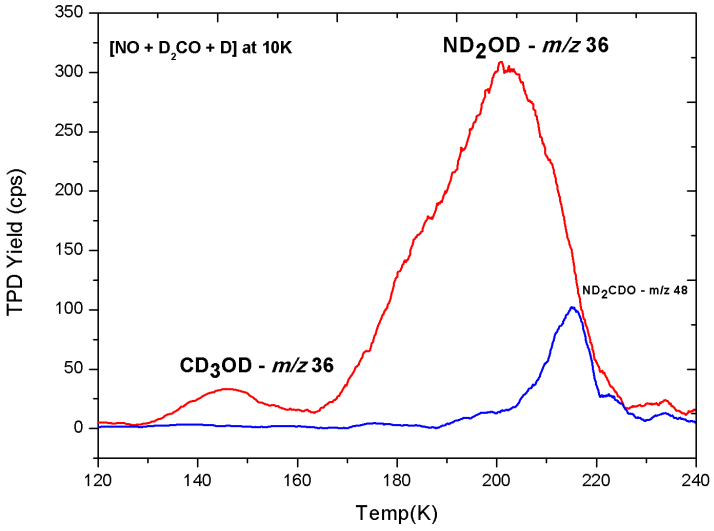

FIGURE B.3: TPD profiles obtained after co-deposition {NO + D_2CO + D} on the golden surface held at 10 K. Mass 36 (first peak-red curve) represents the trace of CD_3OD desorbing from around 130-160 K. The second peak of mass 36 is the trace of ND_2OD desorbing from around 160-210 K. Deuterated formamide (ND_2CDO) (m/z 48-blue curve) desorbs around 190-230 K.

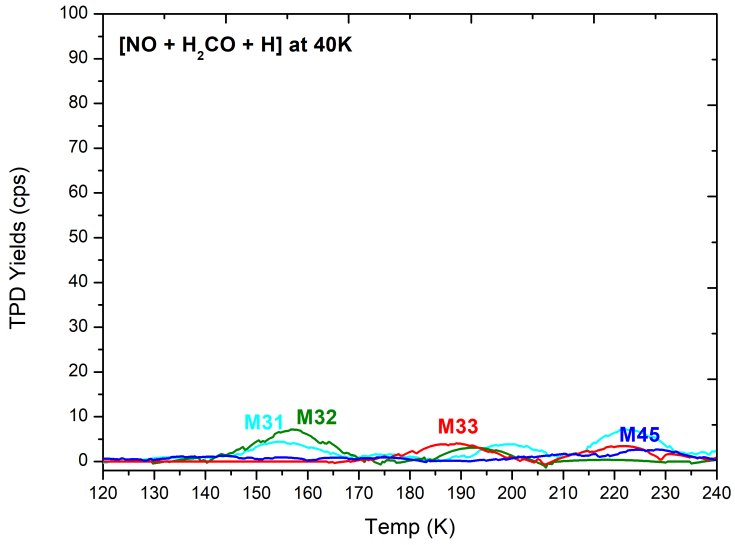

FIGURE B.4: TPD profiles obtained after co-deposition {NO + H_2CO + H} on the golden surface maintained at 40 K. The trace of CH_3OH (m/z 31 - cyan curve), NH_2OH (m/z 33 - red curve), and NH_2CHO (m/z 45 - blue curve) are mostly reduced. Excepting mass 32 (green curve), it may represent both of the traces of CH_3OH or the cracking pattern of (N_2ONO_2) formed in sub-reactions of the {NO+H} chemistry at 40 K.

B.2.3 NO, H_2CO, and H atoms co-deposit on the golden surface maintained at 40 K

Figure B.4 shows the TPD trace obtained after co-deposition {NO + H_2CO + H} on the golden surface held at 40 K. The traces of products (i.e. CH_3OH, NH_2OH, and NH_2CHO) are mostly reduced at 40 K.

B.2.4 Efficiency of layered experiments

Figure B.5 displays the TPD trace of the layer {NH_2OH + H_2CO} system on the golden surface held at 10 K. Figure B.6 presents the normalisation NH_2CHO produced in the layered experiments: H_2CO on top of the NO layer (case B); NO on top of the H_2CO layer (case C) comparing to co-deposition on the golden surface held at 10 K (case A).

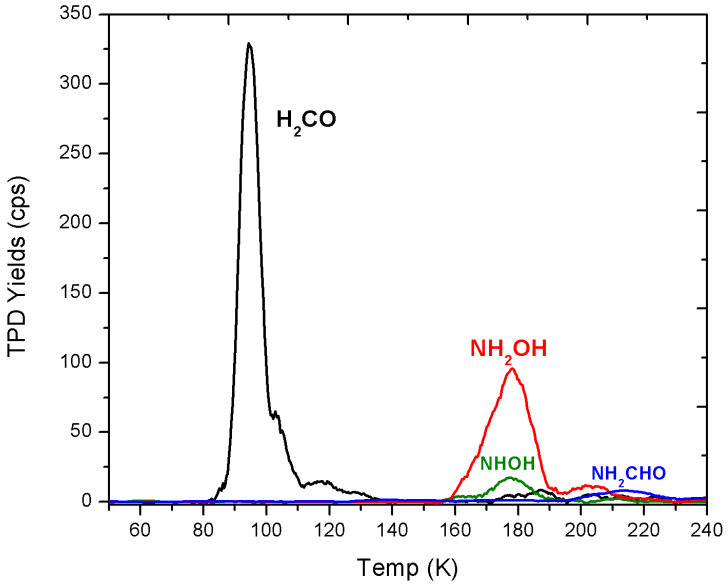

FIGURE B.5: TPD traces obtained by depositing to 5 ML of H_2CO on top of one NH_2OH layer held at 10 K. The NH_2OH layer is produced by co-depositing {NO + H} on the surface at 10 K, and then the surface is annealed to 160 K for releasing other species (i.e N_2O, NO, and H) into the gas phase. The surface temperature is cooled down to 10 K before depositing H_2CO on top of the NH_2OH layer. H_2CO (black curve), NH_2OH (red curve) and cracking pattern NHOH (green curve) remain large, whereas the trace of NH_2CHO (blue curve) is very tiny after completing the exposure. NH_2OH should be accompanied of sense NHOH radicals due to the back reaction.

B.2.5 Co-deposition {NO + H_2CO + H} on porous water ice substrate maintained at 10 K or 40 K

Figures B.7 and B.8 display the TPD profiles obtained after completing the co-deposition on porous water ice held at 10 K and 40 K. NH_2OH and NH_2CHO are enhanced compared to the gold substrate held at 10 K and 40 K. It demonstrates that H_2O enhances the chemical reaction efficiency.

B.2.6 Table of radical reactions

Table B.2 presents the possible reactions between the intermediates and products of NO hydrogenation (vertical) and H_2CO hydrogenation (horizontal) on the grain surface for the formation of NH_2CHO.

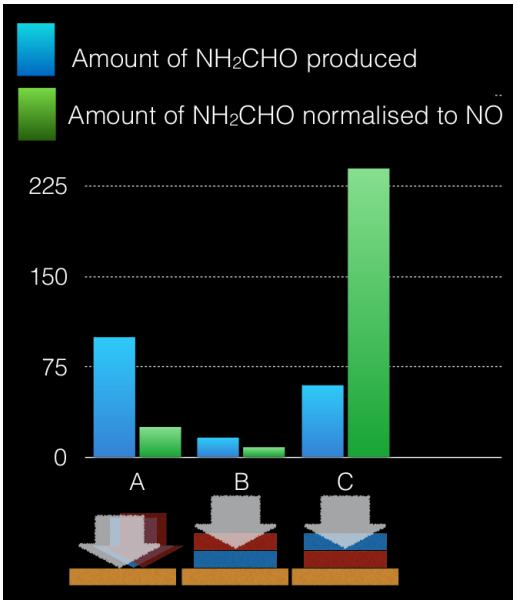

FIGURE B.6: Normalization of NH_2CHO produced: case A) Co-deposition {NO + H_2CO + H}; case B) {H_2CO + H} on top of the layer NO; case C) {NO + H} on top of the layer H_2CO. Amount of NH_2CHO (blue columns) produced in these experiments; Amounts of NH_2CHO (green columns) is normalised to NO. The formation route of NH_2CHO is driven by the hydrogenation of NO in presence of H_2CO, whereas the H_2CO hydrogenation in the presence of NO is not efficient.

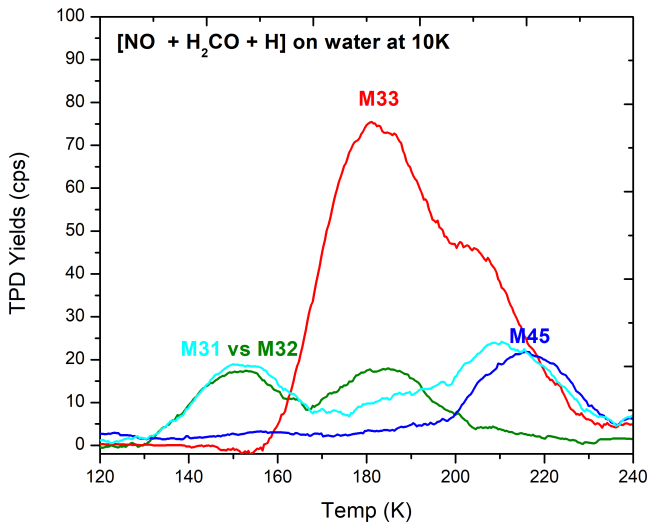

FIGURE B.7: TPD traces obtained after completing the co-deposition on porous water ice substrate held at 10 K. NH_2OH (red curve) and NH_2CHO (blue curve) are enhanced in the presence of H_2O comparing to the gold substrate.

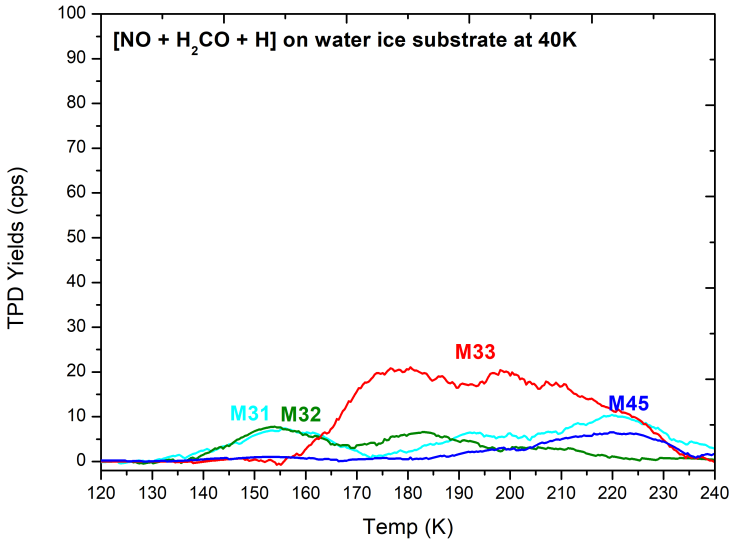

FIGURE B.8: TPD profiles obtained after co-deposition {NO + H_2CO + H} on porous water ice substrate held at 40 K. NH_2OH (red curve), CH_3OH (green curve), and NH_2CHO (blue curve) are raised in the presence of H_2O comparing to the gold substrate held at 40 K.

TABLE B.2: Possible reactions between the intermediates and products of NO hydrogenation (vertical) and H_2CO hydrogenation (horizontal) on the grain surface for the formation of NH_2CHO.

	CO	HCO	H_2CO	CH_3O	CH_3OH
NO	R1A	R1B	R1C	R1D	R1E
HNO	R2A	R2B	R2C	R2D	R2E
H_2NO	R3A	R3B	R3C	R3D	R3E
NH_2OH	R4A	R4B	R4C	R4D	R4E
H_2O	R5A	R5B	R5C	R5D	R5E
OH	R6A	R6B	R6C	R6D	R6E
N_2O	R7A	R7B	R7C	R7D	R7E

After analysing all the experiments, we propose that the formation of formamide should form the reaction R4C:

$$H_2CO + H_2NO \longrightarrow NH_2CHO + OH. \tag{B.1}$$

$$H_2CO + NHOH \longrightarrow NH_2CHO + OH \tag{B.2}$$

B.3 Conclusion

In our experimental conditions, we have investigated the possible chemical pathways of the co-hydrogenation of NO and H_2CO on the grain surface maintained at 10 K or 40 K. At 40 K, chemical reactions are less and products are also reduced. At 10 K, formamide is produced via the chemical reactions of reaction B.1 (H_2CO + NH_2O $\longrightarrow$) and reaction B.2 (H_2CO + NHOH $\longrightarrow$). In the presence of H_2O, the efficiency is raised and the NH_2CHO yield is enhanced on the porous water ice substrate at 10 K and 40 K. Therefore, H_2O has the catalytic role in chemical reactions for the formation of NH_2CHO.

Appendix C

List of publications and conferences

C.1 List of publications

1) **Thermal Desorption of Formamide and Methylamine from Graphite and Amorphous Water Ice Surfaces**. Chaabouni, H., S. Diana, T. Nguyen, and F. Dulieu. Astronomy & Astrophysics 612 (April),2018. EDP Sciences: A47.Doi:10.1051/0004-6361/201731006.

2) **Segregation effect and N_2 binding energy reduction in CO-N_2 system adsorbed on water ice substrates**. T.Nguyen, S.Baouche, E.Congiu, S.Diana, L.Pagani, and F.Dulieu. 2018. Astronomy & Astrophysics (August). Doi: 10.1051/0004-6361/201832774.

3) **Study of the penetration of oxygen and deuterium atoms into porous water ice.** M.Minissale, T.Nguyen, and F.Dulieu. 2018. Submitted to Astronomy & Astrophysics (2018).

4) **Efficient formation route of the pre-biotic molecule formamide on interstellar dust grains.** F.Dulieu, T.Nguyen, E.Congiu, S.Baouche, V.Taquet. To be submitted to Astronomy & Astrophysics.

C.2 List of conferences

C.2.1 Contributed talks

1) **Blowing in the wind** conference, 7th – 13th August 2016, Quy Nhon, Vietnam.

Title: CO and N_2 differential depletion in pre-stellar cores: Experimental study of N_2 desorption induced by the presence of CO on ices.

2) **Journée de l'Ecole Doctorale Science et Ingénierie 2018** , 14th May 2018, Neuville site, University of Cergy Pontoise, France.

Title: Experimental study of the chemical network of methyl Isocyande (CH_3NC) on interstellar dust grains.

3) **Journée Labex Michem 2018**, 5th June, 2018, Sorbonne University, Paris, France.

Title: Experimental study of the chemical network of methyl Isocyande (CH_3NC) on interstellar dust grains.

C.2.2 Contributed posters

1) **Star formation in Different Environmen**t conference, 25th – 29th July 2016, Quy Nhon, Vietnam.

Title: CO and N_2 differential depletion in pre-stellar cores: Experimental study of N_2 desorption induced by the presence of CO on ices.

2) **Complex Organic Molecules in Space** conference, 8th – 10th February 2017, Neuville site in University of Cergy Pontoise, France.

Title: CO and N_2 differential depletion in pre-stellar cores: Experimental study of N_2 desorption induced by the presence of CO on ices.

3) **Journée de l'Ecole Doctorale Science et Ingénierie 2017** , 29th June 2017, Neuville site, University of Cergy Pontoise, France.

Title: CO and N_2 differential depletion in pre-stellar cores: Experimental study of N_2 desorption induced by the presence of CO on ices.

4) **Pre-biotic Molecules in Space and Origins of Life on Earth**, 19th – 23rd March 2018, Physikzentrum Bad Honnef, Germany.

Title : Experimental study of the chemical network of methyl Isocyande (CH_3NC) on interstellar dust grains.

Awards: The best student poster (section Laboratory Astrophysics) in "Pre-biotic Molecules in Space and Origins of Life on Earth " conference, 19th – 23rd March 2018, Physikzentrum Bad Honnef, Germany.

C.2.3 Other attended conferences

1) **Journée de l'Ecole Doctorale Science et Ingénierie 2016**, 23rd June 2016, Neuville site, University of Cergy Pontoise, France.

2) **Workshop Saint Florent: Processus physico-chimiques d'intérêt astrophysique: Les molécules complexes**, 12th – 15th , June 2017, Corse, France.

List of Figures

1.1 Star formation cycle. Credits: Bill Saxton, NRAO/AUI/NSF 5
1.2 Infrared spectrum of W33A taken with the Infrared Space Observatory, taken from Gibb et al. (2000). 7
1.3 Schematic illustration of some processes that take place on dust grains. Image adapted from Dulieu et al. (2013) 8

2.1 Schematic top view of VENUS at LERMA Cergy. Image adapted from *Sow et al in preparation* 18
2.2 The location of the sample holder in the main chamber (top panel), four laser beams are shined through the atomic/molecular beamlines to ensure a good centering and a correct overlapping. The schematic of cryostat with longitudinal section of the sample holder (bottom panel). 20
2.3 Photo of the beamlines system for VENUS before moving to the new laboratory in March 2018. The beamline system component consists of the right, central, top and bottom beams. Central beam is behind the right beam on the photo. 21
2.4 Photo of QMS is at the low position (left panel) and the schematic of QMS at the high position (right panel). 22
2.5 Photos of the external and internal Vertex 70v (top and left panel) and MCT detector (right panel) 24
2.6 The fragment distribution of the CH_3NC molecule with the different relative intensity. Mass 41 represents CH_3NC^+ (red curve), mass 39 and 40 correspond to $CHNC^+$ (blue curve) and CH_2NC^+ (green curve). 25
2.7 Three different TPD profiles corresponds to the zero, first, and second order n of the desorption kinetics. 27
2.8 CO_2 beam flux as a function of source flux. 30
2.9 Integrated area of CO_2 by using IR spectrometer (top panel) and TPD-QMS (bottom panel) for three beams. The red triangles, blue stars, and orange circles exhibit the integrated area of CO_2 for the right, central, and top beams, respectively. 31
2.10 Evolution of the integrated area of NH_3 and H_2CO as the function of exposed time. 32

2.11 Ratio between remaining NH_3 and original NH_3 (brown squares); remaining H_2CO and original H_2CO (blue circles) as the function of the NH_3 flux. The remnant and consumption of NH_3 (brown and red squares) increased with the NH_3 flux, whereas the remnant (blue circles) and consumption (violet triangles) of H_2CO are mostly unchanged during the process. 32
2.12 H_2 plasma in the right beam of VENUS. 33

3.1 TPD curves of different doses of $^{15}N_2$ desorbing from c-ASW (top panel), of ^{13}CO from c-ASW (middle panel) and from p-ASW (bottom panel). 41
3.2 TPD spectra of different doses of ^{13}CO (top panel) and $^{15}N_2$ (bottom panel) from poly-crystalline water ice (PCI). 42
3.3 Binding energy of pure ^{13}CO (top panel) and pure $^{15}N_2$ (bottom panel) on compact amorphous solid water ice, as a function of coverage, obtained using the classical inversion method, assuming $n = 1$ and $A = 10^{13}$ s^{-1}. 44
3.4 Binding energy of pure ^{13}CO (top) and pure $^{15}N_2$ (bottom) on poly-crystalline water ice, as a function of coverage ($n = 1$, $A = 10^{13}$ s^{-1}). 45
3.5 Binding energy of pure ^{13}CO on porous amorphous water ice, as a function of coverage ($n = 1$, $A = 10^{13}$ s^{-1}). 46
3.6 TPD profiles of various mixtures of CO and N_2 deposited on poly-crystalline water ice (PCI) substrate. CO and N_2 are plotted with dashed and solid lines, respectively. Each colour corresponds to one experiment. CO is always the most abundant species with and its coverage varying between 0.45 ML to 1.2 ML, whereas N_2 coverage remains around 0.1 ML. 48
3.7 Experimental (dotted) and simulated (solid) desorption traces of CO:N_2 mixtures from c-ASW (top panel) and from PCI (bottom panel). Blue and red arrows indicate the position of the highest temperature at which the most tightly bound molecules desorb, calculated from the energy values reported in Table 3.2. Vertical dashed lines represent the highest temperature desorption in pure ices experiments, calculated from the energy values reported in Table 3.1. 51
3.8 Binding energy distributions of pure CO and N_2 (dashed lines) and of a 0.65 ML-CO–0.35 ML-N_2 mixture (solid lines) on c-ASW (top panel) and of a 0.91 ML-CO–0.09 ML-N_2 mixture on PCI (bottom panel), obtained using the classical inversion method. The black solid line is the sum of CO (solid blue line) and N_2 (red solid line) energy distributions calculated during the CO:N_2 mixture experiment. 53

4.1 IR spectra obtained after the deposition of 4 ML of NO at 10K on gold (red line), and after NO (4ML) and H (16 ML) codeposition (blue line). 63

4.2 TPD profiles of pure {NO} (red curve) and {NO +H} (blue lines). m/z 30, 33 and 44 are displayed corresponding respectively to NO, NH_2OH, and N_2O. 64
4.3 Influence of the surface temperature: TPD traces of m/z=30 (NO, green lines), m/z= 33 (NH_2OH, red lines) and m/z= 44 (N_2O, blue lines) for co-deposition experiments of {NO+H} on gold substrate held at 8 K (upper panel), and 40 K (lower panel). Curves are offset for clarity purpose. 65
4.4 NH_2OH TPD (left panel) and N_2O TPD (right panel) at different surface temperatures. Each temperature (8, 10, 12, 20, 24, 30, 35, 40, 42K) correspond to one specific co-deposition experiment {NO+H}. Curves are smoothed by adjacent averaging for a better visibility. NH_2OH amounts is decreasing with T_s whereas N_2O is increasing. The vertical black arrows represent the evolution of the peak with the temperature of the substrate. 66
4.5 Integrated areas of NH_2OH (blue circles) and N_2O (red squares) desorptions as a function of the surface temperature, obtained after the same co-deposition of NO and H 67
4.6 The sketch of the NO+H reactive system 68
4.7 TPD profiles of masses $m/z = 36$ a.m.u. (in red) and $m/z = 44$ (in blue) corresponding respectively to ND_2OD and N_2O recorded after a co-deposition experiment of {NO+D} at 10 K. 69
4.8 Blue circles: NH_2OH integrated areas after the co-deposition of NO molecules and H atoms. Red circles: ND_2OD integrated areas after the co-deposition of NO molecules and D atoms. ND_2OD is less than NH_2OH at the same surface temperatures. 72
4.9 TPD profiles of NH_2OH desorbing after {NO+H} codeposition experiment on gold surface (red) and water ice substrate (blue), at the same sample temperature of 10 K. 73
4.10 *Top panel:* TPD profile of initial ND_2OD (black curve) and remaining ND_2OD (cyan curve) after reacting with H atoms at 10 K. *Bottom panel:* TPD profiles of products detected after the exposition of H atoms to a ND_2OD a film. m/z 35 (red curve), m/z 34 (green curve), m/z 33 (violet curve), and m/z 36 (cyan curve) . . . 74

5.1 Schematic top-view of the VENUS set-up and the FT-RAIRS facility. 80
5.2 Scheme of the experimental protocol: a) deposition of 1 ML of NO at 40 K; b) deposition of X ML of H_2O at 40 K; c) cool down at 10 K in the case of D-exposure experiments; d) deposition of D atoms at 10 K or of O atoms at 40 K, recording continuously IR spectra; e) TPD profiles of the species of interest. 81
5.3 Number of adsorption sites expressed in ML as a function of water ice thickness, derived from a King and Wells methods. 83

5.4 IR spectra obtained by exposing to 1 ML of NO held at 40 K to different amount of O atoms: 0, 0.2, 0.4, 0.8, and 2.0 ML. The red curve does not present any IR signature since it has been considered as the reference spectrum. Curves are offset for clarity. 85
5.5 Kinetics of NO consumption and NO_2 formation obtained by integrating IR peaks of NO and NO_2 as a function of O-atom fluence for five different thickness of water ices (0, 2, 3, 6, and 10 ML) held at 40 K. 85
5.6 TPD curves at mass 30 and 46 after O-exposure of NO/H_2O ice for different thickness of water ices held at 40 K: 0 ML in (*a*), 3 ML in (*b*), 6 ML in (*c*), and 10 ML in (*d*). 87
5.7 Comparison between model (solid lines) and experimental data (dots). Experimental data have been obtained by integrating IR peak of NO following to different fluences of D atoms for three different thickness of water ices (0, 3, and 6 ML) deposited on top of NO held at 40 K. Simulated curves have been obtained by using the α_0 law for a deuterium bulk diffusion of 280 K. 88
5.8 Colored zone: possible values of NO located inside the bulk of ice (NO_b=α) as a function of the water ice layer thickness (WIL). Blue points : measured amounts of unreacted NO. Blue, red and green lines are representing 3 possible parametrized repartitions of initially covered NO molecules 91
5.9 Left panel: χ^2 values comparing model and data for different α laws as a function of bulk diffusion energy. α_0 corresponds to exact experimental values of unreacted species. Right panel: Comparison between model (lines) and experimental data (dots). Experimental data have been obtained by integrating IR peaks of NO and NO_2 as a function of O-atom fluence for five different thickness of water ices (0, 2, 3, 6, and 10 ML) held at 40 K. Simulated curves have been obtained by using three laws for the α parameter (α_1, α_2, and α_3) and measured experimental values (α_0) for the best case corresponding to the minimum χ^2 of left panel. For α_0 any choice of diffusion parameter greater than 950 K gives similar results. . . . 93

6.1 Integrated areas of NO band (stars) and H_2CO band (squares) as a function of deposited dose on the gold-coated substrate held at 10 K. Blue and red symbols are obtained in pure H_2CO and pure NO experiments, and brown symbols are obtained in the NO+H_2CO+H (co-deposition) experiment. 100
6.2 TPD profiles obtained after co-depostion of NO+D_2CO+D on gold held at 10 K (top panel), and TPD profiles after co-deposition of NO+H_2CO+H on porous ASW ice at 10 K(bottom panel). 102
6.3 Relative abundance of products obtained from co-deposition of NO, H_2CO, H on bare gold and on porous water ice at 10 K. 103

6.4 Fractional abundance of solid species on grains relative to water ice for an astrochemical model in which the effect of a H-abstraction of NH_2OH is shown. The left panel indicates abundances with H-abstraction and the right panel shows abundances when H abstraction is not taken into account. 105

7.1 FT-RAIRS spectra of pure CH_3NC (top panel) and CH_3CN (bottom panel) deposited separately at 10 K for different surface coverages. 112

7.2 TPD traces of CH_3NC (red curve) and CH_3CN (blue curve) obtained after separate depositions of 6 ML of the species, on the gold surface held at 10 K. 113

7.3 Evolution of the area of the 2250 cm^{-1} IR band of CH_3CN as function of deposition time on the substrate held at 10 K. H is co-deposited during the initial and final phases (black squares and blue triangles) and is absent (red circles) in the second phase. . . . 114

7.4 Top panel: Evolution of the area of the 2176 cm^{-1} IR band of CH_3NC as function of deposition time on the substrate held at 10 K. CH_3NC deposition in blue, and $\{CH_3NC + H\}$ co-deposition in red. Bottom panel: TPD trace (m/z 41) of pure CH_3NC (blue curve) and the remaining part of CH_3NC (red curve) obtain after the same depositions. 115

7.5 *Top panel:* TPD traces of $CH_3NCH_2^+$ (m/z 43 - solid red curve) and cracking pattern m/z 42 (CH_3NCH^+-dash red curve) desorb around 90-115 K; remaining CH_3NC^+ (m/z 41 - solid blue curve) and cracking pattern m/z 39 and 40 (dash blue curves) desorb around 110-125 K; finally, dimethylamine ($CH_3NHCH_3^+$) (m/z 45 - solid green curve) and cracking patterns m/z 44 (dash green curve), m/z 43 (solid red curve), and m/z 42 (dash red curve) desorb around 120-145 K. *Bottom panel:* TPD traces of CH_4^+ (m/z 16-red curve) and HCN^+/HNC^+ (m/z 27-blue curve) are formed from other chemical pathways between CH_3NC and H atoms. 118

7.6 Desorption profiles of pure CH_3NC (blue curve) and $\{CH_3NC + H_2O\}$ (red and green curves). 119

7.7 TPD profiles of the reactivity between CH_3NC and H atoms in the presence of H_2O. CH_3NHCH_3 (M_{CH_3NC} + 4H) (solid green curve) is enhanced after completing the deposition. A part of CH_3NC (M_{CH_3NC} - solid blue curve) and CH_3NCH_2 (M_{CH_3NC+2H} - solid red curve) desorb before H_2O and the other parts are trapped and desorbed with H_2O. 120

7.8 *Top panel*: Pure CH_3NC (blue curve) and remaining CH_3NC (red curve) after completing the reaction with D atoms at 10 K. *Bottom panel*: TPD traces of mass 45 (M_{CH_3NC} + 2D - solid red curve) and cracking pattern (m/z 43, and 44) (dashed red curves) corresponding to CH_3NCD_2. No traces of CH_3NDCD_3 (M_{CH_3NC} + 4D - solid green curve) are detected. 122

7.9 *Top panel:* Remaining CH_3NC (from red to green curves) after completing the reaction with H atoms on the surface with the temperature is ranging from 20 K to 40 K. *Middle panel:* TPD traces of CH_3NCH_2 (M_{CH_3NC} + 2H) (from red to green curves) are gradually reduced with the surface temperature. *Bottom panel:* The trace of Dimethylamine (CH_3NHCH_3 - M_{CH_3NC} + 4H) is not detectable at high temperatures. 124
7.10 Schematic view of the orientation of the CH_3NC molecules which are deposited on the golden surface maintained at 10 K (top panel) and 40 K (bottom panel). 127

A.1 TPD profiles of methanol (m/z=32), NH_2OH (m/z=33), and NH_2CHO (m/z=45) after co-deposition of {NO+H_2CO+H} on porous-ASW ice at 10 K. 134

B.1 Integrated areas of IR bands of pure NO (red stars), pure H_2CO (blue squares) compared to remaining NO and H_2CO (brown stars and squares) that are obtained during the exposure time of H atoms on the gold surface maintained at 10 K. The consumptions of NO and H_2CO (brown stars and squares) indicate that the co-hydrogenation of NO and H_2CO are complete reactions. 136
B.2 TPD profiles obtained after co-deposition {NO + H_2CO + H} on the golden surface maintained at 10 K. TPD masses *m/z* 31 and 32 (first peaks - cyan and green curves) represent methanol (CH_3OH) desorbing from around 140-170 K. Mass 33 (red curve) is the trace of hydroxylamine desorbing from around 160-210 K. The second peaks of masses 31 and 32 are the cracking pattern of hydroxylamine (M33). The trace of NH_2CHO (*m/z* 45 - blue curve) desorbs around 190-230 K. 137
B.3 TPD profiles obtained after co-deposition {NO + D_2CO + D} on the golden surface held at 10 K. Mass 36 (first peak-red curve) represents the trace of CD_3OD desorbing from around 130-160 K. The second peak of mass 36 is the trace of ND_2OD desorbing from around 160-210 K. Deuterated formamide (ND_2CDO) (m/z 48-blue curve) desorbs around 190-230 K. 137
B.4 TPD profiles obtained after co-deposition {NO + H_2CO + H} on the golden surface maintained at 40 K. The trace of CH_3OH (m/z 31 - cyan curve), NH_2OH (m/z 33 - red curve), and NH_2CHO (m/z 45 - blue curve) are mostly reduced. Excepting mass 32 (green curve), it may represent both of the traces of CH_3OH or the cracking pattern of (N_2ONO_2) formed in sub-reactions of the {NO+H} chemistry at 40 K. 138

B.5 TPD traces obtained by depositing to 5 ML of H_2CO on top of one NH_2OH layer held at 10 K. The NH_2OH layer is produced by co-depositing {NO + H} on the surface at 10 K, and then the surface is annealed to 160 K for releasing other species (i.e N_2O, NO, and H) into the gas phase. The surface temperature is cooled down to 10 K before depositing H_2CO on top of the NH_2OH layer. H_2CO (black curve), NH_2OH (red curve) and cracking pattern NHOH (green curve) remain large, whereas the trace of NH_2CHO (blue curve) is very tiny after completing the exposure. NH_2OH should be accompanied of sense NHOH radicals due to the back reaction. . 139

B.6 Normalization of NH_2CHO produced: case A) Co-deposition {NO + H_2CO + H}; case B) {H_2CO + H} on top of the layer NO; case C) {NO + H} on top of the layer H_2CO. Amount of NH_2CHO (blue columns) produced in these experiments; Amounts of NH_2CHO (green columns) is normalised to NO. The formation route of NH_2CHO is driven by the hydrogenation of NO in presence of H_2CO, whereas the H_2CO hydrogenation in the presence of NO is not efficient. . . . 140

B.7 TPD traces obtained after completing the co-deposition on porous water ice substrate held at 10 K. NH_2OH (red curve) and NH_2CHO (blue curve) are enhanced in the presence of H_2O comparing to the gold substrate. 140

B.8 TPD profiles obtained after co-deposition {NO + H_2CO + H} on porous water ice substrate held at 40 K. NH_2OH (red curve), CH_3OH (green curve), and NH_2CHO (blue curve) are raised in the presence of H_2O comparing to the gold substrate held at 40 K. . . . 141

List of Tables

1.1 Density and temperature distribution in the ISM (Draine, 2011, Goldsmith et al., 1969) 5

1.2 Molecules detected in interstellar ices towards protostars. Molecular abundances are related to the water ice (Van Broekhuizen, 2005) . . 11

2.1 Fragment distribution of some species are detected through QMS. The desorption temperature range corresponds to these molecular species. The highest intensity is the main mass signal of species. Mass and relative intensity are indicated in blue and in red respectively. 25

3.1 Pure species: energy ranges of CO and N_2 binding energy distributions measured as a function of coverage on different water ice substrates. 47

3.2 CO:N_2 mixtures: energy ranges for N_2 and CO obtained as a function coverage and [CO]/[N_2] ratio on c-ASW and PCI. 48

4.1 Ratios of the TPD areas of N_2O, NH_2OH (or ND_2OD) obtained after co-deposition experiments and the TPD area of NO in the pure NO experiment. {NO + D} and {NO + H} are performed on a gold substrate hold at 10 K whereas {NO + H} on H_2O is made on a H_2O substrate. 69

6.1 List of discussed experiments 101

7.1 Percentages (%) of the products and remnants after the deposition of pure CH_3NC, {CH_3NC + H_2O}, {CH_3NC + H} and {CH_3NC + H + H_2O} co-depositions on surface held at 10 K. 121

7.2 Percentage (%) of remnants (CH_3NC) and products after completing the co-deposition of CH_3NC and H/D atoms at 10 K. 123

7.3 Percentages (%) of the products and remnants after completing the depositions at different surface temperatures 125

7.4 Intensities of CH_3NC, CH_3CN, and products after completing the reactions with H atoms. Comparison between NIST Chemistry webbook data and our experimental results 129

B.1 List of discussed experiments 135

B.2 Possible reactions between the intermediates and products of NO hydrogenation (vertical) and H_2CO hydrogenation (horizontal) on the grain surface for the formation of NH_2CHO. 141

Bibliography

M. Accolla, E. Congiu, F. Dulieu, G. Manicò, H. Chaabouni, E. Matar, H. Mokrane, J. L. Lemaire, and V. Pirronello. Changes in the morphology of interstellar ice analogues after hydrogen atom exposure. *Physical Chemistry Chemical Physics (Incorporating Faraday Transactions)*, 13:8037, 2011. doi: 10.1039/C0CP01462A.

M. Accolla, E. Congiu, G. Manicò, F. Dulieu, H. Chaabouni, J. L. Lemaire, and V. Pirronello. Morphology of the solid water synthesized through the pathway D + O_2 studied by the sensitive TPD technique. MNRAS, 429:3200–3206, March 2013. doi: 10.1093/mnras/sts578.

M. Accolla, E. Congiu, G. Manicò, F. Dulieu, H. Chaabouni, J. L. Lemaire, and V. Pirronello. Morphology of the solid water synthesized through the pathway D + O2 studied by the sensitive TPD technique. *Monthly Notices of the Royal Astronomical Society*, 429(4): 3200–3206, March 2013. ISSN 1365-2966, 0035-8711. doi: 10.1093/mnras/sts578. URL http://academic.oup.com/mnras/article/429/4/3200/1014531/Morphology-of-the-solid-water-synthesized-through.

Mario Accolla. *Experimental Investigation on the Morphology of Interstellar Ice Analogues*. Theses, Université de Cergy Pontoise, April 2010.

Gilles R Adande, Neville J Woolf, and Lucy M Ziurys. Observations of interstellar formamide: Availability of a prebiotic precursor in the galactic habitable zone. *Astrobiology*, 13(5):439–453, 2013.

M. Akyilmaz, D. R. Flower, P. Hily-Blant, G. Pineau Des Forêts, and C. M. Walmsley. The depletion of NO in pre-protostellar cores. A&A, 462:221–230, January 2007. doi: 10.1051/0004-6361:20066131.

Marco A. Allodi, Sergio Ioppolo, Matthew J. Kelley, Brett A. McGuire, and Geoffrey A. Blake. The structure and dynamics of carbon dioxide and water containing ices investigated via THz and mid-IR spectroscopy. *Physical Chemistry Chemical Physics*, 16(8):3442, 2014. ISSN 1463-9076, 1463-9084. doi: 10.1039/c3cp53767f. URL http://xlink.rsc.org/?DOI=c3cp53767f.

L Amiaud, JH Fillion, S Baouche, F Dulieu, A Momeni, and JL Lemaire. Interaction of d 2 with h 2 o amorphous ice studied by temperature-programed desorption experiments. *The Journal of chemical physics*, 124(9):094702, 2006.

L Amiaud, F Dulieu, J-H Fillion, A Momeni, and J L Lemaire. Interaction of atomic and molecular deuterium with a nonporous amorphous water ice surface between 8 and 30 K. *The Journal of chemical physics*, 127(14):144709, October 2007. ISSN 0021-9606. doi: 10.1063/1.2746323. URL http://scitation.aip.org.ezproxy.obspm.fr/content/aip/journal/jcp/127/14/10.1063/1.2746323.

L. Amiaud, A. Momeni, F. Dulieu, J. H. Fillion, E. Matar, and J.-L. Lemaire. Measurement of the Adsorption Energy Difference between Ortho- and Para-D2 on an Amorphous Ice Surface. *Physical Review Letters*, 100(5):056101, feb 2008. ISSN 0031-9007. doi: 10.1103/PhysRevLett.100.056101. URL http://link.aps.org/doi/10.1103/PhysRevLett.100.056101.

L. Amiaud, J.-H. Fillion, F. Dulieu, A. Momeni, and J.-L. Lemaire. Physisorption and desorption of H2, HD and D2 on amorphous solid water ice. Effect on mixing isotopologue on statistical population of adsorption sites. *Physical Chemistry Chemical Physics*, 17(44):30148–30157, 2015. ISSN 14639076. doi: 10.1039/c5cp03985a.

Edward Anders, Ryoichi Hayatsu, and Martin H. Studier. Interstellar Molecules: Origin by Catalytic Reactions on Grain Surfaces? *The Astrophysical Journal*, 192:L101, September 1974. ISSN 0004-637X, 1538-4357. doi: 10.1086/181601. URL http://adsabs.harvard.edu/doi/10.1086/181601.

Ryo Ando, Kouichiro Nakanishi, Kotaro Kohno, Takuma Izumi, Sergio Martín, Nanase Harada, Shuro Takano, Nario Kuno, Naomasa Nakai, Hajime Sugai, Kazuo Sorai, Tomoka Tosaki, Kazuya Matsubayashi, Taku Nakajima, Yuri Nishimura, and Yoichi Tamura. Diverse Nuclear Star-forming Activities in the Heart of NGC 253 Resolved with 10-pc-scale ALMA Images. *The Astrophysical Journal*, 849(2):81, nov 2017. ISSN 1538-4357. doi: 10.3847/1538-4357/aa8fd4. URL http://stacks.iop.org/0004-637X/849/i=2/a=81?key=crossref.5c7c02d95ef7fa1069418748e088f424.

N. Balucani, C. Ceccarelli, and V. Taquet. Formation of complex organic molecules in cold objects: the role of gas-phase reactions. MNRAS, 449:L16–L20, April 2015. doi: 10.1093/mnrasl/slv009.

V. Barone, C. Latouche, D. Skouteris, F. Vazart, N. Balucani, C. Ceccarelli, and B. Lefloch. Gas-phase formation of the prebiotic molecule formamide: insights from new quantum computations. MNRAS, 453:L31–L35, October 2015. doi: 10.1093/mnrasl/slv094.

A. Belloche, K. M. Menten, C. Comito, H. S. P. Müller, P. Schilke, J. Ott, S. Thorwirth, and C. Hieret. Detection of amino acetonitrile in Sgr B2(N). A&A, 482: 179–196, April 2008. doi: 10.1051/0004-6361:20079203.

A. Belloche, R. T. Garrod, H. S. P. Müller, and K. M. Menten. Detection of a branched alkyl molecule in the interstellar medium: iso-propyl cyanide, September 2014.

E. A. Bergin and W. D. Langer. Chemical Evolution in Preprotostellar and Protostellar Cores. ApJ, 486:316–328, September 1997. doi: 10.1086/304510.

E. A. Bergin and M. Tafalla. Cold Dark Clouds: The Initial Conditions for Star Formation. ARA&A, 45:339–396, September 2007. doi: 10.1146/annurev.astro.45.071206.100404.

E. A. Bergin, D. R. Ciardi, C. J. Lada, J. Alves, and E. A. Lada. Molecular Excitation and Differential Gas-Phase Depletions in the IC 5146 Dark Cloud. ApJ, 557:209–225, August 2001. doi: 10.1086/321625.

B. S. Berland, D. E. Brown, M. A. Tolbert, and S. M. George. Refractive index and density of vapor-deposited ice. Geophys. Res. Lett., 22:3493–3496, 1995. doi: 10.1029/95GL03504.

M. Bertin, M. Doronin, J.-H. Fillion, X. Michaut, L. Philippe, M. Lattelais, A. Markovits, F. Pauzat, Y. Ellinger, and J.-C. Guillemin. Nitrile versus isonitrile adsorption at interstellar grains surfaces. I. Hydroxylated surfaces, February 2017a.

M. Bertin, M. Doronin, X. Michaut, L. Philippe, A. Markovits, J.-H. Fillion, F. Pauzat, Y. Ellinger, and J.-C. Guillemin. Nitrile versus isonitrile adsorption at interstellar grain surfaces. II. Carbonaceous aromatic surfaces, December 2017b.

S. E. Bisschop, H. J. Fraser, K. I. Öberg, E. F. van Dishoeck, and S. Schlemmer. Desorption rates and sticking coefficients for CO and N_2 interstellar ices. A&A, 449:1297–1309, April 2006. doi: 10.1051/0004-6361:20054051.

S. E. Bisschop, J. K. Jørgensen, E. F. van Dishoeck, and E. B. M. de Wachter. Testing grain-surface chemistry in massive hot-core regions. A&A, 465:913–929, April 2007. doi: 10.1051/0004-6361:20065963.

N. Biver, D. Bockelée-Morvan, V. Debout, J. Crovisier, J. Boissier, D. C. Lis, N. Dello Russo, R. Moreno, P. Colom, G. Paubert, R. Vervack, and H. A. Weaver. Complex organic molecules in comets C/2012 F6 (Lemmon) and C/2013 R1 (Lovejoy): detection of ethylene glycol and formamide. A&A, 566: L5, June 2014. doi: 10.1051/0004-6361/201423890.

D Bockelée-Morvan, DC Lis, JE Wink, D Despois, J Crovisier, R Bachiller, DJ Benford, N Biver, P Colom, JK Davies, et al. New molecules found in comet c/1995 o1 (hale-bopp). investigating the link between cometary and interstellar material. *Astronomy and Astrophysics*, 353:1101–1114, 2000.

A. C. A. Boogert, K. M. Pontoppidan, C. Knez, F. Lahuis, J. Kessler-Silacci, E. F. van Dishoeck, G. A. Blake, J.-C. Augereau, S. E. Bisschop, S. Bottinelli, T. Y. Brooke, J. Brown, A. Crapsi, N. J. Evans, II, H. J. Fraser, V. Geers, T. L. Huard, J. K. Jørgensen, K. I. Öberg, L. E. Allen, P. M. Harvey, D. W. Koerner, L. G. Mundy, D. L. Padgett, A. I. Sargent, and K. R. Stapelfeldt. The c2d Spitzer Spectroscopic Survey of Ices around Low-Mass Young Stellar Objects. I. H_2O and the 5-8 μm Bands. ApJ, 678:985–1004, May 2008. doi: 10.1086/533425.

A. C. A. Boogert, P. A. Gerakines, and D. C. B. Whittet. Observations of the icy universe. ARA&A, 53:541–581, August 2015. doi: 10.1146/annurev-astro-082214-122348.

A. M. S. Boonman, E. F. van Dishoeck, F. Lahuis, C. M. Wright, and S. D. Doty. Gas-phase H_2O and CO_2 towards massive protostars. 456:67, November 2000.

J. B. Bossa, P. Theulé, F. Duvernay, F. Borget, and T. Chiavassa. Carbamic acid and carbamate formation in NH{3}:CO{2} ices - UV irradiation versus thermal processes. A&A, 492:719–724, December 2008. doi: 10.1051/0004-6361:200810536.

J. B. Bossa, P. Theule, F. Duvernay, and T. Chiavassa. NH_2CH_2OH Thermal Formation in Interstellar Ices Contribution to the 5-8 μm Region Toward Embedded Protostars. ApJ, 707:1524–1532, December 2009. doi: 10.1088/0004-637X/707/2/1524.

J.-B. Bossa, K. Isokoski, M. S. de Valois, and H. Linnartz. Thermal collapse of porous interstellar ice. A&A, 545:A82, September 2012. doi: 10.1051/0004-6361/201219340.

Emeric Bron, Jacques Le Bourlot, and Franck Le Petit. Surface chemistry in the interstellar medium. *Astronomy & Astrophysics*, 569:A100, sep 2014. ISSN 0004-6361. doi: 10.1051/0004-6361/201322101. URL http://www.aanda.org/articles/aa/full{_}html/2014/09/aa22101-13/aa22101-13.html.

P. Caselli. Grain chemistry in star-forming regions. August 1999.

P. Caselli. Deuterated molecules as a probe of ionization fraction in dense interstellar clouds. Planet. Space Sci., 50:1133–1144, October 2002. doi: 10.1016/S0032-0633(02)00074-0.

Paola Caselli and Cecilia Ceccarelli. Our astrochemical heritage. *The Astronomy and Astrophysics Review*, 20(1):56, oct 2012. ISSN 0935-4956. doi: 10.1007/s00159-012-0056-x. URL http://cdsads.u-strasbg.fr/abs/2012A{%}26ARv..20...56C.

S. Cazaux, V. Cobut, M. Marseille, M. Spaans, and P. Caselli. Water formation on bare grains: When the chemistry on dust impacts interstellar gas. *Astronomy & Astrophysics*, 522:A74, nov 2010. ISSN 0004-6361. doi: 10.1051/0004-6361/201014026. URL http://www.aanda.org/articles/aa/full{_}html/2010/14/aa14026-10/aa14026-10.html.

C. Ceccarelli, P. Caselli, F. Fontani, R. Neri, A. López-Sepulcre, C. Codella, S. Feng, I. Jiménez-Serra, B. Lefloch, J.E. Pineda, C. Vastel, F. Alves, R. Bachiller, N. Balucani, E. Bianchi, L. Bizzocchi, S. Bottinelli, E. Caux, A. Chacón-Tanarro, R. Choudhury, A. Coutens, F. Dulieu, C. Favre, P. Hily-Blant, J. Holdship, C. Kahane, A.J. Al-Edhari, J. Laas, J. Ospina, Y. Oya, L. Podio, A. Pon, A. Punanova, D. Quenard, A. Rimola, N. Sakai, I.R. Sims, S. Spezzano, V. Taquet, L. Testi, P. Theulé, P. Ugliengo, A.I. Vasyunin, S. Viti, L. Wiesenfeld, and S. Yamamoto. Seeds of Life in Space (SOLIS): The Organic Composition Diversity at 300-1000 au Scale in Solar-type Star-forming Regions. *Astrophysical Journal*, 850(2), 2017. ISSN 15384357. doi: 10.3847/1538-4357/aa961d.

J. Cernicharo, C. Kahane, M. Guelin, and J. Gomez-Gonzalez. Tentative detection of CH3NC towards SGR B2, January 1988.

J. Cernicharo, N. Marcelino, E. Roueff, M. Gerin, A. Jiménez-Escobar, and G. M. Muñoz Caro. Discovery of the Methoxy Radical, CH_3O, toward B1: Dust Grain

and Gas-phase Chemistry in Cold Dark Clouds. ApJ, 759:L43, November 2012. doi: 10.1088/2041-8205/759/2/L43.

H. Chaabouni, S. Diana, T. Nguyen, and F. Dulieu. Thermal desorption of formamide and methylamine from graphite and amorphous water ice surfaces, apr 2018. ISSN 0004-6361. URL https://www.aanda.org/10.1051/0004-6361/201731006.

J. E. Chiar, A. J. Adamson, T. H. Kerr, and D. C. B. Whittet. High-Resolution Studies of Solid CO in the Taurus Dark Cloud: Characterizing the Ices in Quiescent Clouds. *The Astrophysical Journal*, 455:234, dec 1995. ISSN 0004-637X. doi: 10.1086/176571. URL http://adsabs.harvard.edu/doi/10.1086/176571.

C. Codella, C. Ceccarelli, P. Caselli, N. Balucani, V. Barone, F. Fontani, B. Lefloch, L. Podio, S. Viti, S. Feng, R. Bachiller, E. Bianchi, F. Dulieu, I. Jiménez-Serra, J. Holdship, R. Neri, J. E. Pineda, A. Pon, I. Sims, S. Spezzano, A. I. Vasyunin, F. Alves, L. Bizzocchi, S. Bottinelli, E. Caux, A. Chacón-Tanarro, R. Choudhury, A. Coutens, C. Favre, P. Hily-Blant, C. Kahane, A. Jaber Al-Edhari, J. Laas, A. López-Sepulcre, J. Ospina, Y. Oya, A. Punanova, C. Puzzarini, D. Quenard, A. Rimola, N. Sakai, D. Skouteris, V. Taquet, L. Testi, P. Theulé, P. Ugliengo, C. Vastel, F. Vazart, L. Wiesenfeld, and S. Yamamoto. Seeds of Life in Space (SOLIS). II. Formamide in protostellar shocks: Evidence for gas-phase formation. A&A, 605:L3, September 2017. doi: 10.1051/0004-6361/201731249.

C Codella, S Viti, B Lefloch, J Holdship, R Bachiller, E Bianchi, C Ceccarelli, C Favre, I Jiménez-Serra, L Podio, et al. Nitrogen oxide in protostellar envelopes and shocks: the asai survey. *Monthly Notices of the Royal Astronomical Society*, 474(4):5694–5703, 2017.

M. P. Collings, M. A. Anderson, R. Chen, J. W. Dever, S. Viti, D. A. Williams, and M. R. S. McCoustra. A laboratory survey of the thermal desorption of astrophysically relevant molecules. *Monthly Notices of the Royal Astronomical Society*, 354(4):1133–1140, nov 2004. ISSN 0035-8711. doi: 10.1111/j.1365-2966.2004.08272.x. URL http://cdsads.u-strasbg.fr/abs/2004MNRAS.354.1133C.

M. P. Collings, V. L. Frankland, J. Lasne, D. Marchione, A. Rosu-Finsen, and M. R. S. McCoustra. Probing model interstellar grain surfaces with small molecules. MNRAS, 449:1826–1833, May 2015. doi: 10.1093/mnras/stv425.

E. Congiu, E. Matar, L. E. Kristensen, F. Dulieu, and J. L. Lemaire. Laboratory evidence for the non-detection of excited nascent H_2 in dark clouds. MNRAS, 397:L96–L100, July 2009. doi: 10.1111/j.1745-3933.2009.00692.x.

E Congiu, H Chaabouni, C Laffon, P Parent, S Baouche, and F Dulieu. Efficient surface formation route of interstellar hydroxylamine through NO hydrogenation. I. The submonolayer regime on interstellar relevant substrates. *The Journal of chemical physics*, 137(5):054713, August 2012a. ISSN 1089-7690. doi: 10.1063/1.4738895. URL http://scitation.aip.org.ezproxy.obspm.fr/content/aip/journal/jcp/137/5/10.1063/1.4738895.

E. Congiu, H. Chaabouni, C. Laffon, P. Parent, S. Baouche, and F. Dulieu. Efficient surface formation route of interstellar hydroxylamine through no hydrogenation. i. the submonolayer regime on interstellar relevant substrates. *The Journal of Chemical Physics*, 137(5):054713, 2012b. doi: 10.1063/1.4738895. URL https://doi.org/10.1063/1.4738895.

E Congiu, H Chaabouni, C Laffon, P Parent, S Baouche, and F Dulieu. Efficient surface formation route of interstellar hydroxylamine through NO hydrogenation. I. The submonolayer regime on interstellar relevant substrates. *The Journal of chemical physics*, 137(5):054713, aug 2012c. ISSN 1089-7690. doi: 10.1063/1.4738895. URL http://scitation.aip.org.ezproxy.obspm.fr/content/aip/journal/jcp/137/5/10.1063/1.4738895.

E. Congiu, G. Fedoseev, S. Ioppolo, F. Dulieu, H. Chaabouni, S. Baouche, J. L. Lemaire, C. Laffon, P. Parent, T. Lamberts, H. M. Cuppen, and H. Linnartz. No Ice Hydrogenation: A Solid Pathway to NH_2OH Formation in Space. ApJ, 750:L12, May 2012. doi: 10.1088/2041-8205/750/1/L12.

E. Congiu, M. Minissale, S. Baouche, H. Chaabouni, A. Moudens, S. Cazaux, G. Manicò, V. Pirronello, and F. Dulieu. Efficient diffusive mechanisms of O atoms at very low temperatures on surfaces of astrophysical interest. *Faraday Discussions*, 168:151, 2014a. doi: 10.1039/C4FD00002A.

E. Congiu, M. Minissale, S. Baouche, H. Chaabouni, A. Moudens, S. Cazaux, G. Manicò, V. Pirronello, and F. Dulieu. Efficient diffusive mechanisms of O atoms at very low temperatures on surfaces of astrophysical interest. *Faraday Discussions*, 168:151, 2014b. doi: 10.1039/C4FD00002A.

Ilsa R. Cooke, Karin I. Öberg, Edith C. Fayolle, Zoe Peeler, and Jennifer B. Bergner. CO Diffusion and Desorption Kinetics in CO_2 Ices. *The Astrophysical Journal*, 852(2):75, January 2018. ISSN 1538-4357. doi: 10.3847/1538-4357/aa9ce9. URL http://stacks.iop.org/0004-637X/852/i=2/a=75?key=crossref.2d25d7ba4cb5fc445e71094c4a066591.

H. M. Cuppen, C. Walsh, T. Lamberts, D. Semenov, R. T. Garrod, E. M. Penteado, and S. Ioppolo. Grain Surface Models and Data for Astrochemistry. *Space Science Reviews*, 212(1-2):1–58, oct 2017a. ISSN 0038-6308. doi: 10.1007/s11214-016-0319-3. URL http://link.springer.com/10.1007/s11214-016-0319-3.

H. M. Cuppen, C. Walsh, T. Lamberts, D. Semenov, R. T. Garrod, E. M. Penteado, and S. Ioppolo. Grain Surface Models and Data for Astrochemistry. *Space Science Reviews*, 212(1-2):1–58, October 2017b. ISSN 0038-6308, 1572-9672. doi: 10.1007/s11214-016-0319-3. URL http://link.springer.com/10.1007/s11214-016-0319-3.

E. Dartois, L. d'Hendecourt, W. Thi, K. M. Pontoppidan, and E. F. van Dishoeck. Combined VLT ISAAC/ISO SWS spectroscopy of two protostellar sources. The importance of minor solid state features. A&A, 394:1057–1068, November 2002. doi: 10.1051/0004-6361:20021228.

D. J. Defrees, A. D. McLean, and E. Herbst. Theoretical investigation of the interstellar CH3NC/CH3CN ratio, June 1985.

N. Dello Russo, R. J. Vervack, Jr., C. M. Lisse, H. A. Weaver, H. Kawakita, H. Kobayashi, A. L. Cochran, W. M. Harris, A. J. McKay, N. Biver, D. Bockelée-Morvan, and J. Crovisier. THE VOLATILE COMPOSITION AND ACTIVITY OF COMET 103p/HARTLEY 2 DURING THE *EPOXI* CLOSEST APPROACH. *The Astrophysical Journal*, 734(1):L8, June 2011. ISSN 2041-8205, 2041-8213. doi: 10.1088/2041-8205/734/1/L8. URL http://stacks.iop.org/2041-8205/734/i=1/a=L8?key=crossref.ad12e91ee668f6132ec7b8d558406adc.

L. B. D'Hendecourt, L. J. Allamandola, and J. M. Greenberg. Time dependent chemistry in dense molecular clouds. I - Grain surface reactions, gas/grain interactions and infrared spectroscopy. A&A, 152:130–150, November 1985.

J. Di Francesco, P. André, and P. C. Myers. Quiescent Dense Gas in Protostellar Clusters: The Ophiuchus A Core. ApJ, 617:425–438, December 2004. doi: 10.1086/425264.

Z. Dohnálek, Greg A. Kimmel, S. A. Joyce, Patrick Ayotte, R. Scott Smith, and Bruce D. Kay. Physisorption of CO on the MgO(100) Surface †. *The Journal of Physical Chemistry B*, 105(18):3747–3751, may 2001. ISSN 1520-6106. doi: 10.1021/jp003174b. URL http://dx.doi.org/10.1021/jp003174b.

Z. Dohnálek, Greg A. Kimmel, Patrick Ayotte, R. Scott Smith, and Bruce D. Kay. The deposition angle-dependent density of amorphous solid water films. *The Journal of Chemical Physics*, 118(1):364–372, 2003. doi: 10.1063/1.1525805. URL https://doi.org/10.1063/1.1525805.

B. T. Draine. Interstellar Dust Grains. ARA&A, 41:241–289, 2003. doi: 10.1146/annurev.astro.41.011802.094840.

B. T. Draine. *Physics of the Interstellar and Intergalactic Medium*. 2011.

B. T. Draine and A. Li. Infrared Emission from Interstellar Dust. IV. The Silicate-Graphite-PAH Model in the Post-Spitzer Era. ApJ, 657:810–837, March 2007. doi: 10.1086/511055.

F. Dulieu, L. Amiaud, S. Baouche, A. Momeni, J.-H. Fillion, and J.L. Lemaire. Isotopic segregation of molecular hydrogen on water ice surface at low temperature. *Chemical Physics Letters*, 404(1-3):187–191, mar 2005. ISSN 00092614. doi: 10.1016/j.cplett.2005.01.044. URL http://www.sciencedirect.com/science/article/pii/S0009261405000746.

F. Dulieu, L. Amiaud, E. Congiu, J.-H. Fillion, E. Matar, A. Momeni, V. Pirronello, and J. L. Lemaire. Experimental evidence for water formation on interstellar dust grains by hydrogen and oxygen atoms. A&A, 512:A30, March 2010. doi: 10.1051/0004-6361/200912079.

F. Dulieu, E. Congiu, J. Noble, S. Baouche, H. Chaabouni, A. Moudens, M. Minissale, and S. Cazaux. How micron-sized dust particles determine the chemistry of our Universe. *Scientific Reports*, 3:1338, February 2013. doi: 10.1038/srep01338.

F. Dulieu, M. Minissale, and D. Bockelée-Morvan. Production of O2 through dismutation of H2O2 during water ice desorption: a key to understanding comet O2 abundances, jan 2017. ISSN 0004-6361. URL http://www.aanda.org/10.1051/0004-6361/201628445.

F. Duvernay, G. Danger, P. Theulé, T. Chiavassa, and A. Rimola. FORMALDEHYDE CHEMISTRY IN COMETARY ICES: ON THE PROSPECTIVE DETECTION OF NH 2 CH 2 OH, HOCH 2 OH, AND POM BY THE ON-BOARD ROSINA INSTRUMENT OF THE ROSETTA MISSION, jul 2014. ISSN 1538-4357. URL http://iopscience.iop.org.ezproxy.obspm.fr/article/10.1088/0004-637X/791/2/75.

William G Fateley, Henry A Bent, and Bryce Crawford Jr. Infrared spectra of the frozen oxides of nitrogen. *The Journal of Chemical Physics*, 31(1):204–217, 1959.

Edith C. Fayolle, Jodi Balfe, Ryan Loomis, Jennifer Bergner, Dawn Graninger, Mahesh Rajappan, and Karin I. Öberg. N2 AND CO DESORPTION ENERGIES FROM WATER ICE. *The Astrophysical Journal*, 816 (2):L28, jan 2016. ISSN 2041-8213. doi: 10.3847/2041-8205/816/2/L28. URL http://iopscience.iop.org.ezproxy.obspm.fr/article/10.3847/2041-8205/816/2/L28.

G. Fedoseev, S. Ioppolo, T. Lamberts, J. F. Zhen, H. M. Cuppen, and H. Linnartz. Efficient surface formation route of interstellar hydroxylamine through no hydrogenation. ii. the multilayer regime in interstellar relevant ices. *The Journal of Chemical Physics*, 137(5):054714, 2012. doi: 10.1063/1.4738893. URL https://doi.org/10.1063/1.4738893.

G. Fedoseev, S. Ioppolo, and H. Linnartz. Deuterium enrichment of ammonia produced by surface N+H/D addition reactions at low temperature. MNRAS, 446:449–458, January 2015. doi: 10.1093/mnras/stu1852.

G. Fedoseev, K.-J. Chuang, E. F. van Dishoeck, S. Ioppolo, and H. Linnartz. Simultaneous hydrogenation and UV-photolysis experiments of NO in CO-rich interstellar ice analogues; linking HNCO, OCN^-, NH_2CHO, and NH_2OH. MNRAS, 460:4297–4309, August 2016. doi: 10.1093/mnras/stw1028.

Jean-Hugues Fillion, Lionel Amiaud, Emanuele Congiu, Francois Dulieu, Anouchah Momeni, and Jean-Louis Lemaire. D(2) desorption kinetics on amorphous solid water: from compact to porous ice films. *Physical chemistry chemical physics : PCCP*, 11(21):4396–4402, 2009. ISSN 1463-9076.

D. N. Friedel, L. E. Snyder, B. E. Turner, and A. Remijan. A Spectral Line Survey of Selected 3 Millimeter Bands toward Sagittarius B2(N-LMH) Using the National Radio Astronomy Observatory 12 Meter Radio Telescope and the Berkeley-Illinois-Maryland Association Array. I. The Observational Data, January 2004.

G. W. Fuchs, H. M. Cuppen, S. Ioppolo, C. Romanzin, S. E. Bisschop, S. Andersson, E. F. van Dishoeck, and H. Linnartz. Hydrogenation reactions in interstellar CO ice analogues. A combined experimental/theoretical approach. A&A, 505: 629–639, October 2009. doi: 10.1051/0004-6361/200810784.

Guido W. Fuchs, Kinsuk Acharyya, Suzanne E. Bisschop, Karin I. Oberg, Fleur A. van Broekhuizen, Helen J. Fraser, Stephan Schlemmer, Ewine F. van Dishoeck, and Harold Linnartz. Comparative studies of o2 and n2 in pure, mixed and layered co ices. *Faraday Discuss.*, 133:331–345, 2006. doi: 10.1039/B517262B. URL http://dx.doi.org/10.1039/B517262B.

R. T. Garrod and E. Herbst. Formation of methyl formate and other organic species in the warm-up phase of hot molecular cores. A&A, 457:927–936, October 2006. doi: 10.1051/0004-6361:20065560.

R. T. Garrod, S. L. Widicus Weaver, and E. Herbst. Complex Chemistry in Star-forming Regions: An Expanded Gas-Grain Warm-up Chemical Model. ApJ, 682:283–302, July 2008. doi: 10.1086/588035.

T. R. Geballe. $H^+{}_3$ between the stars. 358:2359–2559, September 2000. doi: 10.1098/rsta.2000.0663.

P. A. Gerakines, M. H. Moore, and R. L. Hudson. Ultraviolet photolysis and proton irradiation of astrophysical ice analogs containing hydrogen cyanide. Icarus, 170: 202–213, July 2004. doi: 10.1016/j.icarus.2004.02.005.

P. Ghesquière, A. Ivlev, J. A. Noble, and P. Theulé. Reactivity in interstellar ice analogs: role of the structural evolution. *Astronomy & Astrophysics*, 614: A107, jun 2018. ISSN 0004-6361. doi: 10.1051/0004-6361/201732288. URL https://www.aanda.org/10.1051/0004-6361/201732288.

E. L. Gibb, D. C. B. Whittet, W. A. Schutte, A. C. A. Boogert, J. E. Chiar, P. Ehrenfreund, P. A. Gerakines, J. V. Keane, A. G. G. M. Tielens, E. F. van Dishoeck, and O. Kerkhof. An Inventory of Interstellar Ices toward the Embedded Protostar W33A. ApJ, 536:347–356, June 2000. doi: 10.1086/308940.

Fred Goesmann, Helmut Rosenbauer, Jan Hendrik Bredehöft, Michel Cabane, Pascale Ehrenfreund, Thomas Gautier, Chaitanya Giri, Harald Krüger, Léna Le Roy, Alexandra J MacDermott, et al. Organic compounds on comet 67p/churyumov-gerasimenko revealed by cosac mass spectrometry. *Science*, 349 (6247):aab0689, 2015.

D. W. Goldsmith, H. J. Habing, and G. B. Field. Thermal Properties of Interstellar Gas Heated by Cosmic Rays. ApJ, 158:173, October 1969. doi: 10.1086/150181.

P. Gratier, J. Pety, V. Guzmán, M. Gerin, J. R. Goicoechea, E. Roueff, and A. Faure. The IRAM-30 m line survey of the Horsehead PDR. III. High abundance of complex (iso-)nitrile molecules in UV-illuminated gas, September 2013.

Tetsuya Hama, Kazuaki Kuwahata, Naoki Watanabe, Akira Kouchi, Yuki Kimura, Takeshi Chigai, and Valerio Pirronello. THE MECHANISM OF SURFACE DIFFUSION OF H AND D ATOMS ON AMORPHOUS SOLID WATER: EXISTENCE OF VARIOUS POTENTIAL SITES. *The Astrophysical Journal*, 757(2):185, oct 2012. ISSN 0004-637X. doi: 10.1088/0004-637X/757/2/185. URL http://iopscience.iop.org.ezproxy.obspm.fr/0004-637X/757/2/185/article/.

T. I. Hasegawa and E. Herbst. Three-Phase Chemical Models of Dense Interstellar Clouds - Gas Dust Particle Mantles and Dust Particle Surfaces. MNRAS, 263: 589, August 1993. doi: 10.1093/mnras/263.3.589.

T. I. Hasegawa, E. Herbst, and C. M. Leung. Models of gas-grain chemistry in dense interstellar clouds with complex organic molecules. ApJS, 82:167–195, September 1992. doi: 10.1086/191713.

Jiao He, Kinsuk Acharyya, and Gianfranco Vidali. BINDING ENERGY OF MOLECULES ON WATER ICE: LABORATORY MEASUREMENTS AND MODELING. *The Astrophysical Journal*, 825(2): 89, jul 2016. ISSN 1538-4357. doi: 10.3847/0004-637X/825/2/89. URL http://stacks.iop.org/0004-637X/825/i=2/a=89?key=crossref.8852a1ed11ced54dd92ffdaa2e2f4d58.

Jiao He, Shahnewaj M. Emtiaz, and Gianfranco Vidali. Diffusion and Clustering of Carbon Dioxide on Non-porous Amorphous Solid Water. *The Astrophysical Journal*, 837(1):65, March 2017. ISSN 1538-4357. doi: 10.3847/1538-4357/aa5f52. URL http://stacks.iop.org/0004-637X/837/i=1/a=65?key=crossref.47863a22e4adbc3271ab7d9e4c2920cc.

E. Herbst and C. M. Leung. Gas-phase production of complex hydrocarbons, cyanopolyynes, and related compounds in dense interstellar clouds. ApJS, 69: 271–300, February 1989. doi: 10.1086/191314.

E. Herbst and E. F. van Dishoeck. Complex Organic Interstellar Molecules, sep 2009a.

E. Herbst and E. F. van Dishoeck. Complex Organic Interstellar Molecules. ARA&A, 47:427–480, September 2009b. doi: 10.1146/annurev-astro-082708-101654.

Eric Herbst. The chemistry of interstellar space. *Chem. Soc. Rev.*, 30:168–176, 2001. doi: 10.1039/A909040A. URL http://dx.doi.org/10.1039/A909040A.

H. Hidaka, A. Kouchi, and N. Watanabe. Temperature, composition, and hydrogen isotope effect in the hydrogenation of co on amorphous ice surface at 10–20k. *The Journal of Chemical Physics*, 126(20):204707, 2007. doi: 10.1063/1.2735573. URL https://doi.org/10.1063/1.2735573.

H Hidaka, M Watanabe, A Kouchi, and N Watanabe. Formation of deuterated formaldehyde on low temperature surfaces: Isotope effect of quantum tunneling reactions. In *AIP Conference Proceedings*, volume 1543, pages 318–325. AIP, 2013.

K. Hiraoka, A. Yamashita, Y. Yachi, K. Aruga, T. Sato, and H. Muto. Ammonia formation from the reactions of H atoms with N atoms trapped in a solid N2 matrix at 10-30 K. ApJ, 443:363–370, April 1995. doi: 10.1086/175531.

K. Hiraoka, T. Miyagoshi, T. Takayama, K. Yamamoto, and Y. Kihara. Gas-Grain Processes for the Formation of CH_4 and H_2O: Reactions of H Atoms with C, O, and CO in the Solid Phase at 12 K. ApJ, 498:710–715, May 1998. doi: 10.1086/305572.

K. Hiraoka, A. Wada, H. Kitagawa, M. Kamo, H. Unagiike, T. Ueno, T. Sugimoto, T. Enoura, N. Sogoshi, and S. Okazaki. The Reactions of H and D Atoms with Thin Films of Formaldehyde and Methanol at Cryogenic Temperatures. ApJ, 620:542–551, February 2005. doi: 10.1086/426958.

Kenzo Hiraoka, Nagayuki Ohashi, Yosihide Kihara, Kazuyosi Yamamoto, Tetsuya Sato, and Akihiro Yamashita. Formation of formaldehyde and methanol from the reactions of H atoms with solid CO at 10?20 K. *Chemical Physics Letters*, 229(4-5):408–414, nov 1994. ISSN 00092614. doi: 10.1016/0009-2614(94)01066-8. URL http://www.sciencedirect.com/science/article/pii/0009261494010668.

Kenzo Hiraoka, Tetsuya Sato, Shoji Sato, Norihito Sogoshi, Tatsuya Yokoyama, Hideaki Takashima, and Shinichi Kitagawa. Formation of Formaldehyde by the Tunneling Reaction of H with Solid CO at 10 K Revisited. *The Astrophysical Journal*, 577(1):265–270, sep 2002. ISSN 0004-637X. doi: 10.1086/342132. URL http://iopscience.iop.org.ezproxy.obspm.fr/0004-637X/577/1/265/fulltext/.

D. J. Hollenbach, M. W. Werner, and E. E. Salpeter. Molecular Hydrogen in H i Regions. ApJ, 163:165, January 1971. doi: 10.1086/150755.

J. M. Hollis, P. R. Jewell, F. J. Lovas, and A. Remijan. Green Bank Telescope Observations of Interstellar Glycolaldehyde: Low-Temperature Sugar. ApJ, 613: L45–L48, September 2004. doi: 10.1086/424927.

J. M. Hollis, F. J. Lovas, A. J. Remijan, P. R. Jewell, V. V. Ilyushin, and I. Kleiner. Detection of Acetamide (CH_3CONH_2): The Largest Interstellar Molecule with a Peptide Bond. ApJ, 643:L25–L28, May 2006. doi: 10.1086/505110.

R. L. Hudson and M. H. Moore. Reactions of nitriles in ices relevant to Titan, comets, and the interstellar medium: formation of cyanate ion, ketenimines, and isonitriles, December 2004.

E. Iglesias. The chemical evolution of molecular clouds. ApJ, 218:697–715, December 1977. doi: 10.1086/155727.

S. Ioppolo, H. M. Cuppen, C. Romanzin, E. F. van Dishoeck, and H. Linnartz. Laboratory Evidence for Efficient Water Formation in Interstellar Ices. ApJ, 686:1474–1479, October 2008. doi: 10.1086/591506.

S. Ioppolo, Y. van Boheemen, H. M. Cuppen, E. F. van Dishoeck, and H. Linnartz. Surface formation of CO_2 ice at low temperatures. MNRAS, 413:2281–2287, May 2011. doi: 10.1111/j.1365-2966.2011.18306.x.

S Ioppolo, G Fedoseev, M Minissale, E Congiu, F Dulieu, and H Linnartz. Solid state chemistry of nitrogen oxides–part II: surface consumption of NO2. *Physical Chemistry Chemical Physics*, 16(18):8270–82, may 2014. ISSN 1463-9084. doi: 10.1039/c3cp54918f. URL http://cdsads.u-strasbg.fr/abs/2014PCCP...16.8270I.

S. Ioppolo, B. A. McGuire, X. de Vries, B. Carroll, M. Allodi, and G. Blake. THz Time-Domain Spectroscopy of Interstellar Ice Analogs. *IAU General Assembly*, 22:2257519, August 2015.

W. M. Irvine and F. P. Schloerb. Cyanide and isocyanide abundances in the cold, dark cloud TMC-1, July 1984.

I. Jiménez-Serra, A. I. Vasyunin, P. Caselli, N. Marcelino, N. Billot, S. Viti, L. Testi, C. Vastel, B. Lefloch, and R. Bachiller. The Spatial Distribution of Complex Organic Molecules in the L1544 Pre-stellar Core, October 2016.

Izaskun Jiménez-Serra, Anton I Vasyunin, Paola Caselli, Nuria Marcelino, Nicolas Billot, Serena Viti, Leonardo Testi, Charlotte Vastel, Bertrand Lefloch, and Rafael Bachiller. The spatial distribution of complex organic molecules in the l1544 pre-stellar core. *The Astrophysical Journal Letters*, 830(1):L6, 2016.

D. Jing, J. He, J. Brucato, A. De Sio, L. Tozzetti, and G. Vidali. On Water Formation in the Interstellar Medium: Laboratory Study of the O+D Reaction on Surfaces. ApJ, 741:L9, November 2011. doi: 10.1088/2041-8205/741/1/L9.

D. R. Johnson, F. J. Lovas, C. A. Gottlieb, E. W. Gottlieb, M. M. Litvak, M. Guelin, and P. Thaddeus. Detection of interstellar ethyl cyanide, December 1977.

B. M. Jones, C. J. Bennett, and R. I. Kaiser. Mechanistical Studies on the Production of Formamide (H_2NCHO) within Interstellar Ice Analogs. ApJ, 734:78, June 2011. doi: 10.1088/0004-637X/734/2/78.

J. K. Jørgensen, F. L. Schöier, and E. F. van Dishoeck. Molecular inventories and chemical evolution of low-mass protostellar envelopes. A&A, 416:603–622, March 2004. doi: 10.1051/0004-6361:20034440.

C. Kahane, C. Ceccarelli, A. Faure, and E. Caux. Detection of Formamide, the Simplest but Crucial Amide, in a Solar-type Protostar. ApJ, 763:L38, February 2013. doi: 10.1088/2041-8205/763/2/L38.

K. Kawaguchi, M. Ohishi, S.-I. Ishikawa, and N. Kaifu. Detection of isocyanoacetylene HCCNC in TMC-1, February 1992.

Greg A. Kimmel, K. P. Stevenson, Z. Dohnálek, R. Scott Smith, and Bruce D. Kay. Control of amorphous solid water morphology using molecular beams. i. experimental results. *The Journal of Chemical Physics*, 114(12):5284–5294, 2001. doi: 10.1063/1.1350580. URL https://doi.org/10.1063/1.1350580.

David A. King and Michael G. Wells. Molecular beam investigation of adsorption kinetics on bulk metal targets: Nitrogen on tungsten. *Surface Science*, 29(2):454–482, feb 1972. ISSN 0039-6028. doi: 10.1016/0039-6028(72)90232-4. URL https://www.sciencedirect.com/science/article/pii/0039602872902324?via{%}3Dihub.

C. Knez, A. C. A. Boogert, K. M. Pontoppidan, J. Kessler-Silacci, E. F. van Dishoeck, N. J. Evans, II, J.-C. Augereau, G. A. Blake, and F. Lahuis. Spitzer Mid-Infrared Spectroscopy of Ices toward Extincted Background Stars. ApJ, 635:L145–L148, December 2005. doi: 10.1086/499584.

Hitomi Kobayashi, Hiroshi Hidaka, Thanja Lamberts, Tetsuya Hama, Hideyo Kawakita, Johannes Kästner, and Naoki Watanabe. Hydrogenation and Deuteration of C ₂ H ₂ and C ₂ H ₄ on Cold Grains: A Clue to the Formation Mechanism of C

₂ H ₆ with Astronomical Interest. *The Astrophysical Journal*, 837(2):155, mar 2017. ISSN 1538-4357. doi: 10.3847/1538-4357/837/2/155. URL http://stacks.iop.org/0004-637X/837/i=2/a=155?key=crossref.517056deae36314c68f32c6f9d8414c4.

L. E. Kristensen, E. F. van Dishoeck, T. A. van Kempen, H. M. Cuppen, C. Brinch, J. K. Jørgensen, and M. R. Hogerheijde. Methanol maps of low-mass protostellar systems. *Astronomy and Astrophysics*, 516:A57, jun 2010. ISSN 0004-6361. doi: 10.1051/0004-6361/201014182. URL http://dx.doi.org/10.1051/0004-6361/201014182.

L. E. Kristensen, L. Amiaud, J.-H. Fillion, F. Dulieu, and J.-L. Lemaire. H 2 , HD, and D 2 abundances on ice-covered dust grains in dark clouds. *Astronomy & Astrophysics*, 527:A44, jan 2011. ISSN 0004-6361. doi: 10.1051/0004-6361/200912124. URL http://www.aanda.org/articles/aa/full{_}html/2011/03/aa12124-09/aa12124-09.html.

Kuhs, W. F., Bliss, D. V., and Finney, J. L. High-resolution neutron powder diffraction study of ice ic. *J. Phys. Colloques*, 48:C1–631–C1–636, 1987. doi: 10.1051/jphyscol:1987187. URL https://doi.org/10.1051/jphyscol:1987187.

M. Lattelais, F. Pauzat, Y. Ellinger, and C. Ceccarelli. Interstellar Complex Organic Molecules and the Minimum Energy Principle. ApJ, 696:L133–L136, May 2009. doi: 10.1088/0004-637X/696/2/L133.

M. Lattelais, M. Bertin, H. Mokrane, C. Romanzin, X. Michaut, P. Jeseck, J.-H. Fillion, H. Chaabouni, E. Congiu, F. Dulieu, S. Baouche, J.-L. Lemaire, F. Pauzat, J. Pilmé, C. Minot, and Y. Ellinger. Differential adsorption of complex organic molecules isomers at interstellar ice surfaces, August 2011.

Trish Lauck, Leendertjan Karssemeijer, Katherine Shulenberger, Mahesh Rajappan, Karin I. Öberg, and Herma M. Cuppen. CO DIFFUSION INTO AMORPHOUS H $_2$ O ICES. *The Astrophysical Journal*, 801 (2):118, March 2015. ISSN 1538-4357. doi: 10.1088/0004-637X/801/2/118. URL http://stacks.iop.org/0004-637X/801/i=2/a=118?key=crossref.d0cb8ebe90a91565040062f219bc5e5c.

R. J. Laureijs, F. O. Clark, and T. Prusti. IRAS detection of very cold dust in the LYNDS 134 cloud complex. ApJ, 372:185–193, May 1991. doi: 10.1086/169963.

R. Le Gal, P. Hily-Blant, A. Faure, G. Pineau des Forêts, C. Rist, and S. Maret. Interstellar chemistry of nitrogen hydrides in dark clouds. *Astronomy & Astrophysics*, 562:A83, feb 2014. ISSN 0004-6361. doi: 10.1051/0004-6361/201322386. URL http://www.aanda.org/10.1051/0004-6361/201322386.

L. Le Roy, K. Altwegg, H. Balsiger, J.-J. Berthelier, A. Bieler, C. Briois, U. Calmonte, M. R. Combi, J. De Keyser, F. Dhooghe, B. Fiethe, S. A. Fuselier, S. Gasc, T. I. Gombosi, M. Hässig, A. Jäckel, M. Rubin, and C.-Y. Tzou. Inventory of the volatiles on comet 67P/Churyumov-Gerasimenko from Rosetta/ROSINA. A&A, 583:A1, November 2015. doi: 10.1051/0004-6361/201526450.

J. Lequeux. The Interstellar Medium. 2005. doi: 10.1007/b137959.

Christina M. B. Line and R. W. Whitworth. A high resolution neutron powder diffraction study of d2o ice xi. *The Journal of Chemical Physics*, 104(24): 10008–10013, 1996. doi: 10.1063/1.471745. URL https://doi.org/10.1063/1.471745.

H. S. Liszt and B. E. Turner. Microwave detection of interstellar NO. ApJ, 224: L73–L76, September 1978. doi: 10.1086/182762.

A. López, B. Tercero, Z. Kisiel, A. M. Daly, C. Bermúdez, H. Calcutt, N. Marcelino, S. Viti, B. J. Drouin, I. R. Medvedev, C. F. Neese, L. Pszczółkowski, J. L. Alonso, and J. Cernicharo. Laboratory characterization and astrophysical detection of vibrationally excited states of vinyl cyanide in Orion-KL, December 2014.

A. López-Sepulcre, A. A. Jaber, E. Mendoza, B. Lefloch, C. Ceccarelli, C. Vastel, R. Bachiller, J. Cernicharo, C. Codella, C. Kahane, M. Kama, and M. Tafalla. Shedding light on the formation of the pre-biotic molecule formamide with ASAI. MNRAS, 449:2438–2458, May 2015. doi: 10.1093/mnras/stv377.

A López-Sepulcre, Ali A Jaber, E Mendoza, B Lefloch, C Ceccarelli, C Vastel, R Bachiller, J Cernicharo, C Codella, C Kahane, et al. Shedding light on the formation of the pre-biotic molecule formamide with asai. *Monthly Notices of the Royal Astronomical Society*, 449(3):2438–2458, 2015.

R. Luna, R. Luna-Ferrándiz, C. Millán, M. Domingo, G. M. Muñoz Caro, C. Santonja, and M. Á. Satorre. A Fast, Direct Procedure to Estimate the Desorption Energy for Various Molecular Ices of Astrophysical Interest. ApJ, 842:51, June 2017. doi: 10.3847/1538-4357/aa7562.

G. Manicò, G. Ragunì, V. Pirronello, J. E. Roser, and G. Vidali. Laboratory Measurements of Molecular Hydrogen Formation on Amorphous Water Ice. ApJ, 548:L253–L256, February 2001. doi: 10.1086/319116.

E. Matar, E. Congiu, F. Dulieu, A. Momeni, and J. L. Lemaire. Mobility of d atoms on porous amorphous water ice surfaces under interstellar conditions. *Astronomy and Astrophysics*, 492:L17, 2008.

J. S. Mathis, W. Rumpl, and K. H. Nordsieck. The size distribution of interstellar grains. ApJ, 217:425–433, October 1977. doi: 10.1086/155591.

R. Alan May, R. Scott Smith, and Bruce D. Kay. The release of trapped gases from amorphous solid water films. I. "Top-down" crystallization-induced crack propagation probed using the molecular volcano. *The Journal of Chemical Physics*, 138(10):104501, March 2013. ISSN 0021-9606, 1089-7690. doi: 10.1063/1.4793311. URL http://aip.scitation.org/doi/10.1063/1.4793311.

Adam J. McKay, Anita L. Cochran, Michael A. DiSanti, Neil Dello Russo, Harold Weaver, Ronald J. Vervack, Walter M. Harris, and Hideyo Kawakita. Evolution of H 2 O production in comet C/2012 S1 (ISON) as inferred from forbidden oxygen and OH emission. *Icarus*, 309:1–12, July 2018. ISSN 00191035. doi: 10.1016/j.icarus.2018.02.024. URL http://linkinghub.elsevier.com/retrieve/pii/S0019103517308126.

G. J. Melnick and E. A. Bergin. The legacy of SWAS: Water and molecular oxygen in the interstellar medium. *Advances in Space Research*, 36:1027–1030, 2005. doi: 10.1016/j.asr.2005.05.110.

A. Mencos and L. Krim. Isomerization and fragmentation of acetonitrile upon interaction with N(^{4}S) atoms: the chemistry of nitrogen in dense molecular clouds, August 2016.

M. Minissale, E. Congiu, S. Baouche, H. Chaabouni, A. Moudens, F. Dulieu, M. Accolla, S. Cazaux, G. Manicó, and V. Pirronello. Quantum Tunneling of Oxygen Atoms on Very Cold Surfaces. *Physical Review Letters*, 111(5):053201, August 2013. doi: 10.1103/PhysRevLett.111.053201.

M. Minissale, E. Congiu, S. Baouche, H. Chaabouni, A. Moudens, F. Dulieu, M. Accolla, S. Cazaux, G. Manicó, and V. Pirronello. Quantum Tunneling of Oxygen Atoms on Very Cold Surfaces. *Physical Review Letters*, 111(5), July 2013. ISSN 0031-9007, 1079-7114. doi: 10.1103/PhysRevLett.111.053201. URL http://link.aps.org/doi/10.1103/PhysRevLett.111.053201.

M. Minissale, E. Congiu, G. Manicò, V. Pirronello, and F. Dulieu. CO_2 formation on interstellar dust grains: a detailed study of the barrier of the CO + O channel. A&A, 559:A49, November 2013. doi: 10.1051/0004-6361/201321453.

M. Minissale, E. Congiu, and F. Dulieu. Oxygen diffusion and reactivity at low temperature on bare amorphous olivine-type silicate. J. Chem. Phys., 140(7): 074705, February 2014. doi: 10.1063/1.4864657.

M. Minissale, E. Congiu, and F. Dulieu. Oxygen diffusion and reactivity at low temperature on bare amorphous olivine-type silicate. *The Journal of Chemical Physics*, 140(7):074705, February 2014a. ISSN 0021-9606, 1089-7690. doi: 10.1063/1.4864657. URL http://aip.scitation.org/doi/10.1063/1.4864657.

M. Minissale, G. Fedoseev, E. Congiu, S. Ioppolo, F. Dulieu, and H. Linnartz. Solid state chemistry of nitrogen oxides – Part I: surface consumption of NO. *Phys. Chem. Chem. Phys.*, 16(18):8257–8269, 2014b. ISSN 1463-9076, 1463-9084. doi: 10.1039/C3CP54917H. URL http://xlink.rsc.org/?DOI=C3CP54917H.

M. Minissale, F. Dulieu, S. Cazaux, and S. Hocuk. Dust as interstellar catalyst: I. Quantifying the chemical desorption process. *Astronomy and Astrophysics*, 585, 2016. ISSN 14320746 00046361. doi: 10.1051/0004-6361/201525981.

M. Minissale, A. Moudens, S. Baouche, H. Chaabouni, and F. Dulieu. Hydrogenation of CO-bearing species on grains: unexpected chemical desorption of CO. MNRAS, 458:2953–2961, May 2016. doi: 10.1093/mnras/stw373.

M. Minissale, T. Nguyen, and F. Dulieu. To be changed. *Astronomy & Astrophysics*, 577:A2, apr 2018. ISSN 0004-6361. doi: -. URL http://www.aanda.org/10.1051/0004-6361/201424342.

Marco Minissale. *Physique et Chimie sur la surface de la poussière interstellaire : effet de la diffusion des atomes d'oxygène et de la désorption chimique sur le réseau chimique H-C-N-O*. PhD thesis, 2014. URL http://www.theses.fr/2014CERG0721. Thèse de doctorat dirigée par Dulieu, François et Pirronello, Valerio Sciences de la terre et de l'univers - Cergy Cergy-Pontoise 2014.

Minissale, M., Congiu, E., and Dulieu, F. Direct measurement of desorption and diffusion energies of o and n atoms physisorbed on amorphous surfaces. *A&A*, 585:A146, 2016. doi: 10.1051/0004-6361/201526702. URL https://doi.org/10.1051/0004-6361/201526702.

F. Mispelaer, P. Theulé, H. Aouididi, J. Noble, F. Duvernay, G. Danger, P. Roubin, O. Morata, T. Hasegawa, and T. Chiavassa. Diffusion measurements of CO,

HNCO, H_2CO, and NH_3 in amorphous water ice. *Astronomy & Astrophysics*, 555:A13, July 2013. ISSN 0004-6361, 1432-0746. doi: 10.1051/0004-6361/201220691. URL http://www.aanda.org/10.1051/0004-6361/201220691.

H. Miura, T. Yamamoto, H. Nomura, T. Nakamoto, K. K. Tanaka, H. Tanaka, and M. Nagasawa. Comprehensive Study of Thermal Desorption of Grain-surface Species by Accretion Shocks around Protostars. ApJ, 839:47, April 2017. doi: 10.3847/1538-4357/aa67df.

N. Miyauchi, H. Hidaka, T. Chigai, A. Nagaoka, N. Watanabe, and A. Kouchi. Formation of hydrogen peroxide and water from the reaction of cold hydrogen atoms with solid oxygen at 10 K. *Chemical Physics Letters*, 456:27–30, April 2008. doi: 10.1016/j.cplett.2008.02.095.

H. Mokrane, H. Chaabouni, M. Accolla, E. Congiu, F. Dulieu, M. Chehrouri, and J. L. Lemaire. EXPERIMENTAL EVIDENCE FOR WATER FORMATION VIA OZONE HYDROGENATION ON DUST GRAINS AT 10 K. *The Astrophysical Journal*, 705(2):L195–L198, nov 2009. ISSN 0004-637X. doi: 10.1088/0004-637X/705/2/L195. URL http://iopscience.iop.org.ezproxy.obspm.fr/1538-4357/705/2/L195/article/.

Sebastien Muller, A Beelen, John H Black, SJ Curran, Cathy Horellou, Susanne Aalto, F Combes, M Guélin, and C Henkel. A precise and accurate determination of the cosmic microwave background temperature at z= 0.89. *Astronomy & Astrophysics*, 551:A109, 2013.

Michael J Mumma and Steven B Charnley. The chemical composition of comets—emerging taxonomies and natal heritage. *Annual Review of Astronomy and Astrophysics*, 49:471–524, 2011.

K. Murphy, S. Azad, D.W. Bennett, and W.T. Tysoe. Adsorption, decomposition and isomerization of methyl isocyanide and acetonitrile on pd(111), 2000. ISSN 0039-6028. URL http://www.sciencedirect.com/science/article/pii/S0039602800008074.

Javier Navarro-Ruiz, Mariona Sodupe, Piero Ugliengo, Albert Rimola, G. Vidali, and R. Dovesi. Interstellar H adsorption and H ₂ formation on the crystalline (010) forsterite surface: a B3LYP-D2* periodic study. *Physical Chemistry Chemical Physics*, 16(33):17447, apr 2014. ISSN 1463-9076. doi: 10.1039/C4CP00819G. URL http://xlink.rsc.org/?DOI=C4CP00819G.

T. Nguyen, others, and F. Dulieu. To be changed. *Astronomy & Astrophysics*, 577:A2, apr 2018. ISSN 0004-6361. doi: -. URL http://www.aanda.org/10.1051/0004-6361/201424342.

J. A. Noble, F. Dulieu, E. Congiu, and H. J. Fraser. CO_2 Formation in Quiescent Clouds: An Experimental Study of the CO + OH Pathway. ApJ, 735:121, July 2011. doi: 10.1088/0004-637X/735/2/121.

J. A. Noble, P. Theule, F. Mispelaer, F. Duvernay, G. Danger, E. Congiu, F. Dulieu, and T. Chiavassa. The desorption of H 2 CO from interstellar grains analogues. *Astronomy & Astrophysics*, 543:A5, jun 2012. ISSN 0004-6361. doi: 10.1051/0004-6361/201219437. URL http://www.aanda.org/articles/aa/full{_}html/2012/07/aa19437-12/aa19437-12.html.

J. A. Noble, P. Theule, E. Congiu, F. Dulieu, M. Bonnin, A. Bassas, F. Duvernay, G. Danger, and T. Chiavassa. Hydrogenation at low temperatures does not always lead to saturation: the case of HNCO. A&A, 576:A91, April 2015. doi: 10.1051/0004-6361/201425403.

A. Nummelin, P. Bergman, Å. Hjalmarson, P. Friberg, W. M. Irvine, T. J. Millar, M. Ohishi, and S. Saito. A three-position spectral line survey of sagittarius b2 between 218 and 263 ghz. i. the observational data, 1998. URL http://stacks.iop.org/0067-0049/117/i=2/a=427.

Y. Oba, N. Miyauchi, H. Hidaka, T. Chigai, N. Watanabe, and A. Kouchi. Formation of Compact Amorphous H_2O Ice by Codeposition of Hydrogen Atoms with Oxygen Molecules on Grain Surfaces. ApJ, 701:464–470, August 2009. doi: 10.1088/0004-637X/701/1/464.

Y. Oba, N. Watanabe, A. Kouchi, T. Hama, and V. Pirronello. Experimental Study of CO_2 Formation by Surface Reactions of Non-energetic OH Radicals with CO Molecules. ApJ, 712:L174–L178, April 2010. doi: 10.1088/2041-8205/712/2/L174.

Y. Oba, N. Watanabe, A. Kouchi, T. Hama, and V. Pirronello. Neutral radical-molecule reactions CO + OH on cold interstellar ices. In J. Cernicharo and R. Bachiller, editors, *The Molecular Universe*, volume 280 of *IAU Symposium*, page 278, May 2011.

Y. Oba, N. Watanabe, T. Hama, K. Kuwahata, H. Hidaka, and A. Kouchi. Water Formation through a Quantum Tunneling Surface Reaction, OH + H_2, at 10 K. ApJ, 749:67, April 2012. doi: 10.1088/0004-637X/749/1/67.

Y. Oba, T. Tomaru, T. Lamberts, A. Kouchi, and N. Watanabe. An infrared measurement of chemical desorption from interstellar ice analogues. *Nature Astronomy*, 2(3):228–232, mar 2018. ISSN 2397-3366. doi: 10.1038/s41550-018-0380-9. URL http://www.nature.com/articles/s41550-018-0380-9.

Yasuhiro Oba, Takeshi Chigai, Yoshihiro Osamura, Naoki Watanabe, and Akira Kouchi. Hydrogen isotopic substitution of solid methylamine through atomic surface reactions at low temperatures: A potential contribution to the D/H ratio of methylamine in molecular clouds, jan 2014. ISSN 10869379. URL http://doi.wiley.com/10.1111/maps.12096.

K. I. Öberg, F. van Broekhuizen, H. J. Fraser, S. E. Bisschop, E. F. van Dishoeck, and S. Schlemmer. Competition between CO and N_2 Desorption from Interstellar Ices. ApJ, 621:L33–L36, March 2005. doi: 10.1086/428901.

K. I. Öberg, A. C. A. Boogert, K. M. Pontoppidan, S. van den Broek, E. F. van Dishoeck, S. Bottinelli, G. A. Blake, and N. J. Evans, II. The Spitzer Ice Legacy: Ice Evolution from Cores to Protostars. ApJ, 740:109, October 2011. doi: 10.1088/0004-637X/740/2/109.

C. W. Ormel, D. Paszun, C. Dominik, and A. G. G. M. Tielens. Dust coagulation and fragmentation in molecular clouds. I. How collisions between dust aggregates alter the dust size distribution. A&A, 502:845–869, August 2009. doi: 10.1051/0004-6361/200811158.

Grazyna E. Orzechowska, Jay D. Goguen, Paul V. Johnson, Alexandre Tsapin, and Isik Kanik. Ultraviolet photolysis of amino acids in a 100 K water ice matrix: Application to the outer Solar System bodies. *Icarus*, 187(2):584–591, April 2007. ISSN 00191035. doi: 10.1016/j.icarus.2006.10.018. URL http://linkinghub.elsevier.com/retrieve/pii/S0019103506003721.

L. Pagani, J.-R. Pardo, A. J. Apponi, A. Bacmann, and S. Cabrit. L183 (L134N) revisited. III. The gas depletion. A&A, 429:181–192, January 2005. doi: 10.1051/0004-6361:20041044.

L. Pagani, J. Steinacker, A. Bacmann, A. Stutz, and T. Henning. The Ubiquity of Micrometer-Sized Dust Grains in the Dense Interstellar Medium. *Science*, 329:1622, September 2010. doi: 10.1126/science.1193211.

L. Pagani, A. Bourgoin, and F. Lique. A method to measure CO and N_2 depletion profiles inside prestellar cores. A&A, 548:L4, December 2012. doi: 10.1051/0004-6361/201220137.

L. Pagani, C. Favre, P. F. Goldsmith, E. A. Bergin, R. Snell, and G. Melnick. The complexity of Orion: an ALMA view. *Astronomy & Astrophysics*, 604: A32, aug 2017. ISSN 0004-6361. doi: 10.1051/0004-6361/201730466. URL http://www.aanda.org/10.1051/0004-6361/201730466.

M. E. Palumbo. Formation of compact solid water after ion irradiation at 15 K. A&A, 453:903–909, July 2006. doi: 10.1051/0004-6361:20042382.

M. E. Palumbo, G. A. Baratta, G. Leto, and G. Strazzulla. H bonds in astrophysical ices. *Journal of Molecular Structure*, 972:64–67, May 2010. doi: 10.1016/j.molstruc.2009.12.017.

R. Papoular. *Monthly Notices of the Royal Astronomical Society*, 626:489–497, 2005.

V Petrenko and RW Whitworth. Physics of ice. oxford univ. 2002.

Valerio Pirronello, Chi Liu, Joe E Roser, and Gianfranco Vidali. Measurements of molecular hydrogen formation on carbonaceous grains. *Astronomy and Astrophysics*, 344:681–686, 1999.

K. M. Pontoppidan, H. J. Fraser, E. Dartois, W.-F. Thi, E. F. van Dishoeck, A. C. A. Boogert, L. d'Hendecourt, A. G. G. M. Tielens, and S. E. Bisschop. A 3-5 μ m VLT spectroscopic survey of embedded young low mass stars I. Structure of the CO ice. A&A, 408:981–1007, September 2003. doi: 10.1051/0004-6361: 20031030.

K. M. Pontoppidan, E. F. van Dishoeck, and E. Dartois. Mapping ices in protostellar environments on 1000 AU scales. Methanol-rich ice in the envelope of Serpens SMM 4. A&A, 426:925–940, November 2004. doi: 10.1051/0004-6361:20041276.

K. M. Pontoppidan, A. C. A. Boogert, H. J. Fraser, E. F. van Dishoeck, G. A. Blake, F. Lahuis, K. I. Öberg, N. J. Evans, II, and C. Salyk. The c2d Spitzer Spectroscopic Survey of Ices around Low-Mass Young Stellar Objects. II. CO_2. ApJ, 678:1005–1031, May 2008. doi: 10.1086/533431.

Klaus M. Pontoppidan, Cornelis P. Dullemond, Ewine F. van Dishoeck, Geoffrey A. Blake, Adwin C. A. Boogert, Neal J. Evans II, Jacqueline E. Kessler-Silacci, and Fred Lahuis. Ices in the edge-on disk crbr 2422.8-3423: Spitzer spectroscopy and monte carlo radiative transfer modeling. *The Astrophysical Journal*, 622(1):463, 2005. URL http://stacks.iop.org/0004-637X/622/i=1/a=463.

C. Qi, K. I. Öberg, and D. J. Wilner. H_2CO and N_2H^+ in Protoplanetary Disks: Evidence for a CO-ice Regulated Chemistry. ApJ, 765:34, March 2013. doi: 10.1088/0004-637X/765/1/34.

C. Qi, K. I. Öberg, S. M. Andrews, D. J. Wilner, E. A. Bergin, A. M. Hughes, M. Hogherheijde, and P. D'Alessio. Chemical Imaging of the CO Snow Line in the HD 163296 Disk. ApJ, 813:128, November 2015. doi: 10.1088/0004-637X/813/2/128.

D. Quénard, I. Jiménez-Serra, S. Viti, J. Holdship, and A. Coutens. Chemical modelling of complex organic molecules with peptide-like bonds in star-forming regions. MNRAS, 474:2796–2812, February 2018. doi: 10.1093/mnras/stx2960.

R. Scott Smith, C. Huang, , and Bruce D. Kay*. Evidence for Molecular Translational Diffusion during the Crystallization of Amorphous Solid Water. *Journal of Physical Chemistry B*, 101:6123–6126, 1997. doi: 10.1021/JP963278F. URL https://pubs.acs.org/doi/abs/10.1021/jp963278f{#}.

U. Raut, M. Famá, M. J. Loeffler, and R. A. Baragiola. Cosmic Ray Compaction of Porous Interstellar Ices. ApJ, 687:1070–1074, November 2008. doi: 10.1086/592193.

P. Redondo, C. Barrientos, and A. Largo. Some Insights into Formamide Formation through Gas-phase Reactions in the Interstellar Medium. ApJ, 780:181, January 2014. doi: 10.1088/0004-637X/780/2/181.

Anthony J. Remijan, J. M. Hollis, F. J. Lovas, D. F. Plusquellic, and P. R. Jewell. Interstellar isomers: The importance of bonding energy differences, 2005. URL http://stacks.iop.org/0004-637X/632/i=1/a=333.

Albert Rimola, Vianney Taquet, Piero Ugliengo, Nadia Balucani, and Cecilia Ceccarelli. Combined quantum chemical and modeling study of CO hydrogenation on water ice. *Astronomy & Astrophysics*, 572:A70, dec 2014. ISSN 0004-6361. doi: 10.1051/0004-6361/201424046. URL http://www.aanda.org/articles/aa/full{_}html/2014/12/aa24046-14/aa24046-14.html.

J. E. Roser, G. Manicò, V. Pirronello, and G. Vidali. Formation of Molecular Hydrogen on Amorphous Water Ice: Influence of Morphology and Ultraviolet Exposure. ApJ, 581:276–284, December 2002. doi: 10.1086/344200.

Maxime Ruaud, Valentine Wakelam, and Franck Hersant. Gas and grain chemical composition in cold cores as predicted by the Nautilus three-phase model. *Monthly Notices of the Royal Astronomical Society*, 459(4):3756–3767, jul 2016.

ISSN 0035-8711. doi: 10.1093/mnras/stw887. URL https://academic.oup.com/mnras/article-lookup/doi/10.1093/mnras/stw887.

R. H. Rubin, G. W. Swenson, Jr., R. C. Benson, H. L. Tigelaar, and W. H. Flygare. Microwave Detection of Interstellar Formamide. ApJ, 169:L39, October 1971. doi: 10.1086/180810.

Raffaele Saladino, Giorgia Botta, Samanta Pino, Giovanna Costanzo, and Ernesto Di Mauro. Genetics first or metabolism first? the formamide clue. *Chemical Society Reviews*, 41(16):5526–5565, 2012.

S. A. Sandford, J. Aléon, C. M. O. '. Alexander, T. Araki, S. Bajt, G. A. Baratta, J. Borg, J. P. Bradley, D. E. Brownlee, J. R. Brucato, M. J. Burchell, H. Busemann, A. Butterworth, S. J. Clemett, G. Cody, L. Colangeli, G. Cooper, L. D'Hendecourt, Z. Djouadi, J. P. Dworkin, G. Ferrini, H. Fleckenstein, G. J. Flynn, I. A. Franchi, M. Fries, M. K. Gilles, D. P. Glavin, M. Gounelle, F. Grossemy, C. Jacobsen, L. P. Keller, A. L. D. Kilcoyne, J. Leitner, G. Matrajt, A. Meibom, V. Mennella, S. Mostefaoui, L. R. Nittler, M. E. Palumbo, D. A. Papanastassiou, F. Robert, A. Rotundi, C. J. Snead, M. K. Spencer, F. J. Stadermann, A. Steele, T. Stephan, P. Tsou, T. Tyliszczak, A. J. Westphal, S. Wirick, B. Wopenka, H. Yabuta, R. N. Zare, and M. E. Zolensky. Organics Captured from Comet 81P/Wild 2 by the Stardust Spacecraft, December 2006.

P. Schilke, D. J. Benford, T. R. Hunter, D. C. Lis, and T. G. Phillips. A Line Survey of Orion-KL from 607 to 725 GHZ, February 2001.

R. Scott Smith, C. Huang, and B. D. Kay. Evidence for molecular translational diffusion during the crystallization of amorphous solid water. *The Journal of Physical Chemistry B*, 101(32):6123–6126, 1997. doi: 10.1021/jp963278f. URL http://dx.doi.org/10.1021/jp963278f.

Bethmini Senevirathne, Stefan Andersson, Francois Dulieu, and Gunnar Nyman. Hydrogen atom mobility, kinetic isotope effects and tunneling on interstellar ices (I h and ASW). *Molecular Astrophysics*, 6:59–69, 2017. doi: 10.1016/j.molap.2017.01.005.

R J Shannon, R L Caravan, M A Blitz, and D E Heard. A combined experimental and theoretical study of reactions between the hydroxyl radical and oxygenated hydrocarbons relevant to astrochemical environments. *Physical chemistry chemical physics : PCCP*, 16(8):3466–78, feb 2014. ISSN 1463-9084. doi: 10.1039/c3cp54664k. URL http://pubs.rsc.org.ezproxy.obspm.fr/en/content/articlehtml/2014/cp/c3cp54664k.

David Smith. The ion chemistry of interstellar clouds. *Chemical reviews*, 92(7): 1473–1485, 1992.

T. P. Snow and A. N. Witt. Interstellar Depletions Updated: Where All the Atoms Went. ApJ, 468:L65, September 1996. doi: 10.1086/310225.

L. E. Snyder, D. Buhl, P. R. Schwartz, F. O. Clark, D. R. Johnson, F. J. Lovas, and P. T. Giguere. Radio Detection of Interstellar Dimethyl Ether. ApJ, 191: L79, July 1974. doi: 10.1086/181554.

P. M. Solomon, K. B. Jefferts, A. A. Penzias, and R. W. Wilson. Detection of Millimeter Emission Lines from Interstellar Methyl Cyanide. ApJ, 168:L107, September 1971. doi: 10.1086/180794.

Robin J. Speedy, Pablo G. Debenedetti, R. Scott Smith, C. Huang, and Bruce D. Kay. The evaporation rate, free energy, and entropy of amorphous water at 150 K, 1996. ISSN 00219606. URL http://scitation.aip.org/content/aip/journal/jcp/105/1/10.1063/1.471869.

B. Stepnik, A. Abergel, J.-P. Bernard, F. Boulanger, L. Cambrésy, M. Giard, A. P. Jones, G. Lagache, J.-M. Lamarre, C. Meny, F. Pajot, F. Le Peintre, I. Ristorcelli, G. Serra, and J.-P. Torre. Evolution of dust properties in an interstellar filament. A&A, 398:551–563, February 2003. doi: 10.1051/0004-6361:20021309.

K. P. Stevenson, Greg A. Kimmel, Z. Dohnálek, R. Scott Smith, and Bruce D. Kay. Controlling the morphology of amorphous solid water. *Science*, 283(5407): 1505–1507, 1999a. ISSN 0036-8075. doi: 10.1126/science.283.5407.1505. URL http://science.sciencemag.org/content/283/5407/1505.

K. P. Stevenson, Greg A. Kimmel, Z. Dohnálek, R. Scott Smith, and Bruce D. Kay. Controlling the Morphology of Amorphous Solid Water. *Science, New Series*, 283(5407):1505–1507, 1999b. URL http://www.jstor.org/stable/2896908.

M. Tafalla, P. C. Myers, P. Caselli, C. M. Walmsley, and C. Comito. Systematic Molecular Differentiation in Starless Cores. ApJ, 569:815–835, April 2002. doi: 10.1086/339321.

Yamaguchi Takahiro, Shuro Takano, Yoshimasa Watanabe, Nami Sakai, Takeshi Sakai, Sheng-Yuan Liu, Yu-Nung Su, Naomi Hirano, Shigehisa Takakuwa, Yuri Aikawa, et al. The 3 mm spectral line survey toward the lynds 1157 b1 shocked region. i. data. *Publications of the Astronomical Society of Japan*, 64(5):105, 2012.

V. Taquet, C. Ceccarelli, and C. Kahane. Multilayer modeling of porous grain surface chemistry. I. The GRAINOBLE model. A&A, 538:A42, February 2012. doi: 10.1051/0004-6361/201117802.

V. Taquet, E. S. Wirström, S. B. Charnley, A. Faure, A. López-Sepulcre, and C. M. Persson. Chemical complexity induced by efficient ice evaporation in the Barnard 5 molecular cloud. A&A, 607:A20, October 2017. doi: 10.1051/0004-6361/201630023.

Vianney Taquet, Steven B Charnley, and Olli Sipilä. Multilayer formation and evaporation of deuterated ices in prestellar and protostellar cores. *The Astrophysical Journal*, 791(1):1, 2014.

P. Theule, F. Borget, F. Mispelaer, G. Danger, F. Duvernay, J. C. Guillemin, and T. Chiavassa. Hydrogenation of solid hydrogen cyanide HCN and methanimine CH 2 NH at low temperature, oct 2011. ISSN 0004-6361. URL http://www.aanda.org/articles/aa/full{_}html/2011/10/aa17494-11/aa17494-11.html.

P. Theulé, F. Duvernay, G. Danger, F. Borget, J.B. Bossa, V. Vinogradoff, F. Mispelaer, and T. Chiavassa. Thermal reactions in interstellar ice: A step towards molecular complexity in the interstellar medium, oct 2013. ISSN 02731177. URL http://www.sciencedirect.com/science/article/pii/S0273117713004183.

A. G. G. M. Tielens and L. J. Allamandola. *Composition, Structure, and Chemistry of Interstellar Dust*. Springer Netherlands, Dordrecht, 1987. ISBN 978-94-009-3861-8.

A. G. G. M. Tielens and W. Hagen. Model calculations of the molecular composition of interstellar grain mantles. *Astronomy and Astrophysics*, 114:245–260, 1982. URL http://cdsads.u-strasbg.fr/abs/1982A{%}26A...114..245T.

A. G. G. M. Tielens and W. Hagen. Model calculations of the molecular composition of interstellar grain mantles. A&A, 114:245–260, October 1982.

B. E. Turner. Detection of Interstellar Cyanoacetylene. ApJ, 163:L35, January 1971. doi: 10.1086/180662.

A. C. Urso, M. Chojnacki, A. McEwen, and C. Dundas. Ripple-Like Features on Recurring Slope Lineae (RSL) Fans in Valles Marineris, Mars. *LPI Contributions*, 1961:3059, May 2017.

F. A. Van Broekhuizen. *A Laboratory Route to Interstellar Ice*. PhD thesis, Leiden Observatory, Leiden University, P.O. Box 9513, 2300 RA Leiden, The Netherlands, 2005.

H. C. Van de Hulst. The solid particles in interstellar space. *Recherches Astronomiques de l'Observatoire d'Utrecht*, 11:2.i–2.50, 1946.

E. F. van Dishoeck and F. P. Helmich. Infrared absorption of H_2_O toward massive young stars. A&A, 315:L177–L180, November 1996.

E. F. Van Dishoeck, E. Herbst, and D. A. Neufeld. Interstellar Water Chemistry: From Laboratory to Observations. *Chemical Reviews*, 113:9043–9085, December 2013. doi: 10.1021/cr4003177.

Ewine F. Van Dishoeck. Iso spectroscopy of gas and dust: From molecular clouds to protoplanetary disks. *Annual Review of Astronomy and Astrophysics*, 42 (1):119–167, 2004. doi: 10.1146/annurev.astro.42.053102.134010. URL https://doi.org/10.1146/annurev.astro.42.053102.134010.

A. I. Vasyunin and E. Herbst. Reactive Desorption and Radiative Association as Possible Drivers of Complex Molecule Formation in the Cold Interstellar Medium. ApJ, 769:34, May 2013a. doi: 10.1088/0004-637X/769/1/34.

A. I. Vasyunin and E. Herbst. Reactive Desorption and Radiative Association as Possible Drivers of Complex Molecule Formation in the Cold Interstellar Medium. ApJ, 769:34, May 2013b. doi: 10.1088/0004-637X/769/1/34.

A. I. Vasyunin and Eric Herbst. Reactive desorption and radiative association as possible drivers of complex molecule formation in the cold interstellar medium, 2013. URL http://stacks.iop.org/0004-637X/769/i=1/a=34.

A. I. Vasyunin, P. Caselli, F. Dulieu, and I. Jiménez-Serra. Formation of Complex Molecules in Prestellar Cores: A Multilayer Approach. ApJ, 842:33, June 2017. doi: 10.3847/1538-4357/aa72ec.

L. Velilla Prieto, C. Sánchez Contreras, J. Cernicharo, M. Agúndez, G. Quintana-Lacaci, J. Alcolea, V. Bujarrabal, F. Herpin, K. M. Menten, and F. Wyrowski. New N-bearing species towards OH 231.8+4.2. HNCO, HNCS, HC_3N, and NO. A&A, 575:A84, March 2015. doi: 10.1051/0004-6361/201424768.

Valentine Wakelam, Emeric Bron, Stephanie Cazaux, Francois Dulieu, Cécile Gry, Pierre Guillard, Emilie Habart, Liv Hornekær, Sabine Morisset, Gunnar Nyman, Valerio Pirronello, Stephen D. Price, Valeska Valdivia, Gianfranco Vidali, and Naoki Watanabe. H2 formation on interstellar dust grains:

The viewpoints of theory, experiments, models and observations. *Molecular Astrophysics*, 9:1–36, dec 2017. ISSN 2405-6758. doi: 10.1016/J.MOLAP.2017.11.001. URL https://www.sciencedirect.com/science/article/pii/S2405675817300271?via{%}3Dihub.

M. D. Ward and S. D. Price. Thermal Reactions of Oxygen Atoms with Alkenes at Low Temperatures on Interstellar Dust. ApJ, 741:121, November 2011. doi: 10.1088/0004-637X/741/2/121.

N. Watanabe and A. Kouchi. Efficient Formation of Formaldehyde and Methanol by the Addition of Hydrogen Atoms to CO in H_2O-CO Ice at 10 K. ApJ, 571: L173–L176, June 2002. doi: 10.1086/341412.

N. Watanabe, Y. Kimura, A. Kouchi, T. Chigai, T. Hama, and V. Pirronello. Direct measurements of hydrogen atom diffusion and the spin temperature of nascent h2 molecule on amorphous solid water. *Astrophys. J. Lett.*, 714:L233, 2010.

Naoki Watanabe and Akira Kouchi. Efficient Formation of Formaldehyde and Methanol by the Addition of Hydrogen Atoms to CO in H[TINF]2[/TINF]O-CO Ice at 10 K. *The Astrophysical Journal*, 571(2):L173–L176, jun 2002. ISSN 0004637X. doi: 10.1086/341412. URL http://iopscience.iop.org.ezproxy.obspm.fr/1538-4357/571/2/L173/fulltext/.

Naoki Watanabe, Akihiro Nagaoka, Takahiro Shiraki, and Akira Kouchi. Hydrogenation of co on pure solid co and co-h2o mixed ice. *The Astrophysical Journal*, 616(1):638, 2004. URL http://stacks.iop.org/0004-637X/616/i=1/a=638.

M. S. Westley, G. A. Baratta, and R. A. Baragiola. Density and index of refraction of water ice films vapor deposited at low temperatures. *The Journal of Chemical Physics*, 108(8):3321–3326, 1998. doi: 10.1063/1.475730. URL https://doi.org/10.1063/1.475730.

David A Williams and Eric Herbst. It's a dusty universe: surface science in space. *Surface Science*, 500(1-3):823–837, 2002.

L. M. Ziurys. Interstellar Chemistry Special Feature: The chemistry in circumstellar envelopes of evolved stars: Following the origin of the elements to the origin of life, August 2006.

Viktor Zubko, Eli Dwek, and Richard G. Arendt. Interstellar dust models consistent with extinction, emission, and abundance constraints. *The Astrophysical Journal Supplement Series*, 152(2):211, 2004. URL http://stacks.iop.org/0067-0049/152/i=2/a=211.

B. Zuckerman, B. E. Turner, D. R. Johnson, F. O. Clark, F. J. Lovas, N. Fourikis, P. Palmer, M. Morris, A. E. Lilley, J. A. Ball, C. A. Gottlieb, M. M. Litvak, and H. Penfield. Detection of interstellar trans-ethyl alcohol. ApJ, 196:L99–L102, March 1975. doi: 10.1086/181753.

K. I. Öberg, E. C. Fayolle, H. M. Cuppen, E. F. van Dishoeck, and H. Linnartz. Quantification of segregation dynamics in ice mixtures. *Astronomy & Astrophysics*, 505(1):183–194, October 2009. ISSN 0004-6361, 1432-0746. doi: 10.1051/0004-6361/200912464. URL http://www.aanda.org/10.1051/0004-6361/200912464.

Karin I. Öberg, A. C. Adwin Boogert, Klaus M. Pontoppidan, Saskia van den Broek, Ewine F. van Dishoeck, Sandrine Bottinelli, Geoffrey A. Blake, and Neal J. Evans. THE *SPITZER* ICE LEGACY: ICE EVOLUTION FROM CORES TO PROTOSTARS. *The Astrophysical Journal*, 740(2): 109, October 2011. ISSN 0004-637X, 1538-4357. doi: 10.1088/0004-637X/740/2/109. URL http://stacks.iop.org/0004-637X/740/i=2/a=109?key=crossref.9c812e2f007b63b7da1047da227f4678.